



MONASH University

**The fate of transition metals during enhanced
weathering and development of geochemical treatments
for accelerated carbonation of ultramafic mine tailings**

By
Jessica Lorraine Hamilton
Bsc(Hons)

A thesis submitted for the degree of
Doctor of Philosophy

Main Supervisor: Dr. Siobhan A. Wilson
Associate Supervisors: Dr. Bree Morgan, Prof. Ian Cartwright

School of Earth, Atmosphere and Environment
Monash University, 2018

Copyright notice

© Jessica L. Hamilton (2018).

Thesis including published works declaration

I hereby declare that this thesis contains no material which has been accepted for the award of any other degree or diploma at any university or equivalent institution and that, to the best of my knowledge and belief, this thesis contains no material previously published or written by another person, except where due reference is made in the text of the thesis.

This thesis includes one original paper published in a peer reviewed journal, one currently under review, and two un-published manuscripts. The core theme of the thesis is to investigate trace metal mobility during mineral carbonation reactions, and to develop field-scalable geochemical treatments to accelerate mineral carbonation reactions in ultramafic mine tailings. The ideas, development and writing up of all the papers in the thesis were the principal responsibility of myself, the student, working within the School of Earth, Atmosphere and Environment under the supervision of Dr. Siobhan Wilson, Dr. Bree Morgan, and Prof. Ian Cartwright.

The inclusion of co-authors reflects the fact that the work came from active collaboration between researchers and acknowledges input into team-based research. In the case of chapters 2, 3, 4 and 5 my contribution to the work involved the following:

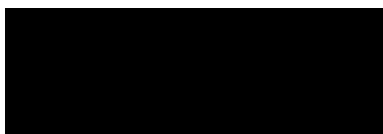
Thesis Chapter	Publication Title	Status (published, in press, accepted or returned for revision, submitted)	Nature and % of student contribution	Co-author name(s) Nature and % of Co-author's contribution*	Co-author(s), Monash student Y/N*
2	Nesquehonite sequesters transition metals and CO ₂ during accelerated carbon mineralisation	Published	79 % Concept, experimental design, data collection and interpretation, and writing. This work builds upon my honours thesis, and some preliminary results from that work (precipitation experiment and ICP-MS data) are included here. This preliminary work contributes approximately 20 % of the results presented in this chapter and it is cited where relevant.	5% - S. Wilson, supervisor 5% - B. Morgan, supervisor 3% - C. Turvey, assisted with interpretation of results 3% - D. Paterson, synchrotron XFM 3% - C. Macrae, Electron microscopy and cathodoluminescence spectroscopy 1% - J. Mccutcheon, assisted with data collection at synchrotron 1% - G. Southam, Advisor and assisted with data collection at synchrotron	N N Y N N N
3	Fate of trace metals during atmospheric	Revisions returned	79 % Concept, experimental design, data collection and	5% - S. Wilson, supervisor	N N

	carbonation of ultramafic mine tailings		interpretation, and writing. This work builds upon my honours thesis, and some preliminary results from that work (collection of samples, XRF and water chemistry analysis) are included here. This preliminary work contributes approximately 10% of the results presented in this chapter and it is cited where relevant.	5% - B. Morgan, supervisor 3% - C. Turvey, assisted with fieldwork and synchrotron data collection 3% - D. Paterson, synchrotron XFM 3% S. Jowitt, Advice and input into manuscript 1% - J. Mccutcheon, assisted with synchrotron data collection 1% - G. Southam, Advisor and assisted with synchrotron data collection	Y N N N
4	Field-based deployment of an automated geochemical treatment system for accelerating carbonation of ultramafic mine tailings: Lessons for pilot projects and carbon accounting in mined landscapes	In preparation	79 % - Conceptualisation, experimental design and construction, field work, data analysis and interpretation, writing.	5% - S. Wilson, supervisor 5% - C. Turvey, assistance in the field, and with XRD analysis 5% - B. Morgan, supervisor 3% - A. Tait, assistance in the field 1 % - S.J. Fallon, isotope data 1% - J. Mccutcheon, assistance in the field 1% - G. Southam, assistance in the field	N Y N N N
5	Accelerating mineral carbonation in ultramafic mines via direct CO ₂ reaction and heap leaching, and potential for base metal enrichment and recovery	In preparation	79 % - Conceptualisation, experimental design and construction, data collection, analysis and interpretation, modelling, and writing.	5% - S. Wilson, supervisor 5% - B. Morgan, supervisor 3% - A. Harrison, geochemical modelling advice 3% - C. Turvey, assisted with fieldwork and data	N N N Y

				collection at synchrotron	
				3% - D. Paterson, synchrotron XFM	N
				1% G. Dipple, Advisor	N
				1% - G. Southam, Advisor and assisted with data collection at synchrotron	N

I have renumbered sections of submitted or published papers in order to generate a consistent presentation within the thesis.

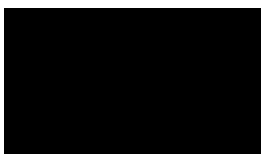
Student signature:



Date: 10 February 2018

The undersigned hereby certify that the above declaration correctly reflects the nature and extent of the student's and co-authors' contributions to this work. In instances where I am not the responsible author I have consulted with the responsible author to agree on the respective contributions of the authors.

Main Supervisor signature:



Date: 5 February 2018

Publications during enrolment

Hamilton, J.L., Wilson, S.A., Morgan, B., Turvey, C.C., Paterson, D., MacRae, C., McCutcheon, J. and Southam, G. (2016). Nesquehonite sequesters transition metals and CO₂ during accelerated carbon mineralisation. *International Journal of Greenhouse Gas Control* **55**, 73-81.

Turvey, C.C., Wilson, S.A., Hamilton, J.L. and Southam, G. (2017) Field-based accounting of CO₂ sequestration in ultramafic mine wastes using portable X-ray diffraction. *American Mineralogist* **102**, 1302-1310.

McCutcheon, J., Turvey, C.C., Wilson, S., Hamilton, J.L. and Southam, G. (2017). Field-based deployment of microbial carbonation for carbon sequestration and stabilization of asbestos mine tailings. *Minerals* **7**, 191.

Table of Contents

Copyright Notice	III
Declaration	V
List of published works	VIII
List of figures	XIV
List of tables	XXI
Acknowledgements	XXIII
Abstract	XXV

Chapter 1

<i>Introduction</i>	1
1.1. Introduction to mineral carbonation as a CO₂ mitigation strategy	2
1.2. Mineral carbonation and the minerals industry	4
1.3. Accelerating mineral carbonation of mine tailings	5
1.4. Application of the literature to the thesis	7
1.5. Layout of the thesis	8
1.6. Chapter 1 references	12

Chapter 2

<i>Nesquehonite sequesters transition metals and CO₂ during accelerated carbon mineralisation</i> ..	25
2.1. Introduction	26
2.2. Methods	
2.2.1. Laboratory experiment: sorption of transition metals to nesquehonite	29
2.2.2. Precipitate mineralogy	32
2.2.3. Trace metal distribution in the precipitate	32
2.3. Results	
2.3.1. Trace metal sorption to precipitate	34
2.3.2. Precipitate mineralogy	35
2.3.3. Trace metal distribution in nesquehonite	35
2.4. Discussion	
2.4.1. Immobilisation of trace metals by nesquehonite	38
2.4.2. Mechanism for immobilisation	39
2.4.3. Role of pH	42
2.4.4. The fate of sorbed metals in nesquehonite	43
2.4.5. Future research	45

2.1. Chapter 2 references	46
----------------------------------------	-----------

Chapter 3

<i>Fate of transition metals during passive carbonation of ultramafic mine tailings via air capture with potential for metal resource recovery</i>	57
----------------------------------------------------------------------------------------------------------------------------------------------------------	-----------

3.1. Introduction	59
--------------------------------	-----------

3.2. Methods	64
---------------------------	-----------

3.2.1. Site description	64
-------------------------------	----

3.2.2. Sample collection	65
--------------------------------	----

3.2.3. Elemental analysis	66
---------------------------------	----

3.2.4. X-ray diffraction analysis	66
-----------------------------------------	----

3.2.5. Scanning electron microscopy	67
-------------------------------------------	----

3.2.6. X-ray fluorescence microscopy	67
--------------------------------------------	----

3.3. Results.....	68
--------------------------	-----------

3.3.1. Field site observations	68
--------------------------------------	----

3.3.2. Trace metal analysis	69
-----------------------------------	----

3.3.3. Mineralogical results	70
------------------------------------	----

3.3.4. Synchrotron XFM analysis.....	72
--------------------------------------	----

3.4. Discussion	79
------------------------------	-----------

3.4.1. Mineralogical hosts of trace metals.....	79
-------------------------------------------------	----

3.4.2. Trace metal mobility during passive mineral carbonation	80
----------------------------------------------------------------------	----

3.4.3. Mg-carbonate minerals sequester trace metals in ultramafic mine tailings.....	83
--------------------------------------------------------------------------------------	----

3.4.4. Outlook for metal mobility during passive and artificially accelerated carbon mineralisation	85
-----------------------------------------------------------------------------------------------------------	----

3.5. Conclusions	88
-------------------------------	-----------

3.6. Chapter 3 references	89
----------------------------------------	-----------

Chapter 4

<i>Field-based deployment of an automated geochemical treatment system for accelerating carbonation of ultramafic mine tailings: Lessons learned for pilot projects and carbon accounting in mined landscapes</i>	104
-------------------------------------------------------------------------------------------------------------------------------------------------------------------------------------------------------------------------	------------

4.1. Introduction	106
--------------------------------	------------

4.1.1. Site description	110
-------------------------------	-----

4.2. Materials and methods.....	111
----------------------------------------	------------

4.2.1. Experimental design and sampling strategy	111
--------------------------------------------------------	-----

4.2.2. Mineralogical and geochemical response to treatment	115
------------------------------------------------------------------	-----

4.2.3. Calculation of neutralising potential	117
4.3. Results.....	119
4.3.1. Experimental deployment.....	119
4.3.2. Mineralogical and geochemical response to treatment.....	122
4.3.3. Calculating neutralising capacity	130
4.4. Discussion	131
4.4.1. Experimental deployment.....	131
4.4.2. Lessons learned for experimental design and deployment of future field trials.....	132
4.4.3. Rapid neutralisation of acid and precipitation of carbonate minerals	134
4.4.4. Resilience and regeneration of Mg-carbonate cements.....	136
4.4.5. Accurate carbon accounting requires both mineralogical and elemental abundance data	141
4.5. Conclusions	147
4.6. Chapter 4 references	151

Chapter 5

<i>Accelerating mineral carbonation at ultramafic mines via direct CO₂ reaction and heap leaching, and potential for base metal enrichment and recovery</i>	<i>163</i>
5.1. Introduction	165
5.2. Methods	169
5.2.1. Tailings material.....	169
5.2.2. Experimental design	169
5.2.2.1. Direct CO ₂ reaction experiment.....	169
5.2.2.2. Acid leaching experiment	170
5.2.3. Leachate chemistry.....	171
5.2.4. Sample processing.....	171
5.2.5. Geochemical analysis	172
5.2.6. Mineralogical analysis.....	172
5.2.7. Imaging.....	173
5.2.8. Geochemical modelling.....	174
5.3. Results.....	176
5.3.1. Direct CO ₂ reaction experiment	176
5.3.1.1. Changes in material properties.....	176
5.3.1.2. Geochemistry and mineralogy of tailings following CO ₂ injection.....	176
5.3.2. Acid leaching experiment.....	178
5.3.2.1. Changes in material properties.....	178

5.3.2.2. Leachate chemistry.....	179
5.3.2.3. Geochemistry and mineralogy of leached tailings	181
5.3.2.4. Mineralogy of leachate precipitates.....	188
5.3.2.5. Geochemical modelling.....	189
5.4. Discussion	193
5.4.1. Direct reaction with flue gas as a short-term carbonation treatment	193
5.4.2. Increase in cementation after reaction with CO ₂	195
5.4.3. Acid heap leaching produces high-Mg leachates	197
5.4.4. Aqueous sulfate limits effectiveness of carbon sequestration	202
5.4.5. Acid leaching leads to enrichment of trace metals	205
5.4.6. Implications for Ni recovery from low-grade ultramafic ore or tailings	209
5.5. Conclusions	210
5.6. Chapter 5 references	211
Chapter 6	
<i>Synthesis and discussion of future research directions</i>	<i>223</i>
6.1. Understanding the fate of trace metals during mineral carbonation	225
6.2. Carbon accounting for accreditation under carbon credit schemes.....	226
6.3. Scaling up geochemical treatments to pilot projects and implementation	228
6.4. Summary of incentives for uptake of mineral carbonation within the mining industry .	229
6.4.1. Direct economic benefits for emissions reduction	230
6.4.2. Waste management.....	231
6.4.3. Production of valuable by-products.....	231
6.4.4. The opportunity to market mineral resources with “green credentials”	231
5.6. Chapter 6 references	232
Appendix 1	
<i>Supporting information for Chapter 2.....</i>	<i>240</i>
Appendix 2	
<i>Supporting information for Chapter 3.....</i>	<i>248</i>
Appendix 3	
<i>Supporting information for Chapter 4.....</i>	<i>256</i>
Appendix 4	
<i>Supporting information for Chapter 5.....</i>	<i>273</i>

List of Figures

Chapter 2

Figure 2.1. BSE micrographs and EPMA maps (coloured) of cross sections through metal-doped nesquehonite crystals. BSE and EPMA data for samples of nesquehonite doped with Cr (A and B), Cu (C and D), Ni (E and F), Co (G and H), and Mn (I and J). 36

Figure 2.2. (A) BSE micrograph of nesquehonite crystals containing Mn (Sample 48 h, 100 mg/L) with sylvite visible as a white precipitate on edges. Note that the darker region in the middle of the array of nesquehonite crystals is dominated by epoxy where the precipitate is not exposed at the surface. (B) Cathodoluminescence image generated by fitting the 1.84 eV peak clearly highlights nesquehonite grains indicating substitution of Mg^{2+} by Mn^{2+} within its crystal structure. 36

Figure 2.3. Maps of spatial distribution of Ni highlight its association with nesquehonite and Fe-oxyhydroxides in the Ni-doped sample. (A) Synchrotron XFM map showing the distribution and concentration of Ni within the Ni-doped sample. (B) Ni versus Fe concentration plot, with region 1 (high Ni, low Fe) selected in the green field. (C) Region 1, highlighted in green on the Ni map, characterizes Ni uptake in nesquehonite. (D) XFM image of contaminant Fe in the Ni doped sample. (E) Ni versus Fe concentration plot, with region 2 (high Ni, high Fe) selected in the green field. (F) Region 2 is highlighted in green on the Fe map and characterises Ni uptake in Fe-bearing trace phases. 37

Chapter 3

Figure 3.1. Map of Woodsreef Mine site showing sampling locations. Labels beginning with an “L” indicate water sample locations from the four pit lakes. Solid phase tailings were collected at all other sample locations. Sample descriptions are listed in Tables S1 and S2. 65

Figure 3.2. BSE-SE micrographs showing: A) Chromite (Chr) in serpentine (Srp) in sample 13WR5-3. B) Disseminated awaruite (Awr) in a serpentine groundmass (13WR1-5). C) EDS analysis of awaruite grain indicated in panel B. D) Hydromagnesite (Hmg) nucleation on chrysotile (Ctl), with pyroaurite (13WR1-4). E) Hydromagnesite cementation of serpentine and awaruite grains in carbonated crust sample 13WR2-4. F) Pyroaurite (Pau) and hydromagnesite carbonate cement between disaggregated serpentine grains (13WR1-4). 71

Figure 3.3. (A) BSE-SEM micrograph of weathered serpentine grain and hydromagnesite precipitate, in sample 13WR2-4. (B – F) XFM element concentration maps of a serpentine grain undergoing carbonation to form hydromagnesite. Si is mapped in green, and the distribution of

each trace metal of interest, Cr, Ni, Mn, Co and Fe is mapped in purple in B, C, D, E, and F, respectively. Note the low level diffuse concentrations throughout the carbonated region, and also μm -scale higher concentrations (especially Ni, Co and Fe) representing trapped grains of minerals such as magnetite and awaruite. (G) Plot of elemental abundances, averaged across the width of the transect, from A to B through serpentine into hydromagnesite (as indicated in F). 74

Figure 3.4. Carbonate surface cement in sample 13WR2-4. (A) Photomicrograph of carbonate cement spanning space between grains at the tailings surface. (B) BSE-SEM micrograph of this area does not show cemented region of interest as it is below the surface of the thin section. (C) Association between Si and Fe from XFM data. The region representing serpentine is highlighted in the top ellipse, and the region representing hydromagnesite is highlighted in the ellipse below. (D) XFM image showing the distribution of Fe in red, Si in green and Ni in blue. (E) Region selected in C (serpentine) is highlighted in green on Fe XFM map. (F) Region selected in C (hydromagnesite) is highlighted in green on Si XFM map. Si concentrations should be treated as semi-quantitative. 77

Chapter 4

Figure 4.1. (A) Aerial image of Woodsreef Chrysotile Mine. Inset indicates the location of the mine within Australia. The experimental site is marked with an 'X' and Ironbark Creek, where water was collected for use in experiments, is indicated with an arrow. (B) Photo of the experimental site, showing the location of plots, and the experimental set up. (C) Diagram of the experimental plots including sampling locations. 112

Figure 4.2. (A) Volumetric water content data from soil moisture probes buried at 5 cm depth in each of the three experimental plots. The period of 10 days over which the equipment was deployed successfully is followed by the water tank drainage event at 3:50 pm on the 11th October. Periods of natural rainfall are indicated, as is the acid tank drainage event. (B) Expanded view showing the volumetric water content of tailings in the acid treatment plot over the duration of the event that drained the acid tank. Saturated conditions are indicated by a period of approximately 5 hours in which volumetric water content does not increase. 121

Figure 4.3. (A) Photographs of the rusted orange layer observed just below the surface of the acid plot after treatment. Bubbles are visible from the release of CO₂ from the dissolution of existing carbonate minerals. (B) Photograph of rusted orange layer within a core hole in the acid plot post-experiment. 123

Figure 4.4. Total carbon, and refined mineral abundances for hydromagnesite, pyroaurite and brucite from XRD data, with depth in acid, water and control plots. 125

Figure 4.5. Cumulative carbon contributions for calcite, pyroaurite and hydromagnesite, calculated from median abundances (refined from XRD data) and median measured total carbon (from combustion analysis). The difference between the sum of mineral C contributions and total carbon is shaded in black as unaccounted carbon. Data points are centred at the median depth of each sample interval. 126

Figure 4.6. Plot of $\delta^{13}\text{C}$ versus $F^{14}\text{C}$ data for samples from the Control-C3 vertical profile, with shaded regions indicating values typical of bedrock-derived carbonate minerals (red) and atmosphere-derived carbonate minerals (blue) modified from Oskierski et al. (2013). 127

Figure 4.7. (A) Backscattered electron (BSE) micrograph of the flaky carbonate precipitate on the surface of a serpentine grain in sample 15WRDC5-12 (sample described by Turvey et al., in prep.a). (B) Enlarged view of euhedral platelets characteristic of hydromagnesite. (C) XRD pattern of white material subsampled from a grain surface, showing the presence of hydromagnesite in the white material. A background pattern was taken of the zero-background quartz mount (in black) showing that the broad ‘humps’ in the carbonate-bearing sample indicate X-ray amorphous material. 129

Figure 4.8. Hydromagnesite abundance with depth along horizontal profiles taken inwards from the vertical face of the experimental area (Fig. 1C). 140

Chapter 5

Figure 5.1. Measured leachate chemistry from heap leaching experiment. 180

Figure 5.2. Average XRF data (with error bars extending to minimum and maximum recorded concentrations) for sampled intervals of the acid-leached and water-leached tailings. 182

Figure 5.3. Overview element concentration maps of the acid-leached (above) and water-leached column thin sections (below), showing the regions concentrated in Fe, Cr, Ni, Mn and Co. The boxed region in white shows the region selected for high resolution mapping (Figure 5.5). 184

Figure 5.4. SEM-BSE micrographs. (A) Region selected for high-resolution XFM mapping (outlined in Fig. 3). (B) Weathered serpentine grain. (C) Pitting and areas of leaching on the serpentine grain. (D) A porous, pitted serpentine grain. (E) Magnified view of D. (F) Brucite grain with Fe and Si rich rind. (G) Magnified view of F, showing Fe-oxide precipitates. (H) Transition-metal-rich brucite grain within the rusted zone. Quantitative element concentrations were extracted from the circled region from synchrotron XFM data. (I) Transition-metal-rich brucite grain from slightly deeper in the rusted zone, containing a higher Ni:Fe ratio. Quantitative element concentrations were extracted from the circled region from synchrotron XFM data. (J)

Brucite with low trace metal content is present below the rusted region and hydromagnesite is observed to precipitate on grain surfaces. 186

Figure 5.5. XFM element concentration maps (Fe, Cr, Co, Ni and Mn) are shown alongside plots of the average element concentrations of the sample as measured across the width of the XFM map. Black dots represent the depth and element concentrations within 91 grains of transition-metal-rich, spherical synthetic brucite..... 188

Figure 5.6. Photographs of precipitates formed via evaporation of leachates collected from the heap leaching column experiments. (A) Mg-sulfate phases formed from acid-treated column leachates and (B) nesquehonite formed from the water-treated column leachates. 188

Figure 5.7. MIN3P modelled pH, porosity, and mineral abundance reported as a volume fraction.190

Figure 5.8. Comparison between measured and modelled results for Mg concentration (A4) and pH (average of all acid leached replicates)..... 191

Figure 5.9. SEM-BSE micrographs of hand samples taken from the base (20–25 cm depth) of the columns with 10 % CO₂ gas. (A) Mg-carbonate cementation (water pre-treated column). (B) Enlarged view of synthetic brucite grains surrounded by carbonate cement in A. (C) Overview of Mg-carbonate cementation (water pre-treated column). (D) Flakey Mg-carbonate precipitate on a synthetic brucite grain surface (water pre-treated column). (E) Enlarged view of flakey Mg-carbonate on brucite in region shown in D. (F) Enlarged view of flakey Mg-carbonate precipitate coating a serpentine grain shown in C. (G) Hydromagnesite platelets as precipitates on serpentine grain surfaces and cement between grains (acid pre-treated column). (H) characteristic blocky morphology of nesquehonite, indispersed with chrysotile (lighter grey). (I) Nesquehonite precipitate on serpentine (water pre-treated column) 197

Appendix 1

Appendix 1: Figure S1 Modified from Hamilton (2013). (A–C) Fibroidal arrays of nesquehonite (Nsq). (D) Nesquehonite fibres coated with sylvite (Syl). (E) Evaporative crust of sylvite on finely crystalline Mg-carbonate. (F) Small sphere of Mg-carbonate fibres, possibly dypingite (Dyp?). (G and H) Baylissite (Bay). 242

Appendix 1: Figure S2 Maps of spatial distribution of Mn highlight its association with nesquehonite and Fe-oxyhydroxides in the Mn-doped sample. (A) Synchrotron XFM image showing the distribution and concentration of Mn within the Mn-doped sample. (B) Mn versus Fe concentration plot, with region 1 (high Mn, low Fe) selected in the green field. (C) Region 1, highlighted in green on the XFM Mn map, characterises Mn uptake in nesquehonite. (D) XFM

image of contaminant Fe in the Mn doped sample. (E) Mn versus Fe concentration plot, with region 2 (high Mn, high Fe) selected in the green field. (F) Region 2 is highlighted in green on the XFM Fe map and characterises Mn uptake in Fe-bearing trace phases. 243

Appendix 1: Figure S3 Maps of spatial distribution of Cu highlight its association with nesquehonite and Fe-oxyhydroxides in the Cu-doped sample. (A) Synchrotron XFM image showing the distribution and concentration of Cu within the Cu-doped sample. (B) Cu versus Fe concentration plot, with region 1 (high Cu, low Fe) selected in the green field. (C) Region 1, highlighted in green on the XFM Cu map, characterises Cu uptake in nesquehonite. (D) XFM image of contaminant Fe in the Cu doped sample. (E) Cu versus Fe concentration plot, with region 2 (high Cu, high Fe) selected in the green field. (F) Region 2 is highlighted in green on the XFM Fe map and characterises Cu uptake in Fe-bearing trace phases. 244

Appendix 1: Figure S4 Maps of spatial distribution of Cr highlight its association with nesquehonite and Fe-oxyhydroxides in the Cr-doped sample. (A) Synchrotron XFM image showing the distribution and concentration of Cr within the Cr-doped sample. (B) Cr versus Fe concentration plot, with region 1 (high Cr, low Fe) selected in the green field. (C) Region 1, highlighted in green on the XFM Cr map, characterises Cr uptake in nesquehonite. (D) XFM image of contaminant Fe in the Cr doped sample. (E) Cr versus Fe concentration plot, with region 2 (high Cr, high Fe) selected in the green field. (F) Region 2 is highlighted in green on the XFM Fe map and characterises Cr uptake in Fe-bearing trace phases. 245

Appendix 1: Figure S5 XANES data for regions representing nesquehonite, and Fe-oxyhydroxide phases, with Cr metal reference spectra from Low et al. (2015), Cr²⁺ spectra from Berry et al. (2004) and all other reference spectra from Vogel et al. (2014)..... 246

Appendix 2

Appendix 2: Figure S1 (A) Chrysotile fibres in vein. (B) Chrysotile slickenside. (C) Partially serpentinised harzburgite kernel. (D) Carbonate minerals forming in cracks appear to aid in the disintegration of serpentinite boulders into smaller cobbles. (E) Vertical carbonate crusts; field of view approximately 2 m. (F) Horizontal carbonate crust as viewed from above. Pen for scale. 249

Appendix 2: Figure S2 XANES spectra for regions shown in SI Figure 3 compared to standard spectra from the literature (Berry and O'Neill, 2004; Low et al., 2015; Vogel et al., 2014). 250

Appendix 3

Appendix 3: Figure S1. Schematic describing the experiment set up. 257

Appendix 3: Figure S2. Photo of the experiment set up.....	257
Appendix 3: Figure S3. Backscattered electron (BSE) micrograph of calcite precipitate on a serpentine grain surface, in sample 15WRDC5-12, collected from 110 to 120 cm depth in a site survey described by Turvey et al. (in prep).	258
 Appendix 4	
Appendix 4: Figure S1. CO ₂ reaction column design.	274
Appendix 4: Figure S2. Photographs of acid-leached columns at the completion of the experiment, showing the rusted layer traced in red marker, and the 2 cm and 5 cm intervals chosen for dissection marked in black on columns A1-3.	274
Appendix 4: Figure S3. Photographs taken during dissection of acid leached column (replicate A3). Note: although the red dotted line on the outside of the column shows the rusted horizon reaches approximately 4 cm depth in places, the bulk of the rusted material is present at 0.5 to 2 cm depth, in the centre of the column. The rusted horizon moved outwards with depth, intersecting the exterior of the column where the dotted red line is marked, and is not present below that point.	275
Appendix 4: Figure S3. Photographs of acid treated column (replicate A1) and water leached column (replicate W3), showing migration of the rusted layer downwards through the column over time.	280
Appendix 4: Figure S5. Isocons (Grant, 1986) plotted using average XRD data for each depth interval in water and acid leached columns.	287
Appendix 4: Figure S6. XRD plot showing mineralogy of each interval. Patterns have been offset for ease of comparison and intensity has been scaled by a factor of two to emphasise low-intensity peaks.	288
Appendix 4: Figure S7. SEM-BSE (backscattered electron) micrographs of the water-leached column. (A) Spherical, porous brucite (Bru) grains (darker grey) intermixed with serpentine (Srp) grains (lighter grey). (B) Higher magnification image of the brucite grain from A. (C) Serpentine grains, with magnetite (Mag) inclusions, at the surface of the water leached column. (D) Higher magnification image of region highlighted in C, showing hydromagnesite (Hmg) cementation at the surface of the water leached column.	293

Appendix 4: Figure S8. XRD plots of precipitates formed by evaporation of leachates from (A) water leaching, and (B) acid leaching experiment. **295**

Appendix 4: Figure S9. MIN3P acid-leaching model predictions of leachate chemistry at 7 cm, 20 cm and 1 m depth. **296**

Appendix 4: Figure S9. (A–C) Nesquehonite crystals within larger Mg-sulfate crystals, all of which precipitated during evaporation of acid-treated column leachates. **297**

List of Tables

Chapter 3

Table 3.1. Elemental abundances generated in GeoPIXE for regions selected within serpentine and hydromagnesite in Figure 3.	73
Table 3.2. Elemental abundances generated in GeoPIXE for regions highlighted in green in Figure 4E, F.	76

Chapter 4

Table 4.1. Carbon accounting using XRD data and total elemental carbon data.....	147
-----------------------------------------------------------------------------------------	-----

Appendix 1

Appendix 1: Table 1 Calculated average percentage of trace metal dopant found in the precipitate portion by ICP-MS.	241
---------------------------------------------------------------------------------------------------------------------------------	-----

Appendix 2

Appendix 2: Table S1. Site location, description, and analysis performed for sample set.....	251
Appendix 2: Table S2. Chemical analysis of water samples from pit lakes.	252
Appendix 2: Table S3. Major oxide abundance data for rock samples measured using XRF.	253
Appendix 2: Table S4. Mineralogical abundance data (in wt. %) determined using XRD.	254

Appendix 3

Appendix 3: Table S1. Water chemistry of Ironbark Creek.	258
Appendix 3: Table S2. Sample characterisation.	259
Appendix 3: Table S3. Mineralogical data.	264
Appendix 3: Table S4. Total and organic carbon measurements, and calculated estimates for the abundance of unaccounted crystallographic carbon.	269
Appendix 3: Table S5. Stable and radiogenic carbon data.	271

Appendix 4

Appendix 4: Table S1. Parameters used in MIN3P model.	275
Appendix 4: Table S2. Initial mineral abundances, input surface areas, and dissolution rate laws used in MIN3P model.....	276
Appendix 4: Table S3. Water chemistry of initial pore water and acidic water used for leaching.	276
Appendix 4: Table S4. Tailings properties after CO ₂ reaction experiment.	277
Appendix 4: Table S5. XRF data (in wt. %) for CO ₂ reacted columns.	278
Appendix 4: Table S6. Rietveld refinement results for CO ₂ reacted experiment.	279
Appendix 4: Table S7. Average tailings properties after leaching experiment.	281
Appendix 4: Table S8. Leachate chemistry for leaching experiment.	282
Appendix 4: Table S9. Volume of recovered leachates, and calculated Mg mass leached.	284
Appendix 4: Table S10. Summary of total leached Mg and calculated carbon sequestration potential (assuming Mg is precipitated as 100 % nesquehonite) in the collected leachate, the subsamples evaporated in Petri dishes, and normalised to a 1-m ² treated area.	286
Appendix 4: Table S11. XRF data (in wt. %) for water and acid leached tailings residues.....	289
Appendix 4: Table S12. Rietveld refinement results for water and acid leached tailings residues.	291
Appendix 4: Table S13. Nitrogen, carbon and hydrogen contents of precipitates evaporated from leachates. Measured mass of C in precipitates is reported as a percentage of predicted carbon mass in precipitates, as calculated from Mg-concentrations in leachate.	294

Acknowledgements

This research was supported by an Australian Government Research Training Program (RTP) Scholarship. It was also supported by student grants from the Australian Institute of Mining and Metallurgy (AusIMM), the Mineralogical Society of America, and the Mineralogical Association of Canada. Funding was also provided by Carbon Management Canada, and the New South Wales Department of Industry. Part of this research was undertaken on the X-ray Fluorescence Microscopy beamline at the Australian Synchrotron, Victoria, Australia (AS173/XFM/12767 and AS152/XFM/9393).

I would like to acknowledge the many people who contributed to this thesis. Firstly, to my supervisors Sasha Wilson, Bree Morgan and Ian Cartwright, and to the members of my advisory committee (Roberto Weinburg, Vanessa Wong, Simon Jowitt and Andrew Frierdich) who provided valuable advice along the way. Sasha and Bree in particular, your wisdom and mentorship have been guiding stars throughout this process. You inspire me to be ambitious, creative and kind, and have shaped me into a researcher and person that I'm proud to be. Thank you for giving me the freedom to lead this project, and the freedom to fail. You taught me how to find magic beans of knowledge within 'failed' experiments, which I'm sure is one of the most important lessons I may ever learn.

Connor, thank you for your friendship, help, and brains (which I have come to rely on). I'm grateful to have been able to share this journey with you, from the lab to our 'round the world adventures! Thank you Al for your help and friendship over the years, and especially for coming along on my crazy plan to acid leach a mine tailings pile. I'm sure it was the best astronaut training outside of NASA. Thanks to everyone in our EGEL lab group, and in the School of Earth, Atmosphere and Environment at Monash for a wonderful time at Monash. In particular I'm grateful to Massimo, Rachelle and Junnell for helping me with in house sample preparation and analyses, and also to the EAE administration staff, Sylvana, Katie, Emily and Christine, for always being so helpful and supportive. This project would not have been possible without the help and advice of Gordon Southam and Jenine McCutcheon from the University of Queensland, and David Paterson from the Australian Synchrotron. Anna Harrison, thank you for your patience and time in teaching me how to use MIN3P, and especially for your recent help and advice in untangling the errors during my latest attempt.

Thank you to my friends, especially the 'Possums', and Katie, who made PhD stress melt away like chocolate on a hot day. Tea parties and weekend adventures with you ensured I had a lot of fun throughout this process, and helped me keep a healthy work-life balance (most of the time).

I owe many thanks to Mum, Dad and Kate, for supporting me throughout my studies, and for being a constant source of love and support. I would not have achieved this if it wasn't for your encouragement and the example you set. Dad, thank you for fixing my leaky experiments, and for your genius and simple design ideas, which made my experiments a success. Sometimes I wondered that maybe you should have been doing this PhD. Kate, thank you for the many coffee chats and for enabling me to pretend to be an ecologist on the side.

Leroy, how can I thank you enough? You are the light of my life, and have always encouraged me to follow this path. Better still, you have followed me across the country to start the next part of my career, which I am eternally grateful for.

Abstract

Mineral carbonation is a promising strategy for CO₂ mitigation and could allow mining operations to offset their greenhouse gas emissions. This thesis investigates the fate of transition metals during both passive and accelerated carbonation of ultramafic rock and mine wastes. Understanding of metal cycling during weathering and carbonation reactions is then used to develop readily scalable geochemical strategies for accelerating mineral carbonation reactions at mine sites while mitigating metal release and optimising opportunities for metal recovery.

The first part of the thesis forms a risk assessment for accelerating silicate weathering and carbon mineralisation reactions, since metal mobility is increased by reaction of minerals with acids or elevated CO₂ in a number of accelerated mineral carbonation scenarios, including enhanced weathering of landscapes, engineered reactors, and geosequestration in mafic or ultramafic rock formations. Transition metals are found to be sequestered at concentrations of 100s of ppm within hydrated Mg-carbonate minerals, and are also present at even higher concentrations in trace Fe-(hydr)oxides in both laboratory experiments and in carbonate crusts that develop on tailings surfaces at Woodsreef Chrysotile Mine in Australia, a natural laboratory used to study passive weathering and mineral carbonation.

The second part of the thesis develops field-portable geochemical treatments to accelerate mineral carbonation in mine tailings. A fully automatic, solar-powered geochemical treatment system was developed to accelerate mineral carbonation by enhancing silicate and brucite dissolution with sulfuric acid, and by optimising soil pore-water saturation via periodic watering. Although it was deployed successfully, a fault caused early termination

of the experiment during a field trial; however, detailed mineralogical and geochemical characterisation of the tailings reveals the extent of passive weathering and carbon sequestration at Woodsreef and other mines has likely been underestimated in the past owing to the presence of X-ray amorphous phases. To address this, a more robust method for estimating carbon sequestration within minerals in ultramafic landscapes is presented.

Finally, two field-scalable methods for accelerating mineral carbonation are trialled in column experiments, which address key limitations of mineral carbonation reactions. Firstly, direct reaction of tailings with 10 % CO₂ gas is found to be an effective means of trapping CO₂ via reaction with brucite in serpentine-rich tailings on the timescale of days to weeks. Secondly, acid leaching (with 0.08 M H₂SO₄ in a heap leaching scenario) targets the dissolution of serpentine, and has the potential to produce high-Mg leachate (~2,300 mg/L Mg) for continuous carbonate precipitation over a longer timescale (months to years). Transition metals leached from the surface of the tailings are found to accumulate at a pH neutralisation horizon at depth. This transition-metal-rich horizon represents a target for reprocessing to extract valuable metals (i.e., Ni, Cr, Co and Mn). However, sulfate in leachate solutions scavenges Mg during evaporation of leachates, inhibiting the formation of Mg-carbonate via air-capture of CO₂, such that the potential for carbon sequestration is not realised (4 % of predicted carbon is sequestered). Recommendations are made to improve experimental design, and for future research to incorporate trace metal recovery into treatments of ultramafic mine tailings for accelerated mineral carbonation.

Chapter 1

Introduction

Jessica L. Hamilton^a

^aSchool of Earth, Atmosphere and Environment, Monash University,
Australia

1.1. Introduction to mineral carbonation as a CO₂ mitigation strategy

The use of fossil fuels is important for meeting our world's growing energy demands; however, their continued use has led to increased levels of anthropogenic greenhouse gases (e.g., CO₂, CH₄, N₂O) in the atmosphere (IPCC 2007, 2014). The most important of these is CO₂, whose concentration within the atmosphere has increased alarmingly in recent decades, making this gas the single largest contributor to anthropogenic radiative forcing and the major cause of global warming (IPCC, 2013; Lacis et al., 2010). CO₂ in the atmosphere has increased from a pre-industrial (pre-1750) concentration of approximately 280 ppm (IPCC, 2007) to over 400 ppm globally (Betts et al., 2016; Pearman et al., 2017). These recently measured atmospheric concentrations are considered unprecedented in at least the last 800,000 years (IPCC, 2014). As a consequence, anthropogenic increases in greenhouse gases are estimated to account for more than half of the observed global mean surface temperature rise from 1951 to 2010 (IPCC, 2013). In order to minimise potentially devastating environmental and societal impacts associated with rapid climate change, such as sea level rise, ocean acidification, and the loss of biodiversity, action must be taken to decrease the amount of anthropogenic greenhouse gas emissions (IPCC, 2014).

Governing bodies have attempted to set national and international targets and goals for limiting or reducing greenhouse gas emissions. One such international agreement, the Paris Agreement, was adopted in 2015 by 192 signatories including Australia, although notably, the United States withdrew from the agreement in 2017 (Ghezloun et al., 2017; Zhang et al., 2017). It has been recognised that merely reducing greenhouse gas emissions will not be enough to avoid the negative impacts of climate change; approximately two thirds of the available carbon emissions budget for keeping warming to below 2 degrees

Celsius (above pre-industrial levels) has already been emitted (IPCC, 2005b, 2014; Lackner, 2003; Rogelj et al., 2016). As such, methods for capturing and storing CO₂ are necessary to implement as complimentary strategies to emissions reduction, not only to prevent environmental damage in the future but to meet our current international obligations (IPCC, 2005b; Rogelj et al., 2016).

Injection of pressurised CO₂ into stable geological aquifers, depleted oil and gas fields, and deep coal seams has the greatest capacity for CO₂ disposal, and over a dozen projects have been implemented at industrial scale, starting with the Sleipner project in Norway in 1996 (Aminu et al., 2017; Herzog, 2017; IPCC, 2005a). However, integration of CO₂ capture, transport, and sub-surface storage remains a challenge and this process poses a great deal of uncertainty, especially in terms of monitoring for potential leakages, social acceptance, and engineering challenges to contain the CO₂ in place for thousands of years (Aminu et al., 2017; IPCC, 2005a; Sanna et al., 2014).

Mineral carbonation is another CO₂ sequestration strategy, which involves the reaction of alkaline minerals with CO₂ to produce carbonate minerals (Herzog, 2002; IPCC, 2005b; Lackner et al., 1995; Oelkers et al., 2008). Mineral carbonation is a natural process in the global carbon cycle, with approximately 100 Mt of carbon bound by silicate mineral weathering each year (Seifritz, 1990a). The potential for carbon sequestration is less than for conventional geological storage; however, mineral carbonation is the only type of carbon sequestration that is ‘permanent’ on a geological timescale, as the products of reaction, Mg-carbonate minerals, are environmentally benign and are known to persist at the Earth’s surface for thousands to millions of years (Herzog, 2002; IPCC, 2005b; Lackner et al., 1995; Oelkers et al., 2008; Voormeij and Simandl, 2004).

Research in mineral carbonation has largely focused on development of processes that use *ex situ* high-temperature industrial reactors (Gerdemann et al., 2007; Goff and Lackner, 1998; Krevor and Lackner, 2011; Lackner, 2002, 2003; Maroto-Valer et al., 2005; Park and Fan, 2003, 2004; Sipilä et al., 2008; Wang and Maroto-Valer, 2011; Zevenhoven and Kavaliauskaite, 2004; Zevenhoven et al., 2011). High energy penalties and financial cost (which range from \$50 to \$300 per tonne CO₂; Sanna et al., 2014) have limited the scale-up of these technologies, although pilot-scale tests have been recently conducted in Québec, Canada (Kemanche et al., 2017), or are currently undergoing, in Newcastle, Australia (Brent et al., 2015). CO₂ can also be injected into mafic to ultramafic geological formations (Kelemen et al., 2011; Matter and Kelemen, 2009; Matter et al., 2016; McGrail et al., 2017; Snæbjörnsdóttir et al., 2014); a notable trial of this strategy is the current CarbFix project in Iceland (Matter et al., 2011; Matter and Kelemen, 2009; Matter et al., 2016). This technology costs approximately (US) \$17 per tonne CO₂, which is approximately double the cost of geological storage in sedimentary basins; however, this is still far outweighed by the current cost of carbon capture and gas separation from flue gas (\$55–\$112 /tonne CO₂; Gislason and Oelkers, 2014) or direct air capture (estimated at \$100–150 US/tonne CO₂ once this technology is fully developed; climeworks.com; carbonengineering.com). Alternatively, CO₂ trapping can be promoted at Earth's surface conditions via enhanced weathering of mining and industrial wastes such as ultramafic and alumina mine tailings, coal fly ash, steel slag, and alkaline and saline wastewaters (e.g., Assima et al., 2012; Bobicki et al., 2012; Bodéan et al., 2014; Bodor et al., 2013; Hitch et al., 2009; Huijgen et al., 2005; Lottermoser, 2011; Manning et al., 2013; Mignardi et al., 2011; Montes-Hernandez et al., 2009; Pronost et al., 2012; Renforth, 2012; Washbourne et al., 2012, 2015; Wilson et al., 2006, 2009a, 2011, 2014).

1.2. Mineral carbonation and the minerals industry

The minerals industry and climate change are inextricably linked; the industry consumes a large amount of energy, while the world requires an increasing supply of raw materials to manufacture clean renewable technologies (Ali et al., 2017). In recent years, there has been a movement towards ‘sustainable development’, which dictates that as important as ensuring the supply of metals to meet the needs of society, mining should be conducted with maximum efficiency and minimal negative impact on the environment and society (Ali et al., 2017; Calas, 2017; De Villiers, 2017; Fleury and Davies, 2012). ‘Sustainable development’ initiatives are motivated when there is economic incentive, such as avoidance of penalties imposed by a carbon price, or opportunity to produce additional value (Calas, 2017; Hitch and Dipple, 2012; Power et al., 2013b).

The minerals industry is also uniquely placed to develop and benefit from mineral carbonation technologies. Ultramafic mine tailings (and other wastes such as slag and fly ash) are ideal materials for mineral carbonation, as they are relatively reactive, and have enhanced surface area due to processing (Hitch and Dipple, 2012; Wilson et al., 2009a). Passive reaction of ultramafic mine tailings already has the capacity to offset considerable emissions (Beaudoin et al., 2017; Beinlich and Austrheim, 2012; Gras et al., 2017; Oskierski et al., 2013; Pronost et al., 2012; Turvey et al., 2017; Wilson et al., 2006, 2009a,b, 2014), and if rates can be accelerated by geochemical treatments and changes to tailings management, 100% of CO₂ emissions could be offset (Power et al., 2014; Wilson et al., 2014).

1.3. Accelerating mineral carbonation of mine tailings

The key rate limiting steps for the acceleration of mineral carbonation are the slow dissolution of silicate minerals, the relatively low concentration of CO₂ in the atmosphere, and passivation of reactive mineral surfaces (e.g., Assima et al., 2013; Assima et al., 2012; Beaudoin et al., 2017; McCutcheon et al., 2015; Tremblay et al., 2011). Although considerable progress has been made in developing treatments to accelerate carbonation of mine tailings and other industrial wastes in *ex situ* reactor scenarios, widespread implementation of this technology is still inhibited by high energy requirements and costs (Kemache et al., 2017; Mouedhen et al., 2017; Power et al., 2013b). At close to ambient conditions, the abundance of brucite [Mg(OH)₂], which is a common but minor component of ultramafic rocks and mine tailings, and the abundance of chrysotile fibres, largely dictates carbonation rate (Assima et al., 2014a; Entezari Zarandi et al., 2017; Harrison et al., 2012). Acceleration of mineral carbonation reactions has been achieved in laboratory settings by directly reacting ultramafic mine tailings with elevated levels of CO₂ and maintaining pore water saturation within an optimum range (Assima et al., 2013, 2014b; Entezari Zarandi et al., 2016; Pronost et al., 2011), periodic water addition (Assima et al., 2012), and the use of additives such as inorganic or organic acids or acid-generating sulfide minerals (Power et al., 2010, 2013a; Romão et al., 2013), and the use of geomicrobial treatments (McCutcheon et al., 2017; McCutcheon et al., 2016; Power et al., 2010). The first *in situ* field-trial to accelerate mineral carbonation involved leaching of chrysotile tailings with sulfuric acid, followed by inoculation with alkalinity-producing cyanobacteria (McCutcheon et al., 2017). This trial resulted in an increase in sequestered carbon; however, the arid conditions at the site were detrimental to the health of the microbial population (McCutcheon et al., 2017). Implementation of acceleration technologies on the scale of a mining operation will require relatively low-cost, low-

energy strategies that ideally make use of conventional technology and expertise (Power et al., 2014).

Utilising waste acid or acid-generating materials produced by mining has been proposed as a low-cost means to enhance dissolution of ultramafic mineral wastes, while simultaneously remediating the waste acid (Power et al., 2010). However, both ultramafic mine tailings and acid mine drainage typically contain up to wt. % abundances of transition metals, which could be either mobilised from acid leached tailings, or introduced with the acid generating material (Olajire, 2013; Power et al., 2010). Whether there is an environmental risk associated with mobilisation of transition metals during accelerated mineral carbonation is a key unresolved question within the field, with implications not only for accelerated carbonation of mine tailings, but also of industrial alkaline wastes, geosequestration by injection of CO₂ into mafic–ultramafic formations, and proposed geo-engineering projects including enhanced weathering in natural landscapes using olivine treatments (IPCC, 2005b; Thomas et al., 2016).

1.4. Application of the literature to the thesis

This thesis resolves this question by assessing the risk of trace metal mobilisation, and the fate of trace metals in both passive and accelerated weathering scenarios. This work forms the risk assessment for implementing acid leaching treatments to mine tailings with a view to implementation on the km² scale. With the aim of paving the way towards ‘carbon neutral mining’, geochemical treatments are trialled that could realistically be employed by the mining industry to offset emissions, and which are unlikely to pose a risk to the environment by release of acidic or metalliferous drainage. A priority in the development of geochemical treatments was to not only minimise the cost of treatment design, materials, and identify value-adding by-products, but to make use of conventional

technology and expertise that are already applied within the mining industry. This is important to increase the likelihood of uptake by the industry, once economic criteria are met. Treatment strategies are trialled in the laboratory and the field, from which valuable lessons for scale-up of these technologies are reported. An improved method for accounting of carbon uptake in mine tailings is developed, and an opportunity identified for producing a secondary transition metal ore as a result of acid leaching treatments used to promote mineral carbonation.

1.5. Layout of the thesis

This thesis consists of four research papers that investigate trace metal mobility in natural ('passive') and engineered mineral carbonation scenarios. The aims of this work are to develop geochemical treatments for accelerating mineral carbonation within ultramafic mine tailings and to assess the associated risk of metal mobility. The thesis progresses from a fundamental study of trace metal uptake by the products of mineral carbonation (Chapter 2), to an investigation of trace metal mobility within a mine tailings environment undergoing mineral carbonation via passive reaction with the atmosphere (Chapter 3). This sets the groundwork for accelerated treatments to be applied, which promote mineral dissolution via reaction with inorganic acids and CO₂, and are conducted in the field (Chapter 4), and in the laboratory using column experiments (Chapter 5). Each research chapter has been written as a stand-alone manuscript, which has been prepared for submission to a peer-reviewed, international journal. Chapter 2 is published as Hamilton et al. (2016), and Chapter 3 has been accepted pending revisions by the *International Journal of Greenhouse Gas Control*. Chapter 4 has been prepared for submission to *Applied Geochemistry*, and Chapter 5 has been prepared for submission to *Economic Geology*. Accordingly, appropriate literature reviews, methodology and references are

contained within each of these chapters. Due to this structure, some repetition is unavoidable in introductory and discussion sections where background information and research themes are presented. Chapter 6 is a final integrated synthesis, which brings together relevant findings from each chapter, expands on the implications of the work and recommends future priorities for research.

The first research paper (Chapter 2) addresses a long-standing question in the field: the fate of trace metals in mineral carbonation scenarios. Experiments simulate Mg-carbonate mineral formation from metalliferous solutions to test the following hypotheses:

H1) Mg-carbonate minerals take up transition metals (Fe, Mn, Co, Cu, Ni, Cr).

H2) The risk of metalliferous drainage from solutions produced for mineral carbonation is low.

These hypotheses are addressed using a combination of Inductively Coupled Plasma Mass Spectrometry (ICP-MS), Scanning Electron Microscopy (SEM) and Energy Dispersive Spectroscopy (EDS), Electron Microprobe (EM) and Cathodoluminescence (CL) spectroscopy, and synchrotron X-ray Fluorescence Microscopy (XFM) and X-ray Absorption Near Edge Spectroscopy (XANES). Trace levels of transition metals are found to be rapidly and effectively sequestered within Mg-carbonate minerals and associated Fe-(hydr)oxide phases. Furthermore, trace metals are retained within mineral phases after recrystallisation from colloidal to mm scale crystals.

Chapter 3 extends this work by investigating natural trace metal mobility at Woodsreef Chrysotile Mine, New South Wales, Australia, where the ultramafic tailings at the site are currently undergoing mineral carbonation reactions at a rate that is several orders of magnitude above background rock weathering rates (Oskierski et al., 2013; Turvey et al.,

2017). Here, laboratory findings from Chapter 2 are tested to see whether they hold true during passive carbonation of tailings in the field:

H3) Mg-carbonate minerals sequester trace metals during passive carbonation in an ultramafic tailings storage facility.

Synchrotron XFM results are used to support bulk geochemistry and water chemistry data to show that transition metals are sequestered within Mg-carbonate cements in the reactive surface of the mine tailings storage facility at Woodsreef. Transition metals appear to be sequestered via two modes: as a diffuse concentration throughout Mg-carbonate minerals, and as μm -scale concentrations associated with Fe-bearing minerals, consistent with experimental results in Chapter 2.

Together, Chapters 2 and 3 provide a risk assessment for the use of acidic treatments to accelerate mineral dissolution for promoting mineral carbonation within mine tailings (implemented in Chapters 4 and 5).

Chapter 5 describes a small-scale demonstration of a geochemical treatment system that maintains pore water saturation at optimum levels by delivering periodic doses of acid or water in order to enhance carbonation of mine tailings. This system was deployed at Woodsreef Chrysotile Mine, in rural New South Wales, Australia to test hypothesis 4.

H4) Geochemical treatments to accelerate mineral carbonation can be implemented at field scale using relatively conventional and inexpensive technology.

The results of this trial highlight the unique challenges of scaling up geochemical treatments to the field, particularly at remote and hazardous sites. The practical lessons learned will inform future improvements in treatment design. In addition, total carbon

measurements were used for carbon accounting in this chapter, and these were compared to estimates from traditional methods involving calculation of CO₂ sequestration rates from quantitative X-ray diffraction (XRD) data, to test hypothesis 5.

H5) Directly measuring carbon content is an effective (and inexpensive) method to account for carbon sequestration by mineral carbonation.

Detailed analysis of the experimental site [by XRD, X-ray Fluorescence (XRF), total carbon analysis, and radiogenic and stable carbon isotope analysis] reveals that the amount of passive mineral carbonation at Woodsreef has been underestimated. An improved method for analysis and accounting of mineral carbonation within mine tailings and landscapes in general is presented, and demonstrates the importance of using multiple analytical techniques to constrain carbon accounting data.

Finally, two further geochemical treatments, which have been proposed as readily scalable technologies that could be implemented at currently operating mines (Power et al., 2014), are trialed in column experiments using tailings material from Woodsreef Chrysotile Mine. These experiments were designed to accelerate mineral carbonation by testing the following hypotheses:

H6) Direct reaction of Woodsreef mine tailings with 10 % CO₂ gas (simulated flue gas) results in rapid carbonation by targeting reaction of brucite.

H7) Acid leaching (simulating a heap leaching scenario) targets silicate mineral dissolution to produce a Mg-rich leachate that can be generated on the long-term (years) as a feedstock for mineral carbonation.

A doubling of carbon content is measured within columns exposed to 10 % CO₂ gas (for four weeks) using total carbon analysis. This is supported by XRD analysis which reveals

that mineralisation of CO₂ forms nesquehonite (MgCO₃·3H₂O) at the expense of brucite. Water chemistry of leachates collected from the heap leaching experiment reveals that acid leaching is effective at producing Mg-rich leachates (2,300 mg/L Mg, sustained at this concentration for 28 days), and geochemical modelling is used to predict progression of the acid leaching treatment over a one-year time frame. However, the introduction of sulfate into solution from sulfuric acid treatments inhibits Mg-carbonate formation in an evaporative setting, such that Mg-sulfate phases form instead. This is identified as a key limitation for leaching using sulfuric acid, and a priority for future research to address. Lastly, the use of synchrotron XFM allowed trace metal mobility to be investigated within the acid-leached columns, testing hypothesis 8.

H8) Trace metals mobilised during acid-leaching treatments are effectively immobilised within the mineral products of mineral carbonation, and do not pose a risk of metalliferous drainage.

Trace metals are shown to accumulate at the pH neutralisation horizon, predominantly in association with Fe-(hydr)oxides, while collected leachate samples generally contain undetectable amounts of trace metals. These results suggest that acid heap leaching could be optimised to produce a potentially re-mineable trace metal enriched horizon as a by-product of mineral carbonation treatments.

The synthesis of this thesis (Chapter 6) provides an overview of the key findings of this work, and discusses broader applications within the mining industry and in the field of climate change mitigation. This discussion highlights the challenges that remain along the road to scaling up mineral carbonation technologies, and also the opportunities that could come from achieving the goal of carbon neutral mines.

1.6. Chapter 1 references

- Ali S.H., Giurco D., Arndt N., Nickless E., Brown G., Demetriades A., Durrheim R., Enriquez M.A., Kinnaird J., Littleboy A., Meinert L.D., Oberhänsli R., Salem J., Schodde R., Schneider G., Vidal O. and Yakovleva N. (2017) Mineral supply for sustainable development requires resource governance. *Nature* 543, 367.
- Aminu M.D., Nabavi S.A., Rochelle C.A. and Manovic V. (2017) A review of developments in carbon dioxide storage. *Applied Energy* 208, 1389-1419.
- Assima G.P., Larachi F., Beaudoin G. and Molson J.W. (2012) CO₂ sequestration in chrysotile mining residues - Implication of watering and passification under environmental conditions. *Industrial & Engineering Chemistry Research* 51, 8726-8734.
- Assima G.P., Larachi F., Beaudoin G. and Molson J. (2013) Dynamics of carbon dioxide uptake in chrysotile mining residues – Effect of mineralogy and liquid saturation. *International Journal of Greenhouse Gas Control* 12, 124-135.
- Assima G.P., Larachi F., Molson J. and Beaudoin G. (2014a) Comparative study of five Québec ultramafic mining residues for use in direct ambient carbon dioxide mineral sequestration. *Chemical Engineering Journal* 245, 56-64.
- Assima G.P., Larachi F., Molson J. and Beaudoin G. (2014b) Emulation of ambient carbon dioxide diffusion and carbonation within nickel mining residues. *Minerals Engineering* 59, 39-44.
- Beaudoin G., Nowamooz A., Assima G.P., Lechat K., Gras A., Entezari Zarandi A., Kandji E.H.B., Awoh A.-S., Horswill M., Turcotte S., Larachi F., Dupuis C., Molson J., Lemieux J.-M., Maldague X., Plante B., Bussière B., Constantin M., Duchesne J., Therrien R. and Fortier R. (2017) Passive mineral carbonation of Mg-rich mine wastes by atmospheric CO₂. *Energy Procedia* 114, 6083-6086.
- Betts R.A., Jones C.D., Knight J.R., Keeling R.F. and Kennedy J.J. (2016) El Niño and a record CO₂ rise. *Nature Climate Change* 6, 806.

- Bobicki E.R., Liu Q., Xu Z. and Zeng H. (2012) Carbon capture and storage using alkaline industrial wastes. *Progress in Energy and Combustion Science* 38, 302-320.
- Bodénan F., Bourgeois F., Petiot C., Augé T., Bonfils B., Julcour-Lebigue C., Guyot F., Boukary A., Tremosa J., Lassin A., Gaucher E.C. and Chiquet P. (2014) Ex situ mineral carbonation for CO₂ mitigation: Evaluation of mining waste resources, aqueous carbonation processability and life cycle assessment (Carmex project). *Minerals Engineering* 59, 52-63.
- Bodor M., Santos R., Gerven T. and Vlad M. (2013) Recent developments and perspectives on the treatment of industrial wastes by mineral carbonation — a review. *Open Engineering* 3, 566-584.
- Brent G.F., Rayson M.S., Kennedy E.M., Stockenhuber M., Collins W.J., Prigge J.D., Hynes R.G., Molloy T.S., Zulfiqar H., Farhang F., Oliver T.O., Hamblin Wang S. and Dawe M. (2015) Mineral carbonation of serpentinite: From the Laboratory to Pilot Scale - The MCi project, *5th International Conference on Accelerated Carbonation for Environmental and Material Engineering 2015*, pp. 394-403.
- Calas G. (2017) Mineral Resources and Sustainable Development. *Elements* 13, 301-306.
- De Villiers J.P.R. (2017) How to Sustain Mineral Resources: Beneficiation and Mineral Engineering Opportunities. *Elements* 13, 307-312.
- Entezari Zarandi A., Larachi F., Beaudoin G., Plante B. and Sciortino M. (2016) Multivariate study of the dynamics of CO₂ reaction with brucite-rich ultramafic mine tailings. *International Journal of Greenhouse Gas Control* 52, 110-119.
- Fleury A.-M. and Davies B. (2012) Sustainable supply chains—minerals and sustainable development, going beyond the mine. *Resources Policy* 37, 175-178.
- Gerdemann S.J., O'Connor W.K., Dahlin D.C., Penner L.R. and Rush H. (2007) Ex situ aqueous mineral carbonation. *Environmental Science & Technology* 41, 2587-2593.

- Ghezloun A., Saidane A. and Merabet H. (2017) The COP 22 New commitments in support of the Paris Agreement. *Energy Procedia* 119, 10-16.
- Gislason S.R. and Oelkers E.H. (2014) Carbon storage in basalt. *Science* 344, 373-374.
- Goff F. and Lackner K.S. (1998) Carbon dioxide sequestering using ultramafic rocks. *Environmental Geosciences* 5, 89-102.
- Hamilton J.L., Wilson S.A., Morgan B., Turvey C.C., Paterson D.J., MacRae C., McCutcheon J. and Southam G., (2016). Nesquehonite sequesters transition metals and CO₂ during accelerated carbon mineralisation. *International Journal of Greenhouse Gas Control* 55, pp.73-81.
- Harrison A.L., Power I.M. and Dipple G.M. (2012) Accelerated carbonation of brucite in Mine Tailings for Carbon Sequestration. *Environmental Science & Technology* 47, 126-134.
- Herzog H. (2002) Carbon sequestration via mineral carbonation: Overview and assessment. MIT Laboratory for Energy and the Environment.
- Herzog, H. (2017) Financing CCS demonstration projects: Lessons learned from two decades of experience. *Energy Procedia* 114, 5691-5700.
- Hitch M., Ballantyne S.M. and Hindle S.R. (2009) Revaluing mine waste rock for carbon capture and storage. *International Journal of Mining, Reclamation and Environment* 24, 64-79.
- Hitch M. and Dipple G.M. (2012) Economic feasibility and sensitivity analysis of integrating industrial-scale mineral carbonation into mining operations. *Minerals Engineering* 39, 268-275.
- Huijgen W.J.J., Witkamp G.-J. and Comans R.N.J. (2005) Mineral CO₂ sequestration by steel slag carbonation. *Environmental Science and Technology* 39, 9676-9682.
- IPCC (2005a) IPCC Carbon dioxide capture and storage. In: Metz B., Davidson O., de Coninck H.C., Loos M., Meyer L.A. (Eds.), IPCC Special Report. Prepared by Working Group III of the Intergovernmental Panel on Climate Change, Cambridge University Press, Cambridge, United Kingdom and New York, USA.

- IPCC (2005b) Mineral Carbonation and Industrial Uses of CO₂, Carbon dioxide capture and storage. Cambridge University Press, United Kingdom and New York, USA.
- IPCC (2007) Climate change 2007: The physical science basis. Contribution of Working Group I to the Fourth Assessment Report of the Intergovernmental Panel on Climate Change, Cambridge University Press, Cambridge, United Kingdom and New York, USA.
- IPCC (2013) IPCC Climate Change 2013: The physical science basis. Contribution of Working Group 1 to the Fifth Assessment Report of the Intergovernmental Panel on Climate Change. Stocker T.F., Qin D., Plattner G.-K., Allen S.K, Boschung J., Naules A., Xia Y., Bex V., Midgley P.M (eds) Cambridge University Press, Cambridge, United Kingdom and New York, USA.
- IPCC (2014) Climate Change 2014: Synthesis Report. Contribution of Working Groups I, II and III to the Fifth Assessment Report of the Intergovernmental Panel on Climate Change. Cambridge University Press, Cambridge, United Kingdom and New York, USA
- Kelemen P.B., Matter J., Streit E.E., Rudge J.F., Curry W.B. and Blusztajn J. (2011) Rates and mechanisms of mineral carbonation in peridotite: Natural processes and recipes for enhanced, in situ CO₂ capture and storage. *Annual Review of Earth and Planetary Sciences* 39, 545-576.
- Kemache N., Pasquier L.-C., Cecchi E., Mouedhen I., Blais J.-F. and Mercier G. (2017) Aqueous mineral carbonation for CO₂ sequestration: From laboratory to pilot scale. *Fuel Processing Technology* 166, 209-216.
- Krevor S.C.M. and Lackner K.S. (2011) Enhancing serpentine dissolution kinetics for mineral carbon dioxide sequestration. *International Journal of Greenhouse Gas Control* 5, 1073-1080.
- Lacis A.A., Schmidt G.A., Rind D. and Ruedy R.A. (2010) Atmospheric CO₂: Principal control knob governing Earth's temperature. *Science* 330, 356-359.
- Lackner K.S., Wendt C.H., Butt D.P., Joyce E.L.J. and Sharp D.H. (1995) Carbon dioxide disposal in carbonate minerals. *Energy* 20, 1153-1170.

- Lackner K.S. (2002) Carbonate chemistry for sequestering fossil carbon. *Annual Review of Energy and the Environment* 27, 193-232.
- Lackner K.S. (2003) A guide to CO₂ sequestration. *Science* 300, 1677-1678.
- Lottermoser B.G. (2011) Recycling, reuse and rehabilitation of mine wastes. *Elements* 7, 405-410.
- Manning D.A.C., Renforth P., Lopez-Capel E., Robertson S. and Ghazireh N. (2013) Carbonate precipitation in artificial soils produced from basaltic quarry fines and composts: An opportunity for passive carbon sequestration. *International Journal of Greenhouse Gas Control* 17, 309-317.
- Maroto-Valer M.M., Fauth D.J., Kuchta M.E., Zhang Y. and Andrésen J.M. (2005) Activation of magnesium rich minerals as carbonation feedstock materials for CO₂ sequestration. *Fuel Processing Technology* 86, 1627-1645.
- Matter J.M. and Kelemen P.B. (2009) Permanent storage of carbon dioxide in geological reservoirs by mineral carbonation. *Nature Geoscience* 2, 837-841.
- Matter J.M., Broecker W.S., Gislason S.R., Gunnlaugsson E., Oelkers E.H., Stute M., Sigurdardóttir H., Stefansson A., Alfreðsson H.A., Aradóttir E.S., Axelsson G., Sigfússon B. and Wolff-Boenisch D. (2011) The CarbFix Pilot Project—Storing carbon dioxide in basalt. *Energy Procedia* 4, 5579-5585.
- Matter J.M., Stute M., Snæbjörnsdóttir S.Ó., Oelkers E.H., Gislason S.R., Aradóttir E.S., Sigfússon B., Gunnarsson I., Sigurdardóttir H., Gunnlaugsson E., Axelsson G., Alfreðsson H.A., Wolff-Boenisch D., Mesfin K., Taya D.F.d.l.R., Hall J., Dideriksen K. and Broecker W.S. (2016) Rapid carbon mineralization for permanent disposal of anthropogenic carbon dioxide emissions. *Science* 352, 1312-1314.
- McCutcheon J., Dipple G.M., Wilson S.A. and Southam G. (2015) Production of magnesium-rich solutions by acid leaching of chrysotile: A precursor to field-scale deployment of microbially enabled carbonate mineral precipitation. *Chemical Geology* 413, 119-131.

- McCutcheon J., Wilson S.A. and Southam G. (2016) Microbially accelerated carbonate mineral precipitation as a strategy for in situ carbon sequestration and rehabilitation of asbestos mine sites. *Environmental Science & Technology* 50, 1419-1427.
- McCutcheon J., Turvey C.C., Wilson S.A., Hamilton J.L. and Southam G. (2017) Microbial mineral carbonation of asbestos mine tailings: Potential applications to carbon storage and tailings stabilization. *Minerals* 7, 191.
- McGrail B.P., Schaef H.T., Spane F.A., Cliff J.B., Qafoku O., Horner J.A., Thompson C.J., Owen A.T. and Sullivan C.E. (2017) Field validation of supercritical CO₂ reactivity with basalts. *Environmental Science & Technology Letters* 4, 6-10.
- Mignardi S., De Vito C., Ferrini V. and Martin R.F. (2011) The efficiency of CO₂ sequestration via carbonate mineralization with simulated wastewaters of high salinity. *Journal of Hazardous Materials* 191, 49-55.
- Montes-Hernandez G., Pérez-López R., Renard F., Nieto J.M. and Charlet L. (2009) Mineral sequestration of CO₂ by aqueous carbonation of coal combustion fly-ash. *Journal of Hazardous Materials* 161, 1347-1354.
- Mouedhen I., Kemache N., Pasquier L.-C., Cecchi E., Blais J.-F. and Mercier G. (2017) Effect of pCO₂ on direct flue gas mineral carbonation at pilot scale. *Journal of Environmental Management* 198, 1-8.
- Oelkers E.H., Gislason S.R. and Matter J. (2008) Mineral carbonation of CO₂. *Elements* 4, 333-337.
- Olajire A.A. (2013) A review of mineral carbonation technology in sequestration of CO₂. *Journal of Petroleum Science and Engineering* 109, 364-392.
- Oskierski H.C., Dlugogorski B.Z. and Jacobsen G. (2013) Sequestration of atmospheric CO₂ in chrysotile mine tailings of the Woodsreef Asbestos Mine, Australia: Quantitative mineralogy, isotopic fingerprinting and carbonation rates. *Chemical Geology* 358, 156-169.

- Park A.-H.A., Jadhav R. and Fan L.-S. (2003) CO₂ mineral sequestration: Chemically enhanced aqueous carbonation of serpentine. *The Canadian Journal of Chemical Engineering* 81, 885-890.
- Park A.-H.A. and Fan L.-S. (2004) CO₂ mineral sequestration: physically activated dissolution of serpentine and pH swing process. *Chemical Engineering Science* 59, 5241-5247.
- Pearman G.I., Fraser P.J. and Garratt J.R. (2017) CSIRO high-precision measurement of atmospheric CO₂ concentration in Australia. Part 2: Cape Grim, surface CO₂ measurements and carbon cycle modelling. *Historical Records of Australian Science* 28, 126-139.
- Power I.M., Dipple G.M. and Southam G. (2010) Bioleaching of ultramafic tailings by *Acidithiobacillus* spp. for CO₂ sequestration. *Environmental Science & Technology* 44, 456-462.
- Power I.M., Harrison A.L., Dipple G.M. and Southam G. (2013a) Carbon sequestration via carbonic anhydrase facilitated magnesium carbonate precipitation. *International Journal of Greenhouse Gas Control* 16, 145-155.
- Power I.M., Harrison A.L., Dipple G.M., Wilson S.A., Kelemen P.B., Hitch M. and Southam G. (2013b) Carbon mineralization: From natural analogues to engineered systems. *Reviews in Mineralogy and Geochemistry* 77, 305-360.
- Power I.M., McCutcheon J., Harrison A.L., Wilson S.A., Dipple G.M., Kelly S., Southam C. and Southam G. (2014) Strategizing carbon-neutral mines: A case for pilot projects. *Minerals* 4, 399-436.
- Pronost J., Beaudoin G., Tremblay J., Larachi F., Duchesne J., Hébert R. and Constantin M. (2011) Carbon sequestration kinetic and storage capacity of ultramafic mining waste. *Environmental Science & Technology* 45, 9413-9420.
- Pronost J., Beaudoin G., Lemieux J.-M., Hébert R., Constantin M., Marcouiller S., Klein M., Duchesne J., Molson J.W., Larachi F. and Maldague X. (2012) CO₂-depleted warm air venting from chrysotile milling waste (Thetford Mines, Canada): Evidence for in-situ carbon capture from the atmosphere. *Geology* 40, 275-278.

- Renforth P. (2012). The potential of enhanced weathering in the UK. *International Journal of Greenhouse Gas Control* 10, 229-243.
- Rogelj J., Den Elzen M., Höhne N., Fransen T., Fekete H., Winkler H., Schaeffer R., Sha, F., Riahi K. and Meinshausen M. (2016) Paris Agreement climate proposals need a boost to keep warming well below 2 C. *Nature* 534, 631-639.
- Romão I.S., Gando-Ferreira L.M. and Zevenhoven R. (2013) Combined extraction of metals and production of Mg(OH)₂ for CO₂ sequestration from nickel mine ore and overburden. *Minerals Engineering* 53, 167-170.
- Sanna A., Uibu M., Caramanna G., Kuusik R. and Maroto-Valer M.M. (2014) A review of mineral carbonation technologies to sequester CO₂. *Chemical Society Reviews* 43, 8049-8080.
- Seifritz W. (1990) CO₂ Disposal by means of Silicates. *Nature* 345, 486.
- Sipilä J., Teir S. and Zevenhoven R. (2008) Carbon dioxide sequestration by mineral carbonation. Literature review update 2005–2007. Åbo Akademi University Faculty of Technology Heat Engineering Laboratory, report VT 2008-1.
- Snæbjörnsdóttir S.Ó., Wiese F., Fridriksson T., Ármansson H., Einarsson G.M. and Gislason S.R. (2014) CO₂ storage potential of basaltic rocks in Iceland and the oceanic ridges. *Energy Procedia* 63, 4585-4600.
- Thomas D.L., Bird D.K., Arnórsson S. and Maher K. (2016) Geochemistry of CO₂-rich waters in Iceland. *Chemical Geology* 444, 158-179.
- Tremblay J., Duchesne J., Beaudoin G., Constantin M., Hebert R., Larachi F., Lemieux J. and Molson J.W. (2011) Enhancement of mineral carbonation of various ultramafic mine tailings. *American Geophysical Union Fall Meeting Abstracts 2011*.
- Turvey C.C., Wilson S.A., Hamilton J.L. and Southam G. (2017) Field-based accounting of CO₂ sequestration in ultramafic mine wastes using portable X-ray diffraction. *American Mineralogist* 102, 1302-1310.

- Voormeij D. and Simandl G. (2004) Geological, ocean, and mineral CO₂ sequestration options: A technical review. *Geoscience Canada* 31, 11-22.
- Wang X. and Maroto-Valer M.M. (2011) Dissolution of serpentine using recyclable ammonium salts for CO₂ mineral carbonation. *Fuel* 90, 1229-1237.
- Washbourne C.L., Renforth P. and Manning D.A.C. (2012) Investigating carbonate formation in urban soils as a method for capture and storage of atmospheric carbon. *Science of the Total Environment* 431, 166-175.
- Washbourne C.-L., Lopez-Capel E., Renforth P., Ascough, P.L. and Manning D.A.C. (2015) Rapid removal of atmospheric CO₂ by urban soils. *Environmental Science & Technology* 49, 5434-5440.
- Wilson S.A., Raudsepp M. and Dipple G.M. (2006) Verifying and quantifying carbon fixation in minerals from serpentine-rich mine tailings using the Rietveld method with X-ray powder diffraction data. *American Mineralogist* 91, 1331-1341.
- Wilson S.A., Dipple G.M., Power I.M., Thom J.M., Anderson R.G., Raudsepp M., Gabites J.E. and Southam G. (2009a) Carbon dioxide fixation within mine wastes of ultramafic-hosted ore deposits: Examples from the Clinton Creek and Cassiar chrysotile deposits, Canada. *Economic Geology* 104, 95-112.
- Wilson S.A., Raudsepp M. and Dipple G.M. (2009b) Quantifying carbon fixation in trace minerals from processed kimberlite: A comparative study of quantitative methods using X-ray powder diffraction data with applications to the Diavik Diamond Mine, Northwest Territories, Canada. *Applied Geochemistry* 24, 2312-2331.
- Wilson S.A., Dipple G.M., Power I.M., Barker S.L.L., Fallon S.J. and Southam G. (2011) Subarctic weathering of mineral wastes provides a sink for atmospheric CO₂. *Environmental Science & Technology* 45, 7727-7736.
- Wilson S.A., Harrison A.L., Dipple G.M., Power I.M., Barker S.L.L., Mayer K.U., Fallon S.J., Raudsepp M. and Southam G. (2014) Offsetting of CO₂ emissions by air capture in mine tailings at the Mount Keith Nickel Mine, Western Australia: Rates, controls and prospects for carbon neutral mining. *International Journal of Greenhouse Gas Control* 25, 121-140.

- Zevenhoven R. and Kavaliauskaite I. (2004) Mineral carbonation for long-term CO₂ storage: an exergy analysis. *International Journal of Thermodynamics* 7, 23-31.
- Zevenhoven R., Fagerlund J. and Songok J.K. (2011) CO₂ mineral sequestration: developments toward large-scale application. *Greenhouse Gases: Science and Technology* 1, 48-57.
- Zhang Y.-X., Chao Q.-C., Zheng Q.-H. and Huang L. (2017) The withdrawal of the U.S. from the Paris Agreement and its impact on global climate change governance. *Advances in Climate Change Research* 8, 213-219.

Declaration for Thesis Chapter 2

Declaration by candidate

In the case of Chapter 2, the nature and extent of my contribution is as follows:

Nature of contribution	Extent of contribution
Concept, experimental design, data collection and interpretation, and writing. This work builds upon my honours thesis, and some preliminary results from that work (precipitation experiment and ICP-MS data) are included here. This preliminary work contributes approximately 20 % of the results presented in this chapter and it is cited where relevant.	79%

The following co-authors contributed to the work. If co-authors are students at Monash University, the extent of their contribution in percentage terms must be stated:

Name	Nature of contribution	Extent of contribution (%)
Siobhan A. Wilson	Supervisory role	5%
Bree Morgan	Supervisory role	5%
Connor C. Turvey	Interpretation of results	3%
David J. Paterson	Synchrotron XFM analysis	3%
Colin MacRae	Electron microscopy	3%
Jenine McCutcheon	Synchrotron XFM data collection	1%
Gordon Southam	Synchrotron XFM data collection	1%

The undersigned hereby certify that the above declaration correctly reflects the nature and extent of the candidate's and co-authors contributions to this work*.

Candidate's signature:



Date: 10 February 2018

Main supervisor's signature:



Date: 5 February 2018

*Note: Where the responsible author is not the candidate's main supervisor, the main supervisor should consult with the responsible author to agree on the respective contributions of the authors.

Chapter 2

Nesquehonite sequesters transition metals and CO₂ during accelerated carbon mineralisation[†]

Jessica L. Hamilton^a, Siobhan A. Wilson^{ab}, Bree Morgan^{ac}, Connor C. Turvey^a, David J. Paterson^d, Colin MacRae^e, Jenine McCutcheon^{fg} and Gordon Southam^f

^aSchool of Earth, Atmosphere and Environment, Monash University, Clayton, Melbourne, VIC 3800, Australia

^bDepartment of Earth and Atmospheric Sciences, University of Alberta, Edmonton, AB T6G 2R3, Canada

^cSchool of Geosciences, The University of Sydney, Camperdown, NSW 2006, Australia

^dAustralian Synchrotron, Clayton, Melbourne, VIC 3168, Australia

^eCSIRO Mineral Resources, Clayton, Melbourne, VIC 3168, Australia

^fSchool of Earth and Environmental Sciences, The University of Queensland, St Lucia, QLD 4072, Australia

^gSchool of Earth and Environment, Maths/Earth and Environment Building, University of Leeds, Leeds, LS2 9JT, United Kingdom

[†]Published in *International Journal of Greenhouse Gas Control*
16/11/2016

Acid leaching of ultramafic rocks to produce Mg^{2+} - and Ca^{2+} -rich solutions for mineral carbonation may inadvertently leach toxic trace metals. This study investigates the capacity of nesquehonite ($MgCO_3 \cdot 3H_2O$), a common product of mineral carbonation at Earth's surface conditions, to sorb Cr, Ni, Mn, Co and Cu from solution. Our results demonstrate that upon precipitation, nesquehonite rapidly sequesters transition metals present in solution at concentrations from 10 to 100 mg/L. Trace metal uptake appears to occur by substitution for Mg^{2+} in the nesquehonite crystal structure, and also by incorporation into minor, metal-rich phases, such as Fe-oxyhydroxides. This indicates that first row transition metals will likely be trapped and stored within Mg-carbonate minerals produced in industrial mineral carbonation reactors and in landscapes modified to capture atmospheric CO_2 via enhanced weathering. Thus, it is unlikely that trace metals will pose an environmental risk in the event of accidental release of wastewater.

2.1. Introduction

Anthropogenic carbon dioxide (CO_2) production is causing the concentration of atmospheric CO_2 to steadily increase, and is likely driving long-term changes to Earth's climate (IPCC, 2013). Consequently, there is a growing necessity to reduce or offset anthropogenic CO_2 emissions, and to develop lasting CO_2 storage solutions (IPCC, 2013). One emerging strategy, carbon mineralisation, enhances the natural process of silicate mineral weathering and CO_2 sequestration by precipitating environmentally benign Mg- and Ca-carbonate minerals (Lackner et al., 1995; Oelkers et al., 2008; Olajire, 2013; Power et al., 2013a; Seifritz, 1990). Importantly, this is the only CO_2 storage option that is considered permanent, given that carbonate minerals are known to persist at the Earth's surface on geological timescales (Lackner et al., 1995).

Carbon mineralisation under Earth's surface conditions is limited due to the slow dissolution kinetics of the silicate minerals which provide the cations necessary for carbonation. To address this issue, acid-leaching of ultramafic rocks and alkaline industrial wastes has been widely employed as a means of accelerating silicate mineral dissolution (e.g., Maroto-Valer et al., 2005; McCutcheon et al., 2015; Park et al., 2003; Power et al., 2010; Teir et al., 2007b). Although enhanced weathering of these minerals (and associated sulfides and oxides) can provide a supply of Mg^{2+} and Ca^{2+} for carbonation to proceed, they also commonly contain low (< 1 wt.%) but significant concentrations of first row transition metals (e.g., Ni, Mn, Cr, Cu, Co) within their crystal structures (Kmetoni, 1984; Margiotta et al., 2012; Natali et al., 2013; Schreier, 1987; Seal et al., 2010; Wunsch et al., 2013). Most of these trace metals are toxic to biota at elevated concentrations and may be mobilised in the acidic solutions used for enhanced dissolution of waste rock or industrial wastes prior to mineral carbonation (Margiotta et al., 2012; Olsson et al., 2014b; Wunsch et al., 2013). Although it has been established that acid is neutralised during silicate mineral dissolution, the fate of mobilised trace metals during this process is an ecological concern that has not yet been adequately investigated (Marcon and Kaszuba, 2013; Olajire, 2013; Seal et al., 2010).

Production and release of metal-rich drainage during carbon mineralisation may cause both on-site and off-site contamination of surface waters, groundwater, soils, and sediments by a number of implementation scenarios, including *ex situ* processing plants, enhanced weathering of ultramafic wastes and landscapes, and *in situ* injection-based projects (Kirsch et al., 2014; Marcon and Kaszuba, 2013; Marcon and Kaszuba, 2015; Oelkers et al., 2008; Olsson et al., 2014a; Olsson et al., 2014b; Seal et al., 2010; Thomas et al., 2013; Wunsch et al., 2013). Proposed enhanced weathering schemes include the application of Mg-silicate minerals to natural landscapes, such as river catchments or

coastal settings (Hartmann et al., 2013; Schuiling and de Boer, 2013), or the treatment of ultramafic mine tailings with sulfuric acid or acid generating sulfide minerals (McCutcheon et al., 2015; McCutcheon et al., 2016; Power et al., 2010). In the case of landscape-scale geoengineering projects, containment or remediation of mobilised metals could be challenging and expensive due to their large spatial footprint. This concern is also relevant to *in situ* injection of CO₂ into basaltic or ultramafic rocks, given that dissolved CO₂ creates an initially acidic environment that could facilitate metal release (Flaathen and Gislason, 2007; Marcon and Kaszuba, 2013; Oelkers et al., 2008; Olsson et al., 2014b; Thomas et al., 2013; Wunsch et al., 2013). The trace metal composition of carbonate mineral products generated in *ex situ* mineral carbonation reactors may also influence their utility as value added products. Therefore, assessing and controlling the mobility of transition metals should be a key consideration during design and implementation of accelerated carbon mineralisation projects.

Mg-rich ultramafic minerals, favoured as feedstock for carbon mineralisation reactions, commonly weather to produce low-temperature hydrated magnesium carbonate minerals, such as nesquehonite (MgCO₃·3H₂O) and hydromagnesite [Mg₅(CO₃)₄(OH)₂·4H₂O] (Oelkers et al., 2008; Power et al., 2013b; Wilson et al., 2009). Nesquehonite is most readily formed at ambient temperatures and pressures at the Earth's surface, decomposing to more thermodynamically stable hydromagnesite over time, or at temperatures above 50°C, depending on the environmental conditions (Davies and Bubela, 1973; Jauffret et al., 2015; Morgan et al., 2015). As a primary mineral product of carbon mineralisation reactions at Earth's surface, nesquehonite and other hydrated Mg-carbonate minerals may represent important, and previously unrecognised sinks for mobilised trace metals. The capacity of Mg-carbonate minerals to sorb potentially hazardous metals is fundamental to understanding and managing the potential environmental risk of metal release from

accelerated carbonation reactions. To date, no other research has investigated the sorption of trace metals to hydrated Mg-carbonate minerals, including nesquehonite, which is the topic of this study.

Our experiments focus on uptake and immobilisation of the trace metals Ni^{2+} , Cr^{3+} , Mn^{2+} , Co^{2+} and Cu^{2+} under conditions relevant to low temperature carbon mineralisation. These transition metals were chosen because (1) they are commonly abundant in ultramafic rocks and industrial wastes; (2) they have the potential to substitute for Mg^{2+} within the crystal structures of minerals due to their similar ionic radii and charge; and (3) some of these elements can be highly toxic to aquatic life and humans when they exceed guideline limits (ANZECC & ARMCANZ, 2000). Given the mineralogy and aqueous conditions of these experiments, these findings could be applied to low temperature *ex situ* mineralisation of ultramafic minerals or alkaline industrial wastes, or enhanced weathering of ultramafic landscapes including mine waste stockpiles.

2.2. Methods

2.2.1. Laboratory experiment: sorption of transition metals to nesquehonite

Precipitation experiments, preliminary X-ray diffraction (XRD) and Inductively Coupled Plasma Mass Spectrometry (ICP-MS) were initially reported in Hamilton (2013), and are expanded upon here. Nesquehonite was synthesised by mixing equal volumes (4.5 mL) of 1.8 M $\text{MgCl}_2 \cdot 6\text{H}_2\text{O}$ and 1.8 M K_2CO_3 (Robie and Hemingway, 1972), in the presence of transition metal solutions (1 mL). Transition metal (Ni, Cr, Mn, Co, Cu) stock solutions were prepared from hydrated divalent metal chloride salts. Trace metals were present at concentrations of 10 and 100 mg/L in parallel experiments. Cr was added in the soluble form of CrCl_2 , and is expected to have rapidly oxidised in the stock solution to Cr^{3+} , the

form commonly present in partially or fully serpentinised ultramafic rocks (Oze et al., 2007).

The $\text{MgCl}_2 \cdot 6\text{H}_2\text{O}$ reagent also contains trace Fe (24 ppm), confirmed by portable X-ray fluorescence (XRF) analysis (Olympus Delta 50 Premium Soil Exploration Analyzer DP4050). This was expected to allow the formation of Fe-bearing phases in these experiments. Because ultramafic rocks typically contain several wt. % of Fe, this allows for better comparison with carbon mineralisation reactions. ICP-MS analysis of starting reagents also reveals trace transition metal contamination in the initial Mg-chloride solution used for nesquehonite synthesis, including significant Cr (approximately 10% of total Cr in the 10 mg/L treatment, or 1% in the 100 mg/L treatment). Since identical volumes of Mg-chloride were added to all experiments, the concentrations of Cr contamination found in control treatments were used to normalise Cr concentrations across all other experiments. Higher levels of the added transition metal solutions provided elevated concentrations of trace metals for the experiments.

Previous studies have shown that when nesquehonite forms from a supersaturated solution, it initially precipitates as a gel-like colloidal suspension, with crystal size increasing over a period of hours to days (Cheng and Li, 2009). As such, two time treatments (5 min and 48 h) were used to assess the relative effectiveness of metal uptake between microcrystalline (5 min) and highly crystalline (48 h) nesquehonite.

The $\text{MgCl}_2 \cdot 6\text{H}_2\text{O}$ stock solution and the transition metal stocks were initially combined in experimental vials prior to the addition of the K_2CO_3 solution. Instantaneous formation of a fine-grained, white precipitate occurred upon addition of the K_2CO_3 solution. Air temperature and atmospheric relative humidity were 23°C and 23%, respectively, at the beginning of the experiment. Following the 5 min and 48 h exposures to the trace metal

solutions, the samples were centrifuged at 4000 rpm for 30 minutes. The supernatant from each vial was separated, syringe filtered (0.2 μm) and acidified to $\text{pH} < 2$ using double distilled HNO_3 .

Each experiment was reproduced in triplicate and parallel control experiments were conducted with Milli-Q water (18.2 $\text{m}\Omega \text{ cm}$) substituted for trace metal reagents. All reagents were analytical grade and prepared in Milli-Q water. Glassware was soaked for a minimum of 24 h in 1 M HCl and thoroughly rinsed with Milli-Q water prior to use. Experiments were conducted in sterile, 10 mL polypropylene centrifuge vials.

We found that nesquehonite synthesised in the polypropylene vials typically did not form many large (i.e., millimetre-scale) crystals after 48 h; instead remaining as fine-grained (micrometre-scale) material. After centrifuging, the separated precipitate fractions were kept in sealed polypropylene vials for six days. They were then emptied into petri dishes to air dry at the ambient temperature in our laboratory. A very small amount of solution remained in the vials, which caused larger crystals ($> 1 \text{ mm}$) of nesquehonite to develop in the six days between centrifuging and emptying vials into petri dishes. Although recrystallisation was observed, a negligible fraction of trace transition metals could have been derived from the small amount of solution remaining in the precipitate during drying. Oven drying was not used at this stage because it can induce decomposition of nesquehonite to less hydrous Mg-carbonate phases.

Two of every three solid phase replicates, and all aqueous solutions, were analysed for Cr, Ni, Mn, Co, and Cu concentrations using ICP-MS, (Thermo Finnigan X series II, quadrupole) in the School of Earth, Atmosphere and Environment at Monash University. Detection limits were $< 0.7 \text{ ppb}$ for all elements analysed. These precipitates were oven dried at 50°C for 24 hours, then ground with an agate mortar and pestle to homogenise.

Precipitate subsamples were then dissolved using double distilled HNO₃, and all samples were diluted with Milli-Q water prior to analysis to bring them within the calibration range. ICP-MS count rates were externally standardised by means of calibration curves created using commercially available stock solutions, and drift corrections were applied using Sc as an internal standard. The instrument variability was <5%. ICP-MS results were initially reported in Hamilton (2013), with further analysis here.

2.2.2. Precipitate mineralogy

Precipitate subsamples from each treatment were prepared for analysis using powder X-ray Diffraction (XRD). Data were collected using a Bruker D8 Focus X-ray diffractometer (School of Chemistry, Monash University) equipped with a scintillation detector. The fine-focus Cu X-ray tube was operated at 40 kV and 40 mA. Data were collected over 2–80° 2 θ , with a step size of 0.02° 2 θ and a count time of 2 s/step. Mineral phases were identified using the ICDD PDF-2 database and the DIFFRAC^{plus} EVA Version 2 software package (Bruker XAS). Predicted mineralogy based on the geochemical constraints of the system was also investigated using PHREEQC modelling (Interactive 3.0.6–7757) with the Pitzer database (Parkhurst and Appelo, 1999). XRD data and PHREEQC modelling results are reported in Hamilton (2013) with extended interpretation here.

2.2.3. Trace metal distribution in the precipitate

Representative subsamples of precipitates were analysed using Scanning Electron Microscopy (SEM) and Energy Dispersive Spectroscopy (EDS). Fibroidal arrays of both large nesquehonite crystals and finely crystalline material from each experiment were mounted on aluminium stubs using adhesive carbon tabs and coated with platinum. Preliminary SEM imaging was performed using a PHILIPS (FEI) XL30 TMP

Environmental Scanning Electron Microscope using a backscattered electron (BSE) detector at 20 kV at The University of Melbourne (Hamilton, 2013). Further BSE and secondary electron (SE) images and EDS data were collected using a JEOL 7001F Field Emission Gun Scanning Electron Microscope (FEG-SEM) in the Monash Centre for Electron Microscopy. Images and EDS data were collected using an accelerating voltage of 15–20 kV.

A JEOL 8500F-CL HyperProbe Field-Emission Gun Electron Probe Microanalyser (FEG-EPMA) at CSIRO Clayton was used to produce elemental and cathodoluminescence (CL) maps from polished cross sections through experimental precipitates mounted in epoxy blocks. Synthetic nesquehonite, precipitated for 48 h from solutions with 100 mg/L trace metals, was analysed for Cr, Ni, Mn, Co, or Cu as appropriate, as well as Mg, K and Cl. The spatial distribution of elements was analysed at 20 kV with a beam current of 40 nA. The defocused beam had a pixel size of 5 μm and a dwell time of 50 ms per pixel. X-rays were detected using wavelength dispersive spectrometry (WDS) and a LIFH crystal. The CL signal within the Mn-doped sample of synthetic nesquehonite was collected in a hyperspectral manner using an integrated spectrometer with optical response from 200–950 nm. CL peaks were identified using the luminescence database of MacRae and Wilson (2008) and fitted with a Gaussian peak using in-house software, Chimage (MacRae et al., 2013).

The surface of the cross sectioned epoxy block used for electron microprobe analysis was re-cut and polished to remove beam damage from EMPA before analysis using the X-ray Fluorescence Microscopy (XFM) beamline at the Australian Synchrotron. Unfortunately, the Co doped sample was destroyed during preparation, and therefore could not be analysed. XFM was conducted with an incident monochromatic X-ray beam of 18.5 keV

focused to $\sim 2.0 \mu\text{m}$ using Kirkpatrick-Baez mirrors. Elemental maps were collected using the Maia detector (Ryan et al., 2010; Ryan et al., 2014) with a step size of $2 \mu\text{m}$ for the Cr-doped sample and $4 \mu\text{m}$ for the Ni-, Mn- and Cu-doped samples. A dwell time of 1.33 msec/pixel was used for all samples. Full spectrum data were processed using the GeoPIXE software program (Ryan, 2000). X-ray Absorption Near Edge Spectroscopy (XANES) was conducted over the energy range 5.96 to 6.12 keV for the Cr absorption edge in the Cr-doped sample. A step size of $2\text{--}5 \mu\text{m}$ and a dwell time of $4\text{--}10 \text{ms}$ were used. Spectra were extracted from regions of interest using GeoPIXE and compared to published standards from the literature (Berry and O'Neill, 2004; Low et al., 2015; Vogel et al., 2014).

In this study, 'sorption' is used to describe trace metal uptake by possible mechanisms including adsorption and absorption because, as a proof of concept experiment, detailed tracing of sorption mechanisms is outside the scope of this study. Methods for more precise determination of the mode of uptake are suggested in the Discussion (Section 2.4).

2.3. Results

2.3.1. Trace metal sorption to precipitate

The experimental results show that Cr, Ni, Mn, Co and Cu were rapidly ($<35 \text{min}$ for 5 min treatment and centrifuging time) removed from solution in both the 10 and 100 mg/L treatments (Appendix 1: Table S1; Hamilton, 2013). The pH of experimental solutions ranged from 8.42 – 9.14. ICP-MS results demonstrate that generally $>99 \text{wt. \%}$ of trace metals are found within the precipitates (median: 99.63 wt.%), with $<3.6 \text{\%}$ variability between replicates (Appendix 1: Table S1; Hamilton, 2013).

2.3.2. Precipitate mineralogy

Precipitates are predominantly composed of nesquehonite and sylvite (KCl), with baylissite [$\text{K}_2\text{Mg}(\text{CO}_3)_2 \cdot 4\text{H}_2\text{O}$] also present at trace abundances, as confirmed by XRD and SEM (Fig. S1; Hamilton, 2013). XFM also reveals distinct Fe-rich phases, likely Fe-oxyhydroxides, associated with nesquehonite crystals. The Fe-oxyhydroxide phases are present at low abundances ($\ll 1$ wt. %), which would make them difficult to detect from XRD patterns given the data acquisition parameters used in this study. PHREEQC simulations were used to predict that sylvite (a highly soluble evaporite mineral) was undersaturated in experimental solutions (Hamilton, 2013), which is consistent with it having formed during sample drying as a thin coating over nesquehonite crystals (Appendix 1: Fig. S1A,B,D, and E). Rare, small spheres (30–60 μm) of another Mg-carbonate phase were also observed in association with nesquehonite fibres and have been tentatively identified as dypingite [$\text{Mg}_5(\text{CO}_3)_4(\text{OH})_2 \cdot 5\text{H}_2\text{O}$] (Appendix 1: Fig S1F) based on known Mg-carbonate decomposition sequences and morphologies (Hamilton, 2013).

2.3.3. Trace metal distribution in nesquehonite

Data from SEM-EDS demonstrate that trace metals are associated with nesquehonite crystals, but were not observed in sylvite above the detection limits of EDS. Cross sections through arrays of nesquehonite fibres allow investigation of the trace metal distribution within crystals, and along the growth axis of the crystals. Electron microscopy reveals that, in general, Ni, Mn, and Cu are distributed relatively evenly within nesquehonite crystals (Fig 2.1). However, in the Cr doped nesquehonite crystal, trace phases containing higher concentrations of Cr appear to align with the growth axis of the nesquehonite crystals (Fig 2.1B). Similarly sized grains of trace phases containing higher trace metal concentrations are also observed in samples containing Ni, Mn and Cu

(Fig 2.1D,F,J). Concentration zoning of Co is observed within nesquehonite, with higher trace metal concentrations on the outer edges of the crystal array (Fig 2.1H).

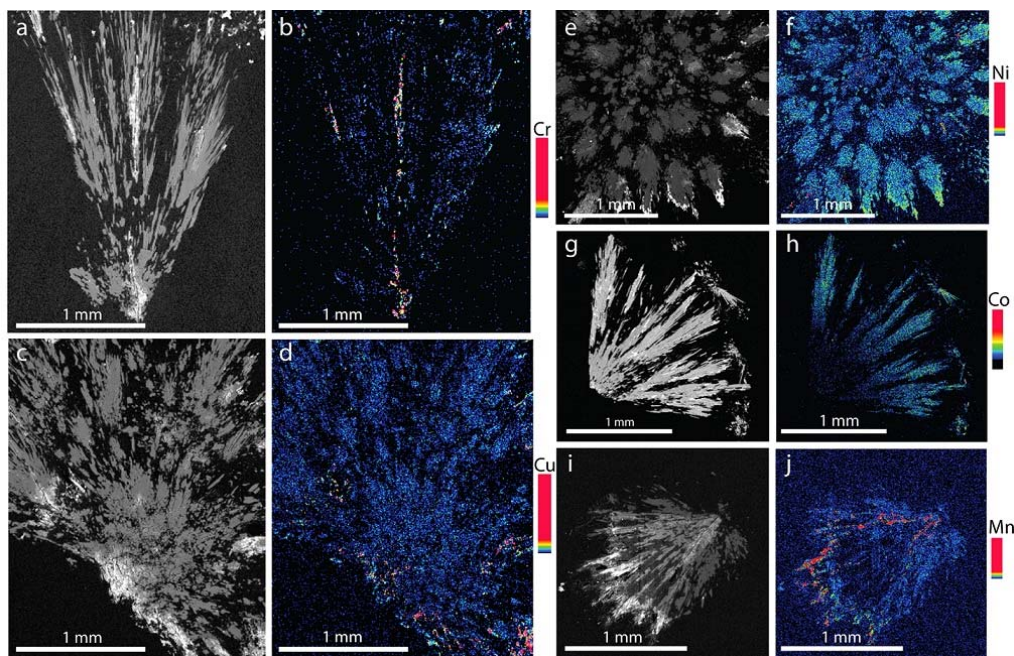


Figure 2.1. BSE micrographs and EPMA maps (coloured) of cross sections through metal-doped nesquehonite crystals. BSE and EPMA data for samples of nesquehonite doped with Cr (A and B), Cu (C and D), Ni (E and F), Co (G and H), and Mn (I and J).

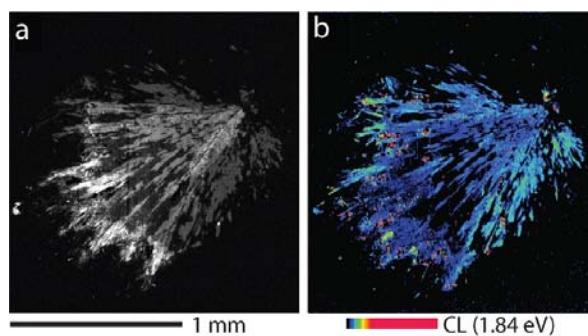


Figure 2.2. (A) BSE micrograph of nesquehonite crystals containing Mn (Sample 48 h, 100 mg/L) with sylvite visible as a white precipitate on edges. Note that the darker region in the middle of the array of nesquehonite crystals is dominated by epoxy where the precipitate is not exposed at the surface. (B) Cathodoluminescence image generated by fitting the 1.84 eV peak clearly highlights nesquehonite grains indicating substitution of Mg^{2+} by Mn^{2+} within its crystal structure.

Cathodoluminescence spectroscopy along with the EPMA reveals a luminescence peak at 1.84 eV in the Mn-doped sample, which clearly illuminates the nesquehonite crystals in the sample (Fig. 2.2).

Synchrotron-based XFM data confirm the association of trace metals with the synthesised nesquehonite crystals (Fig. 2.3, Appendix 1: Fig. S2–4). The regions mapped by EPMA that contain higher concentrations of trace metals are observed as chemically distinct minor (μm -scale) Fe-rich phases by XFM (Fig. 2.3, Appendix 1: Fig. S2–4). XANES spectra show that Cr is dominantly present as Cr^{3+} in both the nesquehonite and the trace Fe-phases, with possible minor Cr^{6+} present in the Fe-bearing phase (Appendix 1: Fig. S5).

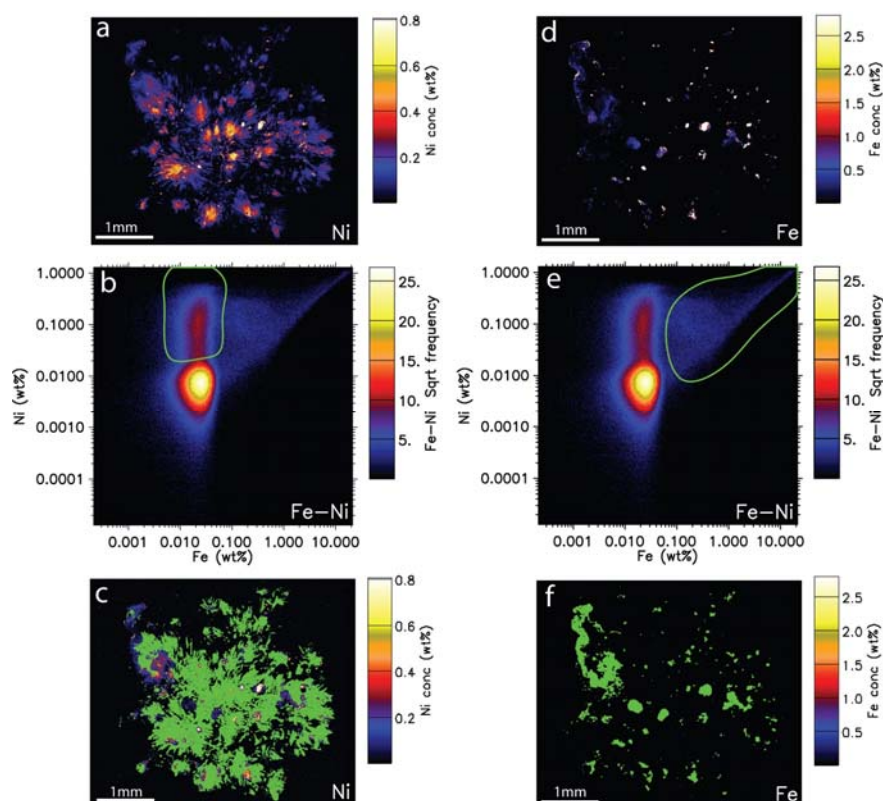


Figure 2.3. Maps of spatial distribution of Ni highlight its association with nesquehonite and Fe-oxyhydroxides in the Ni-doped sample. (A) Synchrotron XFM map showing the distribution and concentration of Ni within the Ni-doped sample. (B) Ni versus Fe concentration plot, with region

1 (high Ni, low Fe) selected in the green field. (C) Region 1, highlighted in green on the Ni map, characterizes Ni uptake in nesquehonite. (D) XFM image of contaminant Fe in the Ni doped sample. (E) Ni versus Fe concentration plot, with region 2 (high Ni, high Fe) selected in the green field. (F) Region 2 is highlighted in green on the Fe map and characterises Ni uptake in Fe-bearing trace phases.

2.4. Discussion

2.4.1. Immobilisation of trace metals by nesquehonite

Our combined ICP-MS, XRD, FEG-EPMA and XFM data show for the first time that trace metals (Cr, Ni, Mn, Co and Cu) are rapidly sorbed by Mg-carbonate minerals, such as nesquehonite, during simulated carbon mineralisation experiments. This finding confirms speculation by Olsson et al. (2014a; 2014b) that trace metals may be sequestered by Mg-carbonate minerals (unspecified mineral species) forming in travertine deposits in the Semail Ophiolite in Oman and the Eyjafjallajökull volcano in Iceland, which have been studied as natural analogues for surface leakage of CO₂ as a result of injection into underground mafic to ultramafic rocks. Our observations are also supported by mass balance calculations made by Teir et al. (2007a) which indicate that Mn and Ni are present as impurities in hydromagnesite, and that Ni and Cu are found in Fe-oxide products, both of which were produced in a pH swing mineral carbonation experiment using serpentine feedstock.

Other common carbonate minerals, such as calcite (CaCO₃) and dolomite [CaMg(CO₃)₂] are known to be effective scavengers of alkaline earth and transition metals (such as Ba, Sr, Cd, Mn, Zn, Co and Ni) by surface adsorption, incorporation into the crystal structure by substitution for Ca or Mg, or as a co-precipitate (Calugaru et al., 2016; Wunsch et al., 2013; Zachara et al., 1991). However, until now, it was not known whether hydrated Mg-carbonate minerals could similarly sequester trace metals.

When supersaturated, nesquehonite is expected to initially precipitate as a gel-like colloidal suspension with crystal size increasing over a period of hours to days (Cheng and Li, 2009). However, we found that the growth of large, macroscopic crystals of nesquehonite was slower in the plastic centrifuge tubes than in the glass beakers used in preliminary experiments. It took several days before large (>1 mm), well-ordered crystals formed in the residual material after centrifuging and removing most of the experimental solution. As such, while the initial precipitates formed after both time treatments were compositionally nesquehonite, they may have been structurally different. ICP-MS results from precipitate and supernatant samples (separated immediately after centrifuging) demonstrate that metal uptake is not limited by crystal size, and occurs instantaneously with formation of the nanoparticulate phase.

2.4.2. Mechanism for immobilisation

Substitution for Mg^{2+} appears to be the most likely mode of metal incorporation in nesquehonite, supported by mapping with EPMA (Fig 2.1), CL spectroscopy (Fig 2.2) and XFM (Fig 2.3). The even distribution of trace metal concentration observed throughout nesquehonite in EPMA and XFM maps suggest that trace metals are incorporated into the crystal structure by substitution, rather than solely by adsorption to crystal surfaces, although the latter mechanism may play a role. CL spectroscopy provides compelling evidence that the relatively even distribution of Mn observed throughout the nesquehonite crystals represents crystallographic trapping via substitution for Mg^{2+} . The CL peak energy for the sample doped with Mn (1.84 eV), which illuminates the nesquehonite crystals, is a close analogy to the luminescence database energy for Mn^{2+} substitution in the Mg^{2+} site in dolomite (1.88 eV) and magnesite (1.82–1.91 eV) (MacRae and Wilson, 2008). Another potential contribution to this CL peak may

be trace Fe in these precipitates, which is likely present as Fe^{3+} and can produce a CL peak at 1.71–1.91 eV in dolomite (MacRae and Wilson, 2008). However, XFM reveals Fe is approximately five times less abundant than Mn in the bulk nesquehonite crystal. As such, the peak at 1.84 eV is more likely to result from Mn^{2+} luminescence. The divalent transition metals tested (Ni^{2+} , Mn^{2+} , Co^{2+} and Cu^{2+}) have similar radii (<15% difference) and charge, are known to substitute for Ca^{2+} and Mg^{2+} in minerals such as calcite, dolomite and magnesite, and form carbonate mineral solid solutions (Comans and Middelburg, 1987; Franklin and Morse, 1983; Lumsden and Lloyd, 1984; Medlin, 1961; Prissok and Lehmann, 1986; Shannon, 1976; Zachara et al., 1991). As such, it is reasonable to predict that these cations substitute for Mg^{2+} in hydrated Mg-carbonates in the same way. This is supported by consistent observations of distribution for all trace metals tested, in EPMA and XFM maps (Fig 2.2, Appendix 1: Fig S2–4). In these experiments, dopant trace metals were present in precipitates at an average of 680 mg/kg (100 mg/L experiments). This is within the capacity of carbonate minerals, such as calcite, to substitute these and similar trace metals (El Ali et al., 1993; Lamble et al., 1997). However, further X-ray Absorption Spectroscopy (XAS) work is required to definitively confirm the sorption mechanism (adsorption versus absorption).

The relatively even distributions of trace Fe (likely Fe^{3+}) and Cr^{3+} (as determined by XANES) within nesquehonite crystals also suggests substitution for Mg^{2+} (absorption), which is likely to be accommodated by coupled substitutions or the generation of structural defects. The possible contribution of Fe^{3+} to the detected Mn CL peak at 1.84 eV, and the known capacity for Fe^{3+} to substitute for Mg^{2+} in dolomite, support this conclusion (Papathanassiou, 2003; Prissok and Lehmann, 1986).

The toxicity of Cr is highly dependent on its oxidation state; Cr^{3+} is relatively immobile and environmentally benign, whereas Cr^{6+} is highly carcinogenic (drinking water limit <0.05 mg/L) (World Health Organisation, 2011). Leaching of Cr from ultramafic rocks by CO_2 rich fluids, and subsequent oxidation to toxic Cr^{6+} , represents a serious environmental concern (Natali et al., 2013). Because Cr^{3+} has a similar ionic radius and charge to Fe^{3+} , it is likely to be incorporated into hydrated Mg-carbonate minerals in a similar way. Cr is expected to have readily oxidised from Cr^{2+} in the soluble chloride salt to Cr^{3+} in the stock solution, and during our precipitation experiments may have undergone some precipitation of phases such as $\text{Cr}(\text{OH})_3$ or $(\text{Fe,Cr})(\text{OH})_3$, which are relatively insoluble at neutral to alkaline pH (Kotaš and Stasicka, 2000; Rai et al., 1989). Despite this, Cr is observed to be distributed throughout nesquehonite crystals similarly to the divalent metals tested, and very little Cr is present in the oxidised form as Cr^{6+} (Fig S5). Because the large crystals analysed by EMPA and XFM formed over a period of several days, this indicates nesquehonite may be an important sink for Cr because it can retain this transition metal even during recrystallisation of small crystals to macroscopic ones. However, in multi-metal experiments or natural systems, competitive sorption may affect the amount of Cr sequestered in mineral form and its retention during mineral recrystallisation and phase transitions. XFM data also reveal an association of Cr with trace Fe-oxyhydroxides, where it likely substitutes for Fe^{3+} (Schwertmann et al., 1989) within the crystal structure or adsorbs to crystal surfaces. It is possible that sequestration of Cr^{3+} in minerals such as nesquehonite or Fe-oxyhydroxides may limit oxidation to toxic Cr^{6+} ; although dissolution of these phases, either by continued re-equilibration with a fluid or a change in environmental conditions, could remobilise Cr. Thus, ensuring long-term stability of Cr-bearing phases produced during accelerated carbon mineralisation is an important consideration.

Ni, Mn, Co and Cu were also associated with these Fe-oxyhydroxides, which have a high affinity for many trace metals (Manceau et al., 2000; Schwertmann et al., 1989; Trolard et al., 1995). This reveals there are multiple pathways for sequestration of potentially toxic transition metals in the carbonation products of ultramafic minerals and alkaline industrial waste materials.

2.4.3. Role of pH

The high alkalinity and pH of our experimental systems also has a key role to play in the immobilisation of trace metals during carbon mineralisation. At near neutral pH, transition metals are expected to be removed from solution by precipitation of hydroxides (Blowes et al., 2014; Lee et al., 2002). As such, the doped trace metals, and Fe in the system, could be expected to have precipitated here as Fe-oxyhydroxides and trace metal hydroxides, due to the low solubility of these metals at the neutral to alkaline pH conditions in the experimental vials. This likely occurred to some extent within the high-pH reagent stock solutions, before the experiments commenced. However, here we find the metals removed from solution are predominantly distributed within nesquehonite, as opposed to associated Fe-oxyhydroxides or other transition metal hydroxides, demonstrating that nesquehonite precipitation appears to be key to trapping metals under conditions relevant to carbon mineralisation.

The effect of pH on metal immobilisation in the context of carbon mineralisation has been demonstrated previously by Power et al. (2010) where Fe, Cu and Zn were immobilised during neutralisation of acidic leachate reacted with chrysotile $[Mg_3Si_2O_5(OH)_4]$ mine tailings. In this system, the neutralisation reaction caused precipitation of the metals from solution and they were found to be associated with the formation of Fe-oxyhydroxides. Power et al. (2010) added pyrite (FeS_2) to treatments to provide a source of acidity,

resulting in Fe-rich experiments with secondary precipitates dominated by Fe-oxyhydroxides; however, they do not report trace metal contents of any carbonate minerals that may have formed during these experiments. Rapid precipitation of Fe-oxide and Mg-carbonate minerals typically occurs after addition of a pH-raising additive in Mg-rich solutions, such as those leached from ultramafic minerals in carbonation reactors (Azdarpour et al., 2015; Park and Fan, 2004; Teir et al., 2007a). Our experimental results are applicable to this process, and indicate that first-row transition metals commonly released by leaching of ultramafic rocks will be incorporated into both Mg-carbonate and Fe-oxyhydroxide mineral products.

2.4.4. The fate of sorbed metals in nesquehonite

Our results demonstrate that nesquehonite is an effective crystallographic trap for transition metals, which may mean that this Mg-carbonate mineral can act as a relatively long-term and stable storage option. Although nesquehonite is the first Mg-carbonate mineral to precipitate at ambient temperatures, it typically decomposes into more stable, less hydrated phases over time, depending on environmental conditions (Ballirano et al., 2010; Ballirano et al., 2013; Davies and Bubela, 1973; Morgan et al., 2015; Schultz et al., 2014). It eventually decomposes to hydromagnesite, which can persist for millennia under neutral to alkaline conditions, and will ultimately form magnesite, which is a thermodynamically stable trap for CO₂ on timescales of millions of years (Ballirano et al., 2010; Ballirano et al., 2013; Davies and Bubela, 1973; Königsberger et al., 1999; Power et al., 2009; Wilson et al., 2006). The fate of sorbed metals during these phase transformations is an important consideration that remains to be determined.

Our experiments indicate that nesquehonite initially precipitated as a colloidal suspension. This is common for carbonate minerals, where crystal growth typically

occurs via initial precipitation of an amorphous precursor phase, prior to the formation of a stable phase (Rodriguez-Navarro and Ruiz-Agudo, 2012). Because a small fraction of residual solution could not be removed from the precipitates by centrifuging, larger crystals were able to form in the solid phase over a period of several days. Crystal growth is likely to have occurred by dissolution–precipitation reactions, or by oriented attachment and aggregation of mineral nanoparticles (Rodriguez-Navarro and Ruiz-Agudo, 2012; Schultz et al., 2014). This may be responsible for the observed alignment of trace Fe-oxyhydroxides along large nesquehonite crystals in the Cr-doped sample (Fig 2.1B). Also, the observed zoning of Co in the Co-doped nesquehonite crystal (Fig 2.1H) could be explained if dissolution–precipitation reactions were occurring to form large crystals. For instance, if preferential incorporation of Mg during reprecipitation of larger crystals was followed by relative enrichment of the surrounding fluid in the trace metal dopant, this might allow greater Co sorption on the outer parts of the growing crystal. These findings are supported by observations that both Mg-carbonate and Fe-oxyhydroxide minerals continuously undergo dissolution-precipitation and re-equilibration reactions when in contact with a solution or humidity (Handler et al., 2014; Mavromatis et al., 2015; Morgan et al., 2015). Whether trace metals are retained during this process, or remobilised, is vital to understanding their longer-term behaviour in the environment. These experiments simulate diagenetic processes involving initial microcrystalline mineral precipitation, followed by a period of recrystallisation or aggregation into larger crystals over several days. Our observations suggest that trace metals will likely be reincorporated into the recrystallised Mg-carbonate phase, at least under the conditions of these experiments. It would be valuable to investigate whether there is any exchange of trace metals amongst Mg-carbonate minerals, Fe-oxyhydroxide

minerals, and the fluid phase over time, especially during carbonate mineral phase transformations.

Trace metals associated with either hydrated Mg-carbonate or Fe-oxyhydroxide minerals may also be susceptible to remobilisation if environmental conditions were to change; for example if they were, respectively (1) exposed to acidic solutions, in which case the carbonate minerals can dissolve, or (2) covered with water or organic material, which may promote reductive mineral dissolution and trace metal release (Königsberger et al., 1999; Ribet et al., 1995). To prevent trace metal remobilisation from accelerated carbon mineralisation projects, the environmental conditions of stockpiled mineral products may need to be managed.

2.4.5. Future research

This study demonstrates that Mg-carbonate and Fe-oxyhydroxide minerals have the capacity to take up transition metals that are common in ultramafic rocks, likely by substitution for Mg²⁺ in the case of Mg-carbonate minerals. The precise mechanisms of sorption, the relative roles of adsorption and absorption, and the specific surface and crystal structure sites for metal uptake could be determined using Extended X-ray Absorption Fine Structure (EXAFS) spectroscopy, as in Frierdich and Catalano (2012) and Massey et al. (2014).

The capacity of nesquehonite to store transition metals (Cr, Ni, Mn, Co, Cu) may also have implications for the use of Mg-carbonate by-products of carbon mineralisation. Mg-carbonate minerals are currently utilised in a number of industrial applications including as raw material for production of magnesia and fire retardants, as rubber-strengthening agents and ingredients in pharmaceutical products (Hollingbery and Hull, 2010; Shan et al., 2012). The Carbon Capture Utilisation and Storage (CCUS) community has suggested

that Mg-carbonates could find additional uses as construction materials, which may help to offset the costs of mineral carbonation projects (Galvez-Martos et al., 2016; Glasser et al., 2016; Olajire, 2013). If carbonation of ultramafic rocks or industrial wastes were implemented on an industrial scale, the capacity of mineral products to sequester potentially hazardous transition metals may be an important consideration for assessing their suitability for use in some industries. On the other hand, the use of nesquehonite precipitation may also have potential applications in environmental remediation of toxic transition metals.

Further research should investigate the possible risk of metal remobilisation from hydrated Mg-carbonate and Fe-oxyhydroxide phases that form during carbon mineralisation reactions, although sorption should be stable under oxidised and neutral to alkaline conditions. Another important avenue to explore will be whether trace metals remain sequestered within the crystal structures of Mg-carbonate minerals during decomposition of nesquehonite to hydromagnesite and ultimately to magnesite.

2.5. Chapter 1 references

- ANZECC (Australian and New Zealand Environment and Conservation Council) and ARMCANZ (Agriculture and Resource Management Council of Australia and New Zealand). (2000) Australian and New Zealand Guidelines for Fresh and Marine Water Quality. National Water Quality Management Strategy Paper No. 4 Volume 1.
- Azdarpour A., Asadullah M., Mohammadian E., Hamidi H., Junin R. and Karaei M.A. (2015) A review on carbon dioxide mineral carbonation through pH-swing process. *Chemical Engineering Journal* 279, 615-630.
- Ballirano P., De Vito C., Ferrini V. and Mignardi S. (2010) The thermal behaviour and structural stability of nesquehonite, $MgCO_3 \cdot 3H_2O$, evaluated by in situ laboratory parallel-beam X-ray powder diffraction: New constraints on CO_2 sequestration within minerals. *Journal of Hazardous Materials* 178, 522-528.

- Ballirano P., De Vito C., Mignardi S. and Ferrini V. (2013) Phase transitions in the Mg-CO₂-H₂O system and the thermal decomposition of dypingite, Mg₅(CO₃)₄(OH)₂·5H₂O: Implications for geosequestration of carbon dioxide. *Chemical Geology* 340, 59-67.
- Berry A.J., O'Neill H.S.C. (2004) A XANES determination of the oxidation state of chromium in silicate glasses. *American Mineralogist* 89, 790-798.
- Blowes D.W., Ptacek C.J., Jambor J.L., Weisener C.G., Paktunc D., Gould W.D. and Johnson D.B. (2014) The Geochemistry of Acid Mine Drainage, in: Turekian, H.D.H.K. (Ed.), *Treatise on Geochemistry (Second Edition)*. Elsevier, Oxford, 131-190.
- Calugaru I.L., Neculita C.M., Genty T., Bussi re B. and Potvin R. (2016) Performance of thermally activated dolomite for the treatment of Ni and Zn in contaminated neutral drainage. *Journal of Hazardous Materials* 310, 48-55.
- Cheng W. and Li Z. (2009) Precipitation of nesquehonite from homogeneous supersaturated solutions. *Crystal Research and Technology* 44, 937-947.
- Comans R.N.J. and Middelburg J.J., (1987) Sorption of trace metals on calcite: Applicability of the surface precipitation model. *Geochimica et Cosmochimica Acta* 51, 2587-2591.
- Davies P.J. and Bubela B. (1973) The transformation of nesquehonite into hydromagnesite. *Chemical Geology* 12, 289-300.
- El Ali A., Barbin V., Calas G., Cervelle B., Ramseyer K. and Bouroulec J. (1993) Mn²⁺-activated luminescence in dolomite, calcite and magnesite: quantitative determination of manganese and site distribution by EPR and CL spectroscopy. *Chemical Geology* 104, 189-202.
- Flaathen T. and Gislason S. (2007) The groundwater beneath Hekla Volcano, Iceland: A natural analogue for CO₂ sequestration. *Geochimica et Cosmochimica Acta* 71, A283.
- Franklin M.L. and Morse J.W. (1983) The interaction of manganese(II) with the surface of calcite in dilute solutions and seawater. *Marine Chemistry* 12, 241-254.
- Friedrich A.J. and Catalano J.G. (2012) Distribution and speciation of trace elements in iron and manganese oxide cave deposits. *Geochimica et Cosmochimica Acta* 91, 240-253.
- Galvez-Martos J.L., Morrison J., Jauffret G., Elsarrag E., AlHorr Y., Imbabi M.S. and Glasser F.P., (2016) Environmental assessment of aqueous alkaline absorption of

carbon dioxide and its use to produce a construction material. *Resources, Conservation and Recycling* 107, 129-141.

- Glasser F.P., Jauffret G., Morrison J., Galvez-Martos J.-L., Patterson N. and Imbabi M.S.-E. (2016) Sequestering CO₂ by mineralisation into useful nesquehonite-based products. *Frontiers in Energy Research* 4, 3.
- Hamilton J.L. (2013). Trace metal mobility during mineral carbonation (honours thesis). Monash University, Clayton, Victoria, Australia.
- Handler R.M., Friedrich A.J., Johnson C.M., Rosso K.M., Beard B.L., Wang C., Latta D.E., Neumann A., Pasakarnis T. and Premaratne W. (2014) Fe (II)-catalyzed recrystallization of goethite revisited. *Environmental Science & technology* 48, 11302-11311.
- Hartman J., West A.J., Renforth P., Köhler P., De La Rocha C.L., Wolf-Gladrow D.A., Dürr H.H. and Scheffran J. (2013) Enhanced chemical weathering as a geoengineering strategy to reduce atmospheric carbon dioxide, supply nutrients, and mitigate ocean acidification. *Reviews of Geophysics* 51, 113-149.
- Hollingbery L.A. and Hull T.R. (2010) The thermal decomposition of huntite and hydromagnesite—A review. *Thermochimica Acta* 509, 1-11.
- IPCC (2013) IPCC Climate Change 2013: The Physical Science Basis. Contribution of Working Group 1 to the Fifth Assessment Report of the Intergovernmental Panel on Climate Change. Stocker T.F., Qin D., Plattner G.-K., Allen S.K., Boschung J., Naules A., Xia Y., Bex V. and Midgley P.M (eds) *Cambridge University Press*, Cambridge, United Kingdom and New York, USA.
- Jauffret G., Morrison J. and Glasser F.P. (2015) On the thermal decomposition of nesquehonite. *Journal of Thermal Analysis and Calorimetry* 122, 601-609.
- Kirsch K., Navarre-Sitchler A.K. Wunsch A. and McCray J.E. (2014) Metal release from sandstones under experimentally and numerically simulated CO₂ leakage conditions. *Environmental Science & Technology* 48, 1436-1442.
- Kmetoni J. (1984) Woodsreef Mill Tailings - Investigation of potential for further utilization as a mineral resource (Stage 1 - Mineralogical Composition). *Department of Mineral Resources*, New South Wales, Report No. 84/11.
- Königsberger E., Königsberger L.-C. and Gamsjäger H. (1999) Low-temperature thermodynamic model for the system Na₂CO₃-MgCO₃-CaCO₃-H₂O. *Geochimica et Cosmochimica Acta* 63, 3105-3119.
- Kotaś J. and Stasicka Z. (2000) Chromium occurrence in the environment and methods of its speciation. *Environmental Pollution* 107, 263-283.

- Lackner K.S., Wendt C.H., Butt D.P., Joyce E.L.J. and Sharp D.H. (1995) Carbon dioxide disposal in carbonate minerals. *Energy* 20, 1153-1170.
- Lamble G., Reeder R. and Northrup P. (1997) Characterization of heavy metal incorporation in calcite by XAFS spectroscopy. *Le Journal de Physique IV* 7, C2-793-C792-797.
- Lee G., Bigham J.M. and Faure G. (2002) Removal of trace metals by coprecipitation with Fe, Al and Mn from natural waters contaminated with acid mine drainage in the Ducktown Mining District, Tennessee. *Applied Geochemistry* 17, 569-581.
- Low F., Kimpton J., Wilson S.A. and Zhang L. (2015) Chromium reaction mechanisms for speciation using synchrotron in-situ high-temperature X-ray diffraction. *Environmental Science & Technology* 49, 8246-8253.
- Lumsden D.N. and Lloyd R.V. (1984) Mn(II) partitioning between calcium and magnesium sites in studies of dolomite origin. *Geochimica et Cosmochimica Acta* 48, 1861-1865.
- MacRae C. and Wilson N.C. (2008) Luminescence database I—minerals and materials. *Microscopy and Microanalysis* 14, 184-204.
- MacRae C., Wilson N.C. and Torpy A. (2013) Hyperspectral cathodoluminescence. *Mineralogy and Petrology* 107, 429-440.
- Manceau A., Schlegel M.L., Musso M., Sole V.A., Gauthier C., Petit P.E. and Trolard F. (2000) Crystal chemistry of trace elements in natural and synthetic goethite. *Geochimica et Cosmochimica Acta* 64, 3643-3661.
- Marcon V. and Kaszuba J. (2013) Trace metal mobilization in an experimental carbon sequestration Scenario. *Procedia Earth and Planetary Science* 7, 554-557.
- Marcon V. and Kaszuba J.P. (2015) Carbon dioxide–brine–rock interactions in a carbonate reservoir capped by shale: Experimental insights regarding the evolution of trace metals. *Geochimica et Cosmochimica Acta* 168, 22-42.
- Margiotta S., Mongelli G., Summa V., Paternoster M. and Fiore S. (2012) Trace element distribution and Cr(VI) speciation in Ca-HCO₃ and Mg-HCO₃ spring waters from the northern sector of the Pollino massif, southern Italy. *Journal of Geochemical Exploration* 115, 1-12.
- Maroto-Valer M.M., Fauth D.J., Kuchta M.E., Zhang Y. and Andrésen J.M. (2005) Activation of magnesium rich minerals as carbonation feedstock materials for CO₂ sequestration. *Fuel Processing Technology* 86, 1627-1645.

- Massey M.S., Lezama-Pacheco J.S., Nelson J.M., Fendorf S. and Maher K. (2014) Uranium incorporation into amorphous silica. *Environmental Science & Technology* 48, 8636-8644.
- Mavromatis V., Bundeleva I.A., Shirokova L.S., Millo C., Pokrovsky O.S., Bénézech P., Ader M. and Oelkers E.H. (2015) The continuous re-equilibration of carbon isotope compositions of hydrous Mg carbonates in the presence of cyanobacteria. *Chemical Geology* 404, 41-51.
- McCutcheon J., Dipple G.M., Wilson S.A. and Southam G. (2015) Production of magnesium-rich solutions by acid leaching of chrysotile: A precursor to field-scale deployment of microbially enabled carbonate mineral precipitation. *Chemical Geology* 413, 119-131.
- McCutcheon J., Wilson S.A. and Southam G. (2016) Microbially accelerated carbonate mineral precipitation as a strategy for in situ carbon sequestration and rehabilitation of asbestos mine sites. *Environmental Science & Technology* 50, 1419-1427.
- Medlin W.L. (1961) Thermoluminescence in aragonite and magnesite. *The Journal of Physical Chemistry* 65, 1172-1177.
- Morgan B., Wilson S.A., Madsen I.C., Gozukara Y.M. and Habsuda J. (2015) Increased thermal stability of nesquehonite ($MgCO_3 \cdot 3H_2O$) in the presence of humidity and CO_2 : Implications for low-temperature CO_2 storage. *International Journal of Greenhouse Gas Control* 39, 366-376.
- Natali C., Boschi C., Baneschi I., Dini A. and Chiarantini L. (2013) Chromium mobility in Tuscan serpentinite bodies; inferences from rodingitization and carbonation. *Mineralogical Magazine* 77, 1829.
- Oelkers E.H., Gislason S.R. and Matter, J. (2008) Mineral carbonation of CO_2 . *Elements* 4, 333-337.
- Olajire A.A. (2013) A review of mineral carbonation technology in sequestration of CO_2 . *Journal of Petroleum Science and Engineering* 109, 364-392.
- Olsson J., Stipp S.L.S. and Gislason S.R. (2014a). Element scavenging by recently formed travertine deposits in the alkaline springs from the Oman Semail Ophiolite. *Mineralogical Magazine* 78, 1479-1490.
- Olsson J., Stipp S.L.S., Makovicky E. and Gislason S.R. (2014b). Metal scavenging by calcium carbonate at the Eyjafjallajökull volcano: A carbon capture and storage analogue. *Chemical Geology* 384, 135-148.

- Oze C., Bird D.K. and Fendorf S. (2007) Genesis of hexavalent chromium from natural sources in soil and groundwater. *Proceedings of the National Academy of Sciences* 104, 6544-6549.
- Papathanassiou A.N. (2003) Study of the polarizable centers in single crystal dolomite (CaMg(CO₃)₂) rich in Fe³⁺ impurities by thermally stimulated depolarization current spectroscopy. *Journal of Physics and Chemistry of Solids* 64, 171-175.
- Park A.-H.A. and Fan L.-S. (2004) CO₂ mineral sequestration: physically activated dissolution of serpentine and pH swing process. *Chemical Engineering Science* 59, 5241-5247.
- Park A.-H.A., Jadhav, R. and Fan L.-S. (2003) CO₂ mineral sequestration: Chemically enhanced aqueous carbonation of serpentine. *The Canadian Journal of Chemical Engineering* 81, 885-890.
- Parkhurst D.L. and Appelo C. (1999) User's guide to PHREEQC (Version 2): A computer program for speciation, batch-reaction, one-dimensional transport, and inverse geochemical calculations.
- Power I.M., Dipple G.M. and Southam G. (2010) Biobleaching of ultramafic tailings by *Acidithiobacillus* spp. for CO₂ sequestration. *Environmental Science & Technology* 44, 456-462.
- Power I.M., Harrison A.L., Dipple G.M., Wilson S.A., Kelemen P.B., Hitch M. and Southam G. (2013a) Carbon mineralisation: From natural analogues to engineered systems. *Reviews in Mineralogy and Geochemistry* 77, 305-360.
- Power I.M., Wilson S.A. and Dipple G.M. (2013b) Serpentinite Carbonation for CO₂ Sequestration. *Elements* 9, 115-121.
- Power I.M., Wilson S.A., Thom J.M., Dipple G.M., Gabites J.E. and Southam G. (2009) The hydromagnesite playas of Atlin, British Columbia, Canada: A biogeochemical model for CO₂ sequestration. *Chemical Geology* 260, 286-300.
- Prissok F. and Lehmann G. (1986) An EPR study of Mn²⁺ and Fe³⁺ in dolomites. *Physics and Chemistry of Minerals* 13, 331-336.
- Rai D., Eary L. and Zachara J. (1989) Environmental chemistry of chromium. *Science of the Total Environment* 86, 15-23.
- Ribet I., Ptacek C.J., Blowes D.W. and Jambor J.L. (1995) The potential for metal release by reductive dissolution of weathered mine tailings. *Journal of Contaminant Hydrology* 17, 239-273.

- Robie R.A. and Hemingway B.S. (1972) The heat capacities at low-temperatures and entropies at 298.15 K of nesquehonite, $\text{MgCO}_3 \cdot 3\text{H}_2\text{O}$, and hydromagnesite. *American Mineralogist* 57, 1768-1781.
- Rodriguez-Navarro C. and Ruiz-Agudo E. (2013) Carbonates: An overview of recent TEM research. Chapter 10, EMU Notes in Mineralogy: Minerals at the Nanoscale. Vol. 14. The Mineralogical Society of Great Britain and Ireland.
- Ryan C.G. (2000) Quantitative trace element imaging using PIXE and the nuclear microprobe. *International Journal of Imaging Systems and Technology* 11, 219-230.
- Ryan C.G., Siddons D.P., Kirkham R., Dunn P.A., Kuczewski A., Moorhead G., De Geronimo G., Paterson D.J., de Jonge M.D., Hough R.M., Lintern M.J., Howard D.L., Kappen P. and Cleverley J. (2010) The new Maia detector system: Methods for high definition trace element imaging of natural material. *AIP Conference Proceedings* 1221, 9-17.
- Ryan C.G., Siddons D.P., Kirkham R., Li Z.Y., Jonge M.D.d., Paterson D.J., Kuczewski A., Howard D.L., Dunn P.A., Falkenberg G., Boesenberg U., Geronimo G.D., Fisher L.A., Halfpenny A., Lintern M.J., Lombi E., Dyl K.A., Jensen M., Moorhead G.F., Cleverley J.S., Hough R.M., Godel B., Barnes S.J., James S.A., Spiers K.M., Alfeld M., Wellenreuther G., Vukmanovic Z. and Borg S. (2014) Maia X-ray fluorescence imaging: Capturing detail in complex natural samples. *Journal of Physics: Conference Series* 499, 012002.
- Schreier H. (1987) Asbestos fibres introduce trace metals into streamwater and sediments. *Environmental Pollution* 43, 229-242.
- Schuling R. and de Boer P. (2013) Six commercially viable ways to remove CO_2 from the atmosphere and/or reduce CO_2 emissions. *Environmental Sciences Europe* 25, 35.
- Schultz L.N., Dideriksen K., Lakshitanov L., Hakim S.S., Mütter D., Haußer F., Bechgaard K. and Stipp S.L.S. (2014) From nanometer aggregates to micrometer crystals: Insight into the coarsening mechanism of calcite. *Crystal Growth & Design* 14, 552-558.
- Schwertmann U. and Gasser U., Sticher H. (1989) Chromium-for-iron substitution in synthetic goethites. *Geochimica et Cosmochimica Acta* 53, 1293-1297.
- Seal R.R., Piatak N.M., Levitan D.M. and Hammarstrom J.M. (2010) Neutral to alkaline mine drainage, carbon sequestration, and arsenic release at the abandoned Vermont Asbestos Group Mine, Belvidere Mountain, Vermont. *Geological Society of America Abstracts with Programs* 42, 449.

- Seifritz W. (1990) CO₂ disposal by means of silicates. *Nature* 345, 486.
- Shan Q., Zhang Y. and Xue X. (2012) Removal of copper from wastewater by using the synthetic nesquehonite. *Environmental Progress & Sustainable Energy* 32, 543-546.
- Shannon R.D. (1976) Revised effective ionic radii and systematic studies of interatomic distances in halides and chalcogenides. *Acta Crystallographica Section A: Crystal Physics, Diffraction, Theoretical and General Crystallography* 32, 751-767.
- Teir S., Kuusik R., Fogelholm C.-J. and Zevenhoven R., (2007a) Production of magnesium carbonates from serpentinite for long-term storage of CO₂. *International Journal of Mineral Processing* 85, 1-15.
- Teir S., Revitzer H., Eloneva S., Fogelholm C.-J. and Zevenhoven R. (2007b) Dissolution of natural serpentinite in mineral and organic acids. *International Journal of Mineral Processing* 83, 36-46.
- Thomas D., Maher K., Bird D., Brown G. and Arnorsson S. (2013) CO₂-rich geothermal areas in Iceland as natural analogues for geologic carbon sequestration. *AGU Fall Meeting Abstracts* 1, 2776.
- Trolard F., Bourrie G., Jeanroy E., Herbillon A.J. and Martin H. (1995) Trace metals in natural iron oxides from laterites: A study using selective kinetic extraction. *Geochimica et Cosmochimica Acta* 59, 1285-1297.
- Vogel C., Adam C., Kappen P., Schiller T., Lipiec E. and McNaughton D. (2014) Chemical state of chromium in sewage sludge ash based phosphorus-fertilisers. *Chemosphere* 103, 250-255.
- Wilson S.A., Raudsepp M. and Dipple G. (2006) Verifying and quantifying carbon fixation in minerals from serpentine-rich mine tailings using the Rietveld method with X-ray powder diffraction data. *American Mineralogist* 91, 1331-1341.
- Wilson S.A., Dipple G.M., Power I.M., Thom J.M., Anderson R.G., Raudsepp M., Gabites J.E. and Southam G. (2009) Carbon dioxide fixation within mine wastes of ultramafic-hosted ore deposits: Examples from the Clinton Creek and Cassiar chrysotile deposits, Canada. *Economic Geology* 104, 95-112.
- World Health Organisation (2011) Guidelines for drinking-water quality, 4th edition. WHO: Geneva.
- Wunsch A., Navarre-Sitchler A.K., Moore J., Ricko A. and McCray J.E. (2013) Metal release from dolomites at high partial-pressures of CO₂. *Applied Geochemistry* 38, 33-47.

Zachara J.M., Cowan C.E. and Resch C.T. (1991) Sorption of divalent metals on calcite.
Geochimica et Cosmochimica Acta 55, 1549-1562.

Declaration for Thesis Chapter 3

Declaration by candidate

In the case of Chapter 3, the nature and extent of my contribution is as follows:

Nature of contribution	Extent of contribution
Concept, experimental design, data collection and interpretation, and writing. This work builds upon my honours thesis, and some preliminary results from that work (collection of sample, XRF and water chemistry analysis) are included here. This preliminary work contributes approximately 10% of the results presented in this chapter and it is cited where relevant.	79%

The following co-authors contributed to the work. If co-authors are students at Monash University, the extent of their contribution in percentage terms must be stated:

Name	Nature of contribution	Extent of contribution (%)
Siobhan A. Wilson	Supervisory role	5%
Bree Morgan	Supervisory role	5%
Connor C. Turvey	Fieldwork and XRD assistance	3%
David J. Paterson	Synchrotron XFM analysis	3%
Simon Jowitt	Advisor	3%
Jenine McCutcheon	Synchrotron XFM data collection	1%
Gordon Southam	Synchrotron XFM data collection	1%

The undersigned hereby certify that the above declaration correctly reflects the nature and extent of the candidate's and co-authors contributions to this work*.

Candidate's signature:



Date: 10 February 2018

Main supervisor's signature:



Date: 5 February 2018

*Note: Where the responsible author is not the candidate's main supervisor, the main supervisor should consult with the responsible author to agree on the respective contributions of the authors.

Chapter 3

Fate of transition metals during passive carbonation of ultramafic mine tailings via air capture with potential for metal resource recovery[†]

Jessica L. Hamilton^a, Siobhan A. Wilson^{ab}, Bree Morgan^{ac}, Connor C. Turvey^a, David J. Paterson^d, Simon M. Jowitt^{ae}, Jenine McCutcheon^{fg} and Gordon Southam^g

^aSchool of Earth, Atmosphere and Environment, Monash University, Clayton, Melbourne, VIC 3800, Australia

^bDepartment of Earth and Atmospheric Sciences, University of Alberta, Edmonton, AB T6G 2R3, Canada

^cSchool of Geosciences, The University of Sydney, Camperdown, NSW 2006, Australia

^dAustralian Synchrotron, Clayton, Melbourne, VIC 3168, Australia

^eDepartment of Geoscience, University of Nevada, Las Vegas, 4505 S. Maryland Pkwy, Las Vegas, NV 89154, USA

^fSchool of Earth and Environment, Maths/Earth and Environment Building, University of Leeds, Leeds, LS2 9JT, United Kingdom

^gSchool of Earth and Environmental Sciences, The University of Queensland, St Lucia, QLD 4072, Australia

[†]In review in *International Journal of Greenhouse Gas Control*
18/10/2017

Mineral carbonation in ultramafic mine tailings is generally accepted to be a safe and long term means of trapping and storing CO₂ within the structures of minerals, but it poses the risk of releasing potentially hazardous metal contaminants from mineral wastes into the environment. Stockpiles of reactive, finely pulverised ultramafic mine tailings are ideal natural laboratories for the observation and promotion of the carbonation of Mg-silicate and Mg-hydroxide waste minerals via reaction with atmospheric or industrial CO₂. However, ultramafic mine tailings commonly contain first-row transition metals (e.g., Cr, Co, Cu, Ni) in potentially toxic concentrations within the crystal structures of Mg-silicates, sulphides, and oxides. These transition metals are likely to be mobilised by mineral carbonation reactions, which require mineral dissolution to supply cations for reaction with carbon. At Woodsreef Chrysotile Mine, New South Wales, Australia, transition metals (i.e., Fe, Cr, Ni, Mn, Co, Cu) are most concentrated within minor oxides (magnetite and chromite) and trace alloys (awaruite, Ni₂₋₃Fe and wairauite, CoFe) in serpentine tailings, however, mobilisation of transition metals appears to occur predominantly during dissolution of serpentine and brucite, which are more abundant and reactive phases, respectively. Here, we present new synchrotron X-ray fluorescence mapping data that provide insights into the mobility of first-row transition metals (Fe, Cr, Ni, Mn, Co, Cu) during weathering and carbonation of ultramafic mine tailings collected from the Woodsreef Chrysotile Mine. These data indicate that the recently precipitated carbonate minerals, hydromagnesite [Mg₅(CO₃)₄(OH)₂·4H₂O] and pyroaurite [Mg₆Fe₂(CO₃)(OH)₁₆·4H₂O] sequester trace metals from the tailings at concentrations of 10s to 100s of ppm, most likely via substitution for Mg or Fe within their crystal structures, or by the physical trapping of small (µm-scale) transition-metal-rich grains (i.e., magnetite, chromite, awaruite), which are stabilised within alkaline carbonate cements. Trace transition metals are present at relatively high concentrations in the bulk

tailings (i.e., ~0.3 wt. % NiO and Cr₂O₃) and they are largely retained within the unaltered mineral assemblage. Mg-carbonate minerals form a cement between grains of partially dissolved gangue minerals at the surface of the tailings, and appear to immobilise transition metals on spatial scales of micrometres and at comparable concentrations to those observed in the gangue minerals. The end result is that trace metals are not present at detectable levels within mine pit waters. Our observations of metal mobility during passive carbonation suggest that mineral products of accelerated carbonation treatments are likely to sequester trace metals. Thus, accelerated carbonation is unlikely to pose an environmental risk in the form of metalliferous drainage so long as the neutralisation potential of the tailings is not exceeded.

Understanding both trace transition metal geochemistry and mineralogy within materials targeted for mineral carbonation could allow optimisation of treatment processes and design for recovery of valuable metals. In *ex situ* reactors employing acid pre-treatments, trace metals mobilised from reactive phases such as serpentine and brucite could potentially be recovered using pH-swing methods, while recalcitrant metal-rich accessory minerals, including magnetite, awaruite and chromite, could be recovered from treated residue material by conventional mineral separation processes. Recovery of valuable metals (i.e., Ni, Cr and Co) as by-products of accelerated mineral carbonation technologies could also provide an important economic incentive to support broader adoption of this technology.

3.1. Introduction

The increasing concentration of anthropogenic CO₂ in the atmosphere is likely driving long-term changes to Earth's climate (Hallett, 2002; IPCC, 2005, 2013). As such, there is a growing need to develop mitigation technologies, both to reduce anthropogenic CO₂

emissions and to capture atmospheric CO₂ from the air for long-term storage in a stable form. Mineral carbonation, which was first proposed as a mitigation strategy for CO₂ emissions by Seifritz (1990), captures CO₂ within the structures of environmentally benign carbonate minerals by enhancing natural silicate weathering, promoting the safe, long-term storage of CO₂. Importantly, this is the only proposed CO₂ storage technology that is considered to be permanent over geological timescales, given that many carbonate minerals are known to persist at the Earth's surface for 1000s of years or longer (Lackner et al., 1995; Oelkers et al., 2008; Olajire, 2013; Seifritz, 1990).

Natural carbonation of mine tailings in Australia, Canada, the U.S.A., and Norway (99 – 6200 g CO₂/m²/y; Beinlich and Austrheim, 2012; Gras et al., 2017, Lechat et al., 2016; Levitan et al., 2009; Oskierski et al., 2013; Pronost et al., 2012; Turvey et al., 2017, Wilson et al., 2006, 2009a,b, 2011, 2014) occurs at rates that are typically orders of magnitude greater than average CO₂ uptake associated with silicate weathering (0.7 – 62.1 g CO₂/m²/y, Power et al., 2013, units converted from Ludwig et al., 1998). The enhanced reactivity of mine tailings is largely due to the orders of magnitude increase in mineral surface area that results from crushing during ore processing (Wilson et al., 2009a). The greatest uptake of CO₂ by mine tailings yet reported occurs at the Mt Keith Nickel Mine in Western Australia, where nearly 40,000 t of atmospheric CO₂ are sequestered annually via natural reaction of the tailings with the atmosphere, representing an 11% offset of the mine's annual greenhouse gas emissions (Wilson et al., 2014). This enhanced reactivity of mineral wastes makes historical and operating mine tailings storage facilities provide ideal settings for observing transition metal mobility during passive mineral carbonation reactions on timescales of years to decades.

Ultramafic rocks are commonly mined for Cr, Ni-Cu-platinum group element sulfides, diamonds, talc, and (historically) chrysotile asbestos. They are also the preferred feedstock material for mineral carbonation because they contain high abundances of silicate minerals with high Mg contents {i.e., olivine $[(\text{Mg,Fe})_2\text{SiO}_4]$ and serpentine $[\text{Mg}_3\text{Si}_2\text{O}_5(\text{OH})_4]$ }, and minor amounts of highly reactive phases such as brucite $[\text{Mg}(\text{OH})_2]$ (Goff and Lackner, 1998; Lackner, 2003; Oelkers et al., 2008; Power et al., 2013). Brucite forms via the hydration of olivine during serpentinisation and is usually present as a common but minor component of ultramafic tailings (1–15 wt. %; Harrison et al., 2012, O’Hanley and Offler, 1992). The lack of strong Si-O bonds within brucite means that it has a reactivity that is orders of magnitude greater than that of Mg-silicates, meaning that the abundance of brucite exerts strong control on mineral carbonation rates under ambient conditions (Harrison et al., 2012; Power et al., 2013). In addition, the serpentine polymorphs, chrysotile and lizardite, consist of a sheet of silica tetrahedra bonded to an octahedral Mg-OH sheet that is commonly referred to as the ‘brucite-like’ layer (e.g., Wicks and O’Hanley, 1988). This ‘brucite-like’ layer is more reactive and dissolves faster than the accompanying Si-rich tetrahedral layer (Park and Fan, 2004, Rozalen and Huertas, 2013), increasing the reactivity of serpentine and enhancing release of Mg for CO₂ sequestration. The Mg²⁺ cations released by the dissolution of these minerals in meteoric water react with dissolved atmospheric CO₂ to precipitate as hydrated carbonate minerals such as hydromagnesite $[\text{Mg}_5(\text{CO}_3)_4(\text{OH})_2 \cdot 4\text{H}_2\text{O}]$ and nesquehonite ($\text{MgCO}_3 \cdot 3\text{H}_2\text{O}$), with Mg:CO₂ ratios and hydration states that are dependent on local environmental conditions (Ballirano et al., 2013; Davies and Bubela, 1973; Hänchen et al., 2008; Morgan et al., 2015; Wilson et al., 2009a). Acid leaching, or the addition of acid generating materials, has been widely employed to accelerate CO₂ uptake in ultramafic materials because it increases the rate of silicate mineral dissolution

and the availability of Mg^{2+} cations for reaction (e.g., Maroto-Valer et al., 2005; Park and Fan, 2004; Power et al., 2010; Teir et al., 2007b). Following acid leaching, pH-swing methods can then be used to increase pH to alkaline conditions to allow precipitation of carbonate minerals (Park and Fan, 2004). In highly reactive mineral wastes, particularly where brucite is present, mineral dissolution under ambient conditions can provide sufficient alkalinity to induce carbonate precipitation (Harrison et al., 2013; Power et al., 2013). However, ultramafic rocks commonly contain several wt. % Fe as well as low concentrations (< 1 wt. %) of other first row transition metals (e.g., Ni, Mn, Cr, Co, Cu). These are typically found within the crystal structures of Mg-silicate, Mg-hydroxide, sulphide, and oxide minerals as well as within alloy minerals such as awaruite ($Ni_{12-3}Fe$) and wairauite (CoFe) (Challis and Long, 1964; Goff and Lackner, 1998; Kmetoni, 1984; Margiotta et al., 2012; Natali et al., 2013; Schreier, 1987; Sciortino et al., 2015). First row transition metals may be mobilised by dissolution of their mineral hosts during either natural weathering reactions or the artificially accelerated reactions that can be used to enhance mineral carbonation rates (Margiotta et al., 2012; Oelkers et al., 2008; Olajire, 2013; Olsson et al., 2014a,b; Schreier, 1987; Teir et al., 2007a). Because first-row transition metals can be toxic to biota in elevated concentrations, concern has been raised that the release of metalliferous waters from mineral carbonation facilities or geoengineered landscapes could adversely affect natural systems (Olsson et al., 2014b). Consequently, the potential mobility of trace metals during carbonation reactions is an essential consideration for implementation of *ex situ* mineral carbonation technologies, *in situ* enhanced weathering of ultramafic landscapes or mineral wastes, and *in situ* CO_2 injection into rock formations (Hamilton et al., 2016; Kirsch et al., 2014; Marcon and Kaszuba, 2013; Marcon and Kaszuba, 2015; Oelkers et al., 2008; Olajire, 2013; Olsson et

al., 2014a; Olsson et al., 2014b; Seal et al., 2010; Thomas et al., 2013; Thomas et al., 2016).

Previous studies have reported elevated concentrations of trace metals (particularly Ni, Cr³⁺ and carcinogenic Cr⁶⁺) in soils and waters associated with serpentinites (Margiotta et al., 2012; McClain and Maher, 2016; Morrison et al., 2015; Schreier, 1987; Schreier and Lavkulich, 2015). Uptake of these trace metals by Fe-hydroxide and clay minerals has been documented in serpentinites (Morrison et al., 2015), but the influence of hydrated Mg-carbonate minerals on trace metal mobility within ultramafic environments is relatively unexplored. This is a critical knowledge gap, given that hydrated Mg-carbonate minerals are commonly present in high abundances [up to 14.6 wt. % hydromagnesite; (Oskierski et al., 2013)] in passively carbonated mine tailings, and therefore may provide an important sink for potentially toxic trace metals.

Hamilton *et al.* (2016) demonstrated that Mg-carbonate minerals and Fe-oxyhydroxide phases sequester transition metals during their formation in laboratory experiments designed to emulate the Mg- and transition-metal-rich conditions produced during accelerated mineral carbonation. However, the mobility of potentially toxic trace metals during naturally occurring mineral carbonation in ultramafic landscapes has not yet been extensively explored. Here, we investigate (1) the mineral sources of trace transition metals and the mobility of these metals during weathering, and (2) the sequestration of trace transition metals by carbonate minerals and associated alteration phases at the Woodsreef Chrysotile Mine in New South Wales, Australia. This study provides a framework for understanding the fundamental geochemical processes, and associated environmental risks, that accompany the carbonation of transition-metal-rich ultramafic rocks. This is essential information for both the development of low-temperature

technologies for enhancing carbon mineralisation using acidic treatments, and for the geosequestration of industrial CO₂ during injection into mafic to ultramafic formations. In addition, an understanding of transition metal mineralogy and mobility during mineral carbonation reactions is used to identify potential opportunities for recovery of metals from ultramafic mine wastes.

3.2. Methods

3.2.1. Site description

The chrysotile deposit at Woodsreef lies within the Great Serpentine Belt, in the Southern New England Fold Belt of northeastern New South Wales, Australia. The ultramafic rocks at Woodsreef have been variably serpentinised and contain partially serpentinised harzburgite as well as massive and schistose serpentinite (Glen and Butt, 1981). The massive serpentinite has formed from partially serpentinised harzburgite by the transformation of forsterite and pyroxene minerals into serpentine phases and magnetite (Glen and Butt, 1981; O'Hanley and Offler, 1992; Oskierski et al., 2013). Large bodies and small kernels of partially serpentinised harzburgite still remain within the massive and schistose serpentinites, which host the chrysotile [Mg₃Si₂O₅(OH)₄] deposit (Glen and Butt, 1981).

The Woodsreef Chrysotile Mine is located approximately 500 km northwest of Sydney in New South Wales, Australia (Fig. 1). The now derelict site occupies approximately 400 ha, and hosts four mine pits, now partially filled with water. The most recent and productive period of chrysotile asbestos mining at Woodsreef was conducted by Chrysotile Corporation between 1971 and 1983. This mining produced 500,000 t of chrysotile, 75 Mt of waste rock, and 24.2 Mt of dry-milled tailings (Assargiotis, 2013;

Merrill et al., 1980; Oskierski et al., 2013; Woodsreef Taskforce, 2011). The Woodsreef tailings have since been investigated as a potential resource for nickel (Ni), chromium (Cr), magnetite, magnesium and silica (Kmetoni, 1984; Laughton and Green, 2002; Sylvester and Stagg, 2008). Passive carbonation of tailings at Woodsreef has been occurring over the past three decades (Oskierski et al., 2013; Turvey et al., 2017), resulting in the sequestration of an estimated 1,400 t of CO₂ within the hydromagnesite crusts located in the upper 2 cm of the tailings pile, and up to 70,000 t of CO₂ stored within pyroaurite at depth, although questions remain about source of carbon in this phase (Oskierski et al., 2013).

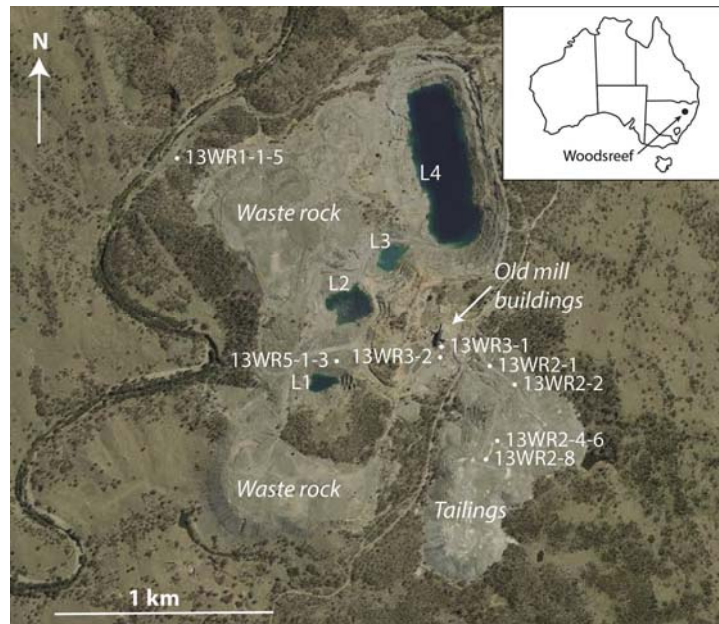


Figure 3.1. Map of Woodsreef Mine site showing sampling locations. Labels beginning with an “L” indicate water sample locations from the four pit lakes. Solid phase tailings were collected at all other sample locations. Sample descriptions are listed in Appendix 2: Tables S1 and S2.

3.2.2. Sample collection

Hand samples of serpentinite ore and waste rock from the mine pits and surrounding stockpiles were targeted to capture both the starting composition of tailings at Woodsreef

and the products of mineral carbonation. These samples include serpentinite [n=6, including massive serpentinite (n=2) and partially serpentinised harzburgite (n=4)]. Samples of bulk tailings (n=2), and vertical and horizontal carbonate crusts forming within the tailings storage facility (n=5) were also collected. Sample descriptions and GPS co-ordinates are provided in Table S1. Water samples were also collected from each of the four mine pits, passed through 0.2 µm syringe driven filters and preserved to pH < 2 by addition of a few drops of nitric acid (50%) for later analysis of major cations (Ca²⁺, Mg²⁺, Na⁺, K⁺) by Inductively Coupled Plasma–Atomic Emission Spectrometry (ICP-AES) and anions (Cl⁻ by discrete analyser, HCO₃⁻ by titration, S by ICP-AES and reported as SO₄²⁻). The pH of the pit lake water was measured in the field using a calibrated pH meter (Thermo Scientific Orion 5 Star). Field observations are reported in Hamilton (2013), and expanded here (section 3.3.1. Elemental analysis).

3.2.3. Elemental analysis

The concentrations of a suite of dissolved trace elements (As, Ba, Be, Ca, Co, Cr, Cu, Mn, Ni, Pb, V, Zn, Fe) within the mine pit water samples were determined using Inductively Coupled Plasma–Mass Spectrometry (ICP-MS) at the ALS Group Environmental Division laboratories (Brisbane, Queensland). Bulk elemental analysis of solid phase samples was completed using X-ray Fluorescence (XRF), and total C and S concentrations were determined using a LECO instrument at SGS Australia (Newburn, Western Australia). Pit lake water chemistry and bulk rock geochemistry were initially reported in Hamilton (2013), and are interpreted here.

3.2.4. X-ray diffraction analysis

Solid phase samples for X-ray diffraction (XRD) were pulverised using a ring mill prior to the addition of a 10 wt. % fluorite (CaF₂) internal standard and micronising under

anhydrous ethanol in a McCrone Micronising Mill using agate grinding elements. The samples were then dried, disaggregated and back-loaded into cavity mounts for analysis using a Bruker D8 Advance Eco X-ray diffractometer, fitted with a Cu radiation source and operated at 40 kV and 25 mA, in the Monash X-ray Platform. Data were collected over 2–80° 2 θ with a step size of 0.02° 2 θ and a count time of 2 s/step. Mineral phases were identified using the ICDD PDF-2 database and the DIFFRACplus EVA Version 2 software package (Bruker AXS, 2004). Rietveld refinements (Bish and Howard, 1988; Hill and Howard, 1987; Rietveld, 1969) were completed using Topas Version 5 (Bruker AXS, 2004). The Rietveld refinement methodology outlined by Wilson et al. (2006) was used for quantification of mineral abundances in these serpentine-rich samples.

3.2.5. Scanning electron microscopy

Ten samples of waste rock and tailings were set in epoxy resin and cut into 30 μ m thick polished thin sections. The least weathered serpentinites and partially serpentinised harzburgites were selected to capture the composition of the original source rocks. Thin sections were also produced from a range of tailings samples to reflect variability in the extent of carbonation at Woodsreef. Thin sections were carbon coated and analysed using scanning electron microscopy and energy dispersive X-ray spectroscopy (SEM-EDS) employing a JEOL 7001F Field Emission Gun Scanning Electron Microscope (FEG-SEM) with backscattered electron (BSE) images collected at 15–20 kV at the Monash Centre for Electron Microscopy, Monash University, Clayton, Australia.

3.2.6. X-ray fluorescence microscopy

Representative carbonate crust samples (13WR2-4 and 13WR2-8) analysed by SEM were prepared as thin sections on quartz slides for trace element analysis using X-ray fluorescence microscopy (XFM) at the Australian Synchrotron, Clayton, Australia.

Synchrotron X-ray Fluorescence Microscopy (XFM) allows rapid quantitative elemental analysis over large areas (such as a geological thin section) at high resolution (using pixel sizes as small as $\sim 2 \mu\text{m}$) with ppb-level sensitivity (Paterson et al., 2011; Ryan et al., 2014). In addition, the XFM beamline at the Australian Synchrotron can generate X-ray Absorption Near Edge Spectroscopy (XANES) maps, which are used here to investigate the speciation of Cr within weathered carbonate crusts from Woodsreef Mine.

Fast preliminary scans were conducted with an incident monochromatic X-ray beam of 18.5 keV focused to $\sim 2.0 \mu\text{m}$ using Kirkpatrick-Baez mirrors, a step size of $2 \mu\text{m}$, and a dwell time of 40 msec/pixel. Following this, the energy of the X-ray beam was reduced to 12.9 keV to enable better detection of the trace metals in small areas of interest identified during the preliminary scans of entire thin sections. These areas of interest were mapped using a step size of $1 \mu\text{m}$ and a dwell time of 1000 msec/pixel to optimise counting statistics. Elemental abundance data were collected using a Maia detector (Ryan et al., 2010; Ryan et al., 2014) and the full spectrum of data were processed using the GeoPIXE software program (Ryan, 2000).

Cr K-edge XANES analysis was undertaken over a region of interest within a carbonate crust sample (13WR2-8) over an energy range of 5.96 to 6.12 keV with a step size of $4 \mu\text{m}$ and a dwell time of 8 ms. GeoPIXE was used to process the resulting data and to assess spatial variations in oxidation state with spectra compared against published standards (Berry and O'Neill, 2004; Low et al., 2015; Vogel et al., 2014).

3.3. Results

3.3.1. Field site observations

Chrysotile was observed as exposed veins and forming slickensides in serpentinite and partially serpentinitised harzburgite in the mine pit walls and in cobbles from the waste rock and tailings piles at the Woodsreef Mine (Appendix 2: Fig. S1A,B; Hamilton, 2013). Partially serpentinitised harzburgite is commonly present as kernels within a serpentinite matrix (Appendix 2: Fig. S1C) that is dark in colour and has a waxy texture (Appendix 2: Fig. S1C). The serpentinite surrounding harzburgite pods appears to have weathered by cracking perpendicular to the surface of the pods and shedding a carbonated alteration halo (Appendix 2: Fig. S1C). A number of large boulders appeared to be disintegrating, most likely as a result of expansive forces and reaction-driven cracking generated by carbonate mineral precipitation (Beinlich and Austrheim, 2012). White carbonate minerals, identified by their characteristic effervescence when exposed to HCl, were prevalent on weathering surfaces and in cracks (Appendix 2: Fig. S1D). Heavily carbonated crusts within the tailings pile form as both vertical ridges on weathering faces (Appendix 2: Fig. S1E) and as horizontal cemented surfaces (Appendix 2: Fig. S1F; Hamilton, 2013).

3.3.2. Trace metal analysis

The ICP–MS analysis of the mine pit water indicates that concentrations of Ni, Cr, Mn, Co and Cu are below instrumental detection limits (<0.001 mg/L) in all samples with the exception of the sample taken from Lake 2 (Fig. 3.1), which contains 0.002 mg/L Cu (Appendix 2: Table S2; Hamilton, 2013). The pH of pit water ranges from 8.9 to 9.3 with an average value of 9.2 (Appendix 2: Table S2; Hamilton, 2013).

Bulk rock XRF results indicate that Ni, Cr, and Mn are present in all rock and tailings samples that were analysed, with Co being detectable in all but a few samples (detection limit was 0.01 wt. % as CoO; Table S3; Hamilton, 2013). Average Ni concentrations (as

NiO) are 0.29 wt. % in serpentinite waste rock (considered the least weathered samples), 0.26 wt. % in bulk tailings, and 0.25 wt. % in tailings carbonated crusts. Average Cr concentrations (as Cr₂O₃) are highest in serpentinite at 0.36 wt. %, with an intermediate value of 0.34 wt. % in bulk tailings, and lowest in carbonated crusts (0.32 wt. %). Mn concentrations (as MnO) are 0.10 wt. % in serpentinite, 0.12 wt. % in bulk tailings, and 0.10 wt. % in carbonated crusts. Co concentrations (as CoO) are consistently low in all samples and range from <0.01 to 0.02 wt. % with the highest concentrations occurring in serpentinite samples (Hamilton, 2013). However, significant variations are present between samples, reflecting the heterogeneity in lithology and mineralogy observed at the site. In general, transition metals are present at similar abundances in all sample types, but on average are slightly more concentrated in the less weathered serpentinite waste rock compared to bulk tailings and carbonate crust samples.

3.3.3. Mineralogical results

Serpentine minerals dominate the tailings at Woodsreef (67–97 wt. %). Hydromagnesite, pyroaurite [Mg₆Fe₂(CO₃)(OH)₁₆·4H₂O], magnetite (Fe₃O₄), chromite [(Mg,Fe)Cr₂O₄], brucite [Mg(OH)₂], forsterite (Mg₂SiO₄), and enstatite (MgSiO₃) are present as minor minerals, and both calcite and quartz are present at trace abundances. Although we give the formulae for ideal end-member compositions of these minerals, it should be noted that their elemental compositions are variable and subject to substitution. Relict olivine is heavily fractured, and SEM-EDS analysis indicates that this olivine is Mg-rich, and is confirmed to be forsteritic using XRD. Hydromagnesite and pyroaurite are most abundant in carbonated samples (up to 14 wt. % and 19 wt. % respectively). The relative abundances of (1) the serpentine polymorphs, chrysotile and lizardite (antigorite is rare at Woodsreef; O'Hanley and Offler, 1992), and (2) the spinels, magnetite and chromite,

could not be determined by XRD as a result of their structural and compositional similarity (Turvey et al., 2017). However, we were able to confirm the presence of each of these four phases by textural observations (e.g., chrysotile fibres) and elemental analyses using SEM-EDS. Quantitative mineralogical results are provided in Appendix 2: Table S4.

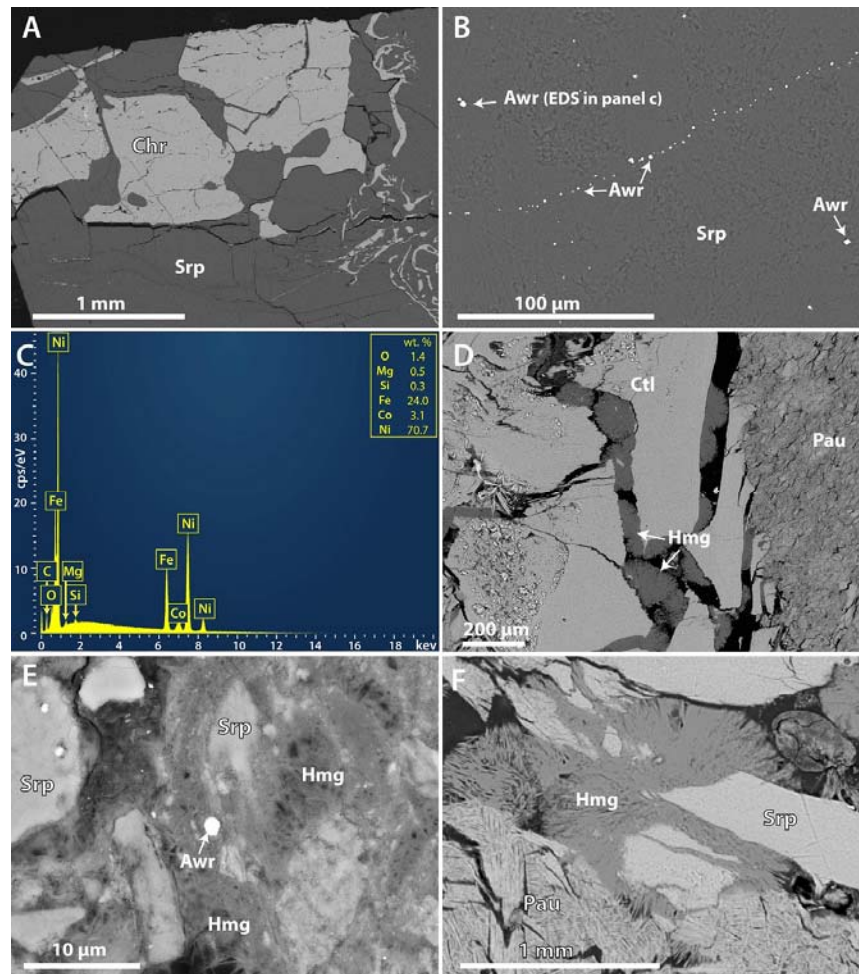


Figure 3.2. BSE-SE micrographs showing: (A) Chromite (Chr) in serpentine (Srp) in sample 13WR5-3. (B) Disseminated awaruite (Awr) in a serpentine groundmass (13WR1-5). (C) EDS analysis of awaruite grain indicated in panel B. (D) Hydromagnesite (Hmg) nucleation on chrysotile (Ctl), with pyroaurite (13WR1-4). (E) Hydromagnesite cementation of serpentine and awaruite grains in carbonated crust sample 13WR2-4. (F) Pyroaurite (Pau) and hydromagnesite carbonate cement between disaggregated serpentine grains (13WR1-4).

SEM-EDS analysis reveals that Cr is present at the greatest concentration in chromite grains, many of which are intergrown with serpentine to resemble a myrmekitic texture (Fig. 3.2A), or are rimmed with overgrowths of magnetite. Magnetite is abundant as dispersed grains and veins within serpentine (Fig. 3.2B). Some grains were found to contain small <5 µm inclusions of Co-Fe and Ni-Fe alloys. Follow up SEM-EDS analysis revealed the presence of the Ni-Fe alloy mineral, awaruite, in partially serpentinised harzburgite. This mineral contains approximately 70 wt. % Ni and 3 wt. % Co, and is commonly disseminated as <5 µm inclusions throughout serpentine in very fine-grained, cross-cutting veins (Fig. 3.2B). The rare Co-Fe alloy is likely wairauite (CoFe), which is found in association with awaruite in serpentinites (Challis and Long, 1964). Hydromagnesite is found extensively in the carbonated tailings and is characterised by a fibrous to platy crystal morphology; it is commonly seen precipitating directly on weathered serpentine grains and in small crevices associated with the disaggregation of grains (Fig. 3.2C–D). It also forms extensive cements that trap and aggregate grains of other minerals, such as serpentine, magnetite and awaruite within carbonated crust samples from the tailings surface (Fig. 3.2C). Pyroaurite is particularly abundant within carbonated chrysotile veins (sample 13WR1-4), where it forms an extensive groundmass (Fig. 3.2C), and is characterised by a layered morphology (Fig. 3.2F), with a yellow-red hue when viewed in plane polarised light. Cr, Mn and Ni are detectable in trace amounts (<1 wt. %) in some serpentine grains by EDS; however, they are not observed in hydromagnesite above the detection limit of this technique. Trace Mn is commonly detected in pyroaurite, whereas trace Co is observed in magnetite and awaruite (~3 wt. %).

3.3.4. Synchrotron XFM Analysis

The two regions selected for detailed synchrotron XFM mapping represent two representative styles of carbonate mineralisation at Woodsreef (1) cementation at grain surfaces within pore spaces in the tailings, and (2) a crust at the surface of the tailings. Figure 3.3A shows an SEM micrograph of a reactive weathering front at the grain boundary between serpentine and hydromagnesite in a carbonated crust sample (13WR2-4). XFM element maps (Fig. 3.3A–F) show the distribution of key metals of interest, and Si within this region. A transect is drawn across this boundary (Fig. 3.3F), and elemental concentrations from the synchrotron XFM data are averaged along the width of the transect (Fig. 3.3G). Most notably, elevated Si concentrations are restricted to the serpentine grain (6.4 wt. % in the serpentine region, as opposed to 0.6 wt. % in the carbonate region; Table 1). It is important to note that the Si peak detected in the X-ray fluorescence spectra could only be partially fitted, and as such, data for this element should only be considered to be semi-quantitative. Stoichiometric serpentine (chrysotile and lizardite) is expected to contain up to 20.3 wt. % Si [in pure $\text{Mg}_3\text{Si}_2\text{O}_5(\text{OH})_4$], indicating that our fit gives an underestimate of Si abundance. Regardless, the relative difference in Si concentrations between serpentine and hydromagnesite is significant because it represents an order of magnitude decrease in Si concentrations across the reaction front.

Table 3.1. Elemental abundances generated in GeoPIXE for regions selected within serpentine and hydromagnesite in Figure 3.3.

<i>Element</i>	Si*	Fe	Mn	Cr	Ni	Co	Cu
<i>Units</i>	<i>wt. %</i>	<i>wt. %</i>	<i>ppm</i>	<i>ppm</i>	<i>ppm</i>	<i>ppm</i>	<i>ppm</i>
Serpentine	6.4	1.6	370	102	917	155	<0.07
Hydromagnesite	0.6	1.3	295	115	889	123	<0.07

*Si peak could only be partially fitted; therefore, these data should be treated as semi-quantitative.

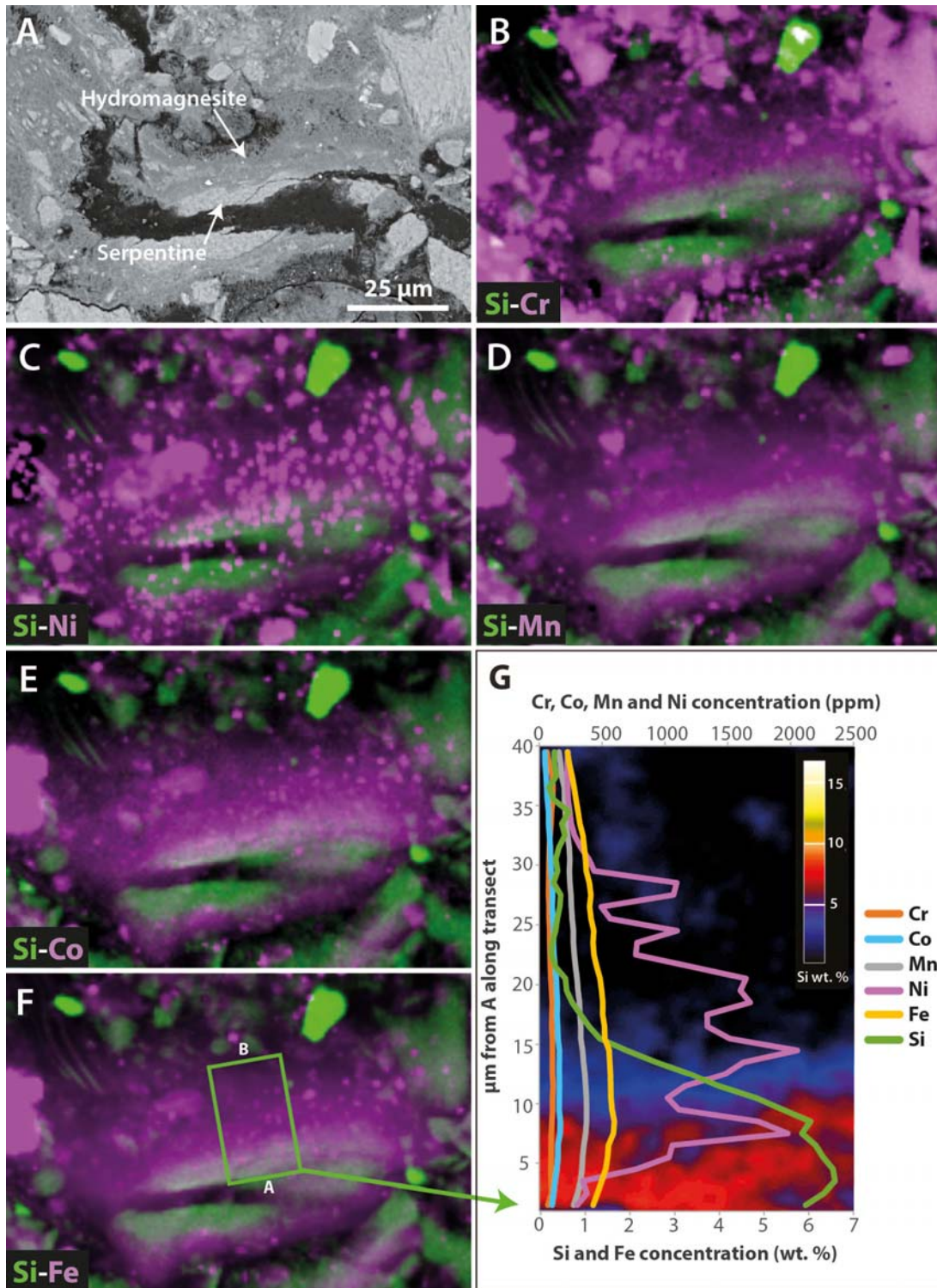


Figure 3.3. (A) BSE-SEM micrograph of weathered serpentine grain and hydromagnesite precipitate, in sample 13WR2-4. (B–F) XFM element concentration maps of a serpentine grain undergoing carbonation to form hydromagnesite. Si is mapped in green, and the distribution of each trace metal of interest, Cr, Ni, Mn, Co and Fe is mapped in purple in B, C, D, E, and F,

respectively. Note the low level diffuse concentrations throughout the carbonated region, and also μm -scale higher concentrations (especially Ni, Co and Fe) representing trapped grains of minerals such as magnetite and awaruite. (G) Plot of elemental abundances, averaged across the width of the transect, from A to B through serpentine into hydromagnesite (as indicated in F).

In comparison to Si, Fe and trace transition metals (Mn, Cr, Ni, Co) are present at comparable abundances in both regions (Table 1, Fig. 3.3). These metals are present within the hydromagnesite that nucleated at the surface of the serpentine grain at average abundances of 1.6 wt. % (Fe), 370 ppm (Mn), 102 ppm (Cr), 917 ppm (Ni), and 155 ppm (Co). The same elements are present at 1.3 wt. % (Fe), 295 ppm (Mn), 115 ppm (Cr), 889 ppm (Ni), and 123 ppm (Co) in the adjacent serpentine grain (Table 1). The high contrast between Si concentrations coincident with less dramatic differences in trace metal concentrations is observed both in Figure 3.3 and in a carbonate cement that spans a gap at the tailings surface (Fig. 3.4; Table 2). In this example, the carbonate cement appears to have precipitated across a space between grains at the surface of the tailings, as opposed to direct precipitation at a serpentine grain boundary. This is consistent with the process of carbonate formation via evaporation and wicking (Wilson et al., 2011), whereby Mg-rich fluids, in which the Mg is sourced from serpentine and brucite dissolution, are drawn to the surface by evaporation-driven capillary rise. Mineral precipitation occurs when Mg and dissolved CO_3^{2-} are sufficiently concentrated via evaporation to induce hydromagnesite saturation (Wilson et al., 2011).

Fe and trace transition metals (Mn, Ni, Cr, Co) appear to exhibit two styles of distribution within the two forms of hydromagnesite mineralisation described above: (1) homogeneously dispersed within both serpentine and carbonate phases at concentrations of 100s to 1000s of ppm, and (2) concentrated in discrete, μm -scale regions. The highest concentrations of Ni (3.4 wt.%) and Co (1.8 wt.%) occur in discrete regions less than 5 μm in size, and coincide with elevated concentrations of Fe (reported at up to 68.5 wt. %

for regions containing the largest, 10–20- μm sized, grains of magnetite). Because XFM is a transmission technique that samples the entire volume of a specimen, concentrations of these discrete μm -scale points are averaged over the 30- μm deep thin section, thus actual concentrations of Ni, Co and Fe within those small grains are likely higher. Our SEM-EDS results, which are more appropriate for sampling surface features, confirm that three μm -scale grains exposed at the surface of the sample are high in Fe, or both Fe and Ni, indicating the presence of magnetite and awaruite. As such, the <5 μm -scale grains visible within the whole sample depth in XFM are also interpreted to be trapped magnetite and awaruite grains (Fig. 3.3C,E,F). Fe concentrations within the serpentine grain shown in Figure 3.3 (1.6 wt. % Fe, in Table 1), and the silicate mineral region highlighted in Figure 3.4 (1.0 wt.% Fe, in Table 2), are slightly lower although not dissimilar to measurements of Fe abundance in lizardite [1.6 – 2.3 wt. % Fe; using electron microprobe, O'Hanley and Dyar (1993)] and chrysotile [1.9 – 2.3 wt. % Fe^{2+} and 1.1 – 1.4 wt. % Fe^{3+} ; using atomic absorption spectroscopy, Glen and Butt (1981)] in samples from Woodsreef.

Table 3.2. Elemental abundances generated in GeoPIXE for regions highlighted in green in Figure 3.4E–F.

<i>Element</i>	Si*	Fe	Mn	Cr	Ni	Co	Cu
<i>Units</i>	<i>wt. %</i>	<i>wt. %</i>	<i>ppm</i>	<i>ppm</i>	<i>ppm</i>	<i>ppm</i>	<i>ppm</i>
Serpentine	3.1	1.0	329	281	510	74	<0.07
Hydromagnesite	<0.013	0.5	114	76	294	11	<0.07

*Si peak could only be partially fitted; therefore, these data should be treated as semi-quantitative.

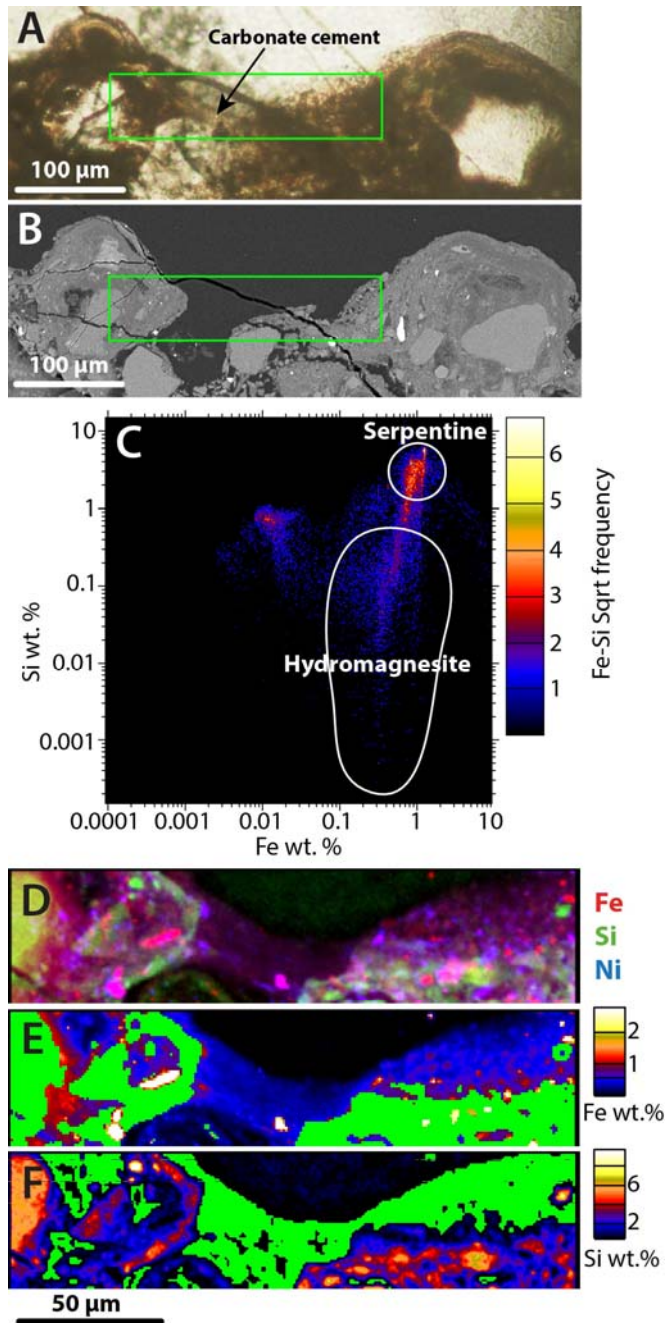


Figure 3.4. Carbonate surface cement in sample 13WR2-4. (A) Photomicrograph of carbonate cement spanning space between grains at the tailings surface. (B) BSE-SEM micrograph of this area does not show cemented region of interest as it is below the surface of the thin section. (C) Association between Si and Fe from XFM data. The region representing serpentine is highlighted in the top ellipse, and the region representing hydromagnesite is highlighted in the ellipse below. (D) XFM image showing the distribution of Fe in red, Si in green and Ni in blue. (E) Region selected in C (serpentine) is highlighted in green on Fe XFM map. (F) Region selected in C

(hydromagnesite) is highlighted in green on Si XFM map. Si concentrations should be treated as semi-quantitative.

The presence of Cr within hydromagnesite cements, at evenly distributed low-level concentrations, and in discrete μm -scale concentrations, indicates that mobilisation of Cr into solution and liberation of small chromite particles is occurring within the weathered tailings. Cr K-edge XANES analysis reveals Cr is present as Cr^{3+} in chromite, serpentine, and pyroaurite, whereas Cr^{6+} is not detected in the scanned area (Appendix 2: Fig. S2).

Pyroaurite also contains trace metals at 100s to 1000s ppm level concentrations (107 ppm Cr, 440 ppm Ni, 784 ppm Co, 0.3 wt. % Mn and 8.2 wt. % Fe). However, uncertainty exists about the formation mechanism of pyroaurite at Woodsreef as it can form via reaction of brucite with atmospheric CO_2 , but it was also detected in fresh tailings at Woodsreef (Slansky, 1983), suggesting it could be a hydrothermal alteration product. Pyroaurite is prone to the exchange of interlayer anions, such as CO_3^{2-} , (Bish, 1980; Miyata, 1983), and stable carbon and oxygen isotopic data for pyroaurite-rich samples reported by Oskierski et al. (2013) give an ambiguous signature that could result from (1) mixing of an atmospheric source of carbon with a metamorphic source of carbon, (2) formation of pyroaurite from a modern organic carbon source (although no such source is present in the tailings at Woodsreef), or (3) kinetic depletion of ^{13}C during either exchange of atmospheric CO_2 for metamorphic CO_2 in pyroaurite or formation of sedimentary pyroaurite from atmospheric CO_2 . As such, although pyroaurite is identified as a host for trace metals in the Woodsreef tailings, it is unclear whether these trace metals were inherited in pyroaurite that was originally found in the ore or were sequestered during carbonation in the tailings post-mining. Therefore, this study focuses on hydromagnesite as a model phase for examining trace metal uptake in the products of passive mineral carbonation by air capture.

3.4. Discussion

3.4.1. Mineralogical hosts of trace metals

Weathering has formed a Mg-carbonate-rich crust at the surface of the tailings, but the bulk of the tailings at depth appears less altered, thus the tailings are considered an attractive target material for promoting mineral carbonation reactions (McCutcheon et al., 2015, 2016, 2017; Oskiersky et al., 2013; Turvey et al., 2017). We find that the bulk of trace metals within the tailings remain within the original mineral assemblage, of silicates, oxides and alloys, with some being sequestered within alteration minerals (hydromagnesite and possibly pyroaurite) in surface crusts, and none detected in mine pit waters. XRF analyses of bulk samples show that Cr_2O_3 and NiO are both present at concentrations of ~ 0.3 wt. % in the Woodsreef Mine tailings (Appendix 2: Table S3). Amongst the metals investigated, Cr is of particular environmental concern because it can form the toxic carcinogen Cr^{6+} in its most oxidised state (Kotaś and Stasicka, 2000). Our SEM-EDS analyses show that Cr is predominantly hosted in chromite, whereas synchrotron XFM mapping reveals that Cr is also distributed homogeneously at low concentrations (approximately 100 ppm) within grains of serpentine, possibly by substitution for Mg within the crystal structures of lizardite and chrysotile. This is unsurprising given that a variety of divalent and trivalent cations, including Fe^{2+} , Fe^{3+} , Cr^{2+} , Cr^{3+} , Ni^{2+} , Mn^{2+} , and Co^{2+} , can readily substitute for structural Mg^{2+} in serpentine minerals (Anbalagan et al., 2008; Anbalagan et al., 2010; Cralley et al., 1968; Morgan et al., 1973; O'Hanley and Dyar, 1993, 1998; Ristić et al., 2011; Schreier, 1987).

Our XFM results confirm that Ni is also distributed throughout serpentine minerals at low levels; however, we also commonly observe μm -scale inclusions of the Ni-Fe alloy mineral, awaruite, within partially serpentinised harzburgite, consistent with observations

made by O'Hanley and Dyar (1993). Awaruite forms from Ni mobilised by serpentinisation of olivine at low temperature and low water-to-rock ratios (Sciortino et al., 2015).

3.4.2. Trace metal mobility during passive mineral carbonation

Hydromagnesite and other hydrated Mg-carbonate minerals are common weathering products of serpentine minerals, forsterite and brucite (Harrison et al., 2015; Wilson et al., 2011; Wilson et al., 2009a), all of which are present within the Woodsreef tailings (Oskierski et al., 2013; Slansky, 1983; Turvey et al., 2017). An early investigation of tailings mineralogy did not detect hydromagnesite in the tailings at Woodsreef (Slansky, 1983). Today, evidence of serpentinite weathering to produce carbonate crusts is observed at a large scale in the field, as rocks and boulders disintegrate due to the expansive forces of carbonate mineral formation, and in textural observations and mineral associations viewed in thin sections (Fig. 3.2). Small grains of minor oxide minerals such as magnetite and chromite, and alloy minerals such as awaruite (Fig. 3.2E in contrast, do not appear to be significantly altered, but they are liberated by weathering of serpentine and incorporated as inclusions in the extensive hydromagnesite cements that have developed within the surficial tailings material. These hydromagnesite cements formed recently (since 1983) once tailings were deposited in the storage facility and they are known to have been produced from a modern atmospheric CO₂ source (Oskierski et al., 2013; Turvey et al., 2017). Serpentine minerals, forsterite and brucite are still present in the tailings; therefore, it is likely that weathering reactions will continue to sequester atmospheric CO₂ within hydromagnesite into the future. However, Wilson et al. (2014) found that the nucleation of hydromagnesite on the surfaces of mineral grains, and

formation of thick (mm-scale) efflorescent cements at tailings surfaces slows carbonation reactions by passivating reactive surfaces and limiting CO₂ ingress into deeper tailings.

The most likely source of the Mg in hydromagnesite forming in the Woodsreef tailings is from the dissolution of serpentine minerals, brucite and trace amounts of forsterite (Oskierski et al., 2013). Brucite is the most soluble of these phases under acidic to neutral conditions (i.e., rainwater; Palandri and Kharaka, 2004); thus, it is likely that mineral carbonation at the site is attributable to carbonation of this minor phase as has been observed previously at the Mount Keith nickel mine (Wilson et al., 2014). As such, brucite dissolution could be a significant source of mobilised trace metals, given it forms a solid solution with a wide range of divalent metal cations, including Fe, Ca, Ni, Co, Mn, Zn, Cd (Brindley and Kao, 1984). Serpentinite hosted brucite commonly contains high concentrations of substituted Fe (Mumpton, 1966) and Ni (Grguric, 2003); with the distribution coefficient for Ni partitioning between brucite and serpentine being reported as 63 to 1 under conditions typical of serpentinisation (Perruchot, 1973).

However, lizardite and chrysotile typically have a much higher surface area (Bea et al., 2012) and are the most abundant phases (>67 wt. %) at Woodsreef; therefore, they are also likely to contribute cations for mineral carbonation. The transition metals of interest in this study (Fe, Cr, Ni, Mn, Co) substitute for Mg²⁺ in the more reactive ‘brucite layer’ within the structures of serpentine minerals (Anbalagan et al., 2008; Anbalagan et al., 2010; Ristić et al., 2011) meaning they are likely to be leached along with Mg during weathering or accelerated leaching of tailings. Si forms strong bonds with oxygen within the serpentine structure, and is expected to be relatively immobile under the circumneutral conditions that occur during weathering of serpentinite (McCutcheon et al., 2015, 2017). Our XFM data indicate that Si is restricted to serpentine grains whereas Fe

and trace metals (Cr, Ni, Mn, Co) are incorporated into hydromagnesite cements at comparable concentrations, although slightly lower than those found in unweathered serpentine (Table 3.1, 3.2; Fig. 3.3, 3.4). The Fe and trace metals released via dissolution of brucite or serpentine are unlikely to remain soluble under the circumneutral to alkaline conditions expected in mine waters (Stumm and Morgan, 1996). As such, they likely have not travelled far from the source. This may explain why trace metal concentrations are generally higher in both the pyroaurite (which likely formed via carbonation of brucite, although this is not certain), and the hydromagnesite cement precipitated at a serpentine grain boundary (Fig. 3.3, Table 3.1), compared to the lower metal concentrations found in hydromagnesite surface cements, which we suggest formed via evapoconcentration and wicking of Mg-rich pore fluids. A small amount of trace metals may also be lost in runoff waters, although we do not observe detectable concentrations within the mine pit lakes (Appendix 2: Table S2).

Weathering of other minor phases such as forsterite, enstatite, magnetite and chromite likely occurs much more slowly given their slower reaction rates and lower abundances (Palandri and Kharaka, 2004). For this reason, these gangue phases probably do not contribute appreciable Mg and transition metal cations to alteration phases compared to brucite and serpentine. Although dissolution rate constants are not known for awaruite and wairauite, kinetic tests conducted by Kandji et al. (2017) show that awaruite is stable in weathering cells for 6 months and does not release Ni under the tested conditions. It is therefore unlikely that Ni is being appreciably mobilised from awaruite at Woodsreef during passive weathering.

Trace metal concentrations may be particularly elevated in surface and ground waters around ultramafic environments and chrysotile deposits, and in some cases concentrations

exceed local water quality thresholds (Fantoni et al., 2002; Margiotta et al., 2012; McClain and Maher, 2016; Natali et al., 2013; Schreier, 1987). For instance, up to 73 $\mu\text{g/L Cr}^{6+}$ has been reported in ground water associated with an ophiolite in Italy, where the local permissible value is 5 $\mu\text{g/L Cr}^{6+}$ (Fantoni et al., 2002). The trace metals of interest in this study are not detected in the pit lakes at Woodsreef (Appendix 2: Table S2), indicating that either trace metals are not being mobilised from the surrounding waste rock storage piles, or they do not remain dissolved for long enough or at sufficient concentration to be detectable in nearby water bodies. The general lack of trace metals in the pit lakes suggests that sequestration by secondary mineral precipitates, such as hydromagnesite and possibly pyroaurite, plays an important role in limiting trace metal mobility in runoff waters at Woodsreef.

3.4.3. Mg-carbonate minerals sequester trace metals in ultramafic mine tailings

Iron and trace metals (Cr, Ni, Mn, Co) are sequestered within the coatings of hydromagnesite that form within pore spaces at the surfaces of serpentine grains (Fig. 3.3) and as evaporative crusts at the surface of the tailings storage facility (Fig. 3.4). The distribution of Fe within hydromagnesite-rich cements appears to be a useful indicator of the extent of trace metal mobilisation during weathering and carbonation reactions, as Fe and trace metals are spatially associated, with different concentrations corresponding to mineralogy (Fig. 3.3, 3.4). Elevated concentrations (up to wt.% level) of Cr, Ni and Co are measured at distinct, $<5 \mu\text{m}$ -scale regions that are also associated with higher Fe concentrations, most likely representing the incorporation of oxide and alloy mineral grains, such as chromite, magnetite, awaruite or wairauite, as inclusions within carbonate cements. This could also represent precipitation of secondary Fe-hydroxide or oxide minerals which are widespread in the environment and are also common products of

mineral carbonation and weathering reactions (Hamilton et al., 2016; Mumpton and Thompson, 1966; Park and Fan, 2004; Schwertmann and Taylor, 1989). Fe-hydroxide and oxide phases can incorporate trace metals (Cr, Ni, Mn, Co, Cu) by substitution, surface sorption, co-precipitation, or recrystallisation (Manceau et al., 2000; Schwertmann and Taylor, 1989; Trolard et al., 1995). These phases are known to play a role in sequestering trace transition metals from solution during simulated mineral carbonation experiments (Hamilton et al., 2016), therefore is it possible that this also occurs naturally in the Woodsreef tailings.

In addition, trace metals appear to be distributed at low concentrations (10s to 100s of ppm) within hydromagnesite (and pyroaurite), suggesting they have been incorporated into the crystal structure of the mineral, most likely via substitution for Mg (or Mg and Fe in the case of pyroaurite). Common carbonate minerals such as calcite, dolomite and magnesite are known to incorporate a variety of trace metals by substitution for Ca or Mg, or any of the incorporation mechanisms described above (Calugaru et al., 2016; Wunsch et al., 2013; Zachara et al., 1991). Trace metal concentrations within carbonate cements are comparable with those detected in silicate grains, which are considered, along with brucite, to be the dominant sources of mobilised trace metals. This indicates that (1) sequestration of metals occurs effectively over a spatial scale of $\sim 10 \mu\text{m}$ and (2) any loss of transition metals to runoff water is likely to be small under the environmental conditions observed at Woodsreef.

Despite these samples having been collected from a surficial environment in contact with the atmosphere, the oxidised Cr^{6+} species was not detected by Cr K-edge XANES analysis. This is an important finding, since elevated levels of highly toxic, carcinogenic, and mobile Cr^{6+} are often reported in serpentinite-dominated environments (McClain and

Maier, 2016; Morrison et al., 2015; Oze et al., 2007). The crushed Woodsreef tailings have a highly reactive surface area and are exposed to oxic conditions, providing an ideal environment to promote weathering reactions. Here, it is likely that any Cr released by the weathering of brucite, serpentine, and possibly chromite has been and continues to be immobilised by incorporation into hydromagnesite cements (e.g., Table 1, 2; Fig. 3.3B). Extended X-ray absorption fine structure (EXAFS) analysis could possibly be used to shed light on the relative importance of specific mechanisms of trace metal uptake in these samples, such as adsorption or co-precipitation. Nonetheless, our observations demonstrate that hydromagnesite cements forming at the Woodsreef Mine trap trace metals, limiting their mobilisation into the surrounding environment.

These findings are consistent with those of Hamilton et al. (2016), who demonstrated that transition metals (up to 100 mg/L of aqueous Cr, Ni, Mn, Co or Cu) are immobilised during the precipitation of nesquehonite in simulated mineral carbonation experiments. Under alkaline conditions, Mg-carbonate minerals should remain stable hosts for these trace metals, as they are known to persist at Earth's surface conditions for thousands of years (Grant et al., 1987, in Power et al., 2009). Retention of trace metals within nesquehonite has been demonstrated after recrystallisation of nesquehonite from colloidal particles to mm-scale crystals (Hamilton et al., 2016), although further work should investigate metal retention on longer time scales and during decomposition of Mg-carbonate minerals to less hydrated, more stable phases.

3.4.4. Outlook for metal mobility during passive and artificially accelerated carbon mineralisation

The capacity for Mg-carbonate minerals to sequester trace metals is particularly relevant to accelerated mineral carbonation projects, where metal leaching is expected to be

enhanced by acid treatments or reaction with low pH CO₂ streams (Marcon and Kaszuba, 2013; Oelkers et al., 2008; Olsson et al., 2014a; Olsson et al., 2014b). Field and pilot scale accelerated mineral carbonation projects are beginning trials worldwide. For example, *ex situ* mineral carbonation reactors include the pilot scale Mineral Carbonation International project, which uses serpentine from the Great Serpentine Belt (where Woodsreef is located) as feedstock material (Brent et al., 2015), and a project based at an undisclosed cement plant in Québec, Canada, which also uses serpentine-based tailings material (Kemache et al., 2017). In Iceland, *in situ* CO₂ injection has been trialled in mafic to ultramafic formations (Matter et al., 2011; Matter et al., 2016; Okamoto et al., 2006). Proposed *in situ* treatments include sulfuric acid leaching of mine tailings to induce mineral carbonation (McCutcheon et al., 2015, 2016, 2017), or geoengineering scenarios including the application of ultramafic minerals in major river catchments and along coastlines (Hartmann et al., 2013; Schuiling and de Boer, 2013). Here, we find that Mg-carbonate minerals (hydromagnesite and possibly pyroaurite) are likely to be effective sinks for potentially toxic trace metals released by accelerated mineral carbonation in these scenarios.

Romão et al., (2013) propose that trace metal recovery could be incorporated into mineral carbonation technologies, serving a dual purpose of adding value to the mineral carbonation process, and making low grade and otherwise unfeasible ores potentially economic. The Woodsreef Mine tailings have been considered in the past as a potential Ni and Cr resource, and while chromite recovery was considered feasible, no high-grade Ni minerals were identified, thus the processing of serpentine to extract Ni was considered unfeasible by (Kmetoni, 1984). Here, we find that Ni is most concentrated in inclusions of awaruite and Cr is most concentrated within chromite. Only low (100s ppm) concentrations of Ni and Cr are diffusely distributed by substitution for Mg within

serpentine. Given that much of the Ni at Woodsreef appears to be hosted in alloy minerals (56–83 % of estimated total Ni), despite the high abundance of serpentine, the potential for Ni recovery may be more optimistic than previously assumed.

The 24.2 million tonnes of tailings at Woodsreef have a bulk Ni content of 0.2 wt. %, yielding an estimated 48,400 t of contained Ni metal. Mineralogical analyses conducted in this study indicate that these tailings contain 67–97 wt. % serpentine. In addition, the Ni content of serpentine grains in tailings analysed by XFM range between 510–917 ppm Ni. From these ranges of mineral abundance and Ni content, we can estimate that serpentine accounts for 8,300–21,500 t of Ni. Comparing this to our estimate of total Ni in the tailings, 26,900–40,100 t of Ni remains unaccounted for by substitution into serpentine alone, and is therefore likely hosted in awaruite and as trace components in other minor phases such as brucite, pyroaurite and magnetite. If we assume that all of this Ni is present in awaruite (which stoichiometrically contains 58–87 wt. % Ni), we would expect this mineral phase to be present at an abundance of 0.1–0.3 wt. % in the tailings. As such, it is not a surprise that awaruite is not detected in XRD patterns, where detection limits are on the order of 0.5 to 1 wt. % for most mineral phases under the conditions of data collection used in this study.

Processing of Woodsreef tailings or other ultramafic material for mineral carbonation could release Ni by acid leaching serpentine and liberating alloy minerals and spinels. Trace metals leached by the dissolution of serpentine and brucite could potentially be recovered using a step-wise pH swing method (Azdarpour et al., 2015; Park and Fan, 2004; Teir et al., 2007a), whereby trace metals are initially precipitated with Fe-oxides at circumneutral pH before the pH is raised to induce Mg-carbonate mineral precipitation. In addition, crushing, or mechanical activation, is often used to increase reactive surface

area to accelerate mineral carbonation reactions (Li and Hitch, 2016; Park and Fan, 2004). This pre-treatment would likely assist in liberating inclusions of oxides such as magnetite and chromite, and possibly alloys of Ni and Co, although the small size and disseminated distribution of these alloys would likely limit their liberation by mechanical pre-treatment. Magnetic separation has also been recommended as a pre-treatment to enhance the effectiveness of serpentine carbonation because removal of magnetite mitigates the passivating effect of Fe-oxide precipitation on grain surfaces (Huijgen and Comans, 2003; Veetil et al., 2015). Awaruite is a Ni resource of growing interest to the minerals industry (Britten, 2017; Mudd and Jowitt, 2014; Sciortino et al., 2015), and lends itself to gravimetric and/or magnetic separation (Britten, 2017). Thus, if the Woodsreef mine tailings were used as a feedstock in a mineral carbonation reactor, acid leaching of serpentine could be coupled with the above-mentioned separation methods to recover metals of economic value from the Ni-, Cr-, and Co-rich accessory minerals, magnetite, chromite, awaruite, and wairauite, which are more resistant to acid leaching than silicate minerals and brucite. Therefore, extraction of metal resources that are otherwise not economically viable could provide an additional incentive to implement CO₂ sequestration using serpentine-rich materials (Park and Fan, 2004; Romão et al., 2013).

3.5. Conclusions

Naturally forming Mg-carbonate cements are an important and effective sink for trace transition metals mobilised during weathering of ultramafic mine tailings. Trace metals are immobilised within these cements both by incorporation into the Mg-carbonate mineral, hydromagnesite, likely by substitution for Mg, and by physical trapping of metal-rich grains that are liberated during mineral processing and weathering. This indicates that if mineral carbonation of ultramafic materials were to be accelerated,

metalliferous drainage is unlikely to pose an environmental risk. Furthermore, *ex situ* mineral carbonation processes could be optimised for trace metal recovery, which may provide additional value to future reactor projects.

3.6. Chapter 3 references

- Anbalagan G., Sakthi Murugesan K., Balakrishnan M. and Gunasekaran S. (2008) Structural analysis, optical absorption and EPR spectroscopic studies on chrysotile. *Applied Clay Science* 42, 175-179.
- Anbalagan G., Sivakumar G., Prabakaran A.R. and Gunasekaran S. (2010) Spectroscopic characterization of natural chrysotile. *Vibrational Spectroscopy*. 52, 122-127.
- Assargiotis A. (2013) Woodsreef Mine major rehabilitation project—review of environmental factors. Environmental Planning and Assessment, NSW Public Works, Department of Finance and Services. DC11100, 1-131.
- Azdarpour A., Asadullah M., Mohammadian E., Hamidi H., Junin R. and Karaei M.A. (2015) A review on carbon dioxide mineral carbonation through pH-swing process. *Chemical Engineering Journal* 279, 615-630.
- Ballirano P., De Vito C., Mignardi S. and Ferrini V. (2013) Phase transitions in the Mg-CO₂-H₂O system and the thermal decomposition of dypingite, Mg₅(CO₃)₄(OH)₂·5H₂O: Implications for geosequestration of carbon dioxide. *Chemical Geology* 340, 59-67.
- Bea S.A., Wilson S.A., Mayer K.U., Dipple G.M., Power I.M. and Gamazo P. (2012) Reactive Transport Modeling of Natural carbon sequestration in ultramafic mine tailings. *Vadose Zone Journal* 11, 1-17.
- Beinlich A. and Austrheim H. (2012) In situ sequestration of atmospheric CO₂ at low temperature and surface cracking of serpentized peridotite in mine shafts. *Chemical Geology*. 332, 32-44.
- Berry A.J. and O'Neill H.S.C. (2004) A XANES determination of the oxidation state of chromium in silicate glasses. *American Mineralogist* 89, 790-798.

- Bish D.L. (1980) Anion-exchange in takovite: applications to other hydrotalcite minerals. *Bulletin Mineralogie*, 103, 170-175.
- Bish D.L. and Howard S.A. (1988) Quantitative phase analysis using the Rietveld method. *Journal of Applied Crystallography* 21, 86-91.
- Brent G.F., Rayson M.S., Kennedy E.M., Stockenhuber M., Collins W.J., Prigge J.D., Hynes R.G., Molloy T.S., Zulfiqar H., Farhang F., Oliver T.O., Hamblin Wang S. and Dawe M. (2015) Mineral carbonation of serpentinite: From the laboratory to pilot scale - The MCi project, 5th International Conference on Accelerated Carbonation for Environmental and Material Engineering 2015, pp. 394-403.
- Brindley G.W. and Kao C.-C. (1984) Structural and IR relations among brucite-like divalent metal hydroxides. *Physics and Chemistry of Minerals* 10, 187-191.
- Britten R. (2017) Regional metallogeny and genesis of a new deposit type—disseminated awaruite (Ni₃Fe) mineralization hosted in the Cache Creek Terrane. *Economic Geology* 112, 517-550.
- Bruker AXS (2004) Topas V. 3.0: General profile and structure analysis software for powder diffraction data. Bruker AXS, Germany.
- Calugaru I.L., Neculita C.M., Genty T., Bussi re B. and Potvin R. (2016) Performance of thermally activated dolomite for the treatment of Ni and Zn in contaminated neutral drainage. *Journal of Hazardous Materials* 310, 48-55.
- Challis G.A. and Long J.V.P. (1964) Wairauite - a new cobalt-iron mineral. *Mineralogical Magazine* 33, 942-948.
- Cralley L.J., Keenan R.G., Kupel R.E., Kinser R.E. and Lynch J.R. (1968) Characterization and solubility of metals associated with asbestos fibers. *American Industrial Hygiene Association Journal* 29, 569-573.
- Davies P.J. and Bubela B. (1973) The transformation of nesquehonite into hydromagnesite. *Chemical Geology* 12, 289-300.
- Fantoni D., Brozzo G., Canepa M., Cipolli F., Marini L., Ottonello G. and Zuccolini M. (2002) Natural hexavalent chromium in groundwaters interacting with ophiolitic rocks. *Environmental Geology* 42, 871-882.

- Glen R.A. and Butt B.C. (1981) Chrysotile asbestos at Woodsreef, New South Wales. *Economic Geology* 76, 1153-1169.
- Goff F. and Lackner K.S. (1998) Carbon dioxide sequestering using ultramafic rocks. *Environmental Geoscience* 5, 89-102.
- Grant B. (1987) Magnesite, brucite and hydromagnesite occurrences in British Columbia. Open File Report of the British Columbia Geological Survey Branch No 1987-13.
- Gras A., Beaudoin, G., Molson, J., Plante, B., Bussière, B., Lemieux, J.M. and Dupont, P.P. (2017) Isotopic evidence of passive mineral carbonation in mine wastes from the Dumont Nickel Project (Abitibi, Quebec). *International Journal of Greenhouse Gas Control* 60, 10-23.
- Grguric B.A. (2003) Minerals of the MKD5 nickel deposit, Mount Keith, Western Australia. *Australian Journal of Mineralogy* 9, 55-71.
- Hallett J. (2002) Climate change 2001: The scientific basis. Edited by J. T. Houghton, Y. Ding, D. J. Griggs, N. Noguer, P. J. van der Linden, D. Xiaosu, K. Maskell and C. A. Johnson. Contribution of Working Group I to the Third Assessment Report of the Intergovernmental Panel on Climate Change, Cambridge University Press, Cambridge. 2001. 881 pp. ISBN 0521 01495 6. *Quarterly Journal of the Royal Meteorological Society*. 128, 1038-1039.
- Hamilton J.L. (2013). Trace metal mobility during mineral carbonation (honours thesis). Monash University, Clayton, Victoria, Australia.
- Hamilton J.L., Wilson S.A., Morgan B., Turvey C.C., Paterson D.J., MacRae C., McCutcheon J. and Southam G. (2016) Nesquehonite sequesters transition metals and CO₂ during accelerated carbon mineralisation. *International Journal of Greenhouse Gas Control* 55, 73-81.
- Hänchen M., Prigiobbe V., Baciocchi R. and Mazzotti M. (2008) Precipitation in the Mg-carbonate system—effects of temperature and CO₂ pressure. *Chemical Engineering Science* 63, 1012-1028.
- Harrison A.L., Dipple G.M., Power I.M. and Mayer K.U. (2015) Influence of surface passivation and water content on mineral reactions in unsaturated porous media:

- Implications for brucite carbonation and CO₂ sequestration. *Geochimica et Cosmochimica Acta* 148, 477-495.
- Harrison, A.L., Power, I.M. and Dipple, G.M., (2012). Accelerated carbonation of brucite in mine tailings for carbon sequestration. *Environmental Science and Technology* 47, 126-134.
- Hartmann J., West A.J., Renforth P., Köhler P., De La Rocha C.L., Wolf-Gladrow D.A., Dürr H.H. and Scheffran J. (2013) Enhanced chemical weathering as a geoengineering strategy to reduce atmospheric carbon dioxide, supply nutrients, and mitigate ocean acidification. *Reviews of Geophysics* 51, 113-149.
- Hill R. and Howard C. (1987) Quantitative phase analysis from neutron powder diffraction data using the Rietveld method. *Journal of Applied Crystallography* 20, 467-474.
- Huijgen W.J.J. and Comans R.N.J. (2003) Carbon dioxide sequestration by mineral carbonation. Literature Review. Energy research Centre of the Netherlands ECN.
- IPCC (2005) IPCC Carbon dioxide capture and storage. In: Metz B., Davidson O., de Coninck H.C., Loos M., Meyer L.A. (Eds.), IPCC Special Report. Prepared by Working Group III of the Intergovernmental Panel on Climate Change, Cambridge University Press, Cambridge and New York.
- IPCC (2013) IPCC Climate Change 2013: The Physical Science Basis. Contribution of Working Group 1 to the Fifth Assessment Report of the Intergovernmental Panel on Climate Change. Stocker T.F., Qin D., Plattner G.-K., Allen S.K, Boschung J., Naules A., Xia Y., Bex V., Midgley P.M (eds) Cambridge University Press, Cambridge, United Kingdom and New York, USA.
- Kandji E.H.B., Plante B., Bussière B., Beaudoin G. and Dupont P.-P. (2017) Kinetic testing to evaluate the mineral carbonation and metal leaching potential of ultramafic tailings: case study of the Dumont Nickel Project, Amos, Québec. *Applied Geochemistry* 84, 262-267.
- Kemache N., Pasquier L.-C., Cecchi E., Mouedhen I., Blais J.-F. and Mercier G. (2017) Aqueous mineral carbonation for CO₂ sequestration: From laboratory to pilot scale. *Fuel Processing Technology* 166, 209-216.

- Kirsch K., Navarre-Sitchler A.K., Wunsch A. and McCray J.E. (2014) Metal release from sandstones under experimentally and numerically simulated CO₂ leakage conditions. *Environmental Science & Technology* 48, 1436-1442.
- Kmetoni J. (1984) Woodsreef mill tailings—investigation of potential for further utilization as a mineral resource (stage 1—mineralogical composition). Department of Mineral Resources, New South Wales Geological Survey Report GS1984/474.
- Kotaś J. and Stasicka Z. (2000) Chromium occurrence in the environment and methods of its speciation. *Environmental Pollution* 107, 263-283.
- Lackner K.S. (2003) A guide to CO₂ sequestration. *Science* 300, 1677-1678.
- Lackner K.S., Wendt C.H., Butt D.P., Joyce E.L.J. and Sharp D.H. (1995) Carbon dioxide disposal in carbonate minerals. *Energy* 20, 1153-1170.
- Laughton C.A. and Green N. (2002) The Woodsreef magnesium project—an example of sustainable mineral waste processing from mined ore and its utilisation to produce refined metal products. Green Processing 2002, Cairns, Queensland, Australian Institute of Mining and Metallurgy.
- Lechat K., Lemieux J.-M., Molson J., Beaudoin G. and Hébert R. (2016) Field evidence of CO₂ sequestration by mineral carbonation in ultramafic milling wastes, Thetford Mines, Canada. *International Journal of Greenhouse Gas Control* 47, 110-121.
- Levitan, D.M., Hammarstrom, J.M., Gunter, M.E., Seal, R.R., Chou, I.M. and Piatak, N.M., (2009) Mineralogy of mine waste at the Vermont asbestos group mine, Belvidere Mountain, Vermont. *American Mineralogist* 94, 1063-1066.
- Li J. and Hitch M. (2016) Mechanical activation of ultramafic mine waste rock in dry condition for enhanced mineral carbonation. *Minerals Engineering* 95, 1-4.
- Low F., Kimpton J., Wilson S.A. and Zhang L. (2015) Chromium reaction mechanisms for speciation using synchrotron in-situ high-temperature X-ray diffraction. *Environmental Science & Technology* 49, 8246-8253.

- Ludwig, W., Amiotte-Suchet, P., Munhoven, G. and Probst, J.L., (1998) Atmospheric CO₂ consumption by continental erosion: present-day controls and implications for the last glacial maximum. *Global and Planetary Change* 16, 107-120.
- Manceau A., Schlegel M.L., Musso M., Sole V.A., Gauthier C., Petit P.E. and Trolard F. (2000) Crystal chemistry of trace elements in natural and synthetic goethite. *Geochimica et Cosmochimica Acta* 64, 3643-3661.
- Marcon V. and Kaszuba J. (2013) Trace metal mobilization in an experimental carbon sequestration scenario. *Procedia Earth and Planetary Science* 7, 554-557.
- Marcon V. and Kaszuba J.P. (2015) Carbon dioxide–brine–rock interactions in a carbonate reservoir capped by shale: Experimental insights regarding the evolution of trace metals. *Geochimica et Cosmochimica Acta* 168, 22-42.
- Margiotta S., Mongelli G., Summa V., Paternoster M. and Fiore S. (2012) Trace element distribution and Cr(VI) speciation in Ca-HCO₃ and Mg-HCO₃ spring waters from the northern sector of the Pollino massif, southern Italy. *Journal of Geochemical Exploration* 115, 1-12.
- Maroto-Valer M.M., Fauth D.J., Kuchta M.E., Zhang Y. and Andrésen J.M. (2005) Activation of magnesium rich minerals as carbonation feedstock materials for CO₂ sequestration. *Fuel Processing Technology* 86, 1627-1645.
- Matter J.M., Broecker W.S., Gislason S.R., Gunnlaugsson E., Oelkers E.H., Stute M., Sigurdardóttir, H., Stefansson, A., Alfreðsson, H.A., Aradóttir, E.S., Axelsson, G., Sigfússon B. and Wolff-Boenisch D. (2011) The CarbFix Pilot Project—storing carbon dioxide in basalt. *Energy Procedia* 4, 5579-5585.
- Matter J.M., Stute M., Snæbjörnsdóttir S.Ó., Oelkers E.H., Gislason S.R., Aradóttir E.S., Sigfússon, B., Gunnarsson, I., Sigurdardóttir, H., Gunnlaugsson, E., Axelsson, G., Alfreðsson H.A., Wolff-Boenisch D., Mesfin K., Taya D.F.d.l.R., Hall J., Dideriksen K. and Broecker W.S. (2016) Rapid carbon mineralization for permanent disposal of anthropogenic carbon dioxide emissions. *Science* 352, 1312-1314.
- McClain C.N. and Maher K. (2016) Chromium fluxes and speciation in ultramafic catchments and global rivers. *Chemical Geology* 426, 135-157.

- McCutcheon J., Turvey C.C., Wilson S.A., Hamilton J.L. and Southam G. (2017) Microbial mineral carbonation of asbestos mine tailings: Potential applications to carbon storage and tailings stabilization. *Minerals* 7, 191.
- McCutcheon J., Dipple G.M., Wilson S.A. and Southam G. (2015) Production of magnesium-rich solutions by acid leaching of chrysotile: A precursor to field-scale deployment of microbially enabled carbonate mineral precipitation. *Chemical Geology* 413, 119-131.
- McCutcheon J., Wilson S.A. and Southam G. (2016) Microbially accelerated carbonate mineral precipitation as a strategy for in situ carbon sequestration and rehabilitation of asbestos mine sites. *Environmental Science & Technology* 50, 1419-1427.
- Merrill R.J., Butt B.C., Forrest V.C., Purdon G. and Bramely-Moore R.A. (1980) Asbestos production at Chrysotile Corporation of Australia Pty. Limited, Barraba, NSW. Mining and Metallurgical Practices in Australasia: the Sir Maurice Mawby memorial volume 10, 669-673.
- Miyata S. (1983) Anion-exchange properties of hydrotalcite-like compounds. *Clays and Clay Minerals*, 31(4), 305-311.
- Morgan A., Lally A.E. and Holmes A. (1973) Some observations on the distribution of trace metals in chrysotile asbestos. *Annals of Occupational Hygiene* 16, 231-240.
- Morgan B., Wilson S.A., Madsen I.C., Gozukara Y.M. and Habsuda J. (2015) Increased thermal stability of nesquehonite ($MgCO_3 \cdot 3H_2O$) in the presence of humidity and CO_2 : Implications for low-temperature CO_2 storage. *International Journal Greenhouse Gas Control* 39, 366-376.
- Morrison J.M., Goldhaber M.B., Mills C.T., Breit G.N., Hooper R.L., Holloway J.M., Diehl S.F. and Ranville J.F. (2015) Weathering and transport of chromium and nickel from serpentinite in the Coast Range ophiolite to the Sacramento Valley, California, USA. *Applied Geochemistry* 61, 72-86.
- Mudd G.M. and Jowitt S.M. (2014) A detailed assessment of global nickel resource trends and endowments. *Economic Geology* 109, 1813-1841.

- Mumpton F. (1966) The stability of brucite in the weathering zone of the New Idria Serpentine. *Clays and Clay Mineralogy* 14, 249-257.
- Mumpton F. and Thompson C. (1966) The stability of brucite in the weathering zone of the New Idria serpentinite. *Clays and Clay Mineralogy* 14, 249-257.
- Natali C., Boschi C., Baneschi I., Dini A. and Chiarantini L. (2013) Chromium mobility in Tuscan serpentinite bodies; inferences from rodingitization and carbonation. *Mineralogical Magazine* 77, 1829.
- O'Hanley D.S. and Dyar M.D. (1993) The composition of lizardite 1T and the formation of magnetite in serpentinites. *American Mineralogist* 78, 391-404.
- O'Hanley D.S. and Dyar M.D. (1998) The composition of chrysotile and its relationship with lizardite. *Canadian Mineralogist* 36, 727-739.
- O'Hanley D.S. and Offler R. (1992) Characterization of multiple serpentinization, Woodsreef, New South Wales. *Canadian Mineralogist* 30, 1113-1126.
- Oelkers E.H., Gislason S.R. and Matter J. (2008) Mineral carbonation of CO₂. *Elements* 4, 333-337.
- Okamoto I., Mizuochi Y., Ninomiya A., Kato T., Yajima T. and Ohsumi T. (2006) In-situ test on CO₂ fixation by serpentinite rock mass in Japan, Proceedings of the 8th International Conference on Greenhouse Gas Technologies. Elsevier, Oxford, CD-ROM.
- Olajire A.A. (2013) A review of mineral carbonation technology in sequestration of CO₂. *Journal of Petroleum Science and Engineering* 109, 364-392.
- Olsson J., Stipp S.L.S. and Gislason S.R. (2014a) Element scavenging by recently formed travertine deposits in the alkaline springs from the Oman Semail Ophiolite. *Mineralogical Magazine* 78, 1479-1490.
- Olsson J., Stipp S.L.S., Makovicky E. and Gislason S.R. (2014b) Metal scavenging by calcium carbonate at the Eyjafjallajökull volcano: A carbon capture and storage analogue. *Chemical Geology* 384, 135-148.

- Oskierski H.C. (2013) Natural carbonation of ultramafic rocks in the Great Serpentine Belt, New South Wales, Australia. Ph.D thesis, The University of Newcastle.
- Oskierski H.C., Dlugogorski B.Z. and Jacobsen G. (2013) Sequestration of atmospheric CO₂ in chrysotile mine tailings of the Woodsreef Asbestos Mine, Australia: Quantitative mineralogy, isotopic fingerprinting and carbonation rates. *Chemical Geology* 358, 156-169.
- Oze C., Bird D.K. and Fendorf S. (2007) Genesis of hexavalent chromium from natural sources in soil and groundwater. *Proceedings of the National Academy of Sciences of the United States of America* 104, 6544-6549.
- Palandri J.L. and Kharaka Y.K. (2004) A compilation of rate parameters of water-mineral interaction kinetics for application to geochemical modeling. U.S. Geological Survey Open File Report (OF 2004-1068).
- Park A.H.A. and Fan L.S. (2004) Mineral sequestration: physically activated dissolution of serpentine and pH swing process. *Chemical Engineering Science* 59, 5241-5247.
- Paterson, D., De Jonge, M.D., Howard, D.L., Lewis, W., McKinlay, J., Starritt, A., Kusel, M., Ryan, C.G., Kirkham, R., Moorhead, G. and Siddons, D.P., (2011). The X-ray fluorescence microscopy beamline at the Australian Synchrotron. *AIP Conference Proceedings* 1365, 219-222.
- Perruchot A. (1973) Partage du nickel entre serpentine et brucite au cours de la serpentinisation du périclote. *Contributions to Mineralogy and Petrology* 42, 229-234.
- Power I.M., Dipple G.M. and Southam G. (2010) Bioleaching of ultramafic tailings by *Acidithiobacillus* spp. for CO₂ sequestration. *Environmental Science & Technology* 44, 456-462.
- Power, I.M., Harrison, A.L., Dipple, G.M., Wilson, S.A., Kelemen, P.B., Hitch, M. and Southam, G. (2013) Carbon mineralization: From natural analogues to engineered systems. *Reviews in Mineralogy Geochemistry* 77, 305-360.

- Power I.M., Wilson S.A. and Dipple G.M. (2013) Serpentinite carbonation for CO₂ sequestration. *Elements* 9, 115-121.
- Power, I.M., Wilson, S.A., Thom, J.M., Dipple, G.M., Gabites, J.E. and Southam, G., (2009). The hydromagnesite playas of Atlin, British Columbia, Canada: A biogeochemical model for CO₂ sequestration. *Chemical Geology* 260, 286-300.
- Pronost J., Beaudoin G., Lemieux J.-M., Hébert R., Constantin M., Marcouiller S., Klein M., Duchesne J., Molson J.W., Larachi F. and Maldague X. (2012) CO₂-depleted warm air venting from chrysotile milling waste (Thetford Mines, Canada): Evidence for in-situ carbon capture from the atmosphere. *Geology* 40, 275-278.
- Rietveld H.M. (1969) A profile refinement method for nuclear and magnetic structures. *Journal of Applied Crystallography* 2, 65-71.
- Ristić M., Czakó-Nagy I., Musić S. and Vértes A. (2011) Spectroscopic characterization of chrysotile asbestos from different regions. *Journal of Molecular Structure* 993, 120-126.
- Romão I.S., Gando-Ferreira L.M. and Zevenhoven R. (2013) Combined extraction of metals and production of Mg(OH)₂ for CO₂ sequestration from nickel mine ore and overburden. *Minerals Engineering* 53, 167-170.
- Rozalen, M., and Huertas, F.J., (2013). Comparative effect of chrysotile leaching in nitric, sulfuric and oxalic acids at room temperature. *Chemical Geology* 352, 134-142.
- Ryan C.G. (2000) Quantitative trace element imaging using PIXE and the nuclear microprobe. *Int. Journal of Imaging Systems and Technology* 11, 219-230.
- Ryan C.G., Siddons D.P., Kirkham R., Dunn P.A., Kuczewski A., Moorhead G., De Geronimo G., Paterson D.J., de Jonge M.D., Hough R.M., Lintern M.J., Howard D.L., Kappen P. and Cleverley J. (2010) The new Maia detector system: Methods for high definition trace element imaging of natural material. *AIP Conference Proceedings* 1221, 9-17.
- Ryan C.G., Siddons D.P., Kirkham R., Li Z.Y., de Jonge M.D., Paterson D.J., Kuczewski A., Howard D.L., Dunn P.A., Falkenberg G., Boesenberg U., Geronimo G.D., Fisher L.A., Halfpenny A., Lintern M.J., Lombi E., Dyl K.A., Jensen M.,

- Moorhead G.F., Cleverley J.S., Hough R.M., Godel B., Barnes S.J., James S.A., Spiers K.M., Alfeld M., Wellenreuther G., Vukmanovic Z. and Borg S. (2014) Maia X-ray fluorescence imaging: Capturing detail in complex natural samples. *Journal of Physics: Conference Series* 499, 012002.
- Schreier H. (1987) Asbestos fibres introduce trace metals into streamwater and sediments. *Environmental Pollution* 43, 229-242.
- Schreier H. and Lavkulich L. (2015) Cumulative effects of the transport of asbestos-rich serpentine sediments in the trans-boundary Sumas Watershed in Washington State and British Columbia. *Canadian Water Resources Journal* 40, 262-271.
- Schuiling R. and de Boer P. (2013) Six commercially viable ways to remove CO₂ from the atmosphere and/or reduce CO₂ emissions. *Environmental Sciences Europe* 25, 35.
- Schwertmann U., Gasser U. and Sticher H. (1989) Chromium-for-iron substitution in synthetic goethites. *Geochimica et Cosmochimica Acta* 53, 1293-1297.
- Sciortino M., Mungall J.E. and Muinonen J. (2015) Generation of high-Ni sulfide and alloy phases during serpentization of dunite in the Dumont Sill, Quebec. *Economic Geology* 110, 733-761.
- Seal R.R., Piatak N.M., Levitan D.M. and Hammarstrom J.M. (2010) Neutral to alkaline mine drainage, carbon sequestration, and arsenic release at the abandoned Vermont Asbestos Group Mine, Belvidere Mountain, Vermont. *Abstracts with Programs—Geological Society of America* 42, 449.
- Seifritz W. (1990) CO₂ disposal by means of silicates. *Nature* 345, 486.
- Slansky E. (1983) X-ray identification of minerals in Woodsreef Asbestos Mine Tailings. Geological Survey of New South Wales, Department of Mineral Resources GS1983/285.
- Stumm, W. and Morgan, J.J., (1996). Aquatic Chemistry: Chemical Equilibria and Rates in Natural Waters {*Environmental Science & Technology*}. Wiley.
- Sylvester C.W. and Stagg R.N. (2008) EL-6612 Barraba Silica Project, Annual Report for 17/8/2007 to 16/8/2008. International Minerals Corporation Pty Ltd.

- Teir S., Kuusik R., Fogelholm C.-J. and Zevenhoven R. (2007a) Production of magnesium carbonates from serpentinite for long-term storage of CO₂. *International Journal of Mineral Processing* 85, 1-15.
- Teir S., Revitzer H., Eloneva S., Fogelholm C.-J. and Zevenhoven R. (2007b) Dissolution of natural serpentinite in mineral and organic acids. *International Journal of Mineral Processing* 83, 36-46.
- Thomas D., Maher K., Bird D., Brown G. and Arnórsson S. (2013) CO₂-rich geothermal areas in Iceland as natural analogues for geologic carbon sequestration. *AGU Fall Meeting Abstracts* 1, 2776.
- Thomas D.L., Bird D.K., Arnórsson S. and Maher K. (2016) Geochemistry of CO₂-rich waters in Iceland. *Chemical Geology* 444, 158-179.
- Trolard F., Bourrie G., Jeanroy E., Herbillon A.J. and Martin H. (1995) Trace metals in natural iron oxides from laterites: A study using selective kinetic extraction. *Geochimica et Cosmochimica Acta* 59, 1285-1297.
- Turvey C.C., Wilson S.A., Hamilton J.L. and Southam G. (2017) Field-based accounting of CO₂ sequestration in ultramafic mine wastes using portable X-ray diffraction. *American Mineralogist* 102, 1302-1310.
- Veetil S.P., Mercier G., Blais J.-F., Cecchi E. and Kentish S. (2015) Magnetic separation of serpentinite mining residue as a precursor to mineral carbonation. *International Journal of Mineral Processing* 140, 19-25.
- Vogel C., Adam C., Kappen P., Schiller T., Lipiec E. and McNaughton D. (2014) Chemical state of chromium in sewage sludge ash based phosphorus-fertilisers. *Chemosphere* 103, 250-255.
- Wicks F.J. and O'Hanley D.S. (1988) Serpentine minerals; structures and petrology. *Reviews in Mineralogy and Geochemistry* 19, 91-167.
- Wilson S.A., Dipple G.M., Power I.M., Barker S.L.L., Fallon S.J. and Southam G. (2011) Subarctic weathering of mineral wastes provides a sink for atmospheric CO₂. *Environmental Science & Technology* 45, 7727-7736.

- Wilson S.A., Dipple G.M., Power I.M., Thom J.M., Anderson R.G., Raudsepp M., Gabites J.E. and Southam G. (2009a) Carbon dioxide fixation within mine wastes of ultramafic-hosted ore deposits: Examples from the Clinton Creek and Cassiar chrysotile deposits, Canada. *Economic Geology* 104, 95-112.
- Wilson S.A., Harrison A.L., Dipple G.M., Power I.M., Barker S.L.L., Mayer K.U., Fallon, S.J., Raudsepp, M. and Southam, G. (2014) Offsetting of CO₂ emissions by air capture in mine tailings at the Mount Keith Nickel Mine, Western Australia: Rates, controls and prospects for carbon neutral mining. *International Journal of Greenhouse Gas Control* 25, 121-140.
- Wilson S.A., Raudsepp M. and Dipple G.M. (2006) Verifying and quantifying carbon fixation in minerals from serpentine-rich mine tailings using the Rietveld method with X-ray powder diffraction data. *American Mineralogist* 91, 1331-1341.
- Wilson S.A., Raudsepp M. and Dipple G.M. (2009b) Quantifying carbon fixation in trace minerals from processed kimberlite: A comparative study of quantitative methods using X-ray powder diffraction data with applications to the Diavik Diamond Mine, Northwest Territories, Canada. *Applied Geochemistry* 24, 2312-2331.
- Woodsreef Taskforce (2011) Asbestos and the derelict Woodsreef Mine. Primefact 1118
1. NSW Department of Primary Industries.
- Wunsch A., Navarre-Sitchler A.K., Moore J., Ricko A. and McCray J.E. (2013) Metal release from dolomites at high partial-pressures of CO₂. *Applied Geochemistry* 38, 33-47.
- Zachara J.M., Cowan C.E. and Resch C.T. (1991) Sorption of divalent metals on calcite. *Geochimica et Cosmochimica. Acta* 55, 1549-1562.

Declaration for Thesis Chapter 4

Declaration by candidate

In the case of Chapter 4, the nature and extent of my contribution is as follows:

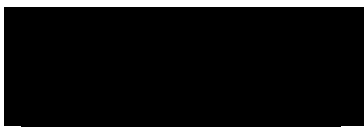
Nature of contribution	Extent of contribution
Conceptualisation, experimental design and construction, field work, data analysis and interpretation, writing.	79%

The following co-authors contributed to the work. If co-authors are students at Monash University, the extent of their contribution in percentage terms must be stated:

Name	Nature of contribution	Extent of contribution (%)
Siobhan A. Wilson	Supervisory role	5%
Connor C. Turvey	Fieldwork , isotope data	5%
Bree Morgan	Supervisory role	5%
Alastair W. Tait	Fieldwork	3%
Stuart J. Fallon	Isotope data	1%
Jenine McCutcheon	Fieldwork	1%
Gordon Southam	Fieldwork	1%

The undersigned hereby certify that the above declaration correctly reflects the nature and extent of the candidate's and co-authors contributions to this work*.

Candidate's signature:



Date: 10 February 2018

Main supervisor's signature:



Date: 5 February 2018

*Note: Where the responsible author is not the candidate's main supervisor, the main supervisor should consult with the responsible author to agree on the respective contributions of the authors.

Chapter 4

Field-based deployment of an automated geochemical treatment system for accelerating carbonation of ultramafic mine tailings: Lessons for pilot projects and carbon accounting in mined landscapes[†]

J.L. Hamilton^a, S.A. Wilson^{ab}, C.C. Turvey^a, B. Morgan^{ac}, A. Tait^a, J. McCutcheon^{de}, S.J. Fallon^f and G. Southam^d

^aSchool of Earth, Atmosphere and Environment, Monash University, Clayton,
Melbourne, VIC 3800, Australia

^bDepartment of Earth and Atmospheric Sciences, University of Alberta, Edmonton, AB T6G 2R3,
Canada

^cSchool of Geosciences, The University of Sydney, Camperdown, NSW 2006, Australia

^dSchool of Earth Sciences, The University of Queensland, St Lucia, QLD 4072, Australia

^eSchool of Earth and Environment, Maths/Earth and Environment Building, University of Leeds,
Leeds, LS2 9JT, United Kingdom

^fResearch School of Earth Sciences, Australian National University, Acton, ACT 2601, Australia

[†]Prepared for submission to *Applied Geochemistry*

Carbonation of ultramafic mine tailings has the potential to offset greenhouse gas emissions from mining by trapping CO₂ within the crystal structures of Mg-carbonate minerals, which form as weathering products in tailings storage facilities. Here, we report the results of a field-based test of a solar powered, independently operating geochemical treatment system, designed to deliver controlled acid or water treatments to accelerate the rate of mine tailings carbonation at Woodsreef Chrysotile Mine, New South Wales, Australia. Pore water saturation was controlled within optimal levels (approximately 18–36 % pore saturation at 5 cm depth) using pumps that turned on or off when pre-determined limits were reached. Wetting and drying cycles were 3 days in length, with approximately 20–30 L of either water or 0.08 M H₂SO₄ delivered in each dose over a period of 6–9 minutes after which the treatment plots were left to dry. Four treatment cycles were completed before an irrigation hose failure on the 10th day of the experiment led (1) to the tank of non-acidified water to spill across the site on that day and (2) to delivery of a single large dose (~900 L) of acidic water to the acidic treatment plot on the 18th day. Although a large volume of acidic water was delivered to the tailings, dissolution of existing carbonate minerals appears to have been restricted to the upper 2 cm of the acid plot. Below 2 cm, mineralogy and geochemistry of the acid-treated tailings was comparable to that in the water-treated plot and a control plot. This is likely a consequence of poor infiltration of treatment solutions and the high neutralising capacity of the tailings, which may also have limited the effectiveness of the acid treatment. As a result, the applied experiment did not accelerate mineral carbonation within the tailings. Detailed analysis of tailings mineralogy using quantitative X-ray diffraction (XRD) and total carbon analyses reveals that previous assessments of passive mineral carbonation at Woodsreef have likely been underestimated. Maximum values for the abundance of total

carbon (up to 0.4 wt. %), as well as the abundances of carbonate minerals (i.e., up to 1.9 wt. % hydromagnesite and up to 2.6 wt. % pyroaurite) are observed between approximately 2 and 30 cm depth in profiles collected within the experimental plots. Carbon content and carbonate mineral abundance both decrease with depth below 30 cm; however, there is a significant underestimate of C content using XRD data compared to elemental analyses which appears to be related to an X-ray amorphous Mg-carbonate phase that persists to depths of at least 1 m. Stable and radiogenic carbon isotope data show a mixing trend between atmospheric and bedrock sources of carbon in bulk tailings, with an increasing component of atmospheric carbon occurring closer to the surface of the tailings. This is consistent with carbon limitation at depth, although the carbon stored within minerals in the tailings at Woodsreef is still predominantly ($F^{14}C > 0.80$) from an atmospheric source even at 1 m depth. Using both XRD and total carbon data, we provide an estimate for passive carbon sequestration in the Woodsreef tailings (11.7 kg CO₂/m², considering only carbonation in the upper 1 m³) and suggest that future studies should employ both XRD and total carbon measurements for carbon accounting. Using these techniques in parallel provides more accurate accounting of CO₂ sequestration by well-crystallised carbonate alteration minerals and X-ray amorphous carbonate phases during passive and accelerated mineral carbonation in landscapes.

4.1. Introduction

Mineral carbonation is a natural process that results in the sequestration of atmospheric CO₂ in mineral form (Seifritz, 1990). This occurs as silicate minerals dissolve in meteoric water, releasing cations such as Mg²⁺, which then react with dissolved carbon dioxide (as CO₃²⁻) to precipitate as Mg-carbonate minerals (Oelkers et al., 2008; Wilson et al., 2009). These carbonate mineral products are known to be stable at Earth's surface conditions for

tens of thousands of years or longer (Lackner et al., 1995), and they are currently utilised in a range of industries including construction and pharmaceuticals (e.g., Glasser et al., 2016; Shan et al., 2012). Accelerated mineral carbonation has been proposed as a strategy to mitigate anthropogenic greenhouse gas emissions (IPCC, 2005, 2013) and pilot studies are now using this technology to sequester industrial CO₂ emissions (Brent et al., 2015; Kemache et al., 2016, 2017; Mouedhen et al., 2017). Ultramafic rocks are favoured for this reaction because they have high Mg-contents and are relatively reactive (e.g., Bobicki et al., 2012; Bodénan et al., 2014; Hitch et al., 2009; Jacobs and Hitch, 2011; Pronost et al., 2011). Crushing and milling further enhances the reactivity of ultramafic rocks; thus, storage facilities for ultramafic mine tailings are ideal locations for observing and accelerating mineral carbonation (Bodor et al., 2013; Wilson et al., 2009). Passive carbonation of ultramafic mineral wastes has been observed at mines in Canada, Australia and Norway (e.g., Beinlich and Austrheim, 2012; Lechat et al., 2016; Oskierski et al., 2013; Pronost et al., 2012; Wilson et al., 2011; Wilson et al., 2009; Wilson et al., 2014), and at Mt Keith Nickel Mine, Western Australia, passive mineral carbonation offsets 11% of this mine's annual CO₂ emissions (Wilson et al., 2014). Accelerating CO₂ sequestration rates at Mt Keith by ten times would make this mine carbon neutral.

Strategies for accelerating mineral carbonation have focussed on overcoming two key rate-limiting factors: (1) the slow dissolution of silicate minerals to release cations for reaction and (2) CO₂ limitation, both of which inhibit carbonate precipitation. Passivation of reactive mineral surfaces by precipitates of silica, Fe-(hydr)oxide or carbonate minerals can also become limiting to carbonation rates over time. A variety of geochemical and geomicrobial methods have been developed to accelerate carbonation of ultramafic materials under experimental conditions including acid leaching and elevated temperature/pressure (Gerdemann et al., 2007; Maroto-Valer et al., 2005; Park and Fan,

2004; Teir et al., 2007b; Chapter 5), elevated CO₂ levels (Entezari Zarandi et al., 2016; Chapter 5), optimised moisture levels (Assima et al., 2013; Harrison et al., 2015), and bacterial inoculation (McCutcheon et al., 2016; Power et al., 2010).

Sulfuric acid is reportedly most effective at enhancing silicate mineral dissolution (Maroto-Valer et al., 2005; Teir et al., 2007b). Further environmental benefits could be found by utilising acid generating material (i.e., sulfide-rich waste rock), produced as a by-product of mining, as a source of sulfuric acid to accelerate dissolution of ultramafic minerals and increase Mg production for mineral carbonation (Power et al., 2010). Mineral carbonation reactions are commonly CO₂ limited in mining environments (Gras et al., 2017; Wilson et al., 2010, 2011, 2014). Exposing ultramafic materials to elevated CO₂ concentrations has been shown to accelerate carbon sequestration rates and, at ambient temperature and pressure, acceleration is primarily achieved via carbonation of brucite [Mg(OH)₂], an accessory mineral in serpentinites (Assima et al., 2014; Harrison et al., 2012). Mineral carbonation reactions are optimised when pore water saturation levels are balanced to allow (1) mineral dissolution and (2) adequate gas–water contact for CO₂ diffusion into the liquid phase (Assima et al., 2012; Harrison et al., 2015). Optimal soil moisture levels have been reported in the range of 20–40% in nickel tailings (Assima et al., 2013), and 35–60% in mixtures of pulverised brucite [Mg(OH)₂] and quartz (SiO₂) (Harrison et al., 2016). Bacteria (e.g., cyanobacteria, sulfate reducing bacteria and urealytic bacteria) can assist in carbonate mineral precipitation by increasing local alkalinity and concentrating Mg²⁺ and carbonate ions near cell walls. The local concentration of these ions can drive saturation of carbonate minerals thereby inducing precipitation (McCutcheon et al., 2016, 2017; Power et al., 2011).

Chemical and biological treatments have been used to successfully accelerate rates of mineral carbonation in the laboratory. Recently, in Canada, *ex situ*, batch reactor processes have advanced to pilot scale tests, whereby serpentinite tailings are pre-treated by grinding and dehydroxylation at elevated temperature, followed by reaction with flue gas containing 12–20% CO₂ at an unnamed cement plant (Kemache et al., 2016, 2017; Mouedhen et al., 2017). Another pilot project is underway in Newcastle, Australia (Brent et al., 2015); however little information about the processes used here is available in the literature. While published results show promise, adjustments are still required to optimise processes (Kemache et al., 2017). High costs have inhibited *ex situ* industrial reactors from being brought to pilot and commercial scale, with recent estimates ranging from ~\$100 U.S./t CO₂ (Power et al., 2013a, 2013b), up to U.S. \$1600/t CO₂ (Azdarpour et al., 2015). Without a high price on carbon, or commercial demand for the products of mineral carbonation, the challenge remains to develop treatments that have a low energy input, relatively low cost, and that are readily scalable (Azdarpour et al., 2015; Power et al., 2013a, 2014). As such, it is important to develop and trial strategies for *in situ* treatments that accelerate mineral carbonation at ambient temperatures and pressures. The first reported field trial for accelerated carbonation of mine tailings was recently carried out at the Woodsreef Mine, New South Wales, Australia (McCutcheon et al., 2017). This trial treated chrysotile-bearing serpentinite tailings with a sulfuric acid pre-leach, which was followed by inoculation of tailings with a cyanobacteria-dominated microbial consortium. McCutcheon et al. (2017) report a doubling of the carbonation rate after 11 weeks within shallow tailings (i.e., between 2–4 cm depth) that had been colonised by cyanobacteria; however, harsh environmental conditions at Woodsreef were detrimental to the health of the microbial community.

Here, we report on an abiological field trial for accelerated tailings carbonation that was conducted at the Woodsreef Mine in parallel with the experiment described by McCutcheon et al. (2017). Our abiological field trial was designed to deliver acid treatments and to control tailings pore water saturation for optimal dissolution of atmospheric CO₂. Importantly, this trial prioritised several key design criteria deemed important for practical success and likelihood of uptake by industry: low cost and energy input, ease of operation, and scalability. The experimental design that we used consists of a solar powered sprinkler system to deliver acid or water treatments and a network of environmental sensors and control systems, including soil moisture probes, which was used to maintain optimum soil saturation levels. We report the successes and challenges associated with deployment of this system, and suggest strategies to improve the effectiveness of field trials for accelerated carbonation of ultramafic landscapes in the future.

4.1.1. Site description

Woodsreef Chrysotile Mine is located approximately 500 km northwest of Sydney in New South Wales (NSW), Australia (Fig. 4.1). The chrysotile deposit at Woodsreef is part of the Great Serpentine Belt (GSB) within the Southern New England Fold Belt. Asbestos fibre was first reported in the area in 1884 and was mined in three intervals from 1918 to 1923, 1958 to 1959, and most recently from 1971 to 1983 by Chrysotile Corporation (Assargiotis 2013). In this latest production period, 500,000 tonnes of chrysotile, 75 million tonnes of waste rock and 24 million tonnes of dry-milled tailings were produced (Assargiotis, 2013; Merrill et al., 1980). The mine was closed in 1983 and is now managed by the Woodsreef Taskforce, a multi-agency committee that includes representatives from state agencies such as the NSW Department of Industry, Hunter

New England Health and WorkCover NSW, and federal agencies including the Australian Environmental Protection Authority, the Ministry of Health, and the Department of Primary Industries (Assargiotis, 2013; Woodsreef Taskforce, 2011).

4.2. Materials and methods

4.2.1. Experimental design and sampling strategy

The experiment was conducted during southern spring from 1st October to 10th November 2015. The experimental site was located on the flat horizontal surface of the tailings storage facility at Woodsreef (Fig. 4.1A–B) in an area adjacent to a ≈ 1 m vertical face, which was used to investigate carbonation on both horizontal and vertical surfaces. The upper few cm of pre-existing carbonated material was removed from both the horizontal and vertical faces of three 1-m² areas to create the acid, water and control treatment plots. The location of samples taken before and after treatments is shown in Figure 1C. Two 30-cm deep cores were taken in each plot (Pre-Exp-C1, -C2, -C3, -C4, -C5, -C6). Cores were sampled using a 4-cm diameter gravel corer in 10 cm intervals (0–10 cm, 10–20 cm and 20–30 cm) at the locations shown in yellow in Figure 4.1C. Two additional 30-cm cores were taken from the regions between each treatment plot where the pre-existing surficial carbonate crust had not been cleared away (Pre-Exp-C7, -C8, Figure 1C). These two cores were collected in four intervals to include the surficial carbonate crust as a separate sample (0–2 cm, 2–10 cm, 10–20 cm, 20–30 cm).

At the completion of the experiment (on November 10th, 2015), samples were taken from three 1-m deep profiles within each plot (Acid-C1, -C2, -C3, Water-C1 -C2, -C3, and Control-C1, -C2, -C3, Fig. 4.1C). Each of these profiles was sampled using the gravel corer at intervals of 0–2 cm, 2–10 cm, 10–20 cm, and 20–30 cm.

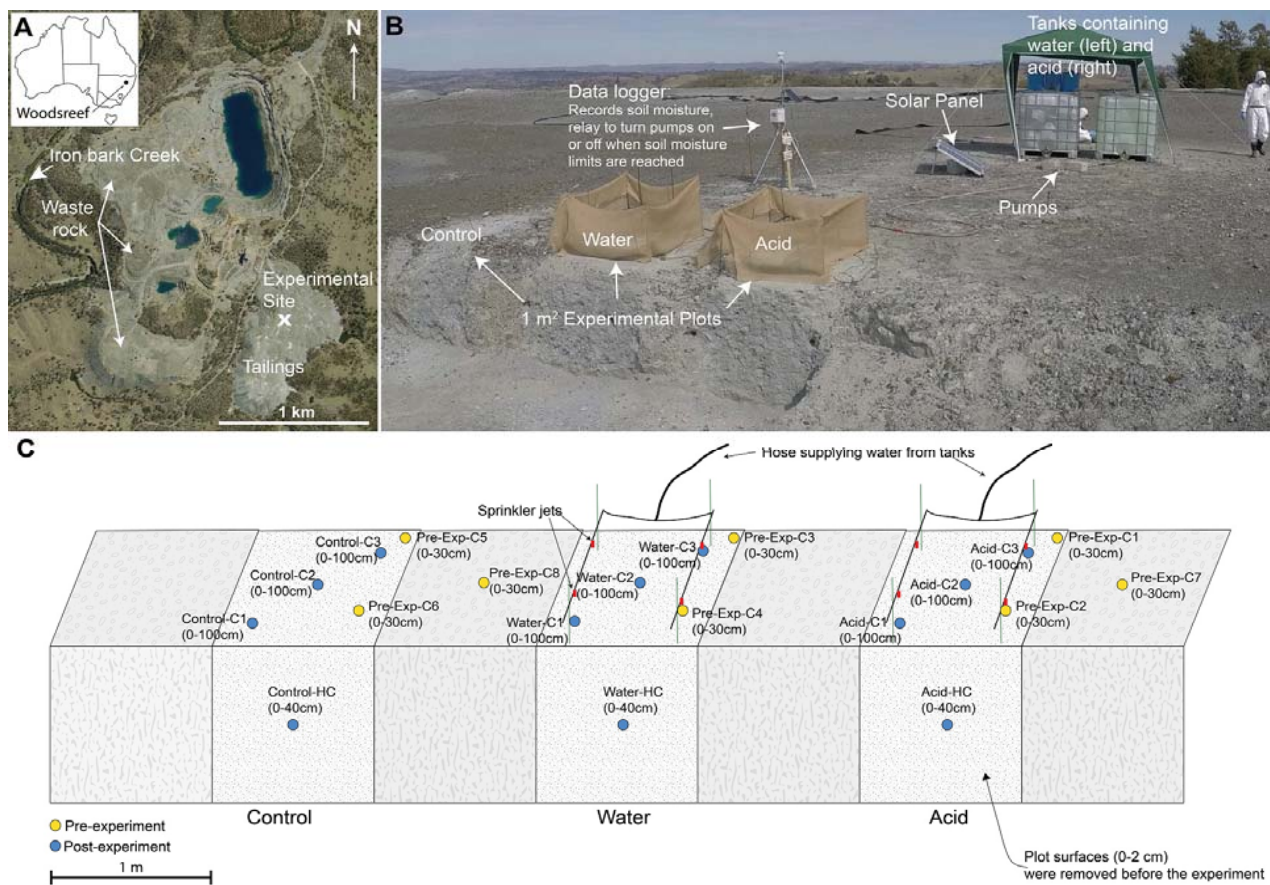


Figure 4.1. (A) Aerial image of Woodsreef Chrysotile Mine. Inset indicates the location of the mine within Australia. The experimental site is marked with an ‘X’ and Ironbark Creek, where water was collected for use in experiments, is indicated with an arrow. (B) Photo of the experimental site, showing the location of plots, and the experimental set up. (C) Diagram of the experimental plots including sampling locations.

Once cored to 30 cm depth, plots were excavated in layers and further hand samples were taken from beneath the initial location of each core at 10-cm intervals down to a depth of 1 m. Samples were also taken in a horizontal profile, inwards from the vertical face of each plot, at 10-cm intervals to a depth of 40 cm (Acid-HC, Water-HC, Control-HC, Figure 4.1C).

Two soil moisture probes (S-SMC-M005, Onset) were inserted horizontally into tailings at 5 and 20 cm depth within the holes left behind after removing cores Pre-Exp-C2 and Pre-Exp-C4 in the acid and water treatment plots respectively (Fig. 4.1C). The probe that was programmed to control the alarm system and pumps was located at 5 cm depth in the water treatment plot (in Pre-Exp-C4, 5 cm depth; Fig. 1C). In addition, a soil temperature probe was inserted on the opposite internal wall of this excavated core hole (approximately 4 cm away) at the same depth (5 cm) as the controlling soil moisture probe. Both Pre-Exp-C2 and Pre-Exp-C4 core holes were then backfilled with tailings material. Due to the observed heterogeneity in tailings properties within and between plots, such as a higher coarse waste rock content in the control plot, probes were used at factory calibration and therefore report semi-quantitative pore water saturation levels. Air temperature and relative humidity were monitored via probes attached to the data logger tripod (Fig. 4.1B). Rainfall events were identified by Bureau of Meteorology records from nearby stations within New South Wales at Barraba, Gunnedah, Inverell and Tamworth (stations 54003, 55023, 56242 and 55325 respectively) (Bureau of Meteorology, 2015).

Soil moisture probe data were recorded at 1-minute intervals using HOBO U30 and HOBO Micro Station data loggers. A lower alarm was set to $0.09 \text{ m}^3/\text{m}^3$ and an upper alarm at $0.18 \text{ m}^3/\text{m}^3$ volumetric water content. These values correspond to a minimum of

18 % and a maximum of 36 % saturation for the tailings at 5 cm depth, which are within the limits of optimum conditions (Assima et al., 2013; Harrison et al., 2015) since we expected the tailings at 20 cm depth to be more saturated than those at 5 cm depth. It was anticipated that regular periods of wetting and drying would enhance mineral dissolution during delivery of treatments, followed by a period of evaporative concentration of pore waters during drying, which would promote mineral carbonation (after Assima et al., 2013). Treatments (either creek water or acidified creek water) were delivered to the water and acid treatment plots simultaneously when the low water content alarm was triggered by the probe installed at 5 cm depth in the water treatment plot. This allowed doses of constant volume to be delivered simultaneously to the water and acid plots.

Acid and water treatment solutions were delivered from two 1000 L intermediate bulk container (IBC) tanks (Fig. 1B). These were installed at the site of the experiment and filled to capacity with water from nearby Ironbark Creek. Creek water was filtered through fabric mesh to remove large particles. The pH of the creek water was 8.5 and alkalinity was determined by titration to be 212 mg/L bicarbonate. Chemical analysis of the creek water is presented in Table S1. 4.2 L of 17.8 M H₂SO₄ (Sigma Aldrich) was added to one of the two tanks to obtain a 0.08 M H₂SO₄ treatment solution. In comparison, McCutcheon et al. (2017) applied a single dose of 0.22 M H₂SO₄, which was determined as the optimum concentration in order to ensure neutralisation and survival of environmental and inoculated bacteria, whilst producing a high-Mg leachate to promote biologically mediated mineralisation of carbonate minerals (McCutcheon et al., 2015, 2017). Here, solutions were intended to be applied repeatedly for up to several months, thus a slightly lower acid concentration was chosen.

Four sprinklers (mister jets) were suspended from stakes 25 cm above the tailings surface, spraying downwards onto each of the acid and creek water treatment plots. This was intended to provide a relatively even spray, whilst minimising solution loss in a breeze. A hessian (or ‘burlap’) cloth barrier was erected to limit cross spraying into adjacent treatment plots (Fig. 4.1B). Sprinkler jets delivered water at a rate of 200 L/h in a test using mains tap pressure, with <5 % difference in rate between the two setups, one of which was used for each of the acid and water treatment plots.

The system described above is comprised of readily available, relatively inexpensive materials. It is 100% solar powered, operates independently, and is similar to systems already in commercial use at a comparable scale to mine tailings storage facilities (e.g., used for optimised irrigation of golf courses).

4.2.2. Mineralogical and geochemical analysis

Core samples were weighed before and after air-drying under ambient laboratory conditions to determine bulk density and pore water saturation levels. All samples were pulverised following drying using a ring mill prior to further analysis. All core samples were prepared for powder X-ray diffraction (XRD) by adding 10 wt. % fluorite (CaF_2) as an internal standard to enable quantification of serpentine minerals using the method of Wilson et al. (2006). They were then milled for 7 minutes under anhydrous ethanol in a McCrone Micronising Mill using agate grinding elements. Following milling, samples were air dried in Petri dishes and disaggregated with an agate mortar and pestle. Each sample was loaded into a back-loading cavity mount against a sheet of frosted glass to minimise preferred orientation of crystallites. XRD patterns were collected using a Bruker D8 Advance Eco X-ray Diffractometer with a Cu source operated at 40 kV and 25 mA. Data were collected over $2-80^\circ 2\theta$, with a step size of $0.02^\circ 2\theta$ and a count time of 2

s/step. Mineral phases were identified using the ICDD PDF-2 database and the DIFFRAC^{plus} EVA Version 2 software package (Bruker ASX).

Quantitative phase analysis was conducted using the modified Rietveld refinement method (Bish and Howard, 1988; Hill and Howard, 1987; Rietveld, 1969) reported by Wilson et al. (2006). The serpentine polymorphs in Woodsreef tailings {chrysotile and lizardite, $[\text{Mg}_3\text{Si}_2\text{O}_5(\text{OH})_4]$ } have disordered crystal structures that result in severe anisotropic peak broadening in powder XRD patterns. As such, their peak profiles cannot be modelled using traditional Rietveld refinement strategies (Turvey et al., 2017; Wilson et al., 2006). Instead, a Pawley phase (Pawley, 1981) is used for structureless pattern fitting of serpentine peaks, while the fluorite internal standard enables quantification by treating serpentine minerals as an amorphous phase. Here, we employ this method with the program Topas v.5 (Bruker AXS) using the fundamental parameters approach (Cheary and Coelho, 1992). Background functions were modelled using fourth-order Chebychev polynomials with an additional $1/x$ function. A default Brindley radius of 0.00025 mm and a packing density of 0.4 were used to correct for microabsorption contrast amongst all phases (Brindley, 1945).

Of the pre-experiment samples, one core from each plot (Pre-Exp-C1, -C3, and -C5, Fig. 4.1C), and the two cores located outside the experimental plots (Pre-Exp-C7, -C8, Fig. 4.1C) were analysed for total carbon content. Carbonate crust samples collected from the upper 0–2 cm of two of these cores (Pre-Exp-C7-0 and Pre-Exp-C8-0) and the 0–10 cm interval of Pre-Exp-C1-1 were analysed for organic carbon in addition to total carbon content. Post experiment samples from 0 to 50 cm depth in the first and second vertical profiles within each plot (Acid-C1, -C2, Water-C1, -C2, Control-C1, -C2, Fig. 4.1C) and extended to 1 m depth in the third profile (Acid-C3, Water-C3, Control-C3, Fig. 4.1C)

were analysed for total carbon, while samples from 0 to 30 cm depth in the third (-C3) profiles were also analysed for organic carbon by combustion. Total carbon and organic carbon were measured by total combustion analysis using a LECO analyser by Bureau Veritas Pty. Ltd. The detection limit for both total and organic carbon is 0.01 wt. %.

Radiocarbon data and $\delta^{13}\text{C}$ (VPDB) values were obtained at the Research School of Earth Sciences, the Australian National University using a Single Stage Accelerator Mass Spectrometer (SSAMS). The instrument is equipped with a gas/graphite hybrid ion source, allowing for direct analysis of CO_2 as well as traditional graphite targets (Fallon et al., 2010). $\delta^{13}\text{C}$ values were obtained using the SSAMS instrument, and are less precise than results that could be obtained with an Isotope Ratio Mass Spectrometer (IRMS). Radiocarbon results are reported as the fraction modern carbon, $F^{14}\text{C}$, as well as conventional radiocarbon ages using the Libby half-life of 5568 years and following the conventions of Stuiver and Polach (1977). Sample preparation backgrounds have been subtracted based on measurement of samples of ^{14}C -free CO_2 .

4.2.3. Calculation of neutralising potential

Neutralising potential (NP) can be used to assess the impact of the acid spill on the geochemistry of the tailings, and inform future treatment requirements, such as the acid concentration or dose that can theoretically be applied without generating acidic drainage. Here, the neutralisation potential is calculated for tailings in the upper 20 cm, which was saturated during the spill according to soil moisture probe data (Fig. 4.2C). Typically, NP calculations only take into account carbonate minerals (Dold, 2017) because non-carbonate minerals are comparatively very slow to react and, thus, generally contribute a negligible amount of neutralising potential (Blowes et al., 2013). NP can be calculated directly from total carbon data, as CaCO_3 equivalent, using Eq. 1, from Wahlström et al.

(2009), where *wt. % C* is the inorganic carbonate (CO_3^{2-}) content [average measured total carbon (0.33 wt. %) minus the average organic carbon content (0.02 wt.% C), from the 0–20 cm intervals of all pre-experiment cores (Fig. 4.1C)] expressed as a mass fraction in wt. % C, and $M(C)$ is the molar mass of carbon. This fraction is multiplied by 10 to convert the mass fraction to units of mol/kg (derived from dividing by the molecular mass of calcite (100.1 g/mol), then multiplying by 1000 g/kg), and multiplied by two because it is assumed that one mol of carbonate can neutralise two mol of acid (Dold, 2017; Wahlström et al., 2009). The calculated NP is in units of mol H^+ /kg material.

$$NP = 2 \cdot 10 \cdot \frac{(\text{wt. \% } C)}{M(C)} \quad (\text{Eq. 1})$$

While most silicate minerals contribute negligible NP compared to carbonate minerals, olivine and serpentine have relatively high neutralising potential, especially where they have a fine grain size (Jambor et al., 2002; Jambor et al., 2007). Since the Woodsreef Mine tailings are fine grained due to crushing of the ore, and because we expect chrysotile to dissolve in the acidic solution that was applied (McCutcheon et al., 2015), we also estimate whole rock neutralising potential of the Woodsreef tailings, and consider this to be a maximum value for neutralising potential. Whole rock NP is calculated by taking the sum of the neutralising potential for each constituent mineral within a sample using Eq. 2 from Lawrence and Scheske (1997).

$$NP = \frac{(\text{wt. \% } \text{min.})}{100} \cdot \frac{1000 \text{ kg}}{1 \text{ tonne}} \cdot \frac{M(\text{CaCO}_3)}{M(\text{min.})} \cdot R \quad (\text{Eq. 2})$$

The variable, *wt. % min.*, is the wt. % abundance of the mineral phase as determined by Rietveld refinement of XRD data [using average refined abundances for the 0–20 cm intervals in all pre-experiment cores, as the acid plot was saturated within this interval during the acid spill event (Fig. 1C)], $M(\text{CaCO}_3)$ is the molar mass of calcite (100.09

g/mol), $M(\text{min.})$ is the molar mass of the mineral. R is the relative reactivity for the mineral at a pH of 5 (compared to a value of 1 for calcite), which is obtained from Table 1 in Lawrence and Scheske (1997) using data from Sverdrup (1990) and Kwong (1993). Almost all of the common carbonate, oxide and silicate minerals found at Woodsreef Mine have known values for R , with the exceptions of magnetite and pyroaurite [$\text{Mg}_6\text{Fe}_2(\text{CO}_3)(\text{OH})_{16}\cdot 4\text{H}_2\text{O}$]. In our calculations, Magnetite is assigned as inert (reactivity = 0.004), while pyroaurite is assigned a reactivity of 1, since dissolution of pyroaurite-type hydrotalcites is observed at pH 4–8 in Imran et al., (2016), and is described as occurring more rapidly in acidic conditions. The resulting whole rock NP calculated using Eq. 2 is in units of kg CaCO_3 /tonne. This value is divided by the molecular weight of calcite (100.1 g/mol) and multiplied by 2 to convert to mols H^+ /kg material. Agreement between the calculated NP method, using mineral abundances refined from XRD data, and measured NP (using a Sobek test) is typically considered to be good, although rocks containing olivine and serpentine are found to have larger deviations (Jambor et al., 2007). Calculated values for the neutralisation potential of the Woodsreef mine tailings are unlikely to give very accurate estimations because neutralising potential will be affected by factors such as grain size and mineral surface area which have not been taken into account here. Nonetheless, it still useful to provide an indication of neutralising potential in comparison to the acid dose applied.

4.3. Results

4.3.1. Experimental deployment

Soil moisture was maintained according to the limits set for the controlling probe in the water treatment plot throughout the first 10 days of the field trial (Fig. 4.2). Effervescence was observed when acidic creek water was initially sprayed onto the acid plot, indicative

of dissolution of pre-existing carbonate alteration minerals. After the sprinkler system was turned on, the upper limit for optimal tailings saturation ($0.18 \text{ m}^3/\text{m}^3$) was reached within 6–9 minutes, with the duration of treatments varying across the four wetting cycles recorded. The doses were delivered in volumes of 20–30 L, calculated from a measured flow rate of 3 L/min (with a variation of 0.1 L/min). Drying cycles lasted approximately three days before the lower volumetric water content limit of $0.09 \text{ m}^3/\text{m}^3$ was reached at the location of the control sensor in the water treatment plot, which triggered the sprinkler system to turn on once again.

Daily soil temperature fluctuations affect volumetric water content readouts, with peaks and troughs correlating to higher soil temperatures during the day and lower temperatures at night (Fig. 4.2A). Tailings pore water saturation levels at 5 cm also fluctuate more than those measured at a depth of 20 cm, with higher values for maximum pore water saturation recorded after treatments and lower minimum values reached at the end of each cycle (Fig. 4.2A). Soil moisture probes at 20 cm depth within the water and control plots record approximately $0.05\text{--}0.15 \text{ m}^3/\text{m}^3$ higher volumetric water content, and fluctuations as a result of watering are less pronounced, compared to probes at 5 cm depth (Fig. 2B). However, the probe installed at a depth of 20 cm within the acid plot does not record wetting and drying cycles during the initial 10 days of successful operation, with only a gradual increase in saturation measured over that period. This suggests that infiltration of the treatment solution at this probe location is poor, although this improves from day 10, and from that point in time onward, the 20-cm probe in the acid plot responds to all subsequent watering or rainfall events similarly to the shallower probe located at 5 cm.

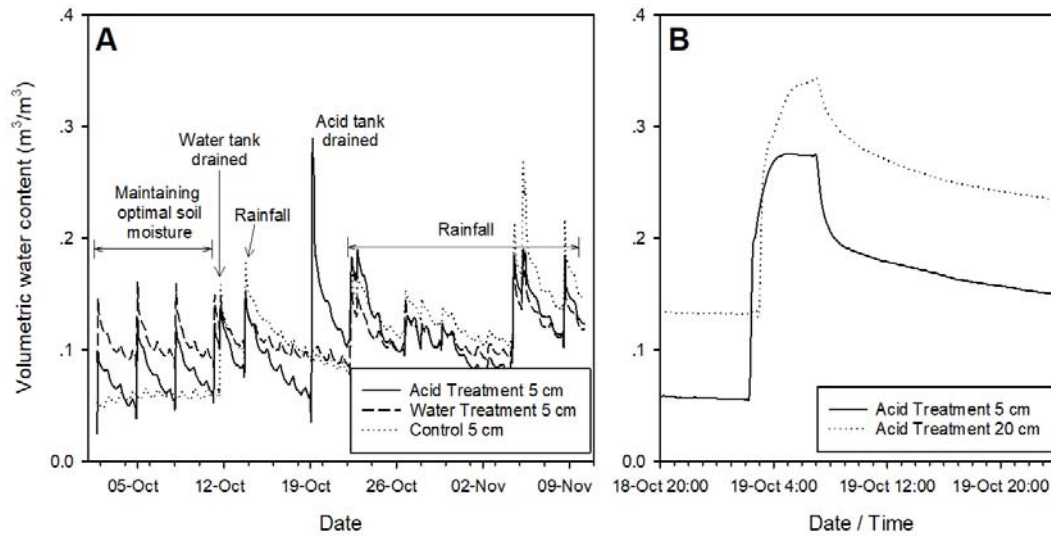


Figure 4.2. (A) Volumetric water content data from soil moisture probes buried at 5 cm depth in each of the three experimental plots. The period of 10 days over which the equipment was deployed successfully is followed by the water tank drainage event at 3:50 pm on the 11th October. Periods of natural rainfall are indicated, as is the acid tank drainage event. (B) Expanded view showing the volumetric water content of tailings in the acid treatment plot over the duration of the event that drained the acid tank. Saturated conditions are indicated by a period of approximately 5 hours in which volumetric water content does not increase.

On day 10 (11th October, 2015), the experiment was interrupted by the failure of the hose outlet from the water tank. Follow up fieldwork revealed the hose was pulled out, possibly by tension as a result of equipment being moved in the high winds that can occur at Woodsreef. This caused the water tank to drain, and the event is recorded as an increase in soil saturation in all plots (Fig. 4.2A), despite no rainfall having been recorded at nearby weather stations. Rainfall is first recorded in the region on the 13th October 2015, after which the tailings at the site of the field trial continued to dry. The control soil moisture probe, at 5 cm within the water plot, triggered the lower saturation alarm at 02:11 am on the 19th October 2015 (Fig. 4.2B), causing the pumps to turn on; however, since the water tank had already been drained, only the acid solution was delivered to the acid plot. The control soil moisture probe in the water treatment plot continued to

measure a reading below the minimum threshold, causing the pumps to continue running until the acid tank had been drained (approximately 900 L), which took just under 5 hours. The shallow (5 cm) soil moisture probe in the acidic plot recorded a maximum volumetric water content of $0.28 \text{ m}^3/\text{m}^3$, and remained saturated until 7:03 am on the same day. Pore water saturation was observed (i.e., a maximum volumetric water content of $0.34 \text{ m}^3/\text{m}^3$) to at least 20 cm depth within the acid plot, where the deepest sensor was located (Fig. 4.2B).

4.3.2. Mineralogical and geochemical response to treatment

Immediately after the first test of the equipment, a distinct rusted orange layer developed approximately 1–2 mm below the tailings surface in the acid plot. After completion of the experiments, the orange layer was found to be extensive across the acidic plot, at approximately 1 cm depth (Fig. 4.3). This layer was not observed in the water or control treatment plots. A sub sample of this material was analysed by XRD, but no additional phase could be identified (orange precipitate, Appendix 3: Table S3). The orange colour, and the presence of this phase at either trace abundance or as an X-ray amorphous phase, indicate that it is likely to be an Fe-oxide precipitate that has formed during neutralisation of the sulfuric acid treatment (as previously described by Power et al., 2010).

Aside from this visual observation, there does not appear to be a substantial difference between pre-experiment and post-experiment mineralogy (XRD, Fig. 4.4, Appendix 3: Table S3) and geochemistry data (Total C, Fig. 4.5, Appendix 3: Table S4). This may be due to the high natural heterogeneity of the tailings and uncertainty in mineralogical abundances introduced by Rietveld refinement, or an indication that the application of water and acid treatments during this experiment had no measureable effect on carbonate mineral abundance and the volume of trapped carbon within the tailings. As such, this

section discusses mineralogical and geochemical trends within the dataset as a whole, to provide a robust characterisation of the tailings, that is representative of passive carbon sequestration since mine closure in 1983.

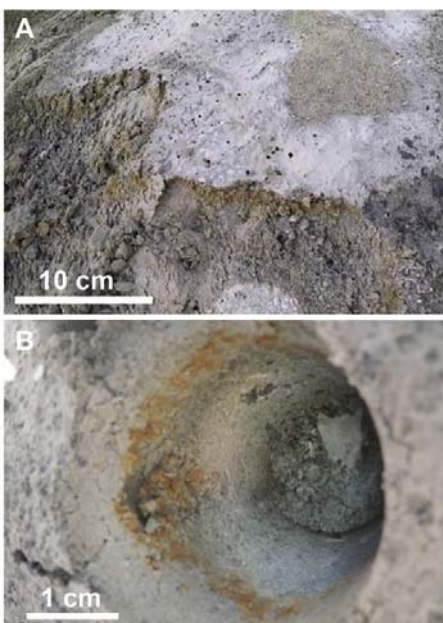


Figure 4.3. (A) Photographs of the rusted orange layer observed just below the surface of the acid plot after treatment. Bubbles are visible from the release of CO₂ from the dissolution of existing carbonate minerals. (B) Photograph of rusted orange layer within a core hole in the acid plot post-experiment.

The serpentine polymorphs [Mg₃Si₂O₅(OH)₄] lizardite, and to a lesser extent chrysotile, dominate the mineralogy of the tailings at approximately 90 wt. % (Table S3). Brucite appears to decrease gradually in abundance from approximately 1 wt. % at depth to <0.5 wt. % in surface crusts (Fig. 4, Table S3). Carbonate minerals present in the Woodsreef tailings include hydromagnesite [Mg₅(CO₃)₄(OH)₂·4H₂O], pyroaurite [Mg₆Fe₂(CO₃)(OH)₁₆·4H₂O] and calcite (CaCO₃). Pyroaurite and hydromagnesite are present at maximum abundance between 2 and 30 cm depth (up to 2.4 and 1.9 wt. % respectively; Fig. 4.4, Appendix 3: Table S3). The abundance of hydromagnesite decreases rapidly with increasing depth below the tailings surface; however, pyroaurite

persists at abundances between 1 and 2 wt. % to a depth of at least 1 m (the maximum depth sampled in this study; Fig. 4.4, Appendix 3: Table S3). In surface crusts (0–2 cm deep) in the acid and water treated plots, both hydromagnesite and pyroaurite are present at lower abundance than they are in the control plot (Fig. 4.4). Although pyroaurite may have been present in the serpentinite ore before mining, isotopic evidence in (Oskierski et al., 2013) suggests that pyroaurite contains modern atmospheric carbon, thus it is considered a host for atmospheric carbon in this study. Gangue carbonate minerals inherited from the ore are found at trace abundance: calcite is present at <0.8 wt. % and magnesite (MgCO_3) was not detected in XRD data from Woodsreef, although it has been reported in a tailings sample and in carbonate veins in wall rock at this site (Oskierski et al., 2013). Chlorite is identified occasionally in XRD patterns, and a broad, low intensity peak was detected at approximately $14^\circ 2\theta$ (Cu $K\alpha$) in three samples: Pre-Exp-C8 (0–2 cm), Acid-C3-6 (40–50 cm) and Control-C3-9 (80–90 cm). This low intensity peak is likely attributable to the presence of the hydrotalcite supergroup mineral, coalingite [$\text{Mg}_{10}\text{Fe}_2(\text{OH})_{24}(\text{CO}_3)\cdot 2\text{H}_2\text{O}$], a gangue mineral that has been previously identified in Woodsreef Mine tailings after density and gravimetric separation to improve detection of trace minerals (Kmetoni, 1984). Coalingite forms due to partial carbonation of brucite within veins containing serpentine, magnetite and brucite in the Woodsreef orebody (Glen and Butt, 1981). Owing to their presence near the detection limit in XRD patterns, it was not possible to include either chlorite or coalingite in stable Rietveld refinements. Instead, these trace phases were excluded from refinements and, where present, they will be included in the refined abundances of serpentine plus or minus amorphous content (Table S3).

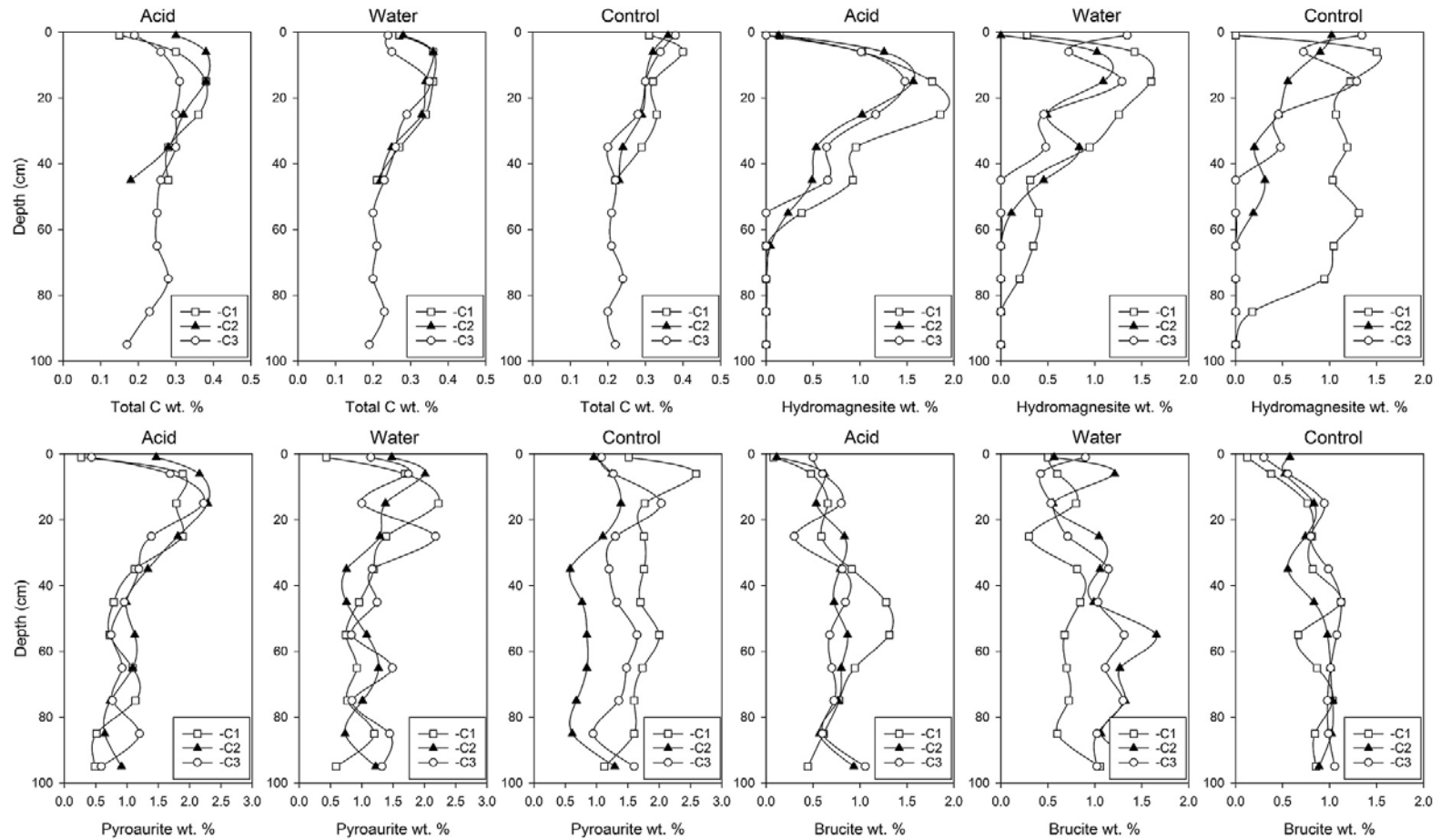


Figure 4.4. Total carbon, and refined mineral abundances for hydromagnesite, pyroaurite and brucite from XRD data, with depth in acid, water and control plots.

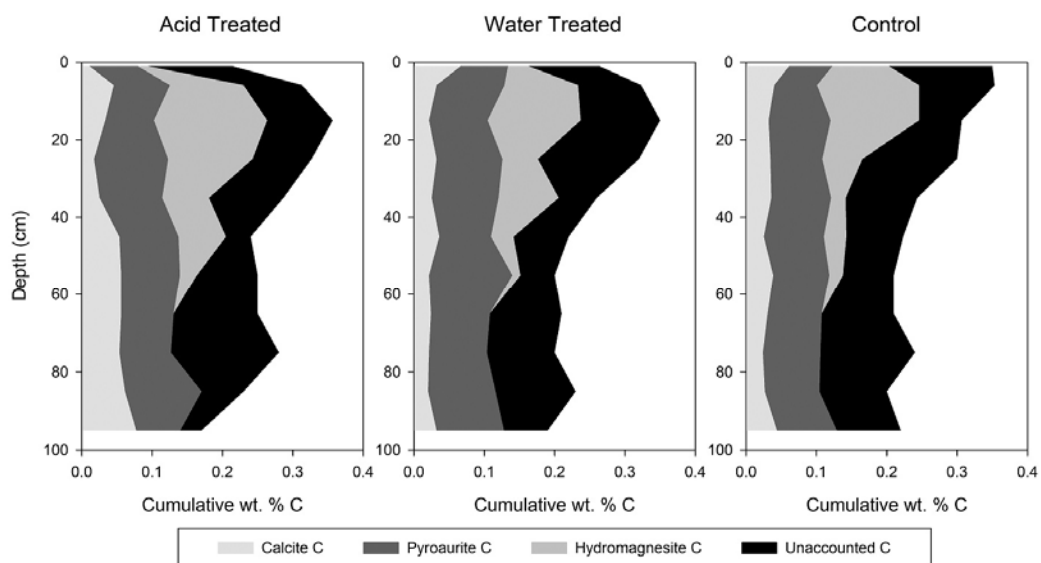


Figure 4.5. Cumulative carbon contributions for calcite, pyroaurite and hydromagnesite, calculated from median abundances (refined from XRD data) and median measured total carbon (from combustion analysis). The difference between the sum of mineral C contributions and total carbon is shaded in black as unaccounted carbon. Data points are centred at the median depth of each sample interval.

From the surface of the tailings to 20 cm depth, average total carbon content increases from approximately 0.20 to 0.35 wt. % in both acidic and water plots, whereas the control plot contains higher carbon at the surface (0.35 wt. %) and >0.3 wt. % carbon in the upper 20 cm (Fig. 4.4). Maximum total carbon in all plots occurs between 2 and 30 cm depth (up to 0.40 wt. % in Control-C1-1), and then decreases with depth below 30 cm to approximately 0.2 wt. % at 1 m (Fig. 4.4). Organic carbon contents in all analysed samples, collected both before and after experiments, are low (average 0.02 wt. %, maximum 0.03 wt. %, detection limit 0.01 wt. %). Total carbon measurements are higher than expected based on the refined abundances of carbonate minerals detected using XRD (Fig. 4.5). When the refined mineral abundances for calcite, pyroaurite and hydromagnesite are used to calculate their contributions to total C, a median of 47 %

relative (range: -2.3% to $+79.7\%$) of total carbon remains unaccounted for across all plots; Fig. 4.5, Appendix 3: Table S4).

Stable and radiogenic carbon data show what appears to be a mixing trend between modern atmospheric carbon, and bedrock carbonate for samples in Control-C3 at 2–10, 40–50 and 90–100 cm depth (Fig. 4.6). A purely modern atmospheric carbon source (during operation of the mine in 1972 – 1983 and following its closure) would give a $F^{14}\text{C}$ value of >1 , whereas bedrock carbon sourced from within the serpentinite orebody would have a $F^{14}\text{C}$ value of ≈ 0 . Here, $F^{14}\text{C}$ values decrease from 0.897 at 2–10 cm, to 0.828 at 40–50 cm, to 0.803 at 90–100 cm depth. This indicates a decreasing atmospheric signature with depth, although carbon is still predominantly from an atmospheric source at 1 m depth in Control-C3.

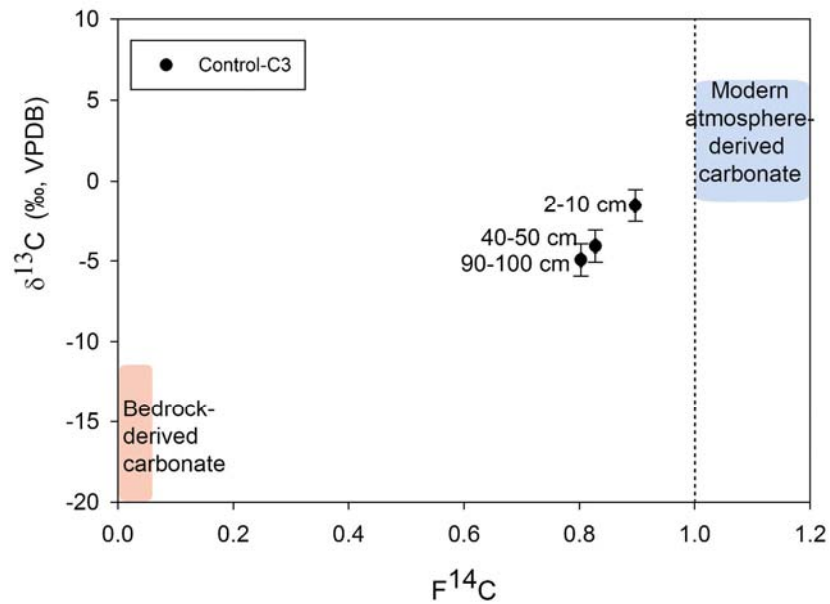


Figure 4.6. Plot of $\delta^{13}\text{C}$ versus $F^{14}\text{C}$ data for samples from the Control-C3 vertical profile, with shaded regions indicating values typical of bedrock-derived carbonate minerals (red) and atmosphere-derived carbonate minerals (blue) modified from Oskierski et al. (2013).

Mineralogical, geochemical and isotopic trends observed in this dataset (decreasing hydromagnesite and pyroaurite abundance, decreasing total carbon, and decreasing fraction of modern carbon with increasing depth) are consistent with XRD, total carbon, and isotopic data from a site-wide survey of passive mineral carbonation at Woodsreef Mine tailings (Turvey et al., in prep.a). Hydromagnesite is only detectable by XRD within the upper 40 cm of seven profiles (ranging from 30 cm to 120 cm depth) sampled across the Woodsreef tailings (Turvey et al., in prep.a). However, total carbon data indicate substantial carbon content persists to at least 1 m, and stable and radiogenic isotope data confirm an atmospheric carbon signature in samples from a depth of up to 1 m (Turvey et al., in prep.a). A white coating on grain surfaces was visible by eye in the deepest sample collected in this site-wide survey (15WRDC5-12, 110–120 cm depth; Turvey et al., in prep.a) even though no hydrated Mg-carbonate minerals were identified by XRD. SEM micrographs collected on this sample as part of the current study show that this phase consists of a mixture of flaky and euhedral platelets (Fig 4.7A–B) that contain Mg, C and O, in abundances approximate to hydromagnesite composition (approximately 8–13 wt. % C measured using EDS). The euhedral platelets are consistent with the morphology taken by hydromagnesite and the flaky, ill-formed ones are more reminiscent of poorly ordered and amorphous hydrated Mg-carbonate phases (Davies and Bubela, 1973; Harrison et al. 2015, 2016). A subsample enriched in this white material was analysed by XRD, revealing characteristic hydromagnesite peaks and substantial amorphous content (Fig. 4.7C).

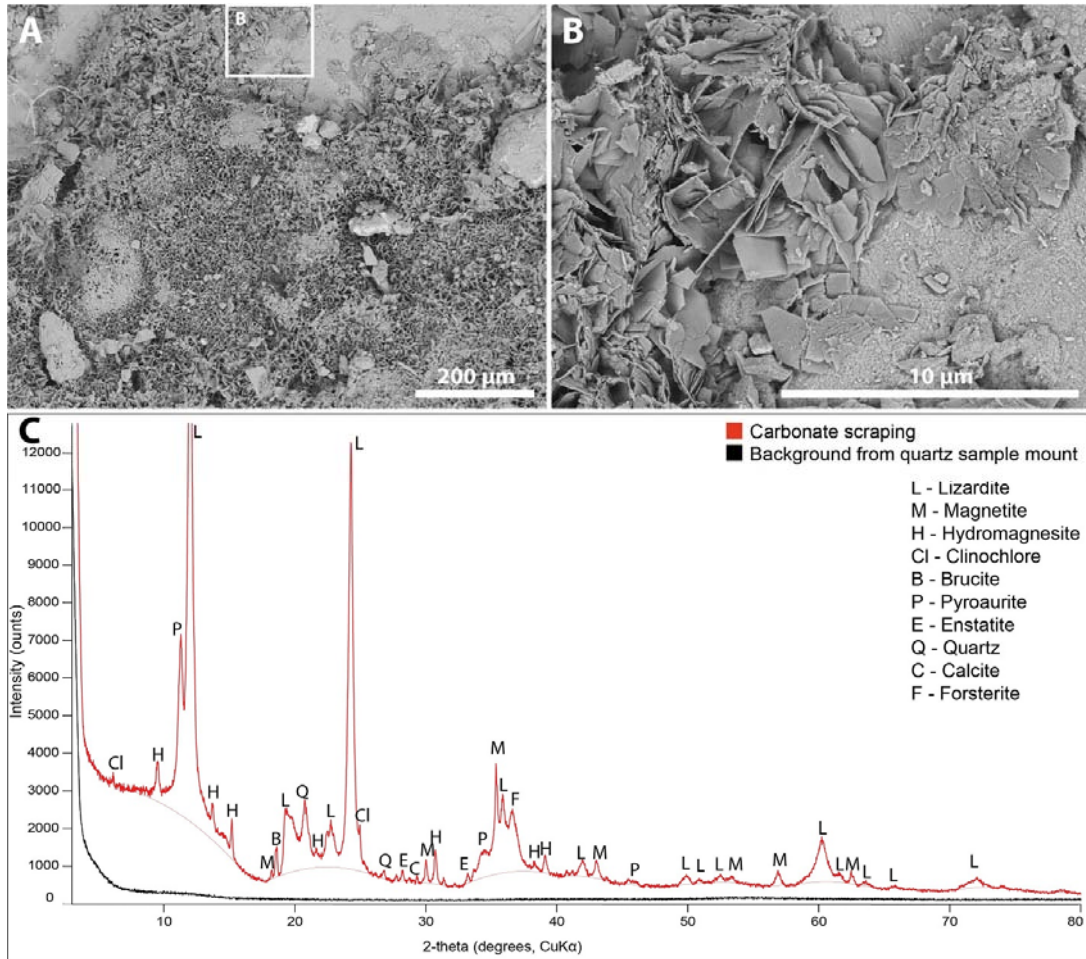


Figure 4.7. (A) Backscattered electron (BSE) micrograph of the flaky carbonate precipitate on the surface of a serpentine grain in sample 15WRDC5-12 (sample described by Turvey et al., in prep.a). (B) Enlarged view of euhedral platelets characteristic of hydromagnesite. (C) XRD pattern of white material subsampled from a grain surface, showing the presence of hydromagnesite in the white material. A background pattern was taken of the zero-background quartz mount (in black) showing that the broad ‘humps’ in the carbonate-bearing sample indicate X-ray amorphous material.

This ‘X-ray amorphous’ carbonate phase is likely the cause (along with the characteristic underestimation of minor phases in Rietveld refinements) of the discrepancy in tailings carbon content as determined by total carbon measurements and calculations from mineralogy (XRD). Turvey et al., (in prep.a) suggest that this Mg-carbonate phase is present within every depth profile analysed from the Woodsreef tailings. If we assume that all of the unaccounted carbon within the dataset from the experimental site is present

as an X-ray amorphous Mg-carbonate phase with a hydromagnesite-like composition (Fig. 4.6), we can estimate an ‘expected hydromagnesite’ mineral abundance. This is an estimate of total hydromagnesite, including the refined hydromagnesite abundance (Appendix 3: Table S3), plus a stoichiometrically predicted abundance for X-ray amorphous ‘hydromagnesite’, calculated from the unaccounted carbon content [carbon content remaining after subtraction of the carbon contributions of known carbonate minerals (hydromagnesite, pyroaurite and calcite), and organic carbon, from total carbon data; Appendix 3: Table S4]. Since hydromagnesite is stoichiometrically 10.27 wt. % carbon, calculated unaccounted carbon content (Appendix 3: Table S4) can be divided by this fraction, giving an estimate of X-ray amorphous ‘hydromagnesite’ abundance, in wt. %, which is then added to refined hydromagnesite abundance to give ‘expected hydromagnesite’ (Appendix 3: Table S4). Expected hydromagnesite abundances range from 0.9 to 2.9 wt. % (Appendix 3: Table S4), whereas refined hydromagnesite abundances from XRD data range from 0 to 1.9 wt. % (Appendix 3: Table S3). Across all samples, an average of 32 % of expected hydromagnesite is accounted for by XRD data (although this ranges from 0 to 104 %; Appendix 3: Table S4).

4.3.3. Calculating neutralising capacity

Carbonate neutralising potential is calculated to be 0.6 mol H⁺/kg, or 143 mol H⁺ in the upper 20 cm (0.2 m³) of the experimental plots (based on average mineralogy from the 0–20 cm interval of pre-experiment cores, using Eq. 1). The pre-existing gangue carbonate minerals and carbonate-bearing alteration phases in the upper 20 cm of the 1-m² acid plot therefore had the capacity to neutralise 90 % of the total 1000 L acid dose applied. When silicate minerals are taken into account in addition to the carbonate phases (NP calculated using Eq. 2), neutralising potential increases to 3.3 mol H⁺/kg, or 867 mol H⁺ in the upper

0.2 m³, a neutralising potential more than five times the acid dose in the 1000 L H₂SO₄ solution. The majority (75 %) of the total neutralising potential is attributed to serpentine.

4.4. Discussion

4.4.1. Effect of the experiment on tailings geochemistry and mineralogy

The short duration of the experiment, the high degree of natural heterogeneity within the tailings, and uncertainties in quantification of key minerals that are present at low abundance (<5 wt. %), make it difficult to accurately quantify small differences in the effects of the acidic or water treatments on the geochemistry or mineralogy of the Woodsreef tailings. Significant changes to geochemistry and mineralogy resulting from the acidic and water treatments appear to be restricted to the 0–2 cm interval in the acidic plot. Application of the acidic treatment caused dissolution of existing carbonate minerals within the 0–2 cm interval (Fig. 4.4) and precipitation of Fe-(hydr)oxides at the neutralisation front (Fig. 4.3). Although the abundances of hydromagnesite and total carbon also appear to be lower in the 0–2 cm interval in the water plot following the experiment, as compared to the control site (Fig. 4.4), lower abundances of carbonate minerals were also reported in surface crusts collected from the water plot before the experiment (Appendix 3: Table S3). Therefore, this can likely be explained by natural heterogeneity between the sites chosen for experimental plots.

To date, this is the most detailed and fine scaled set of quantitative mineralogical and geochemical data ever reported for a site undergoing passive mineral carbonation. While no single site can be considered representative of the tailings as a whole, the high spatial resolution of this dataset allows differentiation between natural heterogeneity (as described above), and consistent geochemical and mineralogical trends on the scale from

10s cm to metres, in both vertical and horizontal dimensions. In general, geochemical and mineralogical trends down profile (from the surface to 1 m depth) are similar between the control, water and acid plots, and are consistent with depth profiles from a site-wide survey (Turvey et al., in prep.a). Therefore our data as a whole can provide important new and detailed insights into the geochemistry and mineralogy of passive carbon mineralisation at the experimental site, which will be useful for interpreting coarser-scale geochemical and mineralogical datasets [such as the site-wide survey conducted by Turvey et al. (in prep.a)]. As such, the following discussion will focus on the geochemical and mineralogical trends identified in the dataset, suggest new directions for future development of field-portable treatments, and propose a new methodology incorporating both mineralogical and geochemical data for more accurate accounting of mineral carbonation of mine tailings.

4.4.2. Lessons learned for experimental design and deployment of future field trials

Although the experiment was interrupted, we have demonstrated the feasibility of deploying a readily scalable, independently operating and inexpensive watering system for maintaining pore water saturation levels within a pre-determined, optimum range for carbonation of mineral wastes. Deployment at a remote locality, and the occupational health and safety restrictions associated with the site (due to the asbestos hazard) presented serious challenges for the experimental design and set up of the experiment, and prohibited on-site monitoring for the full duration of the experiment. Ideally, trials should take place at currently operating mines, in collaboration with industry (i.e., Lechat et al., 2016; Gras et al., 2017), such that equipment can be monitored and any faults can be readily fixed; although in this case, the emptying of the tank occurred quickly (within approximately 5 hours); therefore, improvements should also be made to the experimental

design, such as ensuring all components of the experimental apparatus are anchored carefully to withstand disturbances such as severe weather.

From 19th October 2015 (18 days into the field trial), this experiment is best described as a single dose, acid leach experiment. Although the water spill (11th October) affected all plots, the magnitude of pore water saturation measured (maximum $\sim 0.2 \text{ m}^3/\text{m}^3$ volumetric water content) is comparable to rainfall events measured throughout the experiment, therefore the chemistry of the water is not expected to have caused observable changes to the geochemistry or mineralogy of the tailings as a result of this spill. The use of acid leaching was intended to target dissolution of Mg-silicate and hydroxide minerals, such as the serpentine polymorphs, forsterite and brucite. However, if acid is expended in the dissolution of gangue or secondary carbonate minerals, which causes the release of stored CO_2 and consumes acid, less acid will remain for silicate and hydroxide mineral dissolution.

Ideally, acid treatments should be applied to fresh tailings with limited gangue or secondary carbonate mineral content. At Woodsreef Mine, the tailings have been undergoing passive mineral carbonation for over 30 years, and have developed a carbonate-rich cement at the surface (Oskierski et al., 2013). Therefore, at historical mine sites like Woodsreef, application of acidic treatments may be more effective if applied at depth within the tailings, where carbonate alteration minerals, such as hydromagnesite and pyroaurite, are typically less abundant (Fig. 4.5; Oskierski et al., 2013; Turvey et al., in prep.(a); Wilson et al., 2014). This could be achieved via subsurface irrigation, a developing technology that is beginning to be deployed in low permeability heap leach pads for gold and copper recovery (Ghorbani et al., 2016; Rucker et al., 2017). This typically involves injection of solution via wells within a heap leach pad. If implemented

at Woodsreef or another ultramafic mine, acid will likely be neutralised quickly by silicate mineral and brucite dissolution (and any existing carbonate minerals), and the resulting fluids will be alkaline and rich in Mg, provided neutralising potential is not exceeded (as in McCutcheon et al., 2015, 2016, 2017; Power et al., 2010).

Capillary rise, caused by evaporation, is a key process driving Mg-carbonate mineral formation at Woodsreef and other ultramafic mines, and is expected to draw Mg-rich fluids towards the surface, where they may react with atmospheric CO₂, accumulating Mg-carbonate precipitates in thick efflorescences and cements (Wilson et al., 2009). Therefore, if acidic treatments were introduced at depth within a tailings storage facility, carbonate precipitation would be expected to continue to occur at the surface and in the shallow tailings, via reaction with CO₂ at the tailings–atmosphere interface, thereby allowing dissolution of predominantly silicate minerals and brucite to continue in the interior of the tailings pile. Development of a thick carbonated crust could help stabilise hazardous asbestiform minerals, reducing off-site transport of tailings as windblown dust and contamination of nearby waterways by fibres (McCutcheon et al., 2017, and this experiment). Since loss of water during runoff is a practical issue for treatments applied at the tailings surface (McCutcheon et al., 2017), subsurface irrigation may also allow for better management of water resources.

4.4.3. Rapid neutralisation of acid and precipitation of carbonate minerals

Neutralisation potential calculations (based on both measured total carbon and whole rock neutralising potential — including contributions from silicate, hydroxide and inert minerals) indicate the total H⁺ in the 1000 L dose of acidified creek water (of which approximately 900 L was applied in a single dose) could be neutralised by the material contained in the upper 4 cm of the 1-m² acid treatment plot. Incomplete mineral

dissolution, or development of preferential flow pathways could have transported acidic solutions to greater depths; however, given that a large amount of runoff was observed as a result of poor infiltration during watering tests, the volume of infiltrated solution was likely much less than 1000 L. Consequently, neutralisation likely occurred at an even shallower depth but over a much larger surface area. If treatment had continued as planned, with periodic doses of solution delivered over the course of several months, it is likely that the depth of the observed neutralisation front [as indicated by the Fe-(hydr)oxide layer] would have approached 4 cm depth. However, it should be noted that re-precipitation of carbonate minerals near the surface of the tailings could potentially inhibit progression of the neutralisation front, by repeatedly consuming acid with each dose. An understanding of neutralising potential, and the rates of dissolution and precipitation reactions of both target gangue minerals and secondary weathering products, is critical to predict the success and rate of CO₂ trapping via acid leaching treatments in mine tailings.

The observation of a rusted-orange layer approximately 1 cm below the surface of the tailings in the acid plot indicates precipitation of a secondary mineral phase at a geochemically distinct horizon. This rusted-orange layer was also observed in acid treatment of Woodsreef tailings as part of geomicrobial carbonation trials in the laboratory (McCutcheon et al., 2016) and the field (McCutcheon et al., 2017). Scanning electron microscopy and energy dispersive X-ray spectroscopy results on orange samples from these experiments indicate they are rich in pyroaurite (McCutcheon et al., 2017). However, our more recent XRD analysis of the orange precipitate sample does not show an elevated abundance of pyroaurite (Appendix 3: Table S3). As such, we suggest the orange colouration results from the presence of Fe-(hydr)oxides, which may be either X-ray amorphous, or present at an abundance below the detection limit of our XRD analysis.

This result has been confirmed using laboratory leaching experiments in Chapter 5, and is consistent with observations and SEM-EDS data from chrysotile acid leaching experiments reported by Power et al. (2010).

The source of the iron in the Fe-(hydr)oxide precipitate may be dissolution of magnetite, chrysotile, hydromagnesite, pyroaurite and/or brucite at the surface of the tailings, all of which are known to incorporate Fe into their crystal structures (Grguric, 2003; Wicks and O'Hanley, 1988; Hamilton et al., in review/Chapter 3). Under contact with acidic solution, dissolution of these minerals mobilises Fe, which should subsequently re-precipitate once the solution is neutralised, likely as Fe-(hydr)oxide phases (Azdarpour et al., 2015; Power et al., 2010; Teir et al., 2007a). The depth of the orange layer is within our estimate for the depth of a shallow neutralisation horizon (less than 4 cm below the surface of the tailings); therefore, it is likely that precipitation of this orange layer provides a visual representation of the neutralisation front. Fe-(hydr)oxide phases are known to have a passivating effect on grains of feedstock minerals, which can limit the rate of mineral carbonation (Assima et al., 2012), but they are also known to provide an effective sink for potentially hazardous trace metals that are mobilised during acid treatments used to enhance carbonation (Hamilton et al., 2016; Power et al., 2010; Tier et al., 2007).

4.4.4. Resilience and regeneration of Mg-carbonate cements

Despite the large dose of acidic water that was delivered to the acid plot (900 L of 0.08 M H₂SO₄), the measured abundances of elemental carbon and of carbonate minerals present in shallow tailings (<1 m) and crust samples (0–2 cm) in the acid, water and control plots are comparable. Although hydromagnesite is not detected within the 0–2 cm interval of the acid treated plot, total carbon persists at >0.15 wt. %, whereas total carbon is measured between 0.2 and 0.4 wt. % within surface crusts collected from the water and

control plots, respectively. This may be attributed to the presence of both pyroaurite and calcite, which are still detectable in surface crusts collected from the acid plot (using XRD, Appendix 3: Table S3). If neutralisation occurred at a depth of ~1 cm, as indicated by the orange rusted horizon, it is also likely that the 2-cm thick sample interval used at the surface of the plots includes low abundances of hydromagnesite that is present at depths below the neutralisation horizon (estimated at 1 cm). Thus, the use of a 2-cm sampling interval may result in hydromagnesite abundances below the detection limits of our XRD analyses (estimated on the order of 0.5 wt. % after Wilson et al., 2014). Alternatively, it is also possible that carbonate minerals may have re-precipitated within the acid plot once the acidified creek water was neutralised. Neutralised fluids would likely be alkaline and rich in Mg following dissolution of Mg-carbonates, and possibly brucite and serpentine minerals (McCutcheon et al., 2015, 2016, 2017; Power et al., 2010). Although much of this fluid is expected to have been lost as runoff from the acid plot, the fluid that ingressed into pore spaces within the acid plot is likely to have been transported back to the surface via evaporation-induced capillary rise (McCutcheon et al., 2017). Evaporation may induce saturation and precipitation of hydromagnesite (Wilson et al., 2009), or precipitation may be aided by the presence of native alkalinity generating cyanobacteria (McCutcheon et al., 2017). Endolithic cyanobacteria do occur within the shallow tailings at Woodsreef; however, measured organic carbon contents indicate microbial populations are low (< 0.03 wt. % organic C, Appendix 3: Table S4). In any case, the results of our experiment have important implications for the long-term stability of carbon stored in metastable Mg-carbonate minerals, such as hydromagnesite, particularly in terms of the potential risk of CO₂ release during exposure to acid rain. Magnesite is predicted to be resilient to acid rain (Allen and Brent, 2010); however, the hydrated Mg-carbonate minerals are more soluble than magnesite at low pH

(Königsberger et al., 1999). Here, we find persistence of hydromagnesite in shallow samples (>2 cm depth) that have been exposed to very low pH solutions (pH \approx 1), at which hydromagnesite is expected to dissolve rapidly (Königsberger et al., 1999). It appears the high neutralisation potential of the tailings provides protection to carbon sequestered in Mg-carbonate minerals below the neutralisation horizon (at approximately 1 cm depth, based on the depth of the orange precipitate). Therefore, accidental exposure to a spill of acidic water — or acid rain — does not appear to affect the bulk mineralogy or geochemistry of the tailings, at least at depths below 2 cm under the conditions of our experiment.

Maximum total carbon content (up to 0.4 wt. %), and hydromagnesite and pyroaurite mineral abundance (up to 1.9 and 2.6 wt. % respectively), occurs between 2 and 30 cm depth in all plots, although in the control plot, the zone of maximum total carbon and carbonate mineral abundance also includes the 0–2 cm interval. Dissolution of existing carbonate minerals was observed in the field, and was expected as a result of acid treatments in the 0–2 cm interval of the acid plot, however, the lower average total carbon and carbonate mineral abundance at 0–2 cm in the water treated plot could be explained by inter-site heterogeneity, as explained above (in section 4.4.1). On the other hand, a similar trend is reported by McCutcheon et al. (2017), indicating that the environment below 2 cm depth may be a more favourable for carbonate mineral precipitation. At this depth, tailings are protected from runoff while still being close enough to the surface to maintain a sufficient supply of CO₂ to promote carbonation reactions. Total carbon abundances in all plots decrease with depth below 30 cm to approximately 0.2 wt. % at 1 m. Total carbon data appear relatively consistent between cores, although our dataset is more sparse below 50 cm depth, comprising results only for samples from the third core in each plot (Acid-C3, Water-C3, Control-C3; Fig. 4.5). The gradual decrease in the

abundance of carbon with depth below 30 cm is likely a reflection of CO₂ limitation (i.e., limited ingress of atmospheric CO₂ into pore spaces) at depth within the tailings storage facility at Woodsreef (McCutcheon et al., 2016, 2017; Turvey et al., 2017).

Radiogenic carbon and stable carbon isotope data reveal a mixing trend between modern atmospheric carbon, and bedrock carbonate minerals in samples from 2–10, 40–50 and 90–100 cm depth in core Control-C3 (Fig. 4.6). Values of F¹⁴C of 0.897 at 2–10 cm depth, and 0.803 at 1 m depth, provide evidence that although availability of atmospheric carbon is increasingly limited with depth, sequestration of atmospheric CO₂ still takes place to a depth of at least 1 m within the tailings (Fig. 6). In comparison, Oskierski et al. (2013) found F¹⁴C values between 0.85 and 1.03 in surface cements and horizontal crusts, and lower F¹⁴C values (between 0.26 and 0.62) in deep cements (70–120 cm depth) and bedrock carbonates (magnesite and calcite). δ¹³C values from Control-C3 plot within the range of surface cements and horizontal crusts (-6.7 to -2.0 ‰) reported in Oskierski et al. (2013).

We also see the effects of CO₂ limitation in horizontal cores taken from the vertical face, with hydromagnesite abundance decreasing inwards from the exposed face (from 0.6–0.7 wt. % at 0–2 cm depth, to 0–0.4 wt. % at 30–40 cm depth; Fig 4.8). This explains why C1 cores which were closest to the vertical face of each of the three plots (Fig. 1C) generally have higher hydromagnesite abundance (average of 1.3–1.6 wt. % over the 2–30 cm zone) and carbon content (average of 0.35 wt. % C in the 2–30 cm zone), whereas cores furthest from the vertical face (C3) generally have lower hydromagnesite (averages of 0.8–1.2 wt. %) and elemental C contents (0.29–0.31 wt. %) over the same depth range (Fig. 4.4). Hydromagnesite also persists to greater depth in cores closer to the vertical face, for example in Control-C1, hydromagnesite is detected in XRD data at up to 90 cm

depth, whereas in Control-C3 hydromagnesite is not detected below 30 cm depth (Fig. 4.4, Appendix 3: Table S3). This provides further evidence that CO₂ limitation increases with distance from the surface of both horizontal and vertical tailings surfaces (Fig 4.4, 4.8, Appendix 3: Table S3, S4). Constructing or reworking ultramafic tailings into terraces could be a relatively simple means to increase the surface area of the tailings pile to promote CO₂ sequestration.

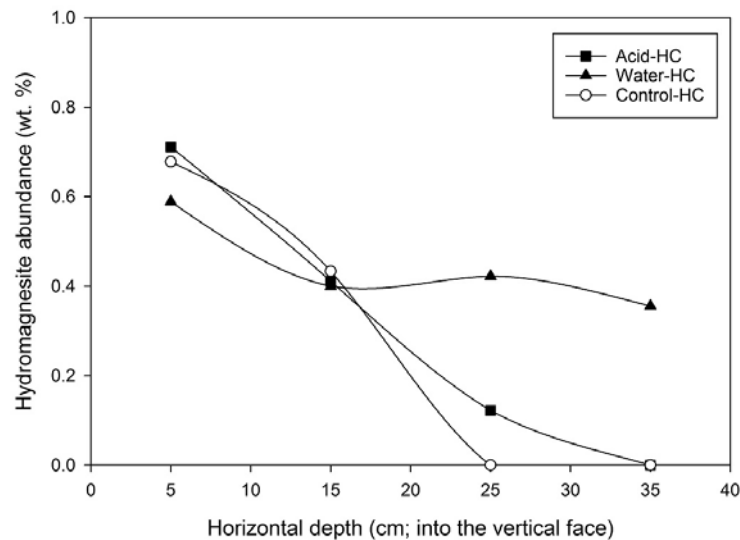


Figure 4.8. Hydromagnesite abundance with depth along horizontal profiles taken inwards from the vertical face of the experimental area (Fig. 1c).

Direct reaction of ultramafic mine tailings with a concentrated CO₂ source, such as the flue gas generated by an onsite diesel power plant, has been suggested as a potential means to address CO₂ limitation and accelerate CO₂ sequestration *in situ* within tailings storage facilities (Power et al., 2014). Although this strategy is not feasible at a derelict mine such as Woodsreef, it may be a low-cost and effective way to increase CO₂ sequestration at currently operating mines that have onsite power generation, such as Mt Keith Mine and the diamond mines in subarctic Canada (Power et al., 2014).

4.4.5. Accurate carbon accounting requires both mineralogical and elemental abundance data

Previous studies of mineral carbonation at Woodsreef report high abundances of hydromagnesite within surficial crusts (up to 14.6 wt. % in Oskierski et al., 2013, and up to 12.5 wt. % in Turvey et al., 2017, in samples from 0–2 cm depth). One deeper sample (upper 30 cm) was analysed by Turvey et al. (2017) and three samples from 70–120 cm depth were analysed by Oskierski et al. (2013). These four deeper samples contained pyroaurite, but no hydromagnesite, thus hydrated Mg-carbonate formation was only considered to occur within the 0–2 cm horizon (Oskierski, 2013; Turvey et al., 2017). As such, previous estimates of passive CO₂ sequestration rates at Woodsreef may be underestimated. These estimates were hampered by the difficulty of sampling coarse, chrysotile-bearing tailings. New sampling methods, developed as part of this study and those of McCutcheon et al. (2017) and Turvey et al. (in prep.a), have improved the size, resolution and robustness of data collection from this setting. McCutcheon et al. (2017) excavated samples from intervals spanning 0–2 cm, 2–4 cm, 4–17 cm, 17–32 cm and 32–47 cm within the Woodsreef tailings, based on visual transitions in grain size within 1-m² test plots. They found that the maximum hydromagnesite abundance (up to 1.9 wt. %) occurred between 2 and 17 cm depth. Hydromagnesite was not detected using XRD in the 0–2 cm intervals in any plot, including the control, and was also absent below 30 cm depth in three out of four plots (McCutcheon et al., 2017).

In the current study, we employed gravel corers, which allowed us to sample a known volume of tailings, to measure bulk density and porosity to 30 cm depth. Following gravel coring, we continued to excavate profiles below each core with shovels to permit sampling to a depth of 1 m. Analysis of our pre- and post-experiment samples reveals a

maximum carbonate mineral abundance between 2 and 30 cm depth. We used two approaches for carbon accounting in this study: (1) direct measurements of the total carbon content in tailings samples by combustion analysis and (2) calculation of total inorganic carbon inferred from stoichiometry using quantitative XRD. Our results reveal that more inorganic carbon is stored in the tailings than can be accounted for by refined abundances of hydromagnesite, pyroaurite and calcite that were measured using XRD methods (Fig. 4.5). This discrepancy becomes particularly important with increasing depth, as hydromagnesite abundance decreases below 30 cm depth (from a maximum of 1.9 wt. % between 2–30 cm depth), and is absent from 6 out of 8 of the cores analyses by 60 cm depth, while total carbon decreases only slightly (from approximately 0.3–0.4 wt. % between 2–30 cm depth) and persists at approximately 0.2 wt. % at 1 m depth in all plots (Figs. 4.4, 4.5).

The modal abundances of trace minerals (<3.5 wt.%), as estimated from Rietveld refinement of XRD data, are typically subject to high relative errors including in samples containing serpentine minerals and other poorly ordered phases [80 % relative error is typical for trace minerals (<3.5 wt.%); Wilson et al., 2006, 2009b; Turvey et al., 2017]. Hydromagnesite, brucite and pyroaurite are all systematically underestimated in Rietveld refinements due to limitations of the fundamental parameters approach, preferred orientation corrections, and overlap of Pawley phase peaks (used to model the peak profile for serpentine minerals in this study) with peaks of minor phases (Turvey et al., in prep.b; Wilson et al., 2006). As such, underestimation of carbonate phases likely explains much of this discrepancy between total carbon abundances and calculated carbon content using refined mineral abundances from XRD. Coalingite, which is qualitatively detected at trace abundance in only three samples collected in the course of this study (Appendix 3: Table S3), may account for some carbon; however, given the low C content of this

mineral (1.4 wt. % C), an average of 9.3 wt. % coalingite would be required to account for the total discrepancy.

Hydrated Mg-carbonate minerals are known to precipitate as 'X-ray amorphous' forms in geochemically similar systems, resulting in discrepancies between total elemental carbon and crystallographic accounts for CO₂ sequestration (Harrison et al., 2015). Therefore, it is likely that the unaccounted carbon observed here (average of 47 wt. % total carbon across all plots, Fig. 4.5, Appendix 3: Table. S4), is present as a similar amorphous Mg-carbonate phase. Figure 4.7 provides evidence for the presence of an X-ray amorphous Mg-carbonate phase at Woodsreef Mine that has a similar composition to that of hydromagnesite and which is consistent with observations of X-ray amorphous Mg-carbonate in laboratory carbonation experiments (Harrison et al., 2015).

An internal standard of a well crystallised phase, such as the fluorite employed here, can be used to account for amorphous content in a sample (Bish and Howard, 1988), but here we have used the internal standard to account for the abundance of serpentine minerals using the structureless fitting procedure of Wilson et al. (2006). As such, the abundance of the X-ray amorphous component is incorporated in the reported abundance for serpentine minerals in this study (Table S3).

Underestimates of carbonate mineral abundances from XRD data lead to underestimation of CO₂ sequestration rates in ultramafic materials if carbon sequestration rates are calculated from XRD data alone. For example, Table 4.1 shows carbon sequestration calculations using average mineral abundances determined by XRD, using the average mineralogy of samples from cores Pre-Exp-C1, -C3, -C5, and Acid-C3, Water-C3 and Control-C3, which are furthest from the vertical face, and are therefore more likely to be representative of the tailings pile as a whole. Note that the 0–2 cm interval of core Acid-

C3 has been excluded from these calculations because it appears to have been affected by the experimental treatment (indicated by visual observation of carbonate mineral dissolution and formation of a rusted horizon, and the absence of carbonate minerals in XRD data from the 0–2 cm zone of the acid plot). Using average mineralogy of the above listed cores, secondary carbon-bearing minerals (hydromagnesite and pyroaurite) in the 0–2 cm zone are estimated to contain 0.04 kg C/m², the 2–30 cm interval contains 0.5 kg C/m², and 30–100 cm interval contains 0.3 kg C/m². In total, XRD data from across the experimental site indicates that the upper 1 m of the Woodsreef tailings contains 0.9 kg C/m², or 3.1 kg CO₂/m², within hydromagnesite and pyroaurite (Table 4.1). This represents a minimum estimate for carbon sequestration, since hydromagnesite and pyroaurite are both systematically underestimated by Rietveld refinement of XRD data for serpentinite ore (Turvey et al., 2017; Wilson et al., 2006), and because we assume that calcite does not contain any atmospheric carbon, as it is present as a gangue mineral at Woodsreef Mine (Oskierski et al., 2013). Calcite is observed as scalenohedral crystals nucleated on the surface of milled serpentine grains at up to 120 cm depth in the Woodsreef tailings (Appendix 3: Fig. S3), which indicates that calcite undergoes dissolution and re-precipitation within the tailings. At Cassiar Chrysotile Mine in Canada, dissolution and re-precipitation of calcite imparts a mixed atmospheric–bedrock carbon signature, although recycled Ca-carbonate minerals are commonly less enriched in ¹⁴C than Mg-carbonate minerals that have an atmospheric source for CO₂ (Wilson et al., 2009). However, during this recycling, replacement of bedrock carbonate with atmospheric carbonate does not lead to a net increase in mineralised carbon, therefore calcite is not considered to contribute to carbon sequestration potential at Woodsreef Mine.

To calculate a passive carbon sequestration rate for Woodsreef Mine from total carbon data, we again use data from core samples furthest from the vertical face across all plots (Pre-Exp C1, -C3, -C5, and Acid-C3, Water-C3 and Control-C3 cores, excluding sample Acid-C3-0). Average inorganic carbon abundance is calculated from the average of measured total carbon data across these samples, minus average organic carbon content (0.02 wt. % C). Average total inorganic carbon within the upper 1 m of the Woodsreef Mine tailings is 3.8 kg C/m² (0–2 cm: 0.1 kg C/m², 2–30 cm: 1.3 kg C/m², 30–100 cm: 2.4 kg C/m²) or 13.8 kg CO₂/m² (Table 4.1). After subtracting the contribution of C from gangue calcite in the tailings (0.6 kg C/m³, the average abundance from XRD), this estimate is refined to 3.2 kg C/m², or 11.7 kg CO₂/m² (Table 4.1). This estimate is nearly four times the calculated amount of sequestered CO₂ that is calculated using XRD data alone, likely due to the combined effects of underestimation of hydromagnesite and pyroaurite with the Rietveld method, and the presence of X-ray amorphous Mg-carbonate phase.

When used alongside stable and radiogenic isotope data, crystallographic data obtained with XRD are crucial for distinguishing between primary carbonate minerals, such as magnesite, dolomite and calcite, and secondary carbonates minerals, such as nesquehonite and hydromagnesite, in serpentine-rich tailings (Wilson et al., 2009). Although gangue carbonate minerals at Woodsreef are present at very low abundance (i.e., calcite, magnesite and coalingite are present at <1 wt. %), other sites, such as the Mount Keith Mine, can contain >10 wt. % of gangue carbonate minerals such as magnesite, dolomite, calcite and various carbon-bearing hydrotalcite minerals of hydrothermal origin (Wilson et al., 2014). Quantification of these phases using XRD allows the contributions of these gangue minerals to be estimated and subtracted from total carbon data, giving the carbon content within secondary carbonate minerals and X-ray amorphous phases. However,

Rietveld refinement error, which is difficult to quantify for a field sample, may be introduced into this calculation as a result of subtracting carbon contributions from refined gangue mineral abundances. In this case, although calcite is present at trace abundance (<0.8 wt. %), its characteristic peaks are well resolved in XRD patterns, therefore error introduced from refinements is likely to be lower than for hydromagnesite and pyroaurite.

CO₂ sequestration rates are expected to vary across the tailings site due to heterogeneity in mineralogy and hydrologic conditions. Therefore, the CO₂ sequestration rate calculated for the ($\approx 5 \text{ m}^2$) experimental site should not be considered representative of the Woodsreef Mine tailings as a whole. Instead, the fine-scale sampling conducted in this study provides a detailed understanding of geochemical and mineralogical trends at a local scale, and provides a model for more comprehensive accounting of carbon sequestration that can be used to assess CO₂ sequestration rates at the landscape-scale in the future (i.e., Turvey et al. in prep.a).

Given that atmospheric CO₂ is sequestered to at least 1 m depth (Fig. 4.6) within Woodsreef tailings, these estimates from total carbon data still represent a minimum amount of CO₂ sequestered at the Woodsreef Mine site. Atmospheric CO₂ has been sequestered over a period of 32 years (the time since mine closure in 1983, and sampling in 2015), giving an estimated rate of 119 g C/m²/y for the upper 1 m of the tailings storage facility at Woodseef (based on conservative total C data, after subtracting calcite C). This rate is three orders of magnitude greater than the background rates measured for silicate weathering in the nearby Victorian Alps, which range between 0.15 and 0.47 g C/m²/y (Hagedorn and Cartwright, 2009).

Table 4.1. Carbon accounting using XRD data and total elemental carbon data.

			Carbon accounting using refined mineral abundances from XRD data										Carbon accounting using total C data		
Depth zone	Volume	Tailings mass*	Calcite abundance	Calcite mass	C in Calcite	Hydromag-nesite abundance	Hydrom-agnesite mass	C in Hydrom-agnesite	Pyroaurite abundance	Pyroaurite mass	C in Pyroaurite	C mass in hydromag-nesite & pyroaurite	C content (minus average organic C: 0.02 wt. %)	C mass	C mass (minus calcite C)
<i>Units:</i>	<i>m³</i>	<i>kg</i>	<i>wt. %</i>	<i>kg/m³</i>	<i>kg/m³</i>	<i>wt. %</i>	<i>kg/m³</i>	<i>kg/m³</i>	<i>wt. %</i>	<i>kg/m³</i>	<i>kg/m³</i>	<i>kg/m³</i>	<i>wt. %</i>	<i>kg/m³</i>	<i>kg/m³</i>
0-2	0.02	24	0.4	0.1	0.0	0.4	0.1	0.0	1.3	0.3	0.0	0.0	0.23	0.05	0.04
2-10	0.08	120	0.3	0.4	0.0	1.2	1.4	0.1	1.7	2.0	0.0	0.2	0.34	0.40	0.36
10-20	0.1	150	0.3	0.4	0.0	1.3	1.9	0.2	1.7	2.5	0.0	0.2	0.34	0.51	0.46
20-30	0.1	150	0.3	0.4	0.0	0.8	1.1	0.1	1.6	2.4	0.0	0.2	0.31	0.46	0.42
30-40	0.1	150	0.2	0.4	0.0	0.6	0.8	0.1	1.0	1.6	0.0	0.1	0.26	0.39	0.35
40-50	0.1	150	0.3	0.5	0.1	0.4	0.6	0.1	1.1	1.6	0.0	0.1	0.23	0.35	0.29
50-60	0.1	150	0.3	0.5	0.1	0.2	0.3	0.0	1.2	1.8	0.0	0.1	0.22	0.33	0.27
60-70	0.1	150	0.3	0.5	0.1	0.0	0.0	0.0	1.4	2.1	0.0	0.0	0.22	0.34	0.28
70-80	0.1	150	0.3	0.4	0.0	0.0	0.0	0.0	1.1	1.7	0.0	0.0	0.24	0.36	0.31
80-90	0.1	150	0.3	0.5	0.1	0.0	0.0	0.0	1.0	1.5	0.0	0.0	0.22	0.33	0.28
90-100	0.1	150	0.4	0.6	0.1	0.0	0.0	0.0	1.1	1.7	0.0	0.0	0.19	0.29	0.21
total, upper 1m	500	650000	Sum of C in calcite: 0.5			Sum of C in secondary carbonates (hydromagnesite & pyroaurite):						1.0	Sum:	3.81	3.27

* calculated using average measured bulk density. 0–2 cm interval uses bulk density of 1.2 g/cm³ (average of 0–10 cm cores), while 2–30 cm and 30–100 cm intervals use bulk density of 1.5 g/cm³ (average of 10–20 and 20–30 cm cores, Table S2).

Previous studies of carbon accounting at Woodsreef report higher carbon sequestration rates within the 0–2 cm zone: 0.78 kg C/m² from Oskierski et al. (2013) and 0.17–0.33 kg C/m² from Turvey et al. (2017). However, Oskierski et al. (2013) assumes a bulk density of 2.7 t/m³, characteristic of solid serpentinite. When the average measured bulk density of tailings in the 0–2 cm interval obtained in this study (i.e., 1.2 t/m³, Appendix 3: Table S2), is applied to the Oskierski et al. (2013) data, this rate is adjusted to 0.32 kg C/m². This measured bulk density (1.2 t/m³, Appendix 3: Table S2) has also been applied to convert the reported rate in Turvey et al. (2017), which was in units of g CO₂/kg material, to directly comparable units (kg C/m²). These estimates from the literature are one to two orders of magnitude higher than those estimated in this study for the 0–2 cm interval, however they based on a limited number (3 samples in Oskierski et al., 2013, and 4 samples in Turvey et al. 2017) of highly carbonated (up to 14.6 wt. % hydromagnesite) vertical crust samples, which are not representative of the tailings storage facility as a whole. Carbonate mineral precipitation often appears to be enhanced on vertical faces compared to horizontal faces (Oskierski et al., 2013; Turvey et al., 2017; Wilson et al., 2009). Construction of new tailings storage facilities or reworking of tailings in historical facilities storage facilities to include terracing could increase CO₂ trapping rates by (1) increasing the surface area of tailings exposed to atmospheric CO₂, and (2) increasing the area of vertical faces, which appear to be favourable for carbonate cement development. Progressive cementation of tailings faces (particularly vertical faces) could also serve to increase the stability of tailings and limit wind-blown fibres from historical chrysotile mines (McCutcheon et al., 2017).

4.5. Conclusions

We have developed and tested a geochemical treatment system designed to moderate tailings pore water saturation using doses of water or acidified water to enhance mineral carbonation rates in ultramafic mine tailings. The experiment ended after a water spill over the experimental site, which was followed by the unintended delivery of approximately 900 L of acidic water to the acid plot. However, the effects of the large acid dose, which are observed as a reduction in total carbon, lower carbonate mineral abundances, and precipitation of an orange rusted layer, are restricted to the upper 2 cm in the acid plot. This result has important implications for the long-term storage of CO₂ in Mg-carbonate minerals, particularly in terms of exposure to changes in environmental conditions such as acid rain. The high neutralising capacity of ultramafic tailings imparts resilience to CO₂ storage in minerals under acidic conditions, even in the case of exposure to a large spill of pH ~1 water. However, the presence of existing carbonate minerals in the shallow tailings limits the effectiveness of acidic treatments when applied to the surface of a tailings storage facility. Runoff was observed to limit infiltration of treatment solutions, likely contributing to a shallower neutralisation horizon than expected. Precipitation of a rusted orange layer, characterised by an Fe-(hydr)oxide precipitate, is considered to represent the neutralisation horizon and may be used to track progression of the neutralisation front with continued acid treatment.

Geochemical changes induced by our experimental treatments were restricted to the upper 0–2 cm of the acid treated plot. Detailed mineralogical and geochemical characterisation of our experimental site provides a robust assessment of passive mineral carbonation since mine closure. Previous estimates of passive mineral carbonation at Woodsreef are likely underestimated, as we find maximum carbonate mineral abundance occurs between

2–30 cm depth, and measured total carbon persists at approximately 0.2 wt. % (compared to a maximum of 0.4 wt. %) to a depth of at least 1 m. A decreasing trend with depth is observed in carbon content, carbonate mineral abundance, and the proportion of atmospheric CO₂ stored in minerals, suggesting that geochemical reactions are limited by carbon availability with increasing depth from both horizontal and vertical surfaces. Still, radiocarbon data reveal a predominantly atmospheric source for carbon in carbonate minerals to a depth of 1 m. Total carbon data are used to estimate passive CO₂ sequestration at the experimental site at Woodsreef Mine, revealing nearly four times more carbon has been sequestered within the tailings than can be accounted for by refined mineral abundances of hydromagnesite and pyroaurite from XRD data alone. This is a consequence of underestimation of these carbonate phases in Rietveld refinement of XRD data, and the likely presence of an X-ray amorphous Mg-carbonate phase. XRD is instead used to refine the abundance of gangue calcite, allowing gangue carbon to be calculated and subtracted from total carbon data. As such, XRD and total carbon measurements should be used together for future accounting of mineral carbonation, in order to account for the contributions not only of gangue carbonate minerals, but also X-ray amorphous carbonate phases.

Future field trials for accelerated carbonation of mine tailings should ideally be conducted in collaboration with industry at currently operating mine sites. In order to maximise CO₂ sequestration by passive reaction with the atmosphere, tailings could be constructed or reworked to include terraces to increase surface area. Geochemical treatments are better suited to fresh tailings that have minimal gangue carbonate mineral content, and should consider employing higher acid concentrations or dose rates in line with the high neutralising capacity of tailings. Since runoff from surface applied treatments resulted in limited infiltration of treatment solutions, future field trials should also explore sub-

surface acid leaching, to maximise acid reaction with target silicate and hydroxide minerals, and avoid reaction with existing or newly precipitated (as a result of treatments) carbonate minerals in the near surface, or, trial reaction with a CO₂ source to address carbon limitation, particularly at depth.

4.6. Chapter 4 references

Allen D.J. and Brent G.F. (2010) Sequestering CO₂ by Mineral Carbonation: Stability against Acid Rain Exposure. *Environmental Science & Technology* 44, 2735-2739.

Assargiotis A. (2013) Woodsreef Mine Major Rehabilitation Project - Review of Environmental Factors. Environmental Planning and Assessment, NSW Public Works, Department of Finance and Services. DC11100, 1-131.

Assima G.P., Larachi F., Beaudoin G. and Molson J. (2013) Dynamics of carbon dioxide uptake in chrysotile mining residues – Effect of mineralogy and liquid saturation. *International Journal of Greenhouse Gas Control* 12, 124-135.

Assima G.P., Larachi, F., Beaudoin G. and Molson J.W. (2012) CO₂ sequestration in chrysotile mining residues - Implication of watering and passification under environmental conditions. *Industrial & Engineering Chemistry Research* 51, 8726-8734.

Assima G.P., Larachi F., Molson J. and Beaudoin, G. (2014) Comparative study of five Québec ultramafic mining residues for use in direct ambient carbon dioxide mineral sequestration. *Chemical Engineering Journal* 245, 56-64.

Azdarpour A., Asadullah M., Mohammadian E., Hamidi H., Junin R. and Karaei M.A. (2015) A review on carbon dioxide mineral carbonation through pH-swing process. *Chemical Engineering Journal* 279, 615-630.

Beinlich A. and Austrheim H. (2012) In situ sequestration of atmospheric CO₂ at low temperature and surface cracking of serpentinized peridotite in mine shafts. *Chemical Geology* 332, 32-44.

- Bish D.L. and Howard S.A. (1988) Quantitative phase analysis using the Rietveld method. *Journal of Applied Crystallography* 21, 86-91.
- Blowes D.W., Ptacek C.J. and Jambor J.L. (2013) Mineralogy of mine wastes and strategies for remediation. Environmental Mineralogy II, *European Mineralogical Union Notes in Mineralogy* 13, 295-338.
- Bobicki E.R., Liu Q., Xu Z. and Zeng H. (2012) Carbon capture and storage using alkaline industrial wastes. *Progress in Energy and Combustion Science* 38, 302-320.
- Bodénan F., Bourgeois F., Petiot C., Augé T., Bonfils B., Julcour-Lebigue, C., Guyot F., Boukary, A., Tremosa J., Lassin A., Gaucher E.C. and Chiquet P. (2014) Ex situ mineral carbonation for CO₂ mitigation: Evaluation of mining waste resources, aqueous carbonation processability and life cycle assessment (Carmex project). *Minerals Engineering* 59, 52-63.
- Bodor, M., Santos, R., Gerven, T. and Vlad, M. (2013) Recent developments and perspectives on the treatment of industrial wastes by mineral carbonation — a review. *Open Engineering* 3, 566-584.
- Brent G.F. Rayson M.S., Kennedy E.M., Stockenhuber M., Collins W.J., Prigge J.D., Hynes R.G., Molloy T.S., Zulfiqar H., Farhang F., Oliver T.O., Hamblin Wang S. and Dawe M. (2015) Mineral carbonation of serpentinite: From the Laboratory to Pilot Scale - The MCi project, 5th International Conference on Accelerated Carbonation for Environmental and Material Engineering 2015, pp. 394-403.
- Brindley G.W. (1945) XLV. The effect of grain or particle size on X-ray reflections from mixed powders and alloys, considered in relation to the quantitative determination of crystalline substances by X-ray methods. *The London, Edinburgh, and Dublin Philosophical Magazine and Journal of Science* 36, 347-369.
- Bureau of Meteorology (2015) Climate Data Online <http://www.bom.gov.au/climate/data>.
- Cheary R.W. and Coelho A. (1992) A fundamental parameters approach to X-ray line-profile fitting. *Journal of Applied Crystallography* 25, 109-121.

- Dold B. (2017) Acid rock drainage prediction: A critical review. *Journal of Geochemical Exploration* 172, 120-132.
- Entezari Zarandi E.A., Larachi F., Beaudoin G., Plante B. and Sciortino M. (2016) Multivariate study of the dynamics of CO₂ reaction with brucite-rich ultramafic mine tailings. *International Journal of Greenhouse Gas Control* 52, 110-119.
- Fallon S.J., Fifield L.K. and Chappell J.M. (2010) The next chapter in radiocarbon dating at the Australian National University: Status report on the single stage AMS. *Nuclear Instruments and Methods in Physics Research Section B: Beam Interactions with Materials and Atoms* 268, 898-901.
- Gerdemann S.J., O'Connor W.K., Dahlin D.C., Penner L.R. and Rush H. (2007) Ex Situ Aqueous Mineral Carbonation. *Environmental Science & Technology* 41, 2587-2593.
- Ghorbani Y., Franzidis J.-P. and Petersen J. (2016) Heap Leaching Technology—Current State, Innovations, and Future Directions: A Review. *Mineral Processing and Extractive Metallurgy Review* 37, 73-119.
- Glasser F.P., Jauffret G., Morrison J., Galvez-Martos J.-L., Patterson N. and Imbabi M.S.-E. (2016) Sequestering CO₂ by mineralization into useful nesquehonite-based products. *Frontiers in Energy Research* 4, 3.
- Glen R.A. and Butt B.C. (1981) Chrysotile asbestos at Woodsreef, New South Wales. *Economic Geology* 76, 1153-1169.
- Gras A., Beaudoin G., Molson J., Plante B., Bussière B., Lemieux J.M. and Dupont P.P. (2017) Isotopic evidence of passive mineral carbonation in mine wastes from the Dumont Nickel Project (Abitibi, Quebec). *International Journal of Greenhouse Gas Control* 60, 10-23.
- Grguric B.A. (2003) Minerals of the MKD5 nickel deposit, Mount Keith, Western Australia. *Australian Journal of Mineralogy* 9, 55-71.
- Hagedorn B. and Cartwright I. (2009) Climatic and lithologic controls on the temporal and spatial variability of CO₂ consumption via chemical weathering: An example from the Australian Victorian Alps. *Chemical Geology* 260, 234-253.

- Hamilton J.L., Wilson S.A., Morgan B., Turvey C.C., Paterson D.J., MacRae C., McCutcheon J. and Southam G. (2016) Nesquehonite sequesters transition metals and CO₂ during accelerated carbon mineralisation. *International Journal of Greenhouse Gas Control* 55, 73-81.
- Hamilton J.L. Wilson S.A. Morgan B., Turvey C.C., Paterson D.J., Jowitt S.M., McCutcheon J. and Southam G. (in review) The fate of trace metals during atmospheric carbonation of ultramafic mine tailings. *International Journal of Greenhouse Gas Control*. in review.
- Harrison A.L., Power I.M. and Dipple G.M. (2012) Accelerated Carbonation of Brucite in Mine Tailings for Carbon Sequestration. *Environmental Science & Technology* 47, 126-134.
- Harrison A.L., Dipple G.M., Power I.M. and Mayer K.U. (2015) Influence of surface passivation and water content on mineral reactions in unsaturated porous media: Implications for brucite carbonation and CO₂ sequestration. *Geochimica et Cosmochimica Acta* 148, 477-495.
- Harrison A.L., Dipple G.M., Power I.M. and Mayer K.U. (2016) The impact of evolving mineral–water–gas interfacial areas on mineral–fluid reaction rates in unsaturated porous media. *Chemical Geology* 421, 65-80.
- Hill R. and Howard C. (1987) Quantitative phase analysis from neutron powder diffraction data using the Rietveld method. *Journal of Applied Crystallography* 20, 467-474.
- Hitch M., Ballantyne S.M. and Hindle S.R. (2009) Revaluing mine waste rock for carbon capture and storage. *International Journal of Mining, Reclamation and Environment* 24, 64-79.
- Imran A., López-Rayó S., Magid J. and Hansen H.C.B. (2016) Dissolution kinetics of pyroaurite-type layered double hydroxide doped with Zn: Perspectives for pH controlled micronutrient release. *Applied Clay Science* 123, pp.56-63.
- IPCC (2005) IPCC Carbon dioxide capture and storage. In: Metz, B., Davidson, O., de Coninck, H.C., Loos, M., Meyer, L.A. (Eds.), IPCC Special Report. Prepared by

Working Group III of the Intergovernmental Panel on Climate Change, Cambridge University Press, Cambridge and New York.

IPCC (2013) IPCC Climate Change 2013: The Physical Science Basis. Contribution of Working Group 1 to the Fifth Assessment Report of the Intergovernmental Panel on Climate Change. Stocker, T.F., Qin, D., Plattner, G.-K., Allen, S.K, Boschung, J., Naules, A., Xia, Y., Bex, V., Midgley, P.M (eds) Cambridge University Press, Cambridge, United Kingdom and New York, USA.

Jacobs A.D. and Hitch M. (2011) Experimental mineral carbonation: approaches to accelerate CO₂ sequestration in mine waste materials. *International Journal of Mining, Reclamation and Environment* 25, 321-331.

Jambor J., Dutrizac J., Groat L. and Raudsepp M. (2002) Static tests of neutralization potentials of silicate and aluminosilicate minerals. *Environmental Geology* 43, 1-17.

Jambor J., Dutrizac J. and Raudsepp M. (2007) Measured and computed neutralization potentials from static tests of diverse rock types. *Environmental geology* 52, 1019-1031.

Kemache N., Pasquier L.-C., Cecchi E., Mouedhen I., Blais J.-F. and Mercier G. (2017) Aqueous mineral carbonation for CO₂ sequestration: From laboratory to pilot scale. *Fuel Processing Technology* 166, 209-216.

Kemache N., Pasquier L.-C., Mouedhen I., Cecchi E., Blais J.-F. and Mercier G. (2016) Aqueous mineral carbonation of serpentinite on a pilot scale: The effect of liquid recirculation on CO₂ sequestration and carbonate precipitation. *Applied Geochemistry* 67, 21-29.

Kmetoni J. (1984) Woodsreef Mill Tailings - Investigation of potential for further utilization as a mineral resource. Department of Mineral Resources, New South Wales 84.

Königsberger E., Königsberger L.-C. and Gamsjäger H. (1999) Low-temperature thermodynamic model for the system Na₂CO₃-MgCO₃-CaCO₃-H₂O. *Geochimica et Cosmochimica Acta* 63, 3105-3119.

- Kwong Y.-T.J. (1993) Prediction and prevention of acid rock drainage from a geological and mineralogical perspective. MEND.
- Lackner K.S., Wendt C.H., Butt D.P., Joyce E.L.J. and Sharp D.H. (1995) Carbon dioxide disposal in carbonate minerals. *Energy* 20, 1153-1170.
- Lawrence R.W. and Scheske M. (1997) A method to calculate the neutralization potential of mining wastes. *Environmental Geology* 32, 100-106.
- Lechat K., Lemieux J.-M., Molson J., Beaudoin G. and Hébert R. (2016) Field evidence of CO₂ sequestration by mineral carbonation in ultramafic milling wastes, Thetford Mines, Canada. *International Journal of Greenhouse Gas Control* 47, 110-121.
- Maroto-Valer M.M., Fauth D.J., Kuchta M.E., Zhang Y. and Andrésen J.M. (2005) Activation of magnesium rich minerals as carbonation feedstock materials for CO₂ sequestration. *Fuel Processing Technology* 86, 1627-1645.
- McCutcheon J., Dipple G.M., Wilson S.A. and Southam G. (2015) Production of magnesium-rich solutions by acid leaching of chrysotile: A precursor to field-scale deployment of microbially enabled carbonate mineral precipitation. *Chemical Geology* 413, 119-131.
- McCutcheon J., Turvey C.C., Wilson S.A., Hamilton J.L. and Southam G. (2017) Microbial mineral carbonation of asbestos mine tailings: Potential applications to carbon storage and tailings stabilization. *Minerals* 7, 191.
- McCutcheon J., Wilson S.A. and Southam G. (2016) Microbially accelerated carbonate mineral precipitation as a strategy for in situ carbon sequestration and rehabilitation of asbestos mine sites. *Environmental Science & Technology* 50, 1419-1427.
- Merrill R.J., Butt B.C., Forrest V.C., Purdon G. and Bramely-Moore R.A. (1980) Asbestos production at Chrysotile Corporation of Australia Pty. Limited, Barraba, NSW. *Mining and Metallurgical Practices in Australasia: the Sir Maurice Mawby memorial volume* 10, 669-673.

- Mouedhen I., Kemache N., Pasquier, L.-C., Cecchi E., Blais J.-F. and Mercier G. (2017) Effect of pCO₂ on direct flue gas mineral carbonation at pilot scale. *Journal of Environmental Management* 198, 1-8.
- Oelkers E.H., Gislason S.R. and Matter J. (2008) Mineral carbonation of CO₂. *Elements* 4, 333-337.
- Oskierski H.C. (2013) Natural carbonation of ultramafic rocks in the Great Serpentine Belt, New South Wales, Australia. Ph.D thesis, The University of Newcastle.
- Oskierski H.C., Dlugogorski B.Z. and Jacobsen G. (2013) Sequestration of atmospheric CO₂ in chrysotile mine tailings of the Woodsreef Asbestos Mine, Australia: Quantitative mineralogy, isotopic fingerprinting and carbonation rates. *Chemical Geology* 358, 156-169.
- Park A.-H.A. and Fan L.-S. (2004) mineral sequestration: physically activated dissolution of serpentine and pH swing process. *Chemical Engineering Science* 59, 5241-5247.
- Pawley G. (1981) Unit-cell refinement from powder diffraction scans. *Journal of Applied Crystallography* 14, 357-361.
- Power I., McCutcheon J., Harrison A.L., Wilson, S.A., Dipple, G.M., Kelly S., Southam C. and Southam G. (2014) Strategizing carbon-neutral mines: A case for pilot projects. *Minerals* 4, 399-436.
- Power I.M., Dipple G.M. and Southam G. (2010) Biobleaching of ultramafic tailings by *Acidithiobacillus* spp. for CO₂ sequestration. *Environmental Science & Technology* 44, 456-462.
- Power I.M., Harrison A.L., Dipple G.M., Wilson S.A., Kelemen P.B., Hitch M. and Southam G. (2013a) Carbon mineralization: From natural analogues to engineered systems. *Reviews in Mineralogy and Geochemistry* 77, 305-360.
- Power I.M., Wilson S.A. and Dipple G.M. (2013b) Serpentine Carbonation for CO₂ Sequestration. *Elements* 9, 115-121.

- Power I.M., Wilson S.A., Small D.P., Dipple G.M., Wan W. and Southam G. (2011) Microbially Mediated Mineral Carbonation: Roles of Phototrophy and Heterotrophy. *Environmental Science & Technology* 45, 9061-9068.
- Pronost J., Beaudoin G., Lemieux J.-M., Hébert R., Constantin M., Marcouiller S., Klein M., Duchesne J., Molson J.W., Larachi F. and Maldague X. (2012) CO₂-depleted warm air venting from chrysotile milling waste (Thetford Mines, Canada): Evidence for in-situ carbon capture from the atmosphere. *Geology* 40, 275-278.
- Pronost J., Beaudoin G., Tremblay J., Larachi F., Duchesne J., Hébert R. and Constantin M. (2011) Carbon sequestration kinetic and storage capacity of ultramafic mining waste. *Environmental Science & Technology* 45, 9413-9420.
- Rietveld H. (1969) A profile refinement method for nuclear and magnetic structures. *Journal of Applied Crystallography* 2, 65-71.
- Rucker D.F., Zaebst R.J., Gillis J., Cain J.C. and Teague B. (2017) Drawing down the remaining copper inventory in a leach pad by way of subsurface leaching. *Hydrometallurgy* 169, 382-392.
- Seifritz W. (1990) CO₂ disposal by means of silicates. *Nature* 345, 486.
- Shan Q., Zhang Y. and Xue X. (2012) Removal of copper from wastewater by using the synthetic nesquehonite. *Environmental Progress & Sustainable Energy* 32, 543-546.
- Stuiver M. and Polach H.A. (1977) Reporting of ¹⁴C Data. *Radiocarbon* 19, 355-363.
- Sverdrup H. (1990) The kinetics of base cation release due to chemical weathering. Lund University Press, Lund.
- Teir S., Kuusik R., Fogelholm C.-J. and Zevenhoven R. (2007a) Production of magnesium carbonates from serpentinite for long-term storage of CO₂. *International Journal of Mineral Processing* 85, 1-15.
- Teir S., Revitzer H., Eloneva S., Fogelholm C.-J. and Zevenhoven R. (2007b) Dissolution of natural serpentinite in mineral and organic acids. *International Journal of Mineral Processing* 83, 36-46.

- Turvey C.C., Wilson S.A., Hamilton J.L., Tait A.W., McCutcheon J., Beinlich A., Fallon S.J., Dipple G.M and Southam, G. (in prep.a) Hydrotalcites and hydrated Mg-carbonates as carbon sinks in serpentinite mineral wastes from the Woodsreef Chrysotile Mine, NSW, Australia. in preparation.
- Turvey C.C., Hamilton J.L. and Wilson S.A. (in prep.b) Comparison of Rietveld analysis methods for quantification of carbon dioxide fixation in ultramafic mine tailings. in preparation.
- Turvey C.C., Wilson S.A., Hamilton J.L. and Southam G. (2017) Field-based accounting of CO₂ sequestration in ultramafic mine wastes using portable X-ray diffraction. *American Mineralogist* 102, 1302-1310.
- Wahlström M., Laine-Ylijoki J. and Kaartinen T. (2009) Acid neutralization capacity of waste-specification of requirement stated in landfill regulations. Nordic Council of Ministers.
- Wicks F.J. and O'Hanley D.S. (1988) Serpentine minerals; structures and petrology. *Reviews in Mineralogy and Geochemistry* 19, 91-167.
- Wilson S.A., Barker S.L.L., Dipple G.M., and Atudorei V. (2010) Isotopic disequilibrium during uptake of atmospheric CO₂ into mine process waters: Implications for CO₂ sequestration. *Environmental Science & Technology* 44(24), 9522-9529.
- Wilson S.A., Dipple G.M., Power I.M., Barker S.L.L., Fallon S.J. and Southam G. (2011) Subarctic Weathering of Mineral Wastes Provides a Sink for Atmospheric CO₂. *Environmental Science & Technology* 45, 7727-7736.
- Wilson S.A., Dipple G.M., Power I.M., Thom J.M., Anderson R.G., Raudsepp M., Gabites J.E. and Southam G. (2009) Carbon dioxide fixation within mine wastes of ultramafic-hosted ore deposits: Examples from the Clinton Creek and Cassiar chrysotile deposits, Canada. *Economic Geology* 104, 95-112.
- Wilson S.A., Harrison A.L., Dipple G.M., Power I.M., Barker S.L.L., Mayer K.U., Fallon S.J., Raudsepp M. and Southam G. (2014) Offsetting of CO₂ emissions by air capture in mine tailings at the Mount Keith Nickel Mine, Western Australia: Rates, controls and prospects for carbon neutral mining. *International Journal of Greenhouse Gas Control* 25, 121-140.

Wilson S.A., Raudsepp M. and Dipple G.M. (2006) Verifying and quantifying carbon fixation in minerals from serpentine-rich mine tailings using the Rietveld method with X-ray powder diffraction data. *American Mineralogist* 91, 1331-1341.

Wilson S.A., Raudsepp M. and Dipple G.M. (2009b) Quantifying carbon fixation in trace minerals from processed kimberlite: A comparative study of quantitative methods using X-ray powder diffraction data with applications to the Diavik Diamond Mine, Northwest Territories, Canada. *Applied Geochemistry* 24, 2312-2331.

Woodsreef Taskforce (2011) Asbestos and the Derelict Woodsreef Mine. Primefact 1118
1. NSW Department of Primary Industries.

Declaration for Thesis Chapter 5

Declaration by candidate

In the case of Chapter 5, the nature and extent of my contribution is as follows:

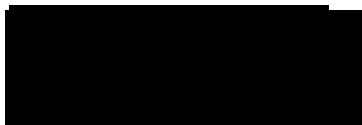
Nature of contribution	Extent of contribution
Conceptualisation, experimental design and construction, data collection, analysis and interpretation, modelling, and writing.	79%

The following co-authors contributed to the work. If co-authors are students at Monash University, the extent of their contribution in percentage terms must be stated:

Name	Nature of contribution	Extent of contribution (%)
Siobhan A. Wilson	Supervisory role	5%
Bree Morgan	Supervisory role	5%
Anna L. Harrison	Modelling advice	3%
Connor C. Turvey	Fieldwork, synchrotron data collection	3%
David J. Paterson	Synchrotron XFM analysis	3%
Gregory M. Dipple	Advisor	1%
Gordon Southam	Advisor, synchrotron XFM data collection	1%

The undersigned hereby certify that the above declaration correctly reflects the nature and extent of the candidate's and co-authors contributions to this work*.

Candidate's signature:



Date: 10 February 2018

Main supervisor's signature:



Date: 5 February 2018

*Note: Where the responsible author is not the candidate's main supervisor, the main supervisor should consult with the responsible author to agree on the respective contributions of the authors.

Chapter 5

Accelerating mineral carbonation in ultramafic mine tailings via direct CO₂ reaction and heap leaching, and potential for base metal enrichment and recovery[†]

Jessica L. Hamilton^a, Siobhan A. Wilson^{ab}, Bree Morgan^{ac}, Anna L. Harrison^d, Connor C. Turvey^a, David J. Paterson^e, Gregory M. Dipple^f and Gordon Southam^g

^aSchool of Earth, Atmosphere and Environment, Monash University, Australia

^bDepartment of Earth and Atmospheric Sciences, University of Alberta, Edmonton, AB T6G 2R3, Canada

^cSchool of Geosciences, The University of Sydney, Camperdown, NSW 2006, Australia

^dGéosciences Environnement Toulouse, Centre National de la Recherche Scientifique, Belin 31400, Toulouse, France

^eAustralian Synchrotron, Clayton, Melbourne, VIC 3168, Australia

^fDepartment of Earth, Atmosphere and Ocean Sciences, The University of British Columbia, Vancouver, BC V6T 1Z4, Canada

^gSchool of Earth Sciences, The University of Queensland, St Lucia, QLD 4072, Australia

[†]Prepared for submission to *Economic Geology*

Accelerated carbonation of ultramafic mine tailings has the potential to offset CO₂ emissions produced by mining ores from Cu–Ni–PGE, podiform chromite, diamondiferous kimberlite and historical chrysotile deposits. Treatments such as acid leaching, reaction of tailings with elevated concentrations of gaseous CO₂, and optimisation of tailings pore water saturation have been shown to enhance CO₂ sequestration rates in laboratory settings. The next challenge is to deploy treatment technologies on the pilot and field scale, whilst minimising cost, energy input, and adverse environmental impacts. Implementation of accelerated tailings carbonation at field-scale will ideally make use of *in situ* treatments or modified ore processing routes that employ conventional technology and expertise, and operate at close to ambient temperatures and pressures. Here, we describe column experiments designed to trial two geochemical treatments that address these criteria: (1) direct reaction of partially saturated ultramafic tailings with synthetic flue gas from power generation (10 % CO₂ in N₂) and (2) repeated heap leaching of ultramafic tailings with dilute sulfuric acid. In the first experiment, we report rapid carbonation of brucite [Mg(OH)₂] in the presence of 10 % CO₂ gas within tailings sampled from the Woodsreef Chrysotile Mine, New South Wales, Australia. Within 4 weeks, we observe a doubling of the amount of CO₂ stored within minerals relative to what is achieved after three decades of passive mineral carbonation via air capture in the field. Our simulated heap leaching experiments, treated daily with 0.08 M H₂SO₄, produce high-Mg leachates that have the potential to sequester 21.4 kg CO₂/m²/y, which is approximately 3.5 times the highest reported rate for passive carbonation in the field (from Clinton Creek Chrysotile Mine, Canada). Although some nesquehonite (MgCO₃·3H₂O) forms from these leachates, most of the Mg is precipitated as Mg-sulfate minerals instead. As such, sulfate removal would be required to maximise CO₂ sequestration potential from acid heap leaching treatments. Geochemical modeling

(MIN3P) is employed to simulate acid leaching experiments and predict the effects of heap leaching for up to five years. Finally, our synchrotron X-ray Fluorescence Microscopy (XFM) results for leached tailings material reveal that valuable trace metals (Ni, Mn, Co, Cr) become highly concentrated within secondary Fe-oxide minerals at the pH neutralisation horizon within our column experiments. This discrete horizon migrates downwards, and modelling predicts it will become increasingly enriched in metals, in response to continued acid leaching. Acid-leaching treatments for accelerated mineral carbonation could therefore be useful for ore processing and recovery of base metals from tailings, waste rock, or low-grade ores.

5.1. Introduction

Mineral carbonation is a natural silicate weathering process that results in trapping of atmospheric CO₂ in mineral form (Seifritz, 1990). Dissolution of Mg-silicate and hydroxide minerals in rainwater or surface water release Mg²⁺ into solution, which reacts with dissolved inorganic carbon to precipitate Mg-carbonate minerals (e.g., Oelkers et al., 2008; Wilson et al., 2009a). Formation of anhydrous MgCO₃ is kinetically inhibited at ambient temperatures and pressures, thus carbon is more commonly sequestered within a series of hydrated Mg-carbonate minerals, such as nesquehonite (MgCO₃·3H₂O) and hydromagnesite [Mg₅(CO₃)₄(OH)₂·4H₂O], whose hydration states depend on environmental conditions such as humidity and temperature (e.g., Davies and Bubela, 1973; Hopkinson et al., 2008; Jauffret et al., 2015; Morgan et al., 2015).

Ultramafic mine tailings storage facilities are ideal settings in which to observe and promote mineral carbonation because they contain large amounts of reactive minerals such as serpentine [Mg₃Si₂O₅(OH)₄], olivine [(Mg,Fe)₂SiO₄] and brucite [Mg(OH)₂]. Furthermore, the reactive surface area of mine tailings is enhanced by crushing and

milling during ore processing (e.g., Bobicki et al., 2012; Wilson et al., 2006, 2009a). Passive carbonation has been observed at a number of derelict mines in Australia, Canada and Norway (e.g., Beinlich and Austrheim, 2012; Gras et al., 2017; Lechat et al., 2016; Oskierski et al., 2013; Pronost et al., 2012; Turvey et al., 2017; Wilson et al., 2006, 2009a, 2009b, 2011), and at the currently operating Mount Keith Ni mine in Western Australia, passive carbonation of mine tailings offsets 11% of the mine's annual CO₂ emissions (Wilson et al., 2014). Acceleration of carbonation over the passive rates observed in tailings storage facilities requires the use of geochemical treatments or changes to tailings management practices. At Mount Keith Mine, achieving a carbonate conversion rate of 11 % would be sufficient to offset 100% of annual CO₂ emissions at that mine (Power et al., 2014; Wilson et al., 2014). Globally, the CO₂ sequestration potential (assuming complete carbonation) of ultramafic mine tailings (from current annual production of Ni, PGM, asbestos, diamond, chromite and talc) has been estimated to be 175 Mt CO₂ per year (Power et al., 2013).

Mineral carbonation is moving beyond laboratory experiments to see implementation in pilot-scale *ex situ* reactors (Brent et al., 2015; Kemache et al., 2017; Kemache et al., 2016; Mouedhen et al., 2017) and trial injections of CO₂ into underground basaltic formations in Iceland (CarbFix project, Matter et al., 2011, 2016) and Washington, USA (Big Sky Carbon Sequestration Partnership, McGrail et al., 2016), with scientific drilling also proposed to assess *in situ* mineral carbonation potential of peridotite in Oman (Oman Drilling Project, Keleman et al., 2013). The results of these pilot tests are encouraging, however the current challenge remains to achieve large-scale accelerated mineral carbonation whilst minimising energy input and economic costs (Power et al., 2014). As such, field-portable, *in situ* treatments that operate at close to ambient temperatures and pressures are an important avenue for development in parallel with *ex situ* reactors and

injection-based technologies. Recent research has developed field-based trials of passive and accelerated carbonation in mine tailings storage facilities (Gras et al., 2017; Hamilton et al., in prep/Chapter 4; Lechat et al. 2016; McCutcheon et al., 2017) and planning has commenced for pilot projects (Mervine et al., in review).

Key limiting factors for mineral carbonation are the slow dissolution of silicate minerals, and CO₂ limitation (Chen et al., 2006, Herzog, 2002). Acid leaching has long been used to accelerate silicate mineral dissolution (Maroto-Valer et al., 2005; Park et al., 2003), and pH-swing methods allow optimisation of conditions firstly to enhance silicate dissolution at low-pH, then to promote carbonate mineral precipitation at high-pH (Park and Fan, 2004). Power et al. (2010, 2014) suggest that waste acid or acid generating materials (e.g., sulfide-rich material produced as a by-product of mining or mineral processing) can be used to enhance silicate mineral dissolution in heap leaching or bioleaching scenarios on the landscape scale within tailings storage facilities. This has the added benefit of neutralising the waste acid, although care should be taken not to exceed neutralising capacity, to avoid producing acidic drainage (Power et al., 2014). Where an on-site CO₂ source is available, such as flue gas from power generation or other equipment, this can be used for direct reaction of tailings (Harrison et al., 2012; Mouedhen et al., 2017). Utilising existing or nearby resources may provide savings in waste management, and reduce the cost of treatments to accelerate mineral carbonation (Power et al., 2014).

Acid leaching poses a potential environmental risk due to mobilisation of trace metals by the dissolution of sulfides, silicate and oxides (Olsson et al., 2014a,b; Thomas et al., 2016). This is particularly relevant to proposed landscape-scale treatments such as heap leaching of ultramafic mine tailings to promote silicate mineral dissolution and

production of Mg-rich leachates. If a leak or spill occurred, acidic and metalliferous leachate solutions could be released into the environment. The fate of trace metals during acid leaching of mined landscapes has not yet been investigated in detail. However, our previous work indicates that if solutions are neutralised, the risk of metalliferous leachate generation is unlikely (Hamilton et al., 2016/Chapter 2; Hamilton et al., in review/Chapter 3). Rapid immobilisation of Fe and trace metals (Ni, Mn, Cr, Co, Cu) within Mg-carbonate minerals and Fe-(hydro)oxides has been demonstrated in laboratory precipitation experiments (Hamilton et al., 2016/Chapter 2) and in a forensic study in a landscape undergoing passive mineral carbonation (Chapter 3). This is also supported by observations of trace metal immobilisation after neutralisation of mineral carbonation leachate fluids in Power et al. (2010, Fe, Cu, and Zn) and in Tier et al. (2007, Ni). In Chapter 4 we estimate that tailings from Woodsreef Chrysotile Mine, in New South Wales, Australia, have an acid neutralising potential of 3.3 mol H⁺/kg. Provided this neutralising potential is not overcome, we predict that acid treatments used to enhance weathering and promote mineral carbonation will be neutralised, and predict that mobilised trace metals will be incorporated into Mg-carbonate and Fe-(hydr)oxide mineral products.

Here, we trial two proposed field-ready strategies for accelerated CO₂ sequestration. These have been investigated in various ways in the laboratory (Assima et al., 2013, 2014; Harrison et al., 2015, 2016; McCutcheon et al., 2016; Power et al., 2010; Pronost et al., 2009, Zarandi et al., 2017a, 2017b), but here we trial them together (acid reaction, optimised pore water saturation and elevated CO₂ reaction), and investigate metal mobility, which has not been examined in detail in the literature. These experiments shed light on how altering the C, S, and Mg cycles in a mined landscape will affect the coupled cycles of first row transition metals. The first experiment trials direct reaction of partially

saturated tailings with flue gas (10 % CO₂ in N) to promote carbonation of brucite. In the second, we simulate a heap leaching treatment in laboratory columns using sulfuric acid to promote dissolution of Mg-silicate minerals, and produce a Mg-rich leachate for precipitation of Mg-carbonate. We report potential CO₂ sequestration rates for each experiment, and discuss the potential for enrichment of valuable trace metals by acid heap leaching, which could add value to mineral carbonation treatments. Enhanced weathering of mine tailings and ultramafic landscapes could be used not only for carbon sequestration, but also for metal resource recovery.

5.2. Methods

5.2.1. Tailings material

Tailings were collected from the derelict Woodsreef Chrysotile Mine, New South Wales, Australia, and were sieved to remove the >1 mm fraction. The bulk tailings sample that we collected from the surface of the tailings storage facility at Woodsreef had been undergoing passive carbonation for approximately three decades (Oskierski et al., 2013; Turvey et al., 2017). As such, the bulk tailings sample was spiked with 2 wt. % Sigma Aldrich brucite {>98 wt. % Mg(OH)₂, with trace periclase (MgO) and hydromagnesite [Mg₅(CO₃)₄(OH)₂·4H₂O], determined by XRD} to better replicate the reactive mineralogy of deeper (>1 m), less weathered tailings (Turvey et al., in prep).

5.2.2. Experimental design

5.2.2.1. Direct CO₂ reaction experiment

A 5.9-kg sample of tailings was pre-mixed with MilliQ water (18.2 MΩ cm) or 0.08 M sulfuric acid (made from MilliQ water), such that the average pore saturation would be 40 % when packed into two columns (25 cm deep, 7.6 cm internal radius) at a bulk density

of 1.3 g/cm³. The base of each column was punctuated with holes, to allow gas flow upwards into the tailings, and lined with fabric mesh to prevent tailings material from falling through (Appendix 4: Fig. S1). A stream of 10 % CO₂ in N₂ gas was delivered into a cavity beneath the base of each column at a rate of 0.06 L/min allowing for infiltration of the gas through the holes and into the tailings (Appendix 4: Fig. S1). Experiments ran for 28 days in a fume hood, and were maintained under laboratory conditions at approximately 22 °C and 40 % humidity.

5.2.2.2. *Acid leaching experiment*

A 60-g sample of tailings was pressed into each of eight 60 mL syringes (1.45 cm internal radius) to a depth of 7 cm, reaching an initial bulk density of 1.3 g/cm³. The base of each syringe was lined with a circle of fabric mesh to prevent particulate matter from draining out of the syringe. 22.66 mL (equivalent to 1 initial pore volume) of MilliQ water or 0.08 M sulfuric acid were added to four replicate columns each day. The eight experiments ran in parallel for a total of 28 days under ambient laboratory conditions in a fume hood. Four replicate experiments were treated with water only and the other four received an identical acidic treatment. Leachate was collected every day from vials that were positioned below each column and passed through a 0.45- μ m syringe filter. Leachate samples were collected prior to addition of the next dose of water or 0.08 M sulfuric acid. An 8 mL aliquot of leachate was sampled from each of the eight experiments every day and was added to replicate Petri dishes to evaporate. The precipitates that formed by evaporation were weighed at the completion of the experiment, and subsamples were prepared for elemental carbon analysis (see subsection 5.2.5. Geochemical analysis), X-ray diffraction (XRD) (see subsection 5.2.6. Mineralogical analysis), and electron microscopy (see subsection 5.2.7. Imaging).

5.2.3. Leachate chemistry

Filtered leachate samples were analysed immediately for pH, using a Thermo Scientific Orion 5 Star pH meter, and alkalinity was measured using a spectrophotometric method within 48 hours (Sarazin et al., 1999). Remaining leachate solutions (after separation of 8 mL for evaporation) from the fourth replicate samples (W4 and A4) were prepared for anion (F, Cl, Br, SO_4^{2-} and NO_3^-) analysis using a Dionex ICS 1100 ion chromatograph, and cation analysis (Na, Mg, K, Ca, Sr, Ba, Al, Si, Mn and Fe) using a Thermo ICAP Duo 7000 ICP-OES, at Monash University's School of Earth, Atmosphere and Environment.

5.2.4. Sample processing

Upon their completion, tailings material was excavated from the large columns used for the direct CO_2 reaction experiment. The columns were sampled between the intervals of 0–5 cm, 5–10 cm, and 10–25 cm, and a hand sample of highly cemented material was collected from the base (20–25 cm) of each enhanced CO_2 experiment column for thin sectioning. Samples were air dried in aluminium trays until no further weight loss was measured (approximately one week). Following drying, samples were homogenised and subsampled for geochemical (XRF and total C) and mineralogical analysis (XRD).

Columns from the heap leaching experiment were sampled at three depth intervals, with the aim of capturing material (1) from above an orange-red, 'rusted' horizon that formed in acidic treatments (0–2 cm), (2) encompassing the rusted horizon (2–5 cm) and (3) material below this horizon (5–7 cm). Note that these estimates were based on the visually observable intersection of the rusted horizon with the sides of each column (Fig. S2). It was determined during dissection of these column experiments that the rusted horizon was domed in shape, and the majority of the rusted material occurred between 0.5 and 2 cm depth (Appendix 4: Fig. S3).

The fourth replicate column of each heap leaching experiment treatment (W4 and A4) was allowed to air dry *in situ* for an additional month, before being infiltrated with 100% ethanol, followed by two infiltrations of a mixture of 50 % ethanol and LR white epoxy resin (a very low-viscosity resin, suitable for light and electron microscopy) and a final infiltration with 100 % LR white epoxy resin. The two resin-filled columns were incubated at 50 °C for one month under desiccating conditions to harden before being cut along their length into 30-µm polished thin sections on quartz glass by Vancouver Petrographics Ltd (Richmond, BC, Canada).

5.2.5. Geochemical analysis

All subsamples of tailings were analysed by Bureau Veritas Pty. Ltd. using X-ray Fluorescence (XRF) to obtain elemental abundances (SiO₂, Al₂O₃, Fe₂O₃, K₂O, MgO, Na₂O, P₂O₅, SO₃, TiO₂, MnO, Cr₂O₃, Ni, Co). Four of the 27 samples selected for elemental analysis were also examined using a LECO analyser to determine total carbon and organic carbon by combustion. The carbon content of the precipitates (n=8) that were produced by evaporation of leachates from the heap leaching experiment was measured using a CHN analyser in the School of Chemistry, Monash University.

5.2.6. Mineralogical analysis

All tailings subsamples were pulverised using a ring mill prior to the addition of a 10 wt. % internal standard of fluorite (CaF₂). Following addition of the fluorite, samples were micronised under anhydrous ethanol in a McCrone Micronising Mill using agate grinding elements. Samples were then dried and disaggregated, and back-loaded into cavity mounts for analysis. XRD patterns were collected with a Bruker D8 Advance Eco X-ray diffractometer, that was fitted with a Cu radiation source and operated at 40 kV and 25 mA, in the Monash X-ray Platform. The precipitates that formed from evaporated

leachates in the heap leaching experiment (replicates W 1–3 and A 1–3) were prepared as smear mounts with anhydrous ethanol owing to their small size. XRD data were collected over 2–80° 2 θ with a step size of 0.02° 2 θ and a count time of 2 s/step. Mineral phases were identified using the ICDD PDF-2 database and the DIFFRACplus EVA Version 2 software package (Bruker AXS). Rietveld refinements (Bish and Howard, 1988; Hill and Howard, 1987; Rietveld, 1969) of XRD patterns collected from the tailings material were completed using Topas Version 5 (Bruker AXS), employing the Rietveld refinement methodology outlined by Wilson et al. (2006) for quantification of mineral abundances in serpentine-rich samples.

5.2.7. Imaging

Precipitates evaporated in the Petri dishes were photographed using a Visionary Digital BK Lab System in the School of Earth, Atmosphere and Environment, Monash University. Thin sections of tailings material, and SEM stubs containing sub-samples of the precipitates evaporated from acid- and water-leached columns (replicates A4 and W4), were iridium coated and analysed using a JEOL 7001F Field Emission Gun Scanning Electron Microscope (FEG-SEM) at the Monash Centre for Electron Microscopy. Backscattered electron (BSE) micrographs and Energy Dispersive Spectroscopy (EDS) data for thin sections were obtained at 10 keV with a live acquisition time of 25 seconds for EDS spectra. BSE images of the precipitates were obtained at 15 keV.

Thin sections of the water- and acid-leached columns (W4, A4) were also imaged at the X-ray fluorescence microscopy (XFM) beamline at the Australian Synchrotron, Clayton, Australia. Overview maps were taken with an incident monochromatic X-ray beam of 18.5 keV at 50- μ m resolution with a dwell time of 2.5 ms and using Kirkpatrick-Baez

mirrors. Selected regions of interest from within the overview maps were then mapped at 2- μm resolution with a dwell time of 0.4 ms. Elemental abundance data were collected using a Maia detector (Ryan et al., 2010; Ryan et al., 2014) and the full spectrum of data were processed using the GeoPIXE software program (Ryan, 2000).

5.2.8. Geochemical Modelling

To predict the impacts and progression of acid leaching treatments over a longer timescale than the laboratory experiments conducted in 7 cm columns, MIN3P (Bea et al., 2012; Mayer et al., 2002) was used to model continuous acid treatment of a 1- m^3 profile over a period of 1 year.

Soil hydraulic properties and mineral reactivity parameters are adapted from Bea et al. (2012), and model parameters used in this study are listed in Table S1-3 in the Supporting Information. Chrysotile was used in the model as the dominant serpentine phase (86.6 wt. %), although the chrysotile rate law (Thom et al., 2013), which was used by Bea et al. (2012), was edited to include trace Fe, such that the formula for chrysotile was $(\text{Mg}_{2.7}, \text{Fe}_{0.3})\text{Si}_2\text{O}_5(\text{OH})_4$. Mineralogical abundances used in the model are based on the average results of Rietveld refinements for three sub-samples of the bulk tailings material used in the column experiments (Appendix 4: Table S2, S12). However, brucite is systematically underestimated by Rietveld refinement of XRD data (Turvey et. al., 2017), and although refined brucite abundance was 0.6 wt. % in the initial material, which was then spiked with 2 wt. % synthetic brucite, the resulting bulk material was estimated by XRD to contain just 1.2 wt. % brucite. As such, the amount of brucite in the model is adjusted to 2.5 wt. % to more accurately reflect the material used in experiments. The value used for the surface area of magnetite was adjusted from the reported BET surface area in White et al. (1994) of 0.1 m^2/g to a value of 0.0001 m^2/g . This is justified firstly

because most magnetite in the tailings material is present as inclusions within grains of serpentine, such that most magnetite grain boundaries were not exposed to acidic fluids during experiments. Furthermore, McCutcheon et al. (2015) did not observe Fe-oxide dissolution during acid leaching experiments on similar chrysotile mine tailings (containing 8 wt. % magnetite) until the concentration of sulfuric acid was increased to 0.54 M (almost 7 times the molarity of sulfuric acid used here). Hydromagnesite, forsterite, calcite and quartz were included in the model using initial abundances that reflect the abundances refined from XRD data for the bulk tailings sample (Appendix 4: Tables S2, S12). Chalcedony (SiO_2), nesquehonite, hematite (Fe_2O_3), ferrihydrite [approximated as $(\text{Fe}^{3+})_2\text{O}_3 \cdot 0.5\text{H}_2\text{O}$], Fe-hydroxide [$\text{Fe}(\text{OH})_2(\text{s})$], gypsum [$\text{CaSO}_4 \cdot 2\text{H}_2\text{O}$], epsomite [$\text{MgSO}_4 \cdot 7\text{H}_2\text{O}$] and hexahydrate [$\text{MgSO}_4 \cdot 6\text{H}_2\text{O}$] were included as possible precipitates with an initial volume of 0 (Table S2). The initial bulk density of the material was set to 1.3 g/cm^3 . The solution dose used in the column leaching experiments (to saturate 7 cm depth) was converted to units per m^3/m^2 in the model ($3.97 \times 10^{-7} \text{ m}^3/\text{m}^2$ day); this was applied daily to the top surface of the modeled tailings. The 1 m^2 modeled area was extended to 1 m depth, such that the effects of experimental treatments could be extrapolated over longer timescales (up to 1 year). Temperature and relative humidity were set to be constant at $22 \text{ }^\circ\text{C}$ and 40 % respectively, to represent conditions in the laboratory during the experiments (Appendix 4: Table S1). The initial condition for the chemical composition of pore water was based on the leachate chemistry from the acid-leached experimental column (A4) on day 1 of the experiment (Appendix 4: Table S3). The model was built so that the base of the 1 m profile was under-saturated, allowing solution to exit the system freely.

5.3. Results

5.3.1. Direct CO₂ reaction experiment

5.3.1.1. *Changes in material properties*

The tailings within both the acid- and water-treated columns dried over the course of the 28-day long experiment from an initial pore water saturation of 40 %, to values between 3 and 14 % by the end of the experiment (Appendix 4: Table S4). The column that was pre-treated with an acidic solution developed a profile of increasing pore water saturation with depth, with 3 % pore saturation at the surface, 11 % from 5–10 cm, and 15 % saturation in the 10–25 cm interval. The column that was pre-treated with water remained more saturated in the 5–10 cm interval (10 % saturation) and became drier near the surface and at depth (5 % saturation in both the 0–5 cm and 10–25 cm intervals). Poor permeability was noted in trial columns, and it may have inhibited development of a typical saturation profile (where saturation increases with depth) in this column. Alternatively, the tailings in the 10–25 cm depth interval of the water-treated column may have dried comparatively more than the acid-treated column as a result of gas flow into the base of the column. In any case, we observe that pore water saturation in both columns was initially within the ideal range to promote mineral carbonation at ambient temperatures and pressures (20–60 %; Assima et al., 2013; Harrison et al., 2015), but by the end of the experiment carbonation was likely inhibited by suboptimal water content which is known to limit brucite dissolution (Harrison et al., 2015). After four weeks, the column that was pre-treated with water had gained 170 g in mass, whereas the acid pre-treated column had gained 101 g (Appendix 4: Table S4).

5.3.1.2. *Geochemistry and mineralogy of tailings following CO₂ injection*

The abundance of carbon present in both the acid- and water-treated columns increased for all depth intervals. A total of 33 g and 26 g of carbon (i.e., 122 g and 97 g of CO₂) was

sequestered within the water and acid pre-treated columns, respectively, over the course of the experiment (calculated from total carbon data in Appendix 4: Table S5). In both columns, the increase in the amount of carbon within the tailings was highest in the deepest sampled interval (10–25 cm), closest to the supply of CO₂ gas into the system (Appendix 4: Table S5). Within the acid pre-treated column, an increase in the amount of C by 3.1×10^{-3} g C/g tailings was observed for the 0–5 cm interval, compared to the total C content of the initial bulk material, with increases in C of 4.0×10^{-3} g C/g observed at 5–10 cm depth and 5.0×10^{-3} g C/g at 10–25 cm depth. In comparison, in the water pre-treated column C increased by 4.4×10^{-3} g C/g from 0–5 cm, 5.8×10^{-3} g C/g between 5–10 cm, and 5.8×10^{-3} g C/g from 10–25 cm.

The amount of brucite present in chrysotile mine tailings is typically underestimated by Rietveld refinement of XRD data because the (0 0 1) peak of brucite overlaps with the (0 1 0) peak of lizardite, whose anisotropic shape is difficult to model (Turvey et al., 2017). It is also well-established that the accuracy of Rietveld refinements declines for phases present at low abundance (e.g., Wilson et al., 2006; Turvey et al., 2017). As such, although the bulk tailings material contained an estimated 0.6 wt. % brucite and was spiked with an additional 2.0 wt. % brucite, our Rietveld refinement results report an average of only 1.2 wt. % brucite in the spiked material that was used in the column experiments (Appendix 4: Table S6). However, the refined abundance of brucite declined in all sampled intervals in both columns after completion of the experiment. The maximum refined abundance of brucite remaining in the columns was 0.8 wt. % within the 10–25 cm interval in the water pre-treated column. Nesquehonite was not present in the initial bulk material, but was present at refined abundances of up to 0.9 and 2.2 wt. % in the 10–25 cm interval of the acid and water columns, respectively. No sulfate phases

were detected using XRD within the acid column even though these tailings were pre-treated with dilute sulfuric acid (Appendix 4: Table S6).

5.3.2. Acid leaching experiment

5.3.2.1. *Changes in material properties*

A red, rusted layer was visually observed to form just under the surface of the acid-leached tailings in all four replicate experiments. This layer migrated downwards toward the base of each of the acid-leached columns over the course of the 4-week long experiment (Appendix 4: Fig. S4). After four weeks, the depth of the rusted layer varied within and between replicates, but it generally intersected the transparent walls of the columns between 2 and 5 cm (Appendix 4: Fig. S2). Dissection of the columns revealed that the rusted horizon was domed in shape, reaching greater depths at the edges of the column near the walls, whereas most of the rusted material occurred near the surface of the tailings between 0.5 and 2 cm depth (Appendix 4: Fig. S3).

At the completion of the experiment, the average bulk density of the leached tailings was lower in the upper 2 cm (1.1 g/cm^3 in both acid and water leached columns). The average bulk density remained unchanged relative to the initial value from the start of the experiment (1.3 g/cm^3) in the 2–5 cm interval for both the water- and acid-leached columns. Finally, average bulk density increased in the deepest interval: 1.5 and 1.4 g/cm^3 in the water- and acid-leached columns, respectively (Appendix 4: Table S7). Average porosity also increased to 0.6 in the upper 0–2 cm after both the water and acid treatments and it decreased to 0.4 within the deepest interval in the water-treated column from an initial value of 0.5 (Appendix 4: Table S7).

5.3.2.2. *Leachate chemistry*

The concentration of Mg in the first sample of leachate collected from each of the water and acid columns was approximately 900 mg/L (Appendix 4: Table S8). Mg concentrations in the leachate from the water-leached experiment fell quickly from this initial high, stabilising at approximately 70 mg/L, whereas Mg concentrations in leachate samples from the acid-treated columns increased quickly and stabilised at approximately 2400 mg/L (Fig. 5.1). Mg concentrations, and volume of solutions recovered, were used to calculate the maximum amount of nesquehonite that could precipitate from the leachate and its potential to store carbon (Appendix 4: Table S10).

The concentration of Si in the first leachate sample collected from each of the treatments was approximately 30 mg/L. The amount of Si in solution decreased over the first 12 days of the experiment when it stabilised at ~1 mg/L (Fig. 5.1). Fe, Ni, Zn and Co are also observed in the initial leachate from both water and acid leaching experiments at parts per billion (ppb or $\mu\text{g/L}$) concentrations, but they were absent or present at concentrations near detection limits for the remainder of the experiment (Appendix 4: Table S8, Fig. 5.1). The concentration of Fe in solution was more variable in both experiments, with occasional leachate samples having elevated abundances; however, Fe was generally below detection and did not exceed 0.5 mg/L (Fig. 5.1).

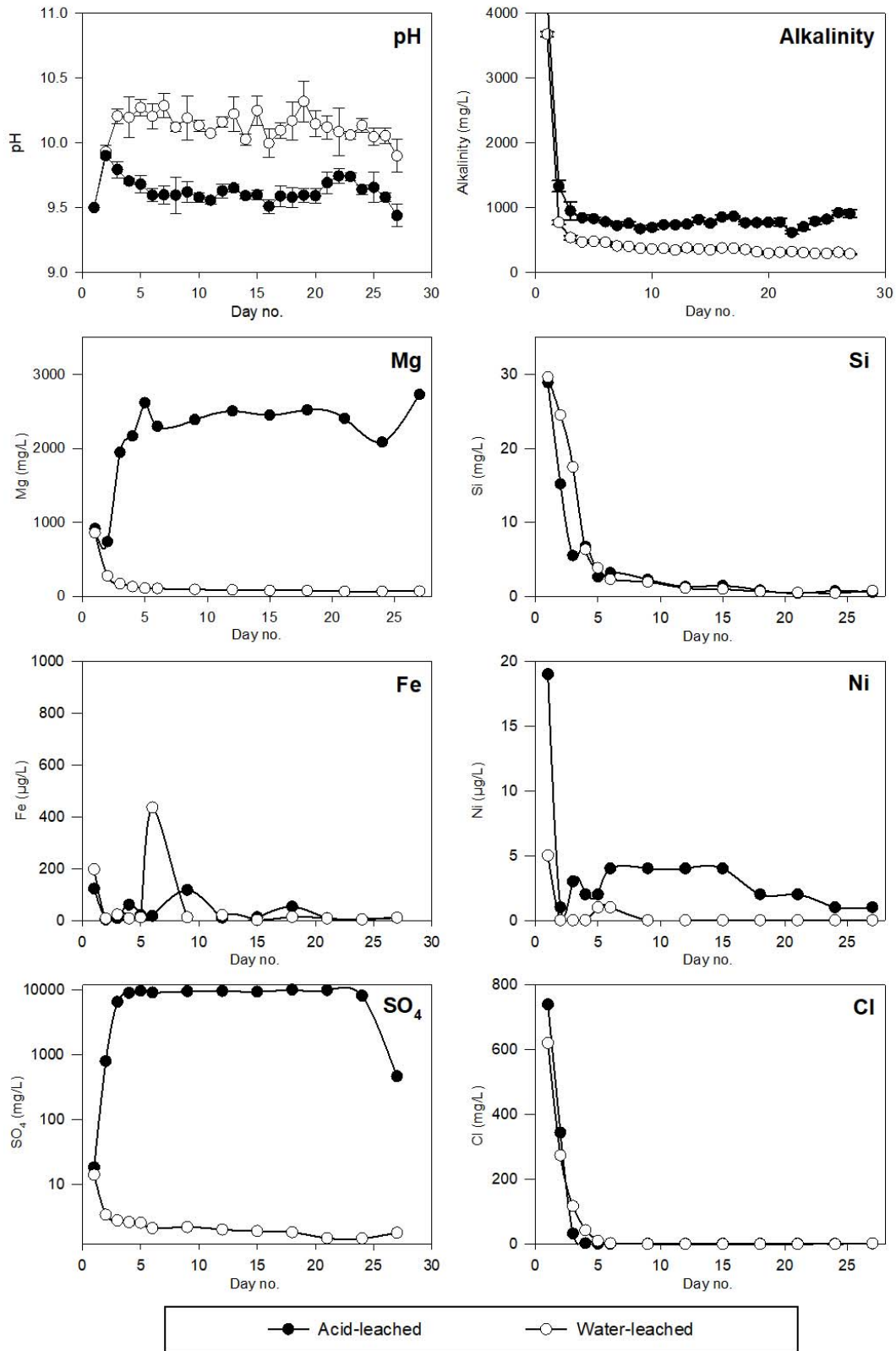


Figure 5.1. Measured leachate chemistry from heap leaching experiment.

5.3.2.3. *Geochemistry and mineralogy of leached tailings*

Mass movement appears to have occurred in all eight of the columns used for the acid- and water-treated experiments. This is evident from changes to the dry mass of the tailings after 28 days of treatment. The dry mass of tailings in the 0–2 cm samples decreased to values between 13.6 g and 15.1 g from an initial value of 17.2 g. The samples collected from 5–7 cm depth experienced a gain in dry mass, increasing from an initial value of 17.2 g to values of 18.7–20.5 g. The middle 2–5 cm zone initially contained 25.8 g of material, and did not change substantially after the experiments, with final mass ranging between 24.3 to 26.9 g. As such, changes in geochemistry are reported herein either as changes in concentration, as relative enrichment or depletion, or as mass loss or gain from the entire column (0–7 cm).

The isocon method (Grant, 1986) is used here to visualise relative enrichment or depletion of elements (some of which are given as major oxides) with respect to Al, which is assumed to be a relatively immobile component in this system (Grant, 1986; Oskierski, 2013). Elements that plot above the isocon, which is drawn through the data point for Al, are considered to be relatively enriched in the altered material, whereas elements falling below the Isocon line are considered to be depleted in the altered material. The elemental composition and mineralogy of water-leached residues are similar to those of the untreated tailings used as starting material. All measured elements and major oxides (MgO, SiO₂, Al₂O₃, Fe₂O₃, CaO, Na₂O, Cr₂O₃, Ni, Co and C) plot close to the Al isocon (Appendix 4: Fig. S5) and XRF data (Appendix 4: Table S11) show that the maximum variation measured for the concentration of any element or major oxide, compared to the initial bulk material, is –0.5 wt. % for MgO in the 0–2 cm interval of replicate W2.

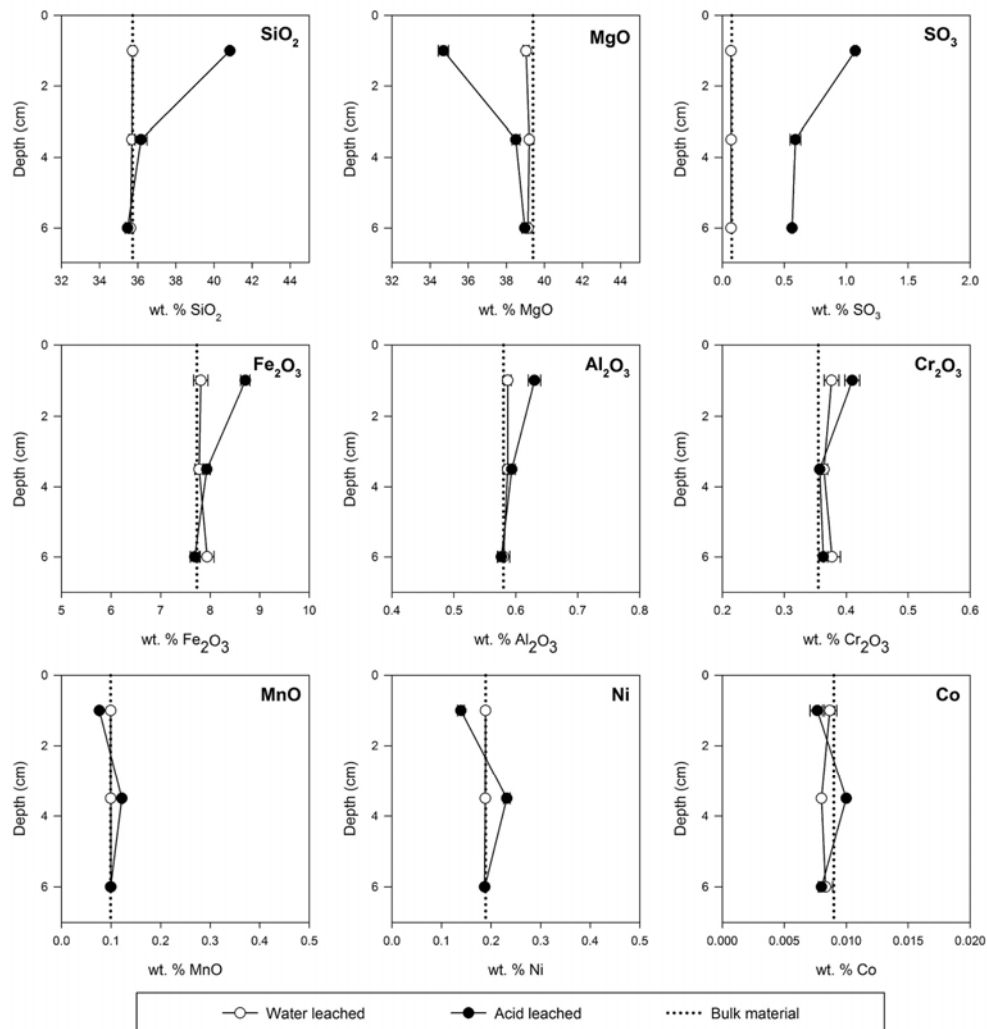


Figure 5.2. Average XRF data (with error bars extending to minimum and maximum recorded concentrations) for sampled intervals of the acid-leached and water-leached tailings.

The mineralogy of the water-leached samples is also similar to that of the untreated tailings (Appendix 4: Fig. S6, Table S12), with a maximum variation of 3.3 wt. % in the refined abundance for serpentine minerals, which is within the range of error for Rietveld refinements of similar samples [1.1 – 6.1 wt.% for synthetic serpentinite tailings containing 74.9–88.8 wt.% serpentine; Turvey et al. (2017)]. On the other hand, the tailings that were leaching with acidic solution are markedly altered (Fig. 5.2, Appendix 4: Fig. S5). The 0–2 cm interval in the acid-leached columns is depleted by 4.7 wt. % in MgO (equivalent to 12 % relative of the initial MgO content), and by 0.12 wt. % in C

(equivalent to 25 % relative of the initial C content) (Fig. 5.2, Appendix 4: Table S11). An average of 7.2 % relative of the total initial mass of Mg has been lost from the columns as a consequence of acid-leaching, having been mobilised into the leachate solutions. In comparison, only 0.8 % relative of the total mass of Mg has been leached from columns that were treated with water.

SiO₂, Fe₂O₃, Al₂O₃, Cr₂O₃ consistently plot along the isocon, indicating that they behave similarly under the experimental conditions (Appendix 4: Fig. S5). XRF data reveal that SiO₂, Fe₂O₃, Al₂O₃, and Cr₂O₃ are all more concentrated in the 0–2 cm interval after acid-leaching. Our XRF data also indicate that SO₃ is enriched in all three depth intervals, but particularly at 0–2 cm, where it is present at concentrations up to 1.1 wt. % (Fig. 5.2). NiO, MnO and CoO on the other hand are depleted in concentration between 0–2 cm, plotting below the isocon, but they are slightly enriched in the 2–5 cm interval (Fig. 5.2, Appendix 4: Fig. S5). Carbon and MgO are depleted from 2–5 cm, although to a lesser extent than within the 0–2 cm interval (Appendix 4: Fig. S4). From 5–7 cm, all elements in the acid-leached columns are present at similar concentration to those within the starting tailings material and the samples from the water-leached column, with the exception of C and CaO, which show a slight enrichment (Fig 5.2, Appendix 4: Fig S5).

Synchrotron XFM maps of the thin sectioned columns (W4 and A4) are shown in Figure 5.3. Maps of the water-leached column show relatively uniform concentrations of all detectable elements with depth. Elemental concentrations in the acid-leached column are more variable, showing lower concentrations of Fe, Mn, Ni, Cr in the upper 1 cm of the column, followed by a progression of horizontal bands that are highly enriched in these elements at different depths within the column. Fe, Cr and Co appear most enriched between 1 and 2 cm, and Ni and Mn between 1.5 and 2.5 cm (Fig. 5.3).

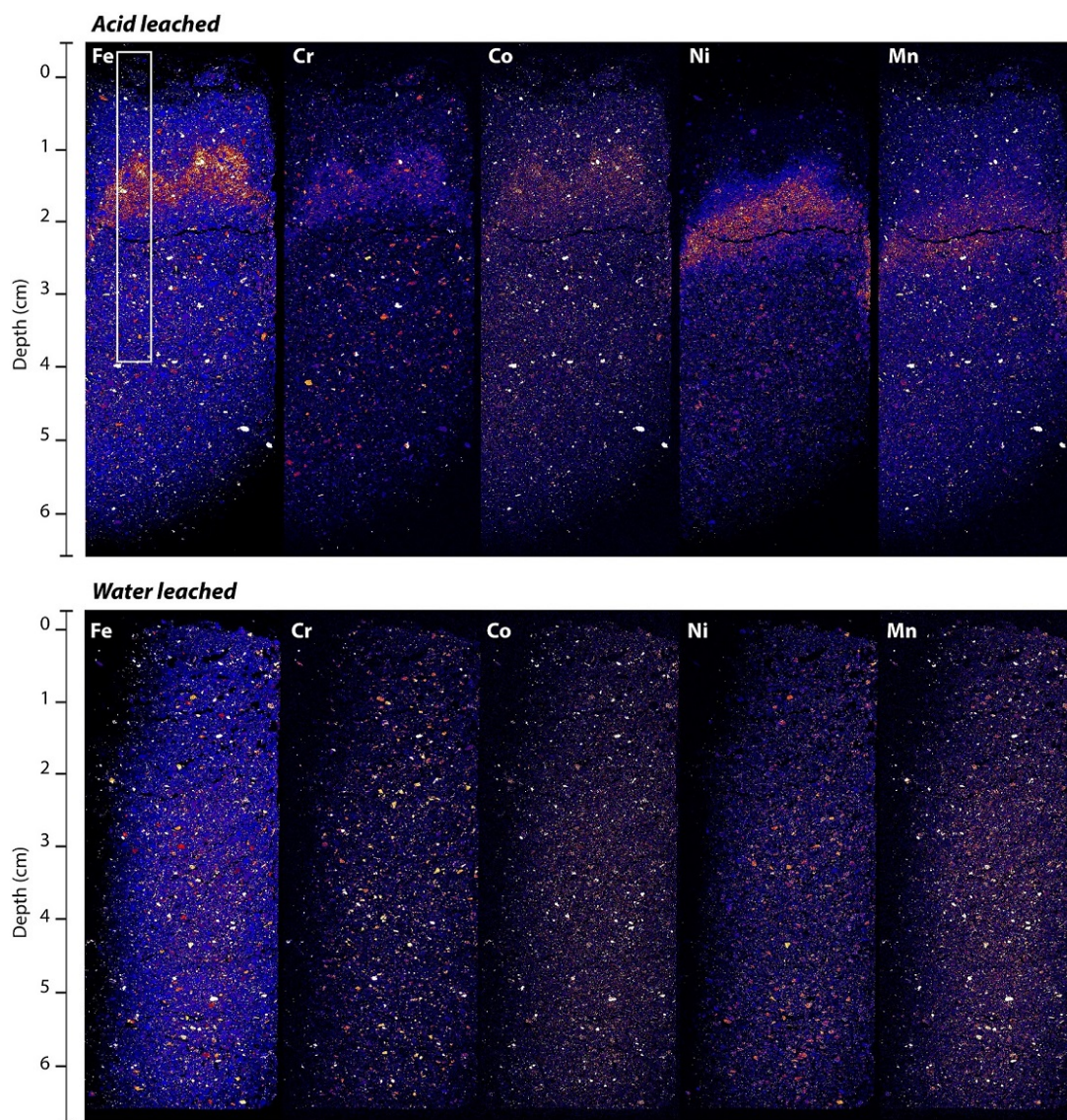


Figure 5.3. Overview element concentration maps of the acid-leached (above) and water-leached column thin sections (below), showing the regions concentrated in Fe, Cr, Ni, Mn and Co. The boxed region in white shows the region selected for high resolution mapping (Figure 5.5).

Below this region, all elemental concentrations in the column material appear similar to those in the water treated column. These bands appear to correspond with the domed shape and approximate depth of the rusted orange horizon. Although an enrichment in sulfur was observed in our XRF data for the acid-leached columns (Fig. 5.2, Appendix 4: Table S11), it is not present at comparable concentrations in the thin-sectioned column (A4) that was imaged with synchrotron XFM. This is likely because sulfate minerals were

dissolved and flushed out of the column during ethanol infiltration as part of the embedding process.

Brucite and hydromagnesite are present at much lower abundance (average 0.4 wt. % and 0.0 wt. % respectively) in the 0–2 cm interval of the acid-leached columns compared to the initial material which contained 1.2 wt.% brucite and 2.9 wt.% hydromagnesite (average of three sub-samples of bulk material; Appendix 4: Table S12). Nesquehonite was not observed to be present in XRD patterns for any of the acid- or water-leached columns. Sulfate mineral phases are also not observed in XRD patterns, although XRF data suggest an average of 1.1 wt. % SO_3 is present within the 0–2 cm interval of the acid-leached columns. Some Mg-sulfate minerals are known to decompose to amorphous phases, including under laboratory conditions and in serpentinite mine tailings (Chipera and Vaniman, 2007; Mills et al., 2011). XRD peaks for serpentine appear qualitatively lower in intensity in tailings from the 0–2 cm interval of the acid leached column compared to patterns collected from the 2–5 cm and 5–7 cm intervals (Appendix 4: Fig. S6); however, the refined abundance for serpentine minerals + amorphous content does not change substantially (Appendix 4: Table S12).

Dissolution features such as pitting are observed in serpentine grains in the acid-leached column, particularly in the upper 1 cm (Fig. 5.4A–C). In some grains, pitting is extensive, producing a porous texture (Fig 5.4D–E). The texture of Fe-oxide (magnetite) grains on the other hand is unaltered as a result of acid leaching. While some weathering features may be a result of passive weathering that occurred during storage of these tailings at the Woodsreef mine, pitting is not observed in BSE images of material subjected to the water leaching treatment (Appendix 4: Fig. S7).

Within the rusted, Fe-rich horizon in the acid-leached column, Figure 5.4F shows a brucite grain (identified as Mg-O composition using EDS, and showing characteristic cleavage) surrounded by a rind of Mg-poor, Fe- and Si-rich material. It is possible that this was a serpentine rind, from which Mg has been leached, leaving a residue rich in Si and Fe. In the same image, a dendritic Fe-oxide precipitate is observed on the surfaces of tailings grains and within pore spaces (Fig. 5.4F–G).

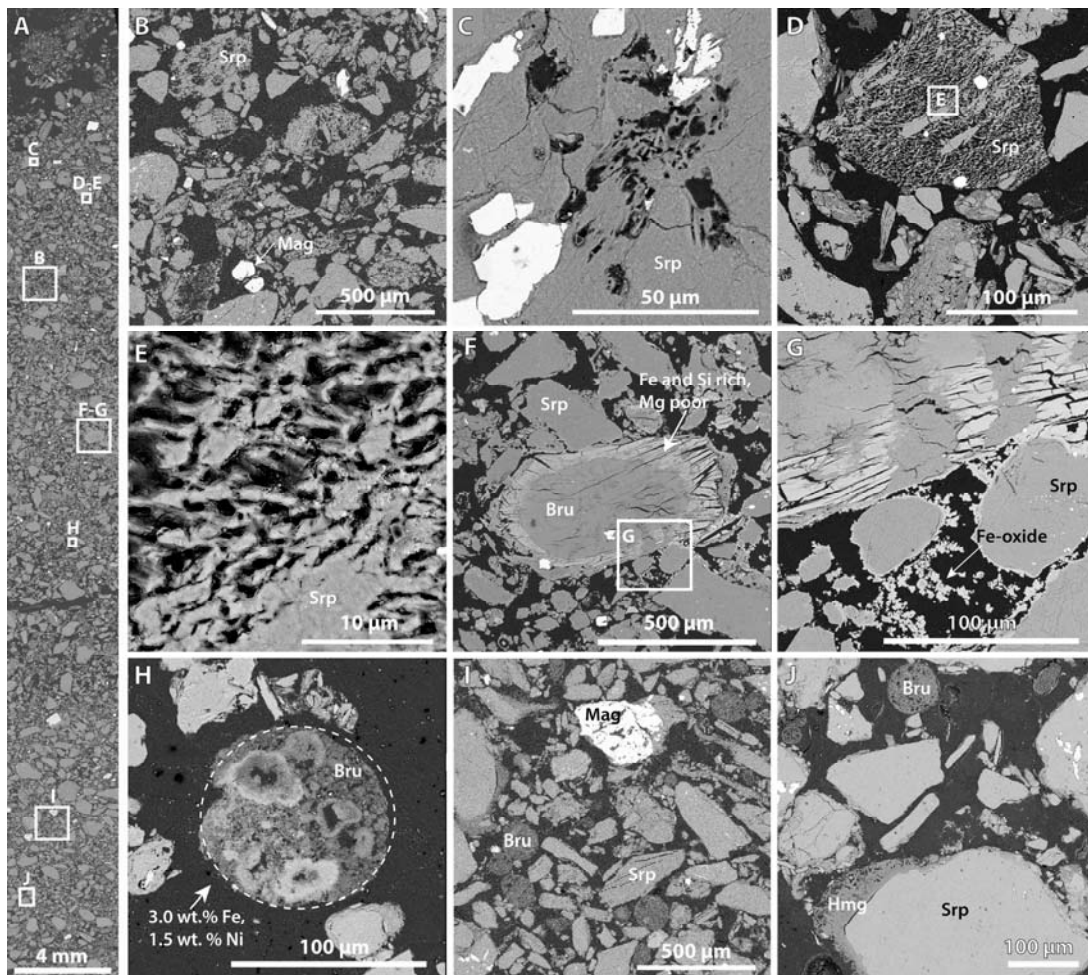


Figure 5.4. SEM-BSE micrographs. (A) Region selected for high-resolution XFM mapping (outlined in Fig. 5.3). (B) Weathered serpentine grain. (C) Pitting and areas of leaching on the serpentine grain. (D) A porous, pitted serpentine grain. (E) Magnified view of D. (F) Brucite grain with Fe and Si rich rind. (G) Magnified view of F, showing Fe-oxide precipitates. (H) Transition-metal-rich brucite grain within the rusted zone. Quantitative element concentrations were extracted from the circled region from synchrotron XFM data. (I) Transition-metal-rich brucite

grain from slightly deeper in the rusted zone, containing a higher Ni:Fe ratio. Quantitative element concentrations were extracted from the circled region from synchrotron XFM data. (J) Brucite with low trace metal content is present below the rusted region and hydromagnesite is observed to precipitate on grain surfaces.

Grains of synthetic brucite, which was introduced as a 2 wt. % spike, are distinguishable from naturally-occurring brucite from the Woodsreef mine by their spherical shape and porous texture (Fig. 5.4H–J, Appendix 4: Fig. S7A–B). Spherical grains of synthetic brucite are observed ubiquitously throughout the water-leached column (Appendix 4: Fig. S7A) and at the base of the acid leached column (i.e., Fig 5.4I). These grains do not contain elevated levels of first row transition metals (as measured with EDS and XFM). Brucite grains are absent within the upper 1 cm of the acid-leached column (Fig. 5.4A–B); however, from approximately 1–3 cm depth within the acid-leached column (A4) the synthetic brucite grains (which are easier to identify than natural brucite grains) are enriched with wt.-% level concentrations of transition metals (i.e., Fig. 5.5), and often contain particularly transition-metal-rich agglomerations (i.e., EDS measures 6 wt. % Ni in lighter shaded, high mean atomic number, areas in Fig. 5.4H). Figure 5.5 shows average elemental compositions (Fe, Cr, Co, Ni and Mn) of 91 synthetic brucite grains within the high resolution XFM map (i.e., quantitative elemental abundance from circled regions that encompass each entire grain, as shown in Fig. 5.4H), which are plotted against the average elemental composition of the sample as measured across the width of the XFM map. Naturally occurring brucite grains also appear to contain similarly high concentrations of metals.

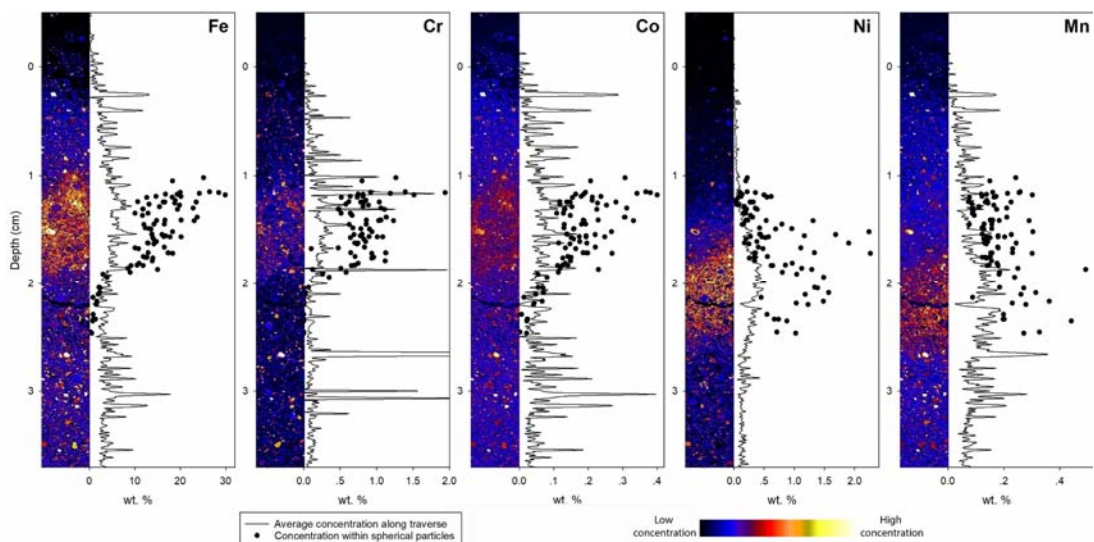


Figure 5.5. XFM element concentration maps (Fe, Cr, Co, Ni and Mn) are shown alongside plots of the average element concentrations of the sample as measured across the width of the XFM map. Black dots represent the depth and element concentrations within 91 grains of transition-metal-rich, spherical synthetic brucite.

5.3.2.4. Mineralogy of leachate precipitates

The precipitates that formed by evaporation of leachates from the water-treated columns are composed of relatively pure nesquehonite (Fig. 5.6A, Appendix 4: Fig. S8A). However, precipitates formed from evaporation of leachates from the acid-treated columns are dominated by the Mg-sulfate minerals, epsomite ($\text{MgSO}_4 \cdot 7\text{H}_2\text{O}$) and hexahydrate ($\text{MgSO}_4 \cdot 6\text{H}_2\text{O}$), with minor nesquehonite and gypsum ($\text{CaSO}_4 \cdot 2\text{H}_2\text{O}$; Fig. 5.6B, Appendix 4: Fig. S8B). The precipitates from the water-leached columns contain an average of 7.90 % C (range 7.69–8.14 wt. % C, $n = 4$; Appendix 4: Table S13). This result is consistent with the observed mineralogy, which is dominated by nesquehonite (stoichiometrically 8.68 wt. % C), with minor chlorartinite [$\text{Mg}_2(\text{CO}_3)\text{Cl}(\text{OH}) \cdot 3\text{H}_2\text{O}$] and artinite [$\text{Mg}_2(\text{CO}_3)(\text{OH})_2 \cdot 3\text{H}_2\text{O}$] which contain 5.58 and 6.11 wt. % C respectively (Appendix 4: Fig. S8A). Chlorartinite likely formed from leachates produced in the initial two to three days, which contained hundreds of mg/L Cl concentrations in both water and

acid leached samples (Appendix 4: Table S8). Cl stabilised at <1 mg/L after approximately a week (Appendix 4: Table S8). All three replicates contain approximately 0.01 g of C each, which agrees well with the estimated carbon trapping potential calculated from Mg concentrations in the leachate from sample W4 (i.e., potential to form 0.11 g of nesquehonite, containing 0.01 g of C; Appendix 4: Table S10). Precipitates from the acid-leached column, which were dominated by Mg-sulfate phases, contain an average of 0.24 wt. % carbon (range 0.19–0.29 wt. % C, $n = 4$; Appendix 4: Table S13). After multiplying carbon content by the mass of the precipitate, it is apparent that the precipitates from each of the acid-leached experiments also contain 0.01 g of C (Appendix 4: Table S13). Thus, in spite of the larger amount of Mg leached by the acid treatments, the same amount of carbon was sequestered by the leachate precipitates from the acid- and water-treated columns.



Figure 5.6. Photographs of precipitates formed via evaporation of leachates collected from the heap leaching column experiments. (A) Nesquehonite formed from the water-treated column leachates and (B) Mg-sulfate phases formed from acid-treated column leachates.

5.3.2.5. *Geochemical modelling*

The MIN3P model of the acid-leached treatment shows the progression of acidic conditions downwards through the column with time (Fig. 5.7). The migration rate of the pH front appears to slow slightly over time: acidity is neutralised (where pH increases

from <4.5 to >4.5) between depths of 8 cm (pH 2.3) and 9 cm (pH 7.5) after 28 days, between 30–31 cm after 6 months, and between 64–65 cm after 1 year (Fig. 5.7).

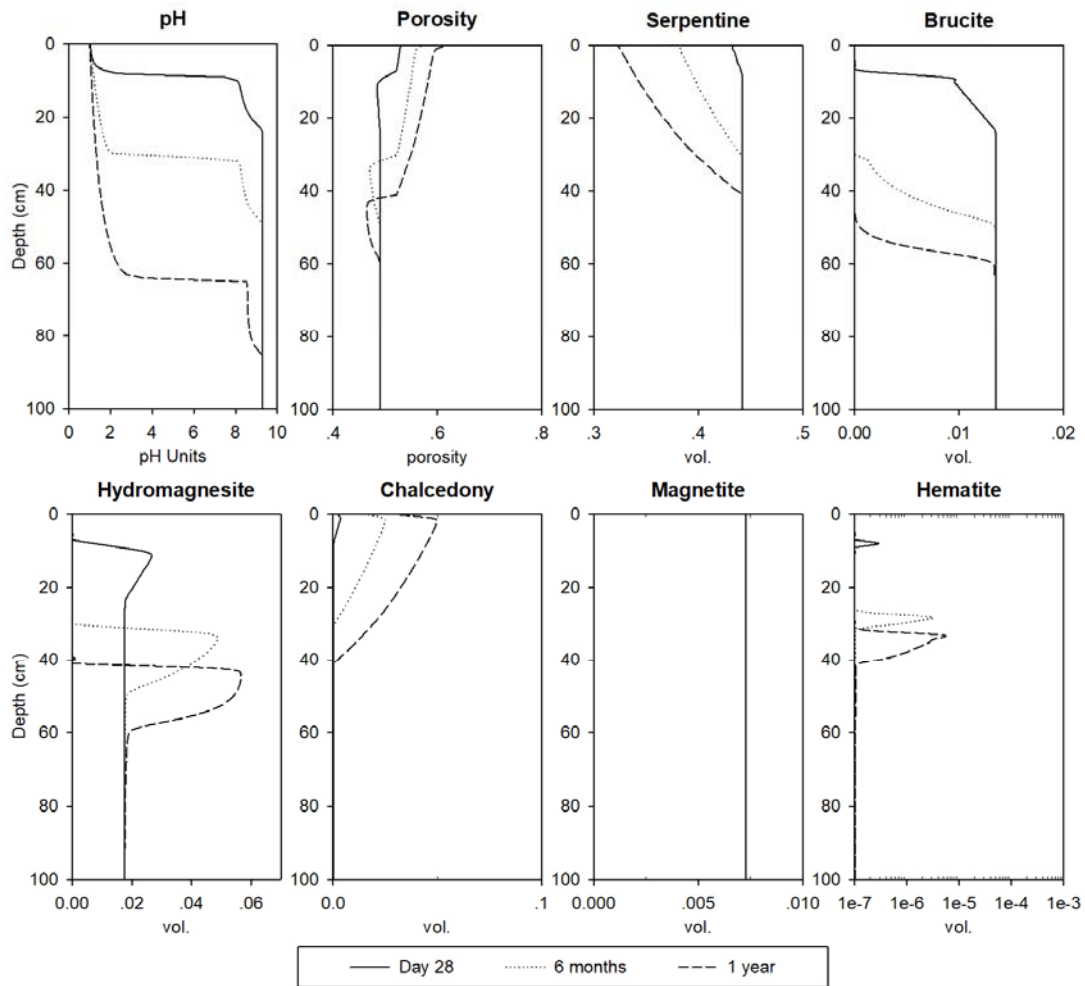


Figure 5.7. MIN3P modelled pH, porosity, and mineral abundance reported as a volume fraction.

Dissolution of brucite, hydromagnesite, chrysotile, calcite, forsterite and magnetite are initiated with the arrival of the acidic front, and brucite, hydromagnesite and calcite buffer pH at approximately 8.5 until they are consumed (Fig. 5.7). The dissolution of chrysotile coincides with saturation of chalcedony. Hydromagnesite precipitates just below the neutralisation horizon (Fig. 5.7). The zone in which hydromagnesite precipitates not only migrates to greater depths in response to the migrating pH front, but

hydromagnesite also accumulates over time within this zone, reaching three times its initial abundance (reported here as a volume fraction) at approximately 34 cm depth after 1 year of acid leaching (Fig. 5.7). At 7 cm depth, equivalent to the base of the experimental columns, Mg concentrations rise rapidly and stabilise at approximately 2300 mg/L within ≈ 10 days as water enriched in Mg from the dissolution of brucite, hydromagnesite and chrysotile at shallower levels within the column flows downwards. These model results resemble the trend in measured concentrations of Mg in the leachates from the acid-treated columns for the first 20 days, however, compared to experimental results, the model predicts lower pH (by 1–2 pH units) throughout the duration of the experiment, and faster progression of the acidic front (A4, in Appendix 4: Table S8; Fig. 5.8).

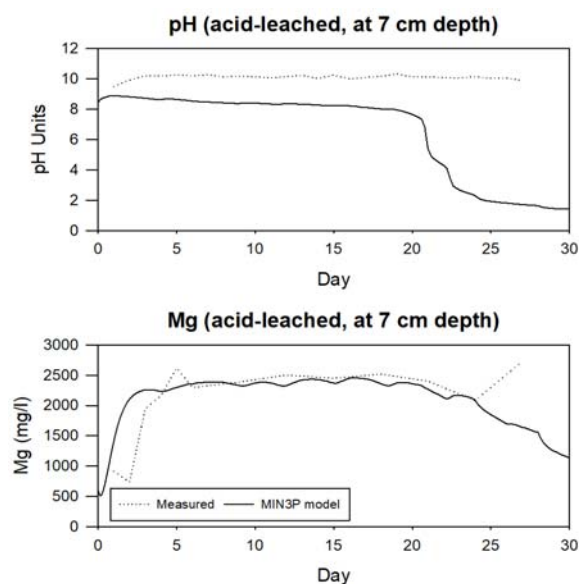


Figure 5.8. Comparison between measured and modelled results for Mg concentration (A4) and pH (average of all acid leached replicates).

After the acidic front has migrated below a particular depth (i.e., 7 cm after 21 days), Mg concentrations are predicted to fall and stabilise at a lower concentration (i.e., 500 mg/L at 7 cm depth), as hydromagnesite and brucite have been consumed, and leaching of Mg

is dominated by dissolution of chrysotile (Appendix 4: Fig. S9). The concentration of Mg within leachates appears to accumulate in solution, such that Mg concentration increases when examined at increasing depth intervals (i.e., 500 mg/L at 7 cm depth, and 1500 mg/L at 20 cm depth). Below the migrating pH front, (i.e., at 1 m depth), Mg concentrations remain steady at approximately 2300 mg/L Mg for the duration of the model (1 year; Appendix 4: Fig. S9).

The pore fluids are undersaturated with respect to magnetite, which is predicted to dissolve in the acidified zone, although not to an extent noticeable in Figure 5.7. Slight dissolution of magnetite also occurs as a constant reduction in volume fraction throughout the whole depth of the profile, indicating dissolution that is not related to progression of the acidic front. Fe released during dissolution of Fe-bearing chrysotile and magnetite is precipitated as hematite in the simulation, which predicts that pore water is saturated with respect to hematite throughout the profile. Hematite accumulates just above the neutralisation front, and increases in vol. % abundance over time as it is re-dissolved in more acidic conditions at shallower depths, and accumulated just before the neutralisation horizon (Fig. 5.7). After 28 days reaction time, this zone of hematite accumulation is within 3–5 cm depth. When magnetite is excluded from the simulation, Fe from chrysotile dissolution precipitates approximately in the same locations, although slightly deeper (4–6 cm depth after 28 days) and to a lesser extent. Pore fluids remain understaturated with respect to nesquehonite and the Fe-bearing solid phases, ferrihydrite and Fe-hydroxide, although precursor ferrihydrite is more likely to have precipitated than hematite in these experiments. The water is also predicted to be unsaturated with respect to gypsum, epsomite and magnesium hexahydrate, with all sulfate expected to remain dissolved in solution.

5.4. Discussion

5.4.1. Direct reaction with flue gas as a short-term carbonation treatment

The decrease in brucite abundance in all depth intervals of the CO₂ reaction experiment indicates that this mineral has reacted with the CO₂ supply. It is difficult to accurately quantify brucite due to the substantial underestimation of brucite abundance by XRD (section 5.3.1.2), however refined abundance drops from an average of 1.2 wt. % in the initial material, to between 0.3 and 0.8 wt. % after the experiment. There is little change in the total mass of hydromagnesite in each column, (-5 g in the water pre-treated column, equivalent to a relative decrease of 5 %, and a 7 g increase in the acid pre-treated column, or relative increase of 7 %), which is calculated using refined hydromagnesite abundances from XRD data, and the mass of each sampled interval. These differences most likely result from a small amount of variation in the initial bulk material (hydromagnesite ranges from 2.7 to 3.1 wt. %) and inherent relative error in Rietveld refinement of hydromagnesite, which has been estimated at up to 55 % relative for synthetic serpentine-rich tailings containing 1.1 wt. % hydromagnesite, using different instruments (Turvey et al., 2017). Nesquehonite was not present in the untreated tailings material used in these experiments, but it is present at up to 2.2 wt. % in the water pre-treated column (10–25 cm) and up to 0.9 wt. % in the acid pre-treated column (10–25 cm) after the experiments. The amount of newly formed nesquehonite can only account for 22 % relative of the total mass of carbon gained in the water pre-treated column, or 11 % relative in the acid pre-treated column, although it is likely that systematic underestimation of nesquehonite also occurs in Rietveld refinements, which may account for some of this discrepancy (Turvey et al., 2017; Wilson et al., 2009b). On the other hand, Harrison et al. (2015) report unaccounted carbon in a brucite carbonation experiment that employed similar conditions

of CO₂ injection into an unsaturated column (where 10 % CO₂ gas flowed through a mixture of brucite and quartz with an initial pore water saturation of 35 or 60 %). Harrison et al. (2015) found that an X-ray amorphous carbonate phase, with a composition similar to that of artinite [Mg₂CO₃(OH)₂·3H₂O], was present as a product of brucite carbonation. If the net gain in carbon in our CO₂ reaction experiments was the result of either nesquehonite or artinite formation, 4.1–6.6 wt. % additional nesquehonite, or 5.8–9.4 wt. % artinite would be required to be present. If either or both of these phases were present at such high relative abundance, they should be easily identifiable and their abundances quantifiable from XRD data; however, this is not the case. The amount of Mg required to form the amount of nesquehonite that was detected here (0.1–2.2 wt. %), plus the above calculated abundance of either X-ray amorphous nesquehonite or artinite, could be provided by carbonation of 1.8–6.0 wt. % brucite in the original material. Given the extensive alteration of brucite observed in SEM (Fig. 9a–d), the reaction of the ≈2.6 wt. % brucite in the columns with CO₂ likely provides the majority of the Mg in crystalline and/or amorphous Mg-carbonate phases. However, the initial abundance of brucite is likely to be higher than estimated from Rietveld refinements (i.e., 0.6 wt. %; Appendix 4: Table S12), and not all of the brucite within the columns reacted with CO₂, thus, serpentine and pre-existing hydromagnesite in the bulk tailings sample may also have contributed Mg to form new Mg-carbonates during our experiments.

Carbonation of brucite (and serpentine) proceeded quickly under elevated CO₂ concentrations employed in our experiments. Within 28 days, both experiments trapped and stored a similar mass of CO₂ (20.1 g CO₂/kg and 16.1 g CO₂/kg in the water and acid pre-treated columns respectively) to that achieved during 33 years (from mine closure in 1983, until collection of the bulk material in 2016) of passive carbonation via air capture at the Woodsreef Mine (17.6 g CO₂/kg). This corresponds to a CO₂ sequestration rate of

261.1 g CO₂/kg/y in the water pre-treated experiment, and 209.8 g CO₂/kg/y in the acid pre-treated experiment, both of which far exceed previous estimates of passive carbonation (as a mass of CO₂ sequestered per kg of tailings) over the past three decades, of 0.8 to 3.9 g CO₂/kg in bulk tailings and 26.4–50.8 g CO₂/kg in surface crusts (0–2 cm depth) from Turvey et al. (2017), and 8.0 g CO₂/kg averaged over the upper 1 m of the tailings pile in Chapter 4 (calculated from data in Table 1, Chapter 4). The experiments conducted by Harrison et al. (2015), which used mixtures of brucite and quartz instead of chrysotile mine tailings, also show rapid carbonation of brucite under similar conditions. Since brucite is present at trace to minor abundances in most ultramafic rocks and mineral wastes, the high rates of CO₂ sequestration measured in experiments such as these can only be maintained while brucite is available for reaction. This treatment option is therefore most useful for fast, short-term carbonation of fresh tailings at the end of the ore processing circuit of an operating mine. Carbonation of serpentine will likely continue, however the cementation of grains (as observed in SEM, Fig. 5.9) may have a passivating effect (as in Harrison et al., 2015, 2016).

5.4.2. Increase in cementation after reaction with CO₂

The tailings in the two columns that were reacted with CO₂ increased in mass over the course of the experiment. The water pre-treated column gained 170 g and the acid pre-treated column gained 101 g, likely from uptake of CO₂ and H₂O into the crystalline mass of newly formed nesquehonite and possible amorphous Mg-carbonate phase as well as sulfate minerals in the acid pre-treated column. As a result, our XRF data from these columns show a slight decrease in the abundances of other major elements, since they now represent a relatively smaller fraction of the total mass of the treated tailings samples (Appendix 4: Table S5). Carbonate precipitation in these column experiments is visible in

SEM micrographs as cement between grains (Fig. 5.9A–C, I) and as arrays of crystals nucleated on grain surfaces (Fig. 5.9D–H). Development of a carbonate cement such as the one observed here on the landscape scale may benefit tailings management by enhancing slope stability in tailings piles (McCutcheon et al., 2017; Wilson et al. 2009a). On the other hand, cementation may also be self-limiting for mineral carbonation reactions in mine tailings because it prevents ingress of water and atmospheric CO₂ into unreacted pore spaces at depth and also limits evaporation which drives formation of carbonate efflorescences (Harrison et al., 2015; Wilson et al., 2009a, 2014).

It is notable that some brucite remains unreacted in these CO₂ injection experiments. This may result because the tailings are partially and heterogeneously saturated such that some pore spaces may not contain enough water to facilitate mineral carbonation reactions (Harrison et al., 2015, 2017). Indeed, pore water saturation levels dropped well below the reported optimum range (35–60 %) defined by Assima et al. (2013) and Harrison et al. (2015) by the end of the experiment, reaching values as low as 3% pore saturation.

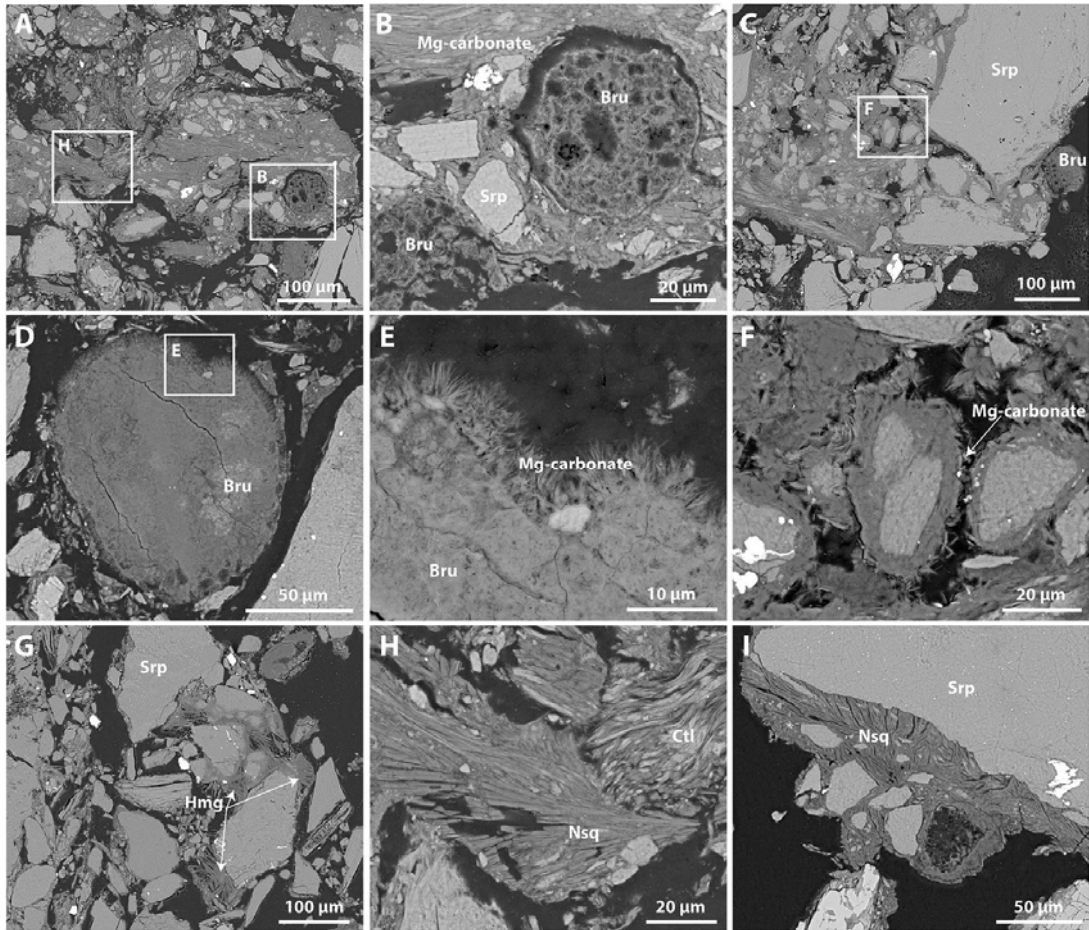


Figure 5.9. SEM-BSE micrographs of hand samples taken from the base (20–25 cm depth) of the columns with 10 % CO₂ gas. (A) Mg-carbonate cementation (water pre-treated column). (B) Enlarged view of synthetic brucite grains surrounded by carbonate cement in A. (C) Overview of Mg-carbonate cementation (water pre-treated column). (D) Flakey Mg-carbonate precipitate on a synthetic brucite grain surface (water pre-treated column). (E) Enlarged view of flakey Mg-carbonate on brucite in region shown in D. (F) Enlarged view of flakey Mg-carbonate precipitate coating a serpentine grain shown in C. (G) Hydromagnesite platelets as precipitates on serpentine grain surfaces and cement between grains (acid pre-treated column). (H) characteristic blocky morphology of nesquehonite, interspersed with chrysotile (lighter grey). (I) Nesquehonite precipitate on serpentine (water pre-treated column)

5.4.3. Acid heap leaching produces high-Mg leachates

Solutions produced by repeatedly acid leaching tailings contain approximately 24 times more Mg compared to those produced by leaching the same material with deionised water

(Fig. 5.1; Appendix 4: Table S10). While some of this Mg is sourced from dissolution of existing Mg-carbonate minerals (i.e., hydromagnesite) in the bulk Woodsreef tailings, and brucite, SEM and XFM data reveal substantial leaching of serpentine grains in the upper 1 cm zone of the column (Fig. 5.4), indicating that dissolution of serpentine minerals is occurring, and due to its high abundance (86 wt. %) is likely to be an important source of Mg for carbonation reactions.

Our reactive transport model extends our understanding of geochemical processes as a result of treatments at a larger spatial (1 m³ profile) and temporal (1 year) scale. The model corresponds well to measured leachate chemistry (at 7 cm depth, which is the base of the column) within the initial three weeks of the experiment, however the model predicts that the acidic front reaches 7 cm depth at day 20 (Fig. 5.8). Measured results indicate a slower progression of the front, with alkaline leachates measured until the end of the experiment on day 28. This can be explained by the systematic underestimation of carbonate mineral abundances by Rietveld refinement of XRD data, and the likely presence of X-ray amorphous Mg-carbonate (Chapter 4; Turvey et al., 2017). The MIN3P model uses initial hydromagnesite abundance from refined XRD data (2.9 wt. %; average of three sub-samples of bulk material), however total carbon data from sub-sample Bulk-1 (which contains 3.1 wt. % hydromagnesite according to XRD data) indicates that an additional 0.5 wt. % hydromagnesite may be present. In addition, while pyroaurite is expected to dissolve under acidic conditions and contribute Mg to solution, it is not included in the model because the dissolution rate law for this minor phase has yet to be determined. As such, the underestimated abundance of carbonate phases in the model imparts a lower pH buffering capacity, such that the acidic front is predicted to progress more quickly than was observed in our experiments.

Modelling of Mg concentrations over a time period of 1 year, at different depths within a 1 m profile of tailings, and treated daily with acidic solution (0.08 M H₂SO₄), reveal two main stages of Mg release. The two stages are at work simultaneously and where they occur depends on the evolving depth of the neutralisation front. In the first stage, above the neutralisation front, Mg concentrations peak at approximately 2400 mg/L and are predominantly controlled by dissolution of hydromagnesite and brucite. Then, when the acidic front passes below the observed depth, Mg concentrations begin to decline and stabilise at a lower concentration (i.e., after 20 days, modeled Mg concentrations at 7 cm depth drop from ~2400 mg/L and decline to ~500 mg/L) when Mg-release transitions to being driven by chrysotile dissolution (Appendix 4: Fig. S9). During this stage, where serpentine dissolution dominates, Mg concentrations are predicted to increase with increasing depth. At 7 cm depth, Mg concentrations are predicted to be approximately 500 mg/L, while at 20 cm depth, still within the acidified zone, above the acidic front, they are approximately 1500 mg/L (Appendix 4: Fig. S9). This indicates that once the initial Mg-carbonates have been dissolved by the acidic solution, Mg concentrations increase with increasing treated thickness of the pile, and appear to approach the concentrations observed in the initial Mg-carbonate and brucite dissolution pulse. However, progression of the acidic front also appears to slow with time; it is predicted to reach 7 cm depth after 20 days, 20 cm after 84 days, and 65 cm after a year. We suggest this is due to increased saturation and water-logging of the profile (pore saturation increases to approximately 90 % within 10 days at 7 cm depth), such that hydraulic properties begin to control progression of the acidic front. Poor permeability was observed to limit the effectiveness of acid treatments in field experiments (Chapter 4; McCutcheon et al., 2017), thus layering of tailings with coarser waste rock, as suggested

in Entezari Zarandi et al. (2017) would likely be beneficial to maintaining high reaction rates in heap leaching treatments for mineral carbonation.

The MIN3P model reveals that the Mg concentrations measured in experimental leachates over a 4-week period are indicative of peak Mg release due to dissolution of pre-existing brucite and hydromagnesite. The model predicts that leaching of brucite and hydromagnesite occurs where pore water is acidic, and hydromagnesite is re-precipitated below the acidic front where pH is alkaline (Fig. 5.7). Since the measured pH of leachate recovered from the acid-treated columns is maintained at >9 throughout the duration of the experiment (Fig. 5.1), leaching of Mg-carbonates in the deeper portion of the column is expected to be negligible (Fig. 5.7). SEM and XFM data reveal a lack of hydromagnesite and brucite, and substantial leaching of serpentine grains in the upper 1 cm zone of the column (Fig. 5.4), indicating that dissolution of serpentine minerals is occurring, and due to its high abundance (86 wt. %) is likely to be an important source of Mg for carbonation reactions once acidic conditions prevail.

As long as leachate chemistry is measured below the acidic front, Mg concentrations remain consistently high, at approximately 2400 mg/L. However, this model does not take into account surface passivation effects, such as the build-up of a siloxane (Si-rich) layer at the surface of serpentine grains due to the preferential leaching of Mg-rich brucite-like layers (Park and Fan, 2004). The Si-rich framework left behind can collapse to form nano-fibriform (if formed from chrysotile) or amorphous silica (Wang et al., 2006), which can limit further reaction (Assima et al., 2012). Passivation of serpentine and sometimes brucite can also occur via precipitation of Fe-oxides, amorphous Si, and Mg-carbonates on mineral surfaces, which we observe in SEM images of these samples (Fig. 4). In the MIN3P model, chalcedony is saturated only in the regions undergoing

chrysotile dissolution, suggesting that Si is relatively immobile, which explains the low Si concentrations measured in leachate samples (Fig. 1).

If the neutralisation front were to pass 7 cm depth (exhausting the total length of our columns), measured Mg concentrations would likely decline more rapidly toward lower residual Mg leaching rates than those predicted by the model. This is likely to result from the increasing effect of surface passivation over time, the slower dissolution rate of serpentine minerals, and the removal of brucite and hydromagnesite from the columns.

Leachate fluid chemistry reveals little detectable Ni, Fe, Mn, Si, Cr, or Co, indicating that all common transition metals (and Si) are effectively immobilised within the columns (Fig. 1) so long as the depth of the neutralisation front does not exceed the length of a column. The consistent concentrations of dissolved cations and anions measured in leachate replicates, and the solution chemistry predicted by MIN3P modeling, indicates that acid heap leaching of ultramafic tailings could be employed on a long term basis (months to years), and could produce a leachate with reliably elevated (>2000 mg/L) Mg concentrations for mineral carbonation over a long time period.

Assuming that Mg will precipitate as nesquehonite by reaction with atmospheric CO₂, we can calculate the amount of CO₂ sequestration within the precipitates. Table S10 shows that the estimated CO₂ sequestration rate from the water treatment (870 g C/m²/y) is within the range of previous estimates for passive sequestration rates reported for the Woodsreef mine [99–4,874 g C m⁻² y⁻¹ Oskierski et al. (2013) and 229–405 g C/m²/y in (Turvey et al., in prep)]. On the other hand, the Mg concentrations in the acidic leachate have the potential to sequester CO₂ at 21,414g C/m²/y; 1–3 orders of magnitude above passive rates measured in the field at Woodsreef (Oskierski et al., 2013; Turvey et al., in prep), and 5 orders of magnitude above background silicate weathering rates in the nearby

Australian Victorian Alps [0.15–0.47 g C/m²/y; (Hagedorn and Cartwright, 2009)]. It is important to note that these rates are calculated from Mg concentrations that include a pulse of Mg from existing carbonate mineral dissolution, thus some of this carbonation potential simply replaces atmospheric carbon lost from pre-existing carbonate phases (hydromagnesite and pyroaurite) during treatments. However, these rates are still useful and indicate a net offsetting of CO₂ can occur as MIN3P models show that Mg concentrations generated by serpentine dissolution (after removal of pre-existing carbonate minerals) accumulate with depth above the acid leaching horizon, approaching ~2000 mg/L with increasing volume of tailings exposed to acidic conditions (Fig. 5.9). Although we relied upon evapoconcentration and air capture to produce carbonate minerals from the leachate generated in our experiments, a flue gas stream such as the one used in our CO₂ reaction experiments could also be employed as part of a mineral carbonation process route that includes repeated leaching of tailings.

5.4.4. Aqueous sulfate limits effectiveness of carbon sequestration

While the assumption that all Mg is precipitated as nesquehonite (\pm minor artinite and chlorartinite) holds true for the precipitates produced in the water-leaching experiments, it does not for the precipitates produced from acid column leachates. These precipitates are dominated by the Mg-sulfate phases, epsomite and hexahydrate, with minor nesquehonite and gypsum. Nesquehonite appears to have formed first, and arrays of fibrous nesquehonite crystals are enveloped by larger lath-like Mg-sulfate crystals (Appendix 4: Fig. S10). The dominance of Mg-sulfate phases is consistent with sulfate scavenging Mg in solution to form MgSO₄ complexes and prohibiting reaction with dissolved CO₂.

Elemental carbon analysis of precipitates reveals that despite the leachates from the acid-treated experiments having an estimated carbon sequestration potential 24 times that of

those produced by water leaching (based on Mg concentrations, Appendix 4: Table S1), leachates from both acid and water treatments trap the same amount of carbon (approximately 0.01 g in each replicate; Appendix 4: Table S13). This means that only 4 % of the potential carbon sequestration capacity is being realised by evaporation of leachates produced in the acid-leaching trial (Appendix 4: Table S13). The carbon content within precipitates obtained from water leachates is also lower than expected (67–75 % of the predicted C mass; Appendix 4: Table S13) given that samples are composed almost entirely of Mg-carbonate phases (Appendix 4: Fig. S8A). One reason for this discrepancy may be that Mg concentrations were only analysed for leachate samples from replicate columns A4 and W4, whereas the carbon content of precipitates was measured for all four replicate columns for both the acid- and water-leached tailings. Moreover, after the first week of the experiment, Mg concentrations in leachate samples were analysed every three days instead of every day, thus average values for Mg concentration (calculated from values for the preceding and subsequent samples) were applied for intermediate days to estimate the daily mass of Mg leached (Appendix 4: Table S9). Differences in leachate sample size and sampling frequency, as well as inherent variation between replicate experiments, appears to have caused an over estimation of CO₂ trapping potential. This potential uncertainty may need to be taken into account if similar tests (periodically collected leachate concentrations) are used to estimate CO₂ sequestration potential for pilot-scale implementation. In any case, it appears that capture of CO₂ from air during evaporation is an ineffective way to sequester carbon when aqueous sulfate is present at high concentration. Sulfate should either be removed from solution, or Mg separated first as a precipitate, before Mg-rich leachates are either left to evaporate or reacted with a concentrated supply of CO₂ (e.g., flue gas) to precipitate carbonate minerals.

Sulfate removal can be achieved by biological treatments using sulfate reducing bacteria, by membrane filtration, ion exchange, or chemical precipitation (Dou et al., 2017). Filtration and ion exchange methods incur high investment and operating costs, limiting their large scale application (Silva et al., 2012); however, chemical precipitation of sulfate has been used for decades to treat waste waters (Dou et al., 2017). This typically involves the addition of lime to increase pH and precipitate gypsum ($\text{CaSO}_4 \cdot 2\text{H}_2\text{O}$), or limestone to sorb sulfate to grain surfaces (Fernando et al., 2018; Silva et al., 2012; Tait et al., 2009; Tolonen et al., 2015). However, gypsum precipitation is inhibited by the presence of Mg in solution (Dou et al., 2017; Tolonen et al., 2015) and the use of limestone or de-carbonated products of limestone incurs a carbon penalty which should be avoided where the goal is to offset carbon emissions. NaOH can be used to raise the pH of solutions produced by leaching of serpentine by H_2SO_4 in *ex situ* mineral carbonation reactor experiments (Maroto-Valer, 2005), and industrial wastewaters (Dou et al., 2017) to precipitate $\text{Mg}(\text{OH})_2$ at approximately pH 11, before SO_4 is precipitated as NaSO_4 , or as ettringite [$\text{Ca}_6\text{Al}_2(\text{SO}_4)_3(\text{OH})_{12} \cdot 26\text{H}_2\text{O}$], respectively. Although this process requires the use of chemical additives, recovery of Mg in the form of brucite provides an ideal material for mineral carbonation, either by reaction with a point source for CO_2 (i.e., the direct flue gas reaction trialed in this study and by Harrison et al., 2015) or via passive reaction with CO_2 in the atmosphere. Alternatively, the low cost and maintenance requirements of biological sulfate reduction in untreated leachate may be a favorable option (Fernando et al., 2018). If the leachate collection pond was designed as an anaerobic wetland, biologically mediated mineralisation by sulfate reducing bacteria could be used to remove sulfate from solution by precipitating sulfide minerals. However, the leachates produced in this study are low in cations other than Mg (Fig. 5.1, Appendix 4: Table S8), thus a source of cations (such as Fe) would likely be required to trap sulfide

in mineral form. A source of organic carbon is also essential, but fortunately, inexpensive wastes including manure, grass cuttings, saw dust, and sewage are ideal substances to promote the growth of sulfate reducing bacteria (Fernando et al., 2018). Moreover, sulfate reducing bacteria are also known to play a role in carbonate mineral precipitation, and it has been proposed that they could be employed to convert CO₂ into carbonate minerals in saline aquifers (Paul et al., 2017). Mg-carbonate (hydromagnesite) is saturated in the leachate solutions produced in this experiment; thus, it would be expected to precipitate within an artificial wetland. Although the use of artificial wetlands requires a large commitment of land and water, and relatively long time-scales (years) for treatment, they are relatively low cost and low maintenance (Fernando et al., 2018). As an alternative to using an artificial wetland as a landscape-scale bioreactor, construction of an *ex situ*, industrial-style bioreactor would allow optimisation of conditions to maximise sulfate reduction, within a shorter timespan, and in a smaller space. Further studies should investigate the feasibility of different sulfate removal methods in the context of mineral carbonation treatments; especially whether sufficient microbial sulfate reduction can be achieved to maximise mineral carbonation potential of high-Mg leachates.

5.4.5. Acid leaching leads to enrichment of trace metals

A rusted-red layer appeared after the first acid treatment (observed in both the CO₂ reaction experiment and the acid heap leaching experiment), just below the surface on the columns, similar to that observed by Power et al. (2010), McCutcheon et al. (2016, 2017) and described in Chapter 4. This layer represents the neutralisation horizon, and it is characterised by precipitation of Fe-oxides and associated transition metals (Power et al., 2010). We observe precipitation of Fe, Co, Cr, Ni, and Mn within this zone, with Fe, Co and Cr precipitating together at a shallower depth than Ni and Mn within each column

(Fig. 5). This observation is consistent with differences in the pH dependent solubility of these transition metals (Stumm and Morgan, 1996). Our XFM maps reveal that tailings grains within the transition-metal-rich horizon is cemented with an Fe-rich precipitate, and that brucite grains are highly enriched in transition metals, and appear to be replaced in parts by transition-metal-rich phases (Fig. 5.5). The association of brucite with specific first-row transition metals is dependent on depth within the neutralisation zone, in the same order described above (Fig. 5.5). Localised increases in alkalinity around brucite grains, as a product of their dissolution, likely drive induce precipitation of transition metals in these micro-environments, explaining the high concentrations we observe in these grains (Fig. 5.5).

Transition metals appear to be leached from mineral grains predominantly within the upper 1 cm of the acid-treated columns, and they accumulate within the neutralisation horizon from 1–3 cm depth (in replicate A4, Figs. 3, 5). The rusted horizon was visually observed to migrate downwards within the columns, becoming more intense in colour over the course of the experiment (Fig. S4), thus we expect that longer treatment leads to greater accumulation of Fe, Co, Cr, Ni and Mn within this horizon. The MIN3P model reproduces a pH neutralisation horizon that increases from pH 2.6 to 8.4 over a depth interval of 4–5 cm after 28 days of acid leaching (Fig. 7). Although this is slightly deeper than our estimate based on visual inspection of the rusted layer in replicate A4, it is more consistent with observed maximum depths of the rusted layer in replicates A1–A3. Another reason that the modelled neutralisation front may occur at a greater depth than in experiments is that solution is applied at a constant rate over time in the model rather than being introduced in discrete doses. In the experiment, pore water saturation increases at the time of solution addition and dries over the following 24 hours. Table S7 shows that 24 hours after the last dose, all intervals in all columns were unsaturated, ranging from 21

% to 75 % pore water saturation. Preferential pathways for flow, and heterogeneity in grain size distribution and arrangement mean that some areas of the tailings material within the acid-leached columns may have been in contact with solution for longer than others, and movement of solutes may be faster or slower in different regions of any given column. These factors could not be accounted for in the model. The domed shape of the rusted horizon, which extends to greater depths towards the outer edges of each column, is evidence for preferential flow within the columns. This heterogeneity likely accounts for the variation in the depth of the rusted horizon both within columns, and between replicates.

The rusted horizon is rich in Fe, and MIN3P models predict that hematite precipitates due to magnetite and serpentine dissolution. Hematite (or more likely precursor ferrihydrite) is predicted to accumulate via cyclic dissolution at the surface where pH is most acidic ($\text{pH} < \approx 1.8$) and re-precipitation closer to the neutralisation front ($\text{pH} > \approx 1.8$). After 28 days, the maximum abundance of hematite is predicted to occur from 7–9 cm depth. Excluding magnetite from the model still results in hematite precipitation, with maximum abundance at a slightly greater depth (i.e., 8–10 cm depth). This reflects the contribution of Fe^{2+} from dissolution of chrysotile and its subsequent oxidation to Fe^{3+} . The surface area for magnetite that we used in our model was adjusted such that magnetite dissolution is negligible compared to dissolution of chrysotile, which is in line with leaching experiments described by McCutcheon et al. (2015). Even with this modification, magnetite still contributes the majority of Fe to solution in the MIN3P model. Hematite is not detectable in XRD data, which is not unexpected because the maximum volume fraction after 28 days (2.88×10^{-7} at 8 cm depth) is equivalent to a mineral abundance of 0.0001 wt. %, which is below XRD detection limits. However, the precipitated phase is not likely to be hematite, but instead could be a precursor phase, such as ferrihydrite,

which lacks long-range order (Michel et al., 2007; Schwertmann and Taylor, 1989). Since the abundance for hematite, ferrihydrite and/or other Fe-(hydr)oxide phases is not known (these are not detectable in our XRD data), it is not possible to constrain the amount of magnetite dissolution to experimental data. However, the ability to reproduce the zone of Fe accumulation in models, with reasonable agreement with experimental observations, allows us to predict that the downward migration of this zone, and the associated accumulation of transition metals, will likely continue with longer treatment. The rate of migration of the Fe- and transition-metal-rich neutralisation front may be affected by factors such as surface passivation and preferential flow pathways within porous media.

Recent work has investigated the possibility of extracting trace metals (Fe, Ni and Cu) as a value-adding product in *ex situ* mineral carbonation of Ni ore and waste rock (Romão et al., 2013). After Fe, the highest concentration of trace metals in the rusted-horizon is Ni (up to ≈ 0.4 wt. % in the bulk enriched horizon, and up to 2.2 wt. % associated with synthetic brucite grains, after 4 weeks of acid leaching), followed by Cr (≈ 0.3 wt. % in enriched horizon, up to 1.9 wt. % in brucite), with lower concentrations of Mn (≈ 0.2 wt. % in enriched horizon, up to 0.5 wt. % in brucite) and Co (≈ 0.1 wt. % in enriched horizon, up to 1.2 wt. % in brucite; Fig. 5).

In the 1980s, Woodsreef Chrysotile Mine was investigated as a potential resource for magnetite, Ni and Cr (Kmetoni, 1984). Fe and Cr predominantly occur in spinels (magnetite and chromite), which are suitable for extraction via gravimetric and magnetic separation. Ni on the other hand was thought to be hosted predominantly within serpentine, as no high-grade Ni-minerals were identified by Kmetoni (1984). Thus, extraction was considered impossible since almost the entire mass of tailings would need to be treated, and bulk Ni concentrations were measured at only 0.3 wt. %. However,

Hamilton et al., (in review/Chapter 3) find the main sources of Ni within the Woodsreef tailings are Ni substitution for Mg in serpentine minerals (approximately 500–900 ppm Ni, relatively evenly distributed) and awaruite (Ni_{2-3}Fe) inclusions within serpentine grains (stoichiometrically 58–87 wt. % Ni) (Chapter 3). Our SEM and XFM data show that leached serpentine grains within the upper 1 cm of the acid leached column (A4) have relatively lower (typically 100–500 ppm) Ni concentrations (Fig. 5). Awaruite is typically detectable as Ni-rich inclusions (≈ 60 wt. % Ni) of approximately 2 μm in size in Woodsreef ore and tailings. These awaruite inclusions are typically aligned in a crosshatching pattern of veins within serpentine grains, but they appear to be less abundant in the upper cm of leached material in the acid-treated column compared with material below 2 cm depth. Although awaruite is predicted to be relatively resistant to leaching in kinetic weathering tests (Kandji et al., 2017), it is possible that these inclusions have either dissolved under the acidic conditions of our experiments or have been physically transported downwards within the column once liberated by dissolution of serpentine. In any case, mobilisation of Ni into solution is occurring under the conditions in our experiments, probably as a result of both serpentine and awaruite dissolution.

5.4.6. Implications for Ni recovery from low-grade ultramafic ore or tailings

Heap (bio)leaching using sulfuric acid has been proposed as a means to extract Ni from low-grade ultramafic Ni-sulfide, and Ni-laterite deposits (Cameron et al., 2009; McDonald and Whittington, 2008; Zhen et al., 2009). However, high Mg concentrations in leachates pose a key challenge for Ni recovery, firstly because the dissolution of silicate minerals consumes acid intended for reaction with sulfides, thus increasing the amount of acid required, and secondly because high Mg content introduces difficulties in

processing of leachates, while the removal and disposal of Mg from pregnant liquor is expensive (Cameron et al., 2009). However, here we find that if the neutralising capacity is not exceeded, Ni and other trace metals (Cr, Co, Mn) will become immobilised and enriched in a discrete neutralisation horizon. As such, heap leaching mimics the geochemical processes that result in laterite ore-formation, on a much shorter timescale. Rather than extracting Ni from high Mg leachates, Ni could be progressively concentrated in solid form, while high Mg leachates may be used for carbon mineralisation to offset the greenhouse gas emissions generated during treatment and processing. The potential to produce a concentrated Ni (and associated trace metals) resource could provide an incentive to treating mine wastes for accelerated mineral carbonation, or in reverse, the opportunity to offset CO₂ emissions could be an incentive to process low-grade Ni ores or reprocess ultramafic tailings.

5.5. Conclusions

Two field-deployable treatment strategies have been trialed to accelerate carbonation of ultramafic mine tailings. Short-term treatment to accelerate CO₂ sequestration rates can be achieved by targeting highly reactive brucite via direct reaction of an onsite CO₂ source with partially saturated tailings. Here, we achieve the equivalent of ~30 years of passive carbonation within 4 weeks, although development of very dry conditions likely limited carbonation of brucite. Complete carbonation of brucite may be achieved if sufficient water content or humidity is maintained within pore spaces. However, once reaction of brucite is complete, carbonation rates will likely decrease due to the lower reactivity of serpentine minerals (Assima et al., 2013; Pronost et al., 2011), and the passivating effect of cementation.

Heap leaching treatments using sulfuric acid effectively leach Mg from silicate minerals, and produce alkaline, Mg-rich leachates for much longer time scales (months to years, depending on the depth of a tailings deposit). These leachates could be carbonated either via air capture during evapoconcentration in a leachate collection pond (simulated in this study using Petri dishes) or by reaction with a concentrated CO₂ source from onsite power generation. The use of sulfuric acid treatments to enhance tailings dissolution leads to sulfate scavenging most of the Mg in solution, the formation of hydrated Mg-sulfate minerals, and an inhibition on conversion of Mg to carbonate minerals. Therefore, sulfate should be separated or removed from solution before precipitation of Mg-carbonate minerals is induced to optimise carbon sequestration.

A further benefit of heap leaching is that trace metals become progressively concentrated at the pH neutralisation front, which migrates downwards with continued acid treatment. Trace metals are immobilised within Fe-(hydr)oxide cements and Fe-rich precipitates that replace brucite grains, which vary in dominant trace metal associations as a function depth within the neutralisation front. With extended treatment time, this Mg-leaching process could also be used to enrich Ni and other transition metals to the point where the pH neutralisation horizon could be considered a secondary ore, an artificial Ni laterite, that may be re-mined to add value to this treatment process.

5.6. Chapter 5 references

- Assima G.P., Larachi F., Beaudoin G. and Molson J. (2013) Dynamics of carbon dioxide uptake in chrysotile mining residues – Effect of mineralogy and liquid saturation. *International Journal of Greenhouse Gas Control* 12, 124-135.
- Assima G.P., Larachi F., Beaudoin G. and Molson J.W. (2012) CO₂ sequestration in chrysotile mining residues - Implication of watering and passification under

environmental conditions. *Industrial & Engineering Chemistry Research* 51, 8726-8734.

Assima G.P., Larachi F., Molson J and Beaudoin G. (2014) New tools for stimulating dissolution and carbonation of ultramafic mining residues. *The Canadian Journal of Chemical Engineering* 92, 2029-2038.

Azdarpour A., Asadullah M., Mohammadian E., Hamidi H., Junin R. and Karaei M.A. (2015) A review on carbon dioxide mineral carbonation through pH-swing process. *Chemical Engineering Journal* 279, 615-630.

Bea S.A., Wilson S.A., Mayer K.U., Dipple G.M., Power I.M. and Gamazo P. (2012) Reactive transport modeling of natural carbon sequestration in ultramafic mine tailings. *Vadose Zone Journal* 11, 1-17.

Beinlich A. and Austrheim H. (2012) In situ sequestration of atmospheric CO₂ at low temperature and surface cracking of serpentinized peridotite in mine shafts. *Chemical Geology* 332, 32-44.

Bish D.L. and Howard S.A. (1988) Quantitative phase analysis using the Rietveld method. *Journal of Applied Crystallography* 21, 86-91.

Bobicki E.R., Liu Q., Xu Z. and Zeng H. (2012) Carbon capture and storage using alkaline industrial wastes. *Progress in Energy and Combustion Science* 38, 302-320.

Brent G.F., Rayson M.S., Kennedy E.M., Stockenhuber M., Collins W.J., Prigge J.D., Hynes R.G., Molloy T.S., Zulfiqar H., Farhang F., Oliver T.O., Hamblin Wang S. and Dawe M. (2015) Mineral carbonation of serpentinite: From the laboratory to pilot scale - The MCi project, 5th International Conference on Accelerated Carbonation for Environmental and Material Engineering 2015, pp. 394-403.

Cameron R.A., Lastra R., Mortazavi S., Gould W.D., Thibault Y., Bedard P.L., Morin L. and Kennedy K.J. (2009) Elevated-pH bioleaching of a low-grade ultramafic nickel sulphide ore in stirred-tank reactors at 5 to 45 °C. *Hydrometallurgy* 99, 77-83.

- Chen Z.Y., O'Connor W.K. and Gerdemann S.J., (2006) Chemistry of aqueous mineral carbonation for carbon sequestration and explanation of experimental results. *Environmental Progress & Sustainable Energy* 25, 161-166.
- Chipera S.J. and Vaniman D.T. (2007) Experimental stability of magnesium sulfate hydrates that may be present on Mars. *Geochimica et Cosmochimica Acta* 71, 241-250.
- Davies P.J. and Bubela B. (1973) The transformation of nesquehonite into hydromagnesite. *Chemical Geology* 12, 289-300.
- Dou W., Zhou Z., Jiang L.-M., Jiang, A., Huang R., Tian X., Zhang W. and Chen D. (2017) Sulfate removal from wastewater using ettringite precipitation: Magnesium ion inhibition and process optimization. *Journal of Environmental Management* 196, 518-526.
- Entezari Zarandi A., Larachi F., Beaudoin G., Plante B., Sciortino M., (2016). Multivariate study of the dynamics of CO₂ reaction with brucite-rich ultramafic mine tailings. *International Journal of Greenhouse Gas Control* 52, 110–119.
- Fernando W.A.M., Ilankoon I.M.S.K., Syed T.H. and Yellishetty M. (2018) Challenges and opportunities in the removal of sulphate ions in contaminated mine water: A review. *Minerals Engineering* 117, 74-90.
- Grant J.A. (1986) The isocon diagram; a simple solution to Gresens equation for metasomatic alteration. *Economic Geology* 81, 1976-1982.
- Gras A., Beaudoin G., Molson J., Plante B., Bussière B., Lemieux J.M. and Dupont P.P. (2017) Isotopic evidence of passive mineral carbonation in mine wastes from the Dumont Nickel Project (Abitibi, Quebec). *International Journal of Greenhouse Gas Control* 60, 10-23.
- Hagedorn B. and Cartwright I. (2009) Climatic and lithologic controls on the temporal and spatial variability of CO₂ consumption via chemical weathering: An example from the Australian Victorian Alps. *Chemical Geology* 260, 234-253.

- Harrison A.L., Dipple G.M., Power I.M. and Mayer K.U. (2015) Influence of surface passivation and water content on mineral reactions in unsaturated porous media: Implications for brucite carbonation and CO₂ sequestration. *Geochimica et Cosmochimica Acta* 148, 477-495.
- Harrison A.L., Dipple G.M., Power I.M. and Mayer K.U. (2016) The impact of evolving mineral–water–gas interfacial areas on mineral–fluid reaction rates in unsaturated porous media. *Chemical Geology* 421, 65-80.
- Harrison A.L., Dipple G.M., Song W., Power I.M., Mayer K.U., Beinlich A. and Sinton D., (2017). Changes in mineral reactivity driven by pore fluid mobility in partially wetted media. *Chemical Geology* 436, 1-11.
- Harrison A.L., Power I.M. and Dipple G.M., (2012). Accelerated carbonation of brucite in mine tailings for carbon sequestration. *Environmental Science & Technology* 47, 126-134.
- Herzog H., (2002). Carbon sequestration via mineral carbonation: overview and assessment. Cambridge, Massachusetts: Massachusetts Institute of Technology, Laboratory for Energy and the Environment.
- Hill R. and Howard C. (1987) Quantitative phase analysis from neutron powder diffraction data using the Rietveld method. *Journal of Applied Crystallography* 20, 467-474.
- Hopkinson L., Kristova P., Rutt K. and Cressey G. (2012) Phase transitions in the system MgO–CO₂–H₂O during CO₂ degassing of Mg-bearing solutions. *Geochimica et Cosmochimica Acta* 76, 1-13.
- Hopkinson L., Rutt K. and Cressey G. (2008) The transformation of nesquehonite to hydromagnesite in the system CaO–MgO–H₂O–CO₂: An experimental spectroscopic study. *The Journal of Geology* 116, 387-400.
- Jauffret G., Morrison J. and Glasser F.P. (2015) On the thermal decomposition of nesquehonite. *Journal of Thermal Analysis and Calorimetry* 122, 601-609.

- Kandji E.H.B., Plante B., Bussière B., Beaudoin G. and Dupont P.-P. (2017) Kinetic testing to evaluate the mineral carbonation and metal leaching potential of ultramafic tailings: Case study of the Dumont Nickel Project, Amos, Québec. *Applied Geochemistry* 84, 262-267.
- Kelemen P., Al Rajhi A., Godard M., Ildefonse B., Köpke J., MacLeod C., Manning C., Michibayashi K., Nasir S., Shock E. and Takazawa E. (2013) Scientific drilling and related research in the Samail ophiolite, Sultanate of Oman. *Scientific Drilling* 15, 64-71.
- Kemache N., Pasquier L.-C., Mouedhen I., Cecchi E., Blais J.-F. and Mercier G. (2016) Aqueous mineral carbonation of serpentinite on a pilot scale: The effect of liquid recirculation on CO₂ sequestration and carbonate precipitation. *Applied Geochemistry* 67, 21-29.
- Kemache N., Pasquier L.-C., Cecchi E., Mouedhen I., Blais J.-F. and Mercier G. (2017) Aqueous mineral carbonation for CO₂ sequestration: From laboratory to pilot scale. *Fuel Processing Technology* 166, 209-216.
- Lechat K., Lemieux J.-M., Molson J., Beaudoin G. and Hébert R. (2016) Field evidence of CO₂ sequestration by mineral carbonation in ultramafic milling wastes, Thetford Mines, Canada. *International Journal of Greenhouse Gas Control* 47, 110-121.
- Matter J.M., Broecker W.S., Gislason S.R., Gunnlaugsson E., Oelkers E.H., Stute M., Sigurdardóttir H., Stefansson A., Alfreðsson H.A., Aradóttir E.S., Axelsson G., Sigfússon B. and Wolff-Boenisch D. (2011) The CarbFix Pilot Project—Storing carbon dioxide in basalt. *Energy Procedia* 4, 5579-5585.
- Matter, J.M. Stute, M. Snæbjörnsdóttir S.Ó., Oelkers E.H., Gislason S.R., Aradóttir E.S., Sigfússon B., Gunnarsson I., Sigurdardóttir H., Gunnlaugsson E., Axelsson G., Alfreðsson H.A., Wolff-Boenisch D., Mesfin K., Taya D.F.d.l.R., Hall J., Dideriksen K. and Broecker W.S. (2016) Rapid carbon mineralization for permanent disposal of anthropogenic carbon dioxide emissions. *Science* 352, 1312-1314.

- Mayer K.U., Frind E.O. and Blowes D.W. (2002) Multicomponent reactive transport modeling in variably saturated porous media using a generalized formulation for kinetically controlled reactions. *Water Resources Research* 38, 1174.
- McCutcheon J., Dipple G.M., Wilson S.A. and Southam G. (2015) Production of magnesium-rich solutions by acid leaching of chrysotile: A precursor to field-scale deployment of microbially enabled carbonate mineral precipitation. *Chemical Geology* 413, 119-131.
- McCutcheon J., Turvey C.C., Wilson S.A., Hamilton J.L. and Southam G. (2017) Microbial mineral carbonation of asbestos mine tailings: Potential applications to carbon storage and tailings stabilization. *Minerals* 7, 191.
- McCutcheon J., Wilson S.A. and Southam G. (2016) Microbially accelerated carbonate mineral precipitation as a strategy for in situ carbon sequestration and rehabilitation of asbestos mine sites. *Environmental Science & Technology* 50, 1419-1427.
- McDonald R.G. and Whittington B.I. (2008) Atmospheric acid leaching of nickel laterites review: Part 1. Sulphuric acid technologies. *Hydrometallurgy* 91, 35-55.
- McGrail B.P., Schaef H.T., Spane F.A., Cliff J.B., Qafoku O., Horner J.A., Thompson C.J., Owen A.T. and Sullivan C.E. (2017) Field validation of supercritical CO₂ reactivity with basalts. *Environmental Science & Technology Letters* 4, 6-10.
- Mervine E.M., Wilson S.A., Power I.M., Dipple G.M., Turvey C.C., Hamilton J.L., Vanderzee S., Maudsepp M., Southam C., Matter J.M., Kelemen P.B., Stiefenhofer J., Miya Z. and Southam G. (in review). Potential for offsetting diamond mine carbon emissions through mineral carbonation of processed kimberlite: An assessment of De Beers mine sites in South Africa and Canada. *Mineralogy and Petrology*, in review.
- Michel F.M., Ehm L., Antao S.M., Lee P.L., Chupas P.J., Liu G., Strongin D.R., Schoonen M.A., Phillips B.L. and Parise J.B. (2007) The structure of ferrihydrite, a nanocrystalline material. *Science*, 316, 1726-1729.

- Mills S.J., Wilson S.A., Dipple G.M. and Raudsepp M. (2010) The decomposition of konyaite: importance in CO₂ fixation in mine tailings. *Mineralogical Magazine* 74, 903-917.
- Morgan B., Wilson S.A., Madsen I.C., Gozukara Y.M. and Habsuda J. (2015) Increased thermal stability of nesquehonite (MgCO₃·3H₂O) in the presence of humidity and CO₂: Implications for low-temperature CO₂ storage. *International Journal of Greenhouse Gas Control* 39, 366-376.
- Mouedhen I., Kemache N., Pasquier L.-C., Cecchi E., Blais J.-F. and Mercier G. (2017) Effect of pCO₂ on direct flue gas mineral carbonation at pilot scale. *Journal of Environmental Management* 198, 1-8.
- Oelkers E.H., Gislason S.R. and Matter J. (2008) Mineral carbonation of CO₂. *Elements* 4, 333-337.
- Olsson J., Stipp S.L.S. and Gislason S.R. (2014a) Element scavenging by recently formed travertine deposits in the alkaline springs from the Oman Semail Ophiolite. *Mineralogical Magazine* 78, 1479-1490.
- Olsson J., Stipp S.L.S., Makovicky E. and Gislason S.R. (2014b) Metal scavenging by calcium carbonate at the Eyjafjallajökull volcano: A carbon capture and storage analogue. *Chemical Geology* 384, 135-148.
- Oskierski H.C. (2013) Natural carbonation of ultramafic rocks in the Great Serpentine Belt, New South Wales, Australia. Ph.D thesis, The University of Newcastle.
- Oskierski H.C., Dlugogorski B.Z. and Jacobsen G. (2013) Sequestration of atmospheric CO₂ in chrysotile mine tailings of the Woodsreef Asbestos Mine, Australia: Quantitative mineralogy, isotopic fingerprinting and carbonation rates. *Chemical Geology* 358, 156-169.
- Park A.-H.A. and Fan L.-S. (2004) CO₂ mineral sequestration: physically activated dissolution of serpentine and pH swing process. *Chemical Engineering Science* 59, 5241-5247.

- Park, A.-H.A., Jadhav R. and Fan L.-S. (2003) CO₂ mineral sequestration: chemically enhanced aqueous carbonation of serpentine. *The Canadian Journal of Chemical Engineering* 81, 885-890.
- Paul V.G., Wronkiewicz D.J. and Mormile M.R. (2017) Impact of elevated CO₂ concentrations on carbonate mineral precipitation ability of sulfate-reducing bacteria and implications for CO₂ sequestration. *Applied Geochemistry* 78, 250-271.
- Power I.M., Dipple G.M. and Southam G. (2010) Bioleaching of ultramafic tailings by *Acidithiobacillus* spp. for CO₂ sequestration. *Environmental Science & Technology* 44, 456-462.
- Power I.M., Harrison A.L., Dipple, G.M., Wilson S.A., Kelemen P.B., Hitch M. and Southam G. (2013) Carbon mineralization: From natural analogues to engineered systems. *Reviews in Mineralogy and Geochemistry* 77, 305-360.
- Power I.M., McCutcheon J., Harrison A.L., Wilson S.A., Dipple G.M., Kelly S., Southam C. and Southam G. (2014) Strategizing carbon-neutral mines: A case for pilot projects. *Minerals* 4, 399-436.
- Pronost J., Beaudoin G., Lemieux J.-M., Hébert R., Constantin M., Marcouiller S., Klein M., Duchesne J., Molson J.W., Larachi F. and Maldague X. (2012) CO₂-depleted warm air venting from chrysotile milling waste (Thetford Mines, Canada): Evidence for in-situ carbon capture from the atmosphere. *Geology* 40, 275-278.
- Pronost J., Beaudoin G., Tremblay J., Larachi F., Duchesne J., Hébert R. and Constantin M. (2011) Carbon sequestration kinetic and storage capacity of ultramafic mining waste. *Environmental Science & Technology* 45, 9413-9420.
- Rietveld H.M. (1969) A profile refinement method for nuclear and magnetic structures. *Journal of Applied Crystallography* 2, 65-71.
- Romão I.S., Gando-Ferreira L.M. and Zevenhoven R. (2013) Combined extraction of metals and production of Mg(OH)₂ for CO₂ sequestration from nickel mine ore and overburden. *Minerals Engineering* 53, 167-170.

- Ryan C.G. (2000) Quantitative trace element imaging using PIXE and the nuclear microprobe. *International Journal of Imaging Systems and Technology* 11, 219-230.
- Ryan C.G., Siddons D.P., Kirkham R., Dunn P.A., Kuczewski A., Moorhead G., De Geronimo G., Paterson D.J., de Jonge M.D., Hough R.M., Lintern M.J., Howard D.L., Kappen P. and Cleverley J. (2010) The new Maia detector system: Methods for high definition trace element imaging of natural material. *AIP Conference Proceedings* 1221, 9-17.
- Ryan C.G., Siddons D.P., Kirkham R., Li Z.Y., Jonge M.D.d., Paterson D.J., Kuczewski A., Howard D.L., Dunn P.A., Falkenberg G., Boesenberg U., Geronimo G.D., Fisher L.A., Halfpenny A., Lintern M.J., Lombi E., Dyl K.A., Jensen M., Moorhead G.F., Cleverley J.S., Hough R.M., Godel B., Barnes S.J., James S.A., Spiers K.M., Alfeld M., Wellenreuther G., Vukmanovic Z. and Borg S. (2014) Maia X-ray fluorescence imaging: Capturing detail in complex natural samples. *Journal of Physics: Conference Series* 499, 012002.
- Sarazin G., Michard G. and Prevot F. (1999) A rapid and accurate spectroscopic method for alkalinity measurements in sea water samples. *Water Research* 33, 290-294.
- Schwertmann U. and Taylor R.M. (1989) Iron Oxides. Minerals in Soil Environments, Chapter 8 (2nd Ed.) *Soil Science Society of America*, Madison, WI, USA.
- Seifritz W. (1990) CO₂ disposal by means of silicates. *Nature* 345, 486.
- Silva A.M., Lima R.M. and Leao V.A. (2012) Mine water treatment with limestone for sulfate removal. *Journal of Hazardous Materials* 221-222, 45-55.
- Stumm W. and Morgan J.J. (1996) Aquatic chemistry: chemical equilibria and rates in natural waters, third ed. *John Wiley & Sons*, New York.
- Tait S., Clarke W.P., Keller J. and Batstone D.J. (2009) Removal of sulfate from high-strength wastewater by crystallisation. *Water Research* 43, 762-772.
- Thom J.G.M., Dipple G.M., Power I.M. and Harrison A.L. (2013) Chrysotile dissolution rates: Implications for carbon sequestration. *Applied Geochemistry* 35, 244-254.

- Thomas D.L., Bird D.K., Arnórsson S. and Maher K. (2016) Geochemistry of CO₂-rich waters in Iceland. *Chemical Geology* 444, 158-179.
- Tolonen, E.-T., Rämö, J. and Lassi, U. (2015) The effect of magnesium on partial sulphate removal from mine water as gypsum. *Journal of Environmental Management* 159, 143-146.
- Turvey C.C., Wilson S.A., Hamilton J.L., McCutcheon J., Tait A.W. and Southam G. (in prep) Assessment of carbon sequestration potential at the Woodsreef Chrysotile Mine, NSW, Australia. in preparation.
- Turvey, C.C., Wilson, S.A., Hamilton, J.L. and Southam, G. (2017) Field-based accounting of CO₂ sequestration in ultramafic mine wastes using portable X-ray diffraction. *American Mineralogist* 102, 1302-1310.
- Wang L., Lu A., Wang C., Zheng X., Zhao D. and Liu R. (2006) Nano-fibriform production of silica from natural chrysotile. *Journal of Colloid and Interface Science* 295, 436-439.
- White A.F., Peterson M.L. and Hochella M.F. (1994) Electrochemistry and dissolution kinetics of magnetite and ilmenite. *Geochimica et Cosmochimica Acta* 58, 1859-1875.
- Wilson S.A., Dipple G.M., Power I.M., Barker S.L.L., Fallon S.J. and Southam G. (2011) Subarctic Weathering of Mineral Wastes Provides a Sink for Atmospheric CO₂. *Environmental Science & Technology* 45, 7727-7736.
- Wilson S.A., Dipple G.M., Power I.M., Thom J.M., Anderson R.G., Raudsepp M., Gabites J.E. and Southam G. (2009a) Carbon dioxide fixation within mine wastes of ultramafic-hosted ore deposits: Examples from the Clinton Creek and Cassiar chrysotile deposits, Canada. *Economic Geology* 104, 95-112.
- Wilson S.A., Harrison A.L., Dipple G.M., Power I.M., Barker S.L.L., Mayer K.U., Fallon S.J., Raudsepp M. and Southam G. (2014) Offsetting of CO₂ emissions by air capture in mine tailings at the Mount Keith Nickel Mine, Western Australia: Rates, controls and prospects for carbon neutral mining. *International Journal of Greenhouse Gas Control* 25, 121-140.

- Wilson S.A., Raudsepp M. and Dipple G.M. (2006) Verifying and quantifying carbon fixation in minerals from serpentine-rich mine tailings using the Rietveld method with X-ray powder diffraction data. *American Mineralogist* 91, 1331-1341.
- Wilson S.A., Raudsepp M. and Dipple G.M. (2009b) Quantifying carbon fixation in trace minerals from processed kimberlite: A comparative study of quantitative methods using X-ray powder diffraction data with applications to the Diavik Diamond Mine, Northwest Territories, Canada. *Applied Geochemistry* 24, 2312-2331.
- Zhen S., Yan Z., Zhang Y., Wang J., Campbell M. and Qin W. (2009) Column bioleaching of a low grade nickel-bearing sulfide ore containing high magnesium as olivine, chlorite and antigorite. *Hydrometallurgy* 96, 337-341.

Chapter 6

Synthesis and discussion of future research directions

Jessica L. Hamilton^a

^aSchool of Earth, Atmosphere and Environment, Monash University, Australia

Mineral carbonation is still an emerging field of research. Trapping of carbon within the structures of minerals was first proposed by Seifritz in 1990, and this idea was developed throughout the 1990s by Lackner et al. (Goff and Lackner, 1998; Lackner et al., 1995). Over the last 20 years, research into this topic has accelerated, with numerous engineering developments broadening the types of strategies employed and increasing the success rates of treatments (e.g., Maroto-Valer et al., 2005; Park and Fan, 2003, 2004; Wang et al., 2015). Recent research has progressed to implementation of accelerated carbonation projects at the pilot- and field-scales (e.g., Brent et al., 2015; Kemache et al., 2016, 2017; Matter et al., 2011, 2016; McCutcheon et al., 2017; Mouedhen et al., 2017). With these advancements, it was imperative that the question of trace metal mobility be addressed. This thesis set out to answer the fundamental question of the fate of mobilised trace metals during mineral carbonation. Of similar importance was the urgency with which CO₂ emissions need to be reduced, in order to avoid potentially devastating impacts of climate change, and to keep our commitments to international emissions reduction agreements (such as the recent Paris Agreement; Knutti et al., 2016; Rogelj et al., 2015, 2016). The mining industry is ideally placed to develop and benefit from mineral carbonation technology, as it produces useful materials for reaction in the form of ultramafic tailings, acid generating materials, and CO₂ emissions. Much of the current research seeks to accelerate carbonation of ultramafic mine tailings in highly engineered, specialised reactors, which incur high energy, capital and operating costs, limiting their viability as a CO₂ mitigation strategy within the near future while carbon prices remain low (Kemache et al., 2017; Power et al., 2014). In order to increase the likelihood of uptake by the industry, there is a need to develop readily scalable mineral carbonation technologies that make use of relatively inexpensive and conventional materials, equipment, and expertise. It should be stressed that uptake of these technologies by the

mining industry will not contribute appreciably to total global emissions reduction, as the global potential for CO₂ sequestration within ultramafic mine tailings has been estimated at up to ~175 Mt of CO₂ / year (Power et al., 2013b), while global CO₂ emissions were estimated at 36.3 ± 1.8 Gt CO₂ in 2016 (Le Quéré et al., 2017). However, adoption of mineral carbonation could have significant impact within the mining industry itself, not only as an emissions reduction strategy, but because the existence of carbon neutral mines would be symbolic as a statement that even an industry with an historically poor environmental track record is taking action on emissions reduction. This message could be powerful and influential, and could have greater impact than the actual amount of mitigated CO₂ emissions.

Here, the discussion will review some of the most important contributions of this thesis to the literature, highlight future priorities for research, and summarise the potential opportunities and impact that this technology could have for the mining industry.

6.1. Understanding the fate of trace metals during mineral carbonation

Chapters 2, 3 and 5 show that trace metals are rapidly and effectively sequestered within common mineral products of carbon mineralisation: Mg-carbonate minerals, and Fe-(hydr)oxides. Furthermore, trace metals are retained in mineral form after re-crystallisation (Chapter 2). These results will help to alleviate concerns that have been raised about the potential environmental risk of trace metal mobilisation as a result of accelerated mineral carbonation, and are relevant to *ex situ* reactors, *in situ* tailings treatment, geosequestration scenarios, and proposed accelerated weathering of natural landscapes (e.g., Flaathen and Gislason, 2007; Kirsch et al., 2014; Marcon and Kaszuba,

2013, 2015; Oelkers et al., 2008; Olajire, 2013; Olsson et al., 2014; Thomas et al., 2016; Wunsch et al., 2013).

On the other hand, results in Chapter 5 indicate that acid leaching treatments for accelerated mineral carbonation cause transition metals to migrate downwards within a tailings profile to accumulate at higher concentration within the neutralisation front over time. This process could potentially be exploited to upgrade concentrations of Ni and other associated trace metals to the extent that this discrete, concentrated horizon could be targeted as a secondary mineral resource, and re-mined. Use of this process could be particularly important in the treatment of tailings from low grade Ni mines, such as those produced at the Mt Keith Mine in Western Australia, where a substantial amount of the Ni resource is deposited in tailings (recovery is typically ~70%, meaning that ~30% of the Ni from this deposit is disposed of in tailings; Grguric et al., 2006). Acid leaching, in a conventional heap leaching scenario, could potentially be used to simultaneously offset the emissions of mining and enhance recovery of Ni from waste tailings.

6.2. Carbon accounting for accreditation under carbon credit schemes

Chapters 4 and 5 develop and demonstrate an improved approach for carbon accounting in minerals that uses total carbon measurements supported by XRD data, to account for X-ray amorphous and gangue carbonate phases. Once a baseline understanding of carbonate geochemistry and mineralogy is established, low-cost total carbon measurements (i.e., AUD \$12 per sample) may be sufficient to monitor continued uptake of atmospheric carbon within ultramafic mine tailings. Integration of quantitative XRD and isotopic methods (>AUD \$400 per sample) could then be used sparingly to confirm mineralogical changes. Improvements in carbon accounting methods could lead to recognition of passive and accelerated mineral carbonation under carbon credit schemes.

Capped carbon markets and carbon taxes are legislated in some 42 national and 25 sub-national jurisdictions around the world, and provide a financial incentive for development of mineral carbonation projects via avoidance of penalties (Crowley, 2017; Hitch and Dipple, 2012). Australia remains the only country to have adopted (in 2012), and subsequently repealed (in 2014) a carbon price (Crowley, 2017). However, the current Australian Emissions Reduction Fund grants ‘carbon credits’ for undertaking projects to reduce emissions or sequester carbon (Australian Government, 2011). These projects must be conducted in accordance with approved methods and must sequester carbon for a ‘permanence period’ at least 25 or 100 years (if 25 years a discount applies; Australian Government, 2011). Increasing soil carbon content is one activity approved under the current policy, and sequestration of soil carbon is measured using carbon combustion analysis (Australian Government, 2011; Macintosh and Waugh, 2012). Carbon credits can then be used (or bought) by large emitters to reduce net emissions below a baseline defined by a regulator, or sold to generate income (Macintosh and Waugh, 2012). Future research should investigate the applicability of the approved method for measuring soil carbon to the measurement of carbon sequestration within mine tailings (via mineral carbonation). Adaptation of the approved method for soils would likely be required to account for gangue carbonate content of tailings (in line with Chapter 4); however, it would be a useful starting point, and development of these methods could lead to the recognition of mineral carbonation as an approved carbon sequestration strategy that is eligible for carbon credits.

6.3. Scaling up geochemical treatments to pilot projects and implementation

This research aims to pave the way towards carbon neutral mining by developing and testing novel, low-cost treatments for carbonating the mineral waste generated by mining. The field trial described in Chapter 4 demonstrates the feasibility of using conventional controlled watering systems (such as those used to irrigate golf courses) to maintain optimum soil saturation levels and deliver geochemical treatments at a mine site. Practical lessons learned from this experiment include the recommendation that future field trials of accelerated carbonation be conducted with industry collaboration at currently operating mine sites, and that more intensive or frequent acid leaching is required to overcome existing neutralising potential within the tailings to target dissolution of serpentine and brucite.

Direct reaction of ultramafic tailings with simulated flue gas (i.e., 10 % CO₂ in N₂) achieves relatively rapid carbonation of brucite to Mg-carbonate (Chapter 5). However, preferential flow pathways need monitoring to ensure maximum reaction of gas with tailings and to minimise loss of industrial CO₂ to the atmosphere. The disadvantage of this method is that it primarily targets brucite, which is typically a trace to minor component of ultramafic tailings, and does not result in substantial carbonation of serpentine, at least on the 28-day time-scale tested here. However, complete carbonation of brucite at a large mine such as Mount Keith would make the mine carbon neutral (Power et al., 2014; Wilson et al., 2014).

The potential to access Mg from silicate minerals such as serpentine, which is typically present at > 80 wt. % abundance in the tailings from Woodsreef and many other ultramafic mines, could lead to higher carbon sequestration rates; however, the scale-up

of acid leaching requires that several challenges be addressed. Firstly, dissolution of existing gangue and secondary carbonate minerals should be avoided; therefore, this treatment approach may not be suited to ultramafic mines that are already highly weathered, or have a high abundance of gangue carbonate minerals. Secondly, promoting formation of an evaporative carbonate crust *in situ* with surface-applied acid treatments will inhibit further carbonation as newly formed carbonate minerals consume acid delivered in subsequent treatments, releasing CO₂ instead of resulting in silicate dissolution. Instead, subsurface leaching or a two-step heap leaching process, with separate leaching and carbonation steps, are better alternatives.

Further research is required to trial the effects of different acid concentrations and application rates, and to solve the sulfate problem, in order to maximise conversion of high-Mg leachates to Mg-carbonate. The economics of different leaching and carbonation steps should also be examined, for instance to compare the cost of (1) passive (wetland) carbonation, (2) reaction of Mg-rich leachates with an elevated CO₂ stream and (3) the use of industrial-style bioreactors for carbonation. Financial modelling and life cycle assessment should take into account the value of byproducts, such as Mg-carbonate minerals, and the potential for trace metal recovery.

6.4. Summary of incentives for uptake of mineral carbonation within the mining industry

Mineral extraction is inherently unsustainable, it is often invasive and damaging to the environment, and as a result, the minerals industry has earned a generally poor public perception (Calas, 2017; De Villiers, 2017). However, the concept of ‘sustainable development’ is gaining popularity within the mining industry. Sustainable development recognises the need to meet global demand for resources, while also adhering to

environmental protections and managing concerns of local communities (Calas, 2017; De Villiers, 2017). Mineral carbonation technology is ideally placed to contribute to this movement, by offsetting the emissions of mining, and potentially enabling the development of carbon neutral mines. There are already several examples of industry–university collaborations that are promoting uptake of mineral carbonation technologies by end users. For instance, De Beers Group – Project Minera recently announced it will conduct a comprehensive characterisation of kimberlite process residues at mines in South Africa and Canada to determine the degree of passive carbonation that has already occurred in tailings storage facilities, and the potential for promotion of mineral carbonation in the future (Mervine et al., in review). Orica has partnered with the University of Newcastle to collaborate on mineral carbonation technology, and development of a pilot scale *ex situ* reactor using CO₂ emissions captured from its ammonia and nitric acid plants (Brent et al., 2015).

While there is certainly motivation around environmental responsibility, economic incentives that are likely to drive adoption of mineral carbonation technologies by the minerals sector can be summarised below:

6.4.1. Direct economic benefits for emissions reduction

With a price on carbon, or policies enabling income generation through carbon credits implemented by most of the world’s largest economies, there is a direct economic benefit for the minerals industry to reduce greenhouse gas emissions. If further reductions are made in the costs of implementing mineral carbonation, and carbon prices increase, mineral carbonation technologies may become increasingly viable in the future.

6.4.2. Waste management

If acid generating material is used to accelerate Mg release from gangue minerals, this may reduce costs associated with neutralising acidic waste (depending on transport costs) while immobilising trace metals within Fe-(hydr)oxides and carbonate minerals forming at the neutralisation front (Chapter 5). Dissolution of tailings for accelerated mineral carbonation may decrease the volume of tailings that must be stored and reduce the health hazard from fibrous chrysotile, which is commonly present at low abundance in ultramafic mineral wastes (McCutcheon et al., 2015). Furthermore, optimising tailings storage facility design to promote mineral carbonation, by terracing or spreading of tailings over a greater surface area, and subsequent development of a carbonate cement may increase tailings stability (McCutcheon et al., 2017; Power et al., 2014; Wilson et al., 2009a).

6.4.3. Production of valuable by-products

In Chapter 5, we identify a novel mechanism for trace metal concentration and recovery from *in situ* treatments: as long as acid treatments are neutralised within the tailings, trace metals will be immobilised and will accumulate at the neutralisation front, while alkaline, high-Mg leachates are continuously generated for use in mineral carbonation reactions. Mg-carbonate, trace-metal enriched in Fe-(hydr)oxides, and silica, are all potentially recoverable by-products of mineral carbonation (Azdarpour et al., 2015; Olajire, 2013).

6.4.4. The opportunity to market mineral resources with ‘green credentials’

Markets are increasingly driving corporate social responsibility, and are ‘pulling’ metals markets by favouring materials that can demonstrate more responsible production (Fleury and Davies, 2012; Young, 2015). Although there are many examples of certification

systems particularly developed to address conflict minerals within the minerals industry (Young, 2015), Ali et al. (2017) suggest that there remains an urgent need to establish a supply chain system, similar to those used in the food industry (i.e., for palm oil, cocoa, fish, and other foods and fibres such as cotton and wood), for tracking of mineral use from source to end of life. Such a system could be used to not only verify ethical production, but to incorporate a notion of ‘metal miles’, and the environmental and energy cost of production and transport (Ali et al., 2017). The existence of such a scheme could allow resources from carbon-neutral mines to be favoured, and more highly valued, by consumer industries such as jewelers, renewable energy, and electronics manufacturers.

In summary, this thesis has contributed an improved understanding of trace metal mobility and environmental risk in mineral carbonation reactions. The improvements to carbon accounting methods developed in this thesis may also facilitate implementation of mineral carbonation and potentially lead to recognition of these treatments under carbon accounting schemes. From here, future work should continue to develop and test mineral carbonation technologies at the field-scale, and in particular, address the problem of Mg scavenging by sulfate during sulfuric acid treatments. The potential to simultaneously offset CO₂ emissions and produce a potentially economic metal deposit from an existing waste product is an exciting avenue for future development.

6.5. Chapter 6 references

Ali S.H., Giurco D., Arndt N., Nickless E., Brown G., Demetriades A., Durrheim R., Enriquez M.A., Kinnaird J., Littleboy A., Meinert L.D., Oberhänsli R., Salem J., Schodde R., Schneider G., Vidal O. and Yakovleva N. (2017) Mineral supply for sustainable development requires resource governance. *Nature* 543, 367.

- Australian Government (2011) Australian Government - ComLaw, 2011. Carbon Credits (Carbon Farming Initiative) Act 2011., <http://www.comlaw.gov.au/Series/C2011A00101/Compilations>. Accessed 28th December, 2017.
- Azdarpour A., Asadullah M., Mohammadian E., Hamidi H., Junin R. and Karaei M.A. (2015) A review on carbon dioxide mineral carbonation through pH-swing process. *Chemical Engineering Journal* 279, 615-630.
- Brent G.F., Rayson M.S., Kennedy E.M., Stockenhuber M., Collins W.J., Prigge J.D., Hynes R.G., Molloy T.S., Zulfiqar H., Farhang F., Oliver T.O., Hamblin Wang S. and Dawe M. (2015) Mineral carbonation of serpentinite: From the Laboratory to Pilot Scale - The MCi project, *5th International Conference on Accelerated Carbonation for Environmental and Material Engineering 2015*, pp. 394-403.
- Calas G. (2017) Mineral Resources and Sustainable Development. *Elements* 13, 301-306.
- Crowley K. (2017) Up and down with climate politics 2013–2016: the repeal of carbon pricing in Australia. *Wiley Interdisciplinary Reviews: Climate Change* 8, e458.
- De Villiers J.P.R. (2017) How to Sustain Mineral Resources: Beneficiation and Mineral Engineering Opportunities. *Elements* 13, 307-312.
- Flaathen T. and Gislason S. (2007) The groundwater beneath Hekla Volcano, Iceland: A natural analogue for CO₂ sequestration. *Geochimica et Cosmochimica Acta* 71, A283.
- Fleury A.-M. and Davies B. (2012) Sustainable supply chains—minerals and sustainable development, going beyond the mine. *Resources Policy* 37, 175-178.
- Goff F. and Lackner K.S. (1998) Carbon dioxide sequestering using ultramafic rocks. *Environmental Geosciences* 5, 89-102.
- Grguric B.A., Rosengren N.M., Fletcher C.M. and Hronsky J.M.A. (2006) Type 2 deposits: geology, mineralogy, and processing of the Mount Keith and Yakabindie orebodies, Western Australia. *Society of Economic Geologists Special Publication* 13, 119–138.

- Hitch M. and Dipple G.M. (2012) Economic feasibility and sensitivity analysis of integrating industrial-scale mineral carbonation into mining operations. *Minerals Engineering* 39, 268-275.
- Kemache N., Pasquier L.-C., Mouedhen I., Cecchi E., Blais J.-F. and Mercier G. (2016) Aqueous mineral carbonation of serpentinite on a pilot scale: The effect of liquid recirculation on CO₂ sequestration and carbonate precipitation. *Applied Geochemistry* 67, 21-29.
- Kemache N., Pasquier L.-C., Cecchi E., Mouedhen I., Blais J.-F. and Mercier G. (2017) Aqueous mineral carbonation for CO₂ sequestration: From laboratory to pilot scale. *Fuel Processing Technology* 166, 209-216.
- Kirsch K., Navarre-Sitchler A.K., Wunsch A. and McCray J.E. (2014) Metal Release from Sandstones under Experimentally and Numerically Simulated CO₂ Leakage Conditions. *Environmental Science & Technology* 48, 1436-1442.
- Knutti R., Rogelj J., Sedláček J. and Fischer E.M. (2016) A scientific critique of the two-degree climate change target. *Nature Geoscience* 9, 13-18.
- Lackner K.S., Wendt C.H., Butt D.P., Joyce E.L.J. and Sharp D.H. (1995) Carbon dioxide disposal in carbonate minerals. *Energy* 20, 1153-1170.
- Le Quéré C., Andrew R.M., Friedlingstein P., Sitch S., Pongratz J., Manning A.C., Korsbakken J.I., Peters G.P., Canadell J.G., Jackson R.B., Boden T.A., Tans P.P., Andrews O.D., Arora V.K., Bakker D.C.E., Barbero L., Becker M., Betts R.A., Bopp L., Chevallier F., Chini L.P., Ciais P., Cosca C.E., Cross J., Currie, K., Gasser T., Harris I., Hauck J., Haverd V., Houghton R.A., Hunt C.W., Hurtt G., Ilyina T., Jain A.K., Kato E., Kautz M., Keeling R.F., Klein Goldewijk K., Körtzinger A., Landschützer P., Lefèvre N., Lenton A., Lienert S., Lima I., Lombardozzi D., Metzl N., Millero F., Monteiro P.M.S., Munro D.R., Nabel J.E.M.S., Nakaoka S.I., Nojiri Y., Padín X.A., Peregon A., Pfeil B., Pierrot D., Poulter B., Rehder G., Reimer J., Rödenbeck C., Schwinger J., Séférian R., Skjelvan I., Stocker B.D., Tian H., Tilbrook B., van der Laan-Luijkx I.T., van der Werf G.R., van Heuven S., Viovy N., Vuichard N., Walker A.P., Watson A.J.,

- Wiltshire A.J., Zaehle S. and Zhu D. (2017) *Global Carbon Budget 2017. Earth System Science Data Discussion* 2017, 1-79.
- Macintosh A. and Waugh L. (2012) An introduction to the carbon farming initiative: Key principles and concepts. *ANU Centre for Climate Law and Policy*.
- Marcon V. and Kaszuba J. (2013) Trace metal mobilization in an experimental carbon sequestration scenario. *Procedia Earth and Planetary Science* 7, 554-557.
- Marcon V. and Kaszuba J.P. (2015) Carbon dioxide–brine–rock interactions in a carbonate reservoir capped by shale: Experimental insights regarding the evolution of trace metals. *Geochimica et Cosmochimica Acta* 168, 22-42.
- Maroto-Valer M.M., Fauth D.J., Kuchta M.E., Zhang Y. and Andrésen J.M. (2005) Activation of magnesium rich minerals as carbonation feedstock materials for CO₂ sequestration. *Fuel Processing Technology* 86, 1627-1645.
- Matter J.M., Broecker W.S., Gislason S.R., Gunnlaugsson E., Oelkers E.H., Stute M., Sigurdardóttir H., Stefansson A., Alfredsson H.A., Aradóttir E.S., Axelsson G., Sigfússon B. and Wolff-Boenisch D. (2011) The CarbFix Pilot Project—Storing carbon dioxide in basalt. *Energy Procedia* 4, 5579-5585.
- Matter J.M., Stute M., Snæbjörnsdóttir S.Ó., Oelkers E.H., Gislason S.R., Aradóttir E.S., Sigfússon B., Gunnarsson I., Sigurdardóttir H., Gunnlaugsson E., Axelsson G., Alfredsson H.A., Wolff-Boenisch D., Mesfin K., Taya D.F.d.l.R., Hall J., Dideriksen K. and Broecker W.S. (2016) Rapid carbon mineralization for permanent disposal of anthropogenic carbon dioxide emissions. *Science* 352, 1312-1314.
- McCutcheon J., Dipple G.M., Wilson S.A. and Southam G. (2015) Production of magnesium-rich solutions by acid leaching of chrysotile: A precursor to field-scale deployment of microbially enabled carbonate mineral precipitation. *Chemical Geology* 413, 119-131.
- McCutcheon J., Turvey C.C., Wilson S.A., Hamilton J.L. and Southam G. (2017) Microbial mineral carbonation of asbestos mine tailings: Potential applications to carbon storage and tailings stabilization. *Minerals* 7, 191.

- Mervine E.M., Wilson S.A., Power I.M., Dipple G.M., Turvey C.C., Hamilton J.L., Vanderzee S., Maudsepp M., Southam C., Matter J.M., Kelemen P.B., Stiefenhofer J., Miya Z. and Southam G. (in review). Potential for offsetting diamond mine carbon emissions through mineral carbonation of processed kimberlite: An assessment of De Beers mine sites in South Africa and Canada. *Mineralogy and Petrology*, in review.
- Mouedhen I., Kemache N., Pasquier L.-C., Cecchi E., Blais J.-F. and Mercier G. (2017) Effect of pCO₂ on direct flue gas mineral carbonation at pilot scale. *Journal of Environmental Management* 198, 1-8.
- Oelkers E.H., Gislason S.R. and Matter J. (2008) Mineral carbonation of CO₂. *Elements* 4, 333-337.
- Olajire A.A. (2013) A review of mineral carbonation technology in sequestration of CO₂. *Journal of Petroleum Science and Engineering* 109, 364-392.
- Olsson J., Stipp S.L.S., Makovicky E. and Gislason S.R. (2014) Metal scavenging by calcium carbonate at the Eyjafjallajökull volcano: A carbon capture and storage analogue. *Chemical Geology* 384, 135-148.
- Park A.-H.A., Jadhav R. and Fan L.-S. (2003) CO₂ mineral sequestration: Chemically enhanced aqueous carbonation of serpentine. *The Canadian Journal of Chemical Engineering* 81, 885-890.
- Park A.-H.A. and Fan L.-S. (2004) CO₂ mineral sequestration: physically activated dissolution of serpentine and pH swing process. *Chemical Engineering Science* 59, 5241-5247.
- Power I.M., Harrison A.L., Dipple G.M., Wilson S.A., Kelemen P.B., Hitch M. and Southam G. (2013) Carbon mineralization: From natural analogues to engineered systems. *Reviews in Mineralogy and Geochemistry* 77, 305-360.
- Power I.M., McCutcheon J., Harrison A.L., Wilson S.A., Dipple G.M., Kelly S., Southam C. and Southam G. (2014) Strategizing carbon-neutral mines: A case for pilot projects. *Minerals* 4, 399-436.

- Rogelj J., Luderer G., Pietzcker R.C., Kriegler E., Schaeffer M., Krey V. and Riahi K. (2015) Energy system transformations for limiting end-of-century warming to below 1.5 °C. *Nature Climate Change* 5, 519-527.
- Rogelj J., Den Elzen M., Höhne N., Fransen T., Fekete H., Winkler H., Schaeffer R., Sha, F., Riahi K. and Meinshausen M. (2016) Paris Agreement climate proposals need a boost to keep warming well below 2 C. *Nature* 534, 631-639.
- Seifritz W. (1990) CO₂ Disposal by means of Silicates. *Nature* 345, 486.
- Thomas D.L., Bird D.K., Arnórsson S. and Maher K. (2016) Geochemistry of CO₂-rich waters in Iceland. *Chemical Geology* 444, 158-179.
- Wang X., Sanna A., Maroto-Valer M.M. and Paulson T. (2015) Carbon dioxide capture and storage by pH swing mineralization using recyclable ammonium salts and flue gas mixtures. *Greenhouse Gases: Science and Technology* 5, 389-402.
- Wilson S.A., Dipple G.M., Power I.M., Thom J.M., Anderson R.G., Raudsepp M., Gabites J.E. and Southam G. (2009a) Carbon dioxide fixation within mine wastes of ultramafic-hosted ore deposits: Examples from the Clinton Creek and Cassiar chrysotile deposits, Canada. *Economic Geology* 104, 95-112.
- Wilson S.A., Harrison A.L., Dipple G.M., Power I.M., Barker S.L.L., Mayer K.U., Fallon S.J., Raudsepp M. and Southam G. (2014) Offsetting of CO₂ emissions by air capture in mine tailings at the Mount Keith Nickel Mine, Western Australia: Rates, controls and prospects for carbon neutral mining. *International Journal of Greenhouse Gas Control* 25, 121-140.
- Wunsch A., Navarre-Sitchler A.K., Moore J., Ricko A. and McCray J.E. (2013) Metal release from dolomites at high partial-pressures of CO₂. *Applied Geochemistry* 38, 33-47.
- Wunsch, A., Navarre-Sitchler, A.K., Moore, J., Ricko, A. and McCray, J.E. (2013) Metal release from dolomites at high partial-pressures of CO₂. *Applied Geochemistry* 38, 33-47.

Young, S.B. (2015) Responsible sourcing of metals: certification approaches for conflict minerals and conflict-free metals. *The International Journal of Life Cycle Assessment*, 1-19.

Appendix 1

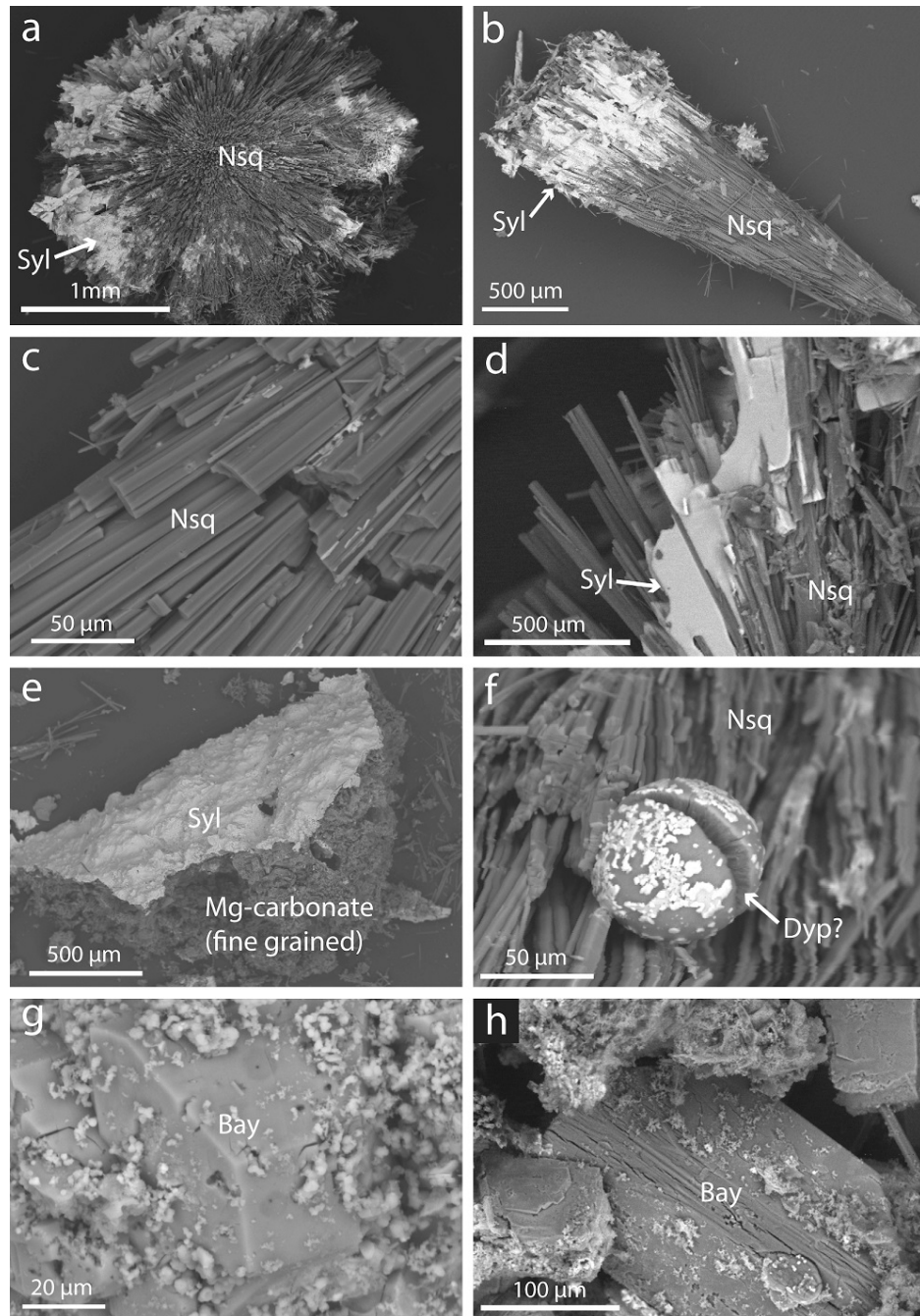
Supplementary information for Chapter 2

Jessica L. Hamilton^a

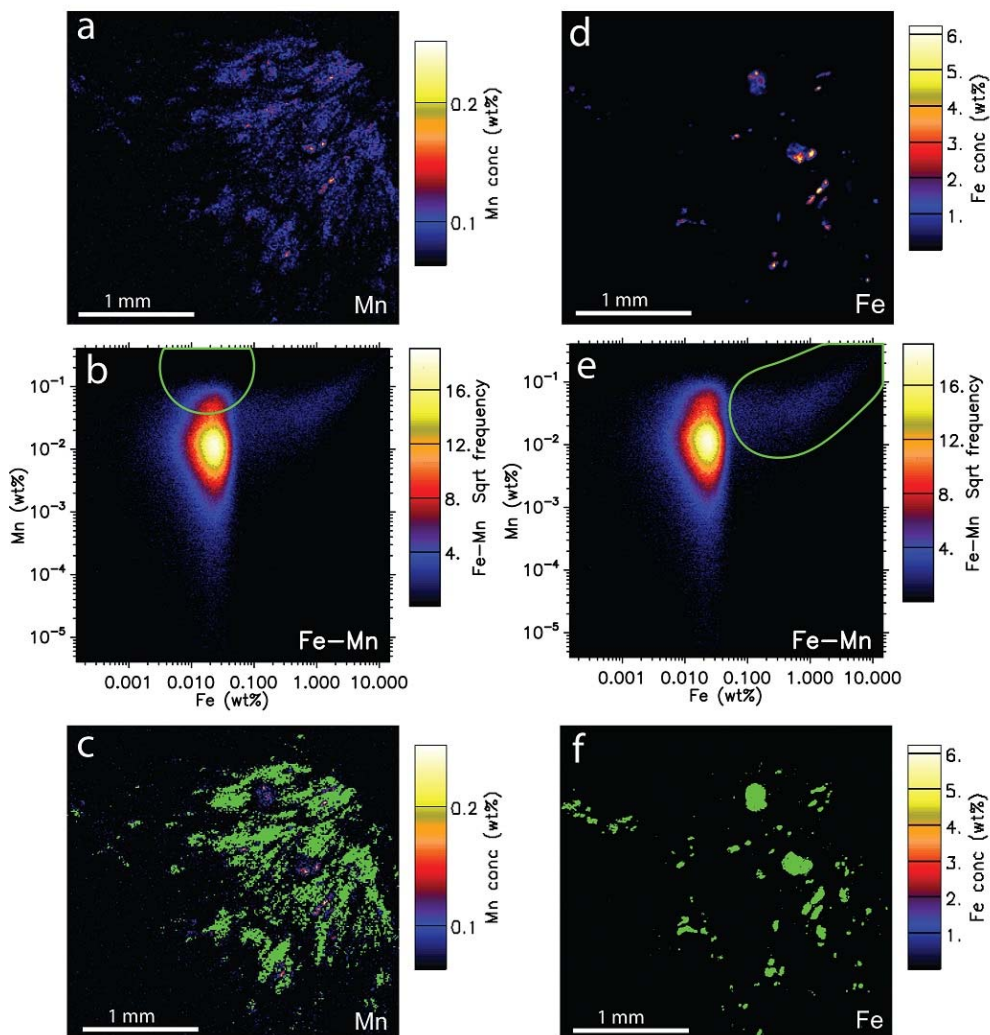
^aSchool of Earth, Atmosphere and Environment, Monash University, Australia

Appendix 1: Table S1. Calculated average percentage of trace metal dopant found in the precipitate portion by ICP-MS.

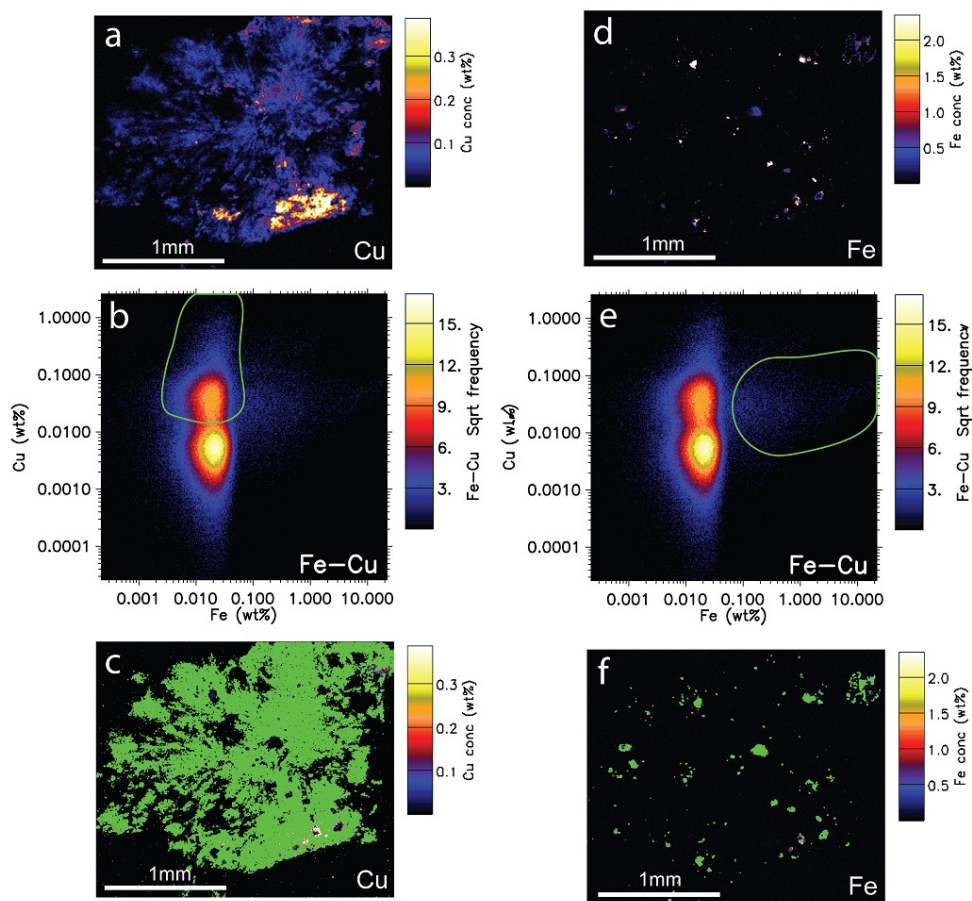
Treatment	Average % Trace Metal in Precipitate				
	Cu	Ni	Mn	Co	Cr
5 min 10 mg/L	99.17 ± 0.53	99.93 ± 0.02	99.53 ± 0.34	99.42 ± 0.25	99.25 ± 0.11
5 min 100	99.75 ± 0.07	99.91 ± 0.02	99.79 ± 0.08	99.96 ± 0.03	99.99 ± 0.01
48 h 10 mg/L	99.92 ± 0.08	94.58 ± 3.55	97.10 ± 2.90	98.59 ± 1.16	99.18 ± 0.44
48 h 100 mg/L	89.87 ± 0.96	98.98 ± 0.29	99.98 ± 0.00	99.74 ± 0.01	99.83 ± 0.02



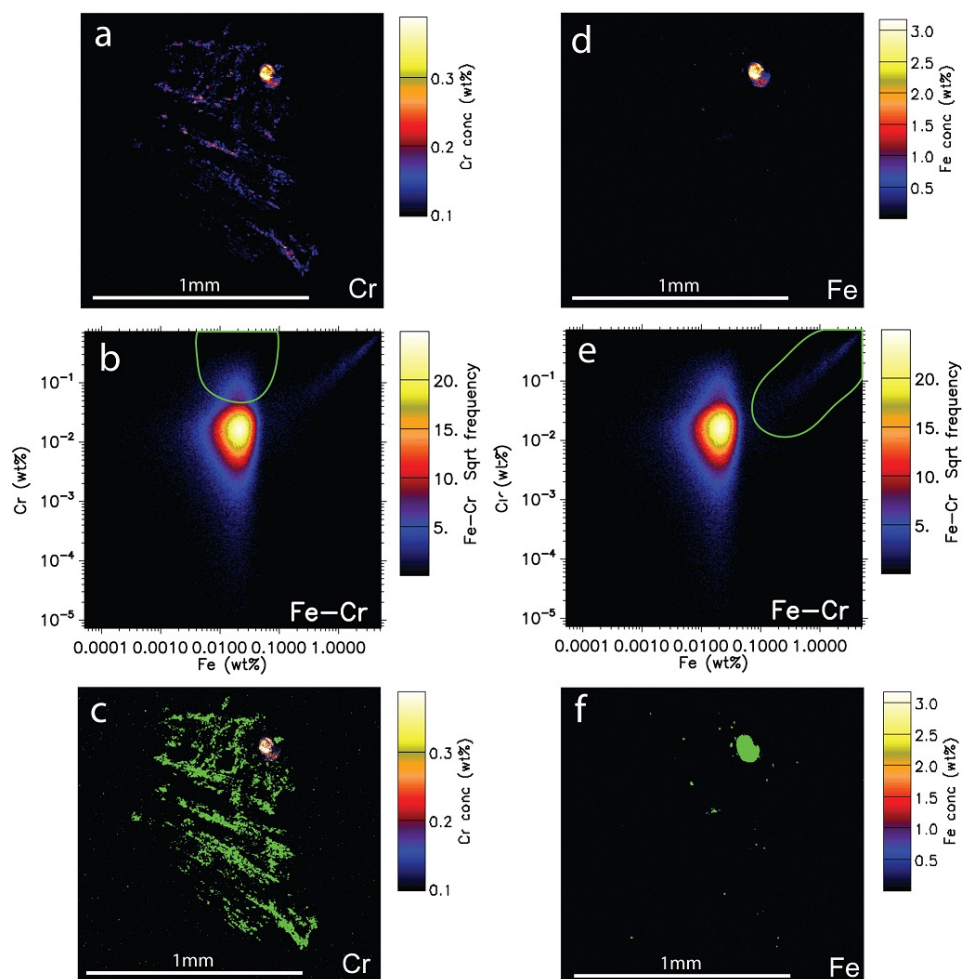
Appendix 1: Figure S1. Modified from Hamilton (2013). (A–C) Fibroidal arrays of nesquehonite (Nsq). (D) Nesquehonite fibres coated with sylvite (Syl). (E) Evaporative crust of sylvite on finely crystalline Mg-carbonate. (F) Small sphere of Mg-carbonate fibres, possibly dypingite (Dyp?). (G and H) Baylissite (Bay).



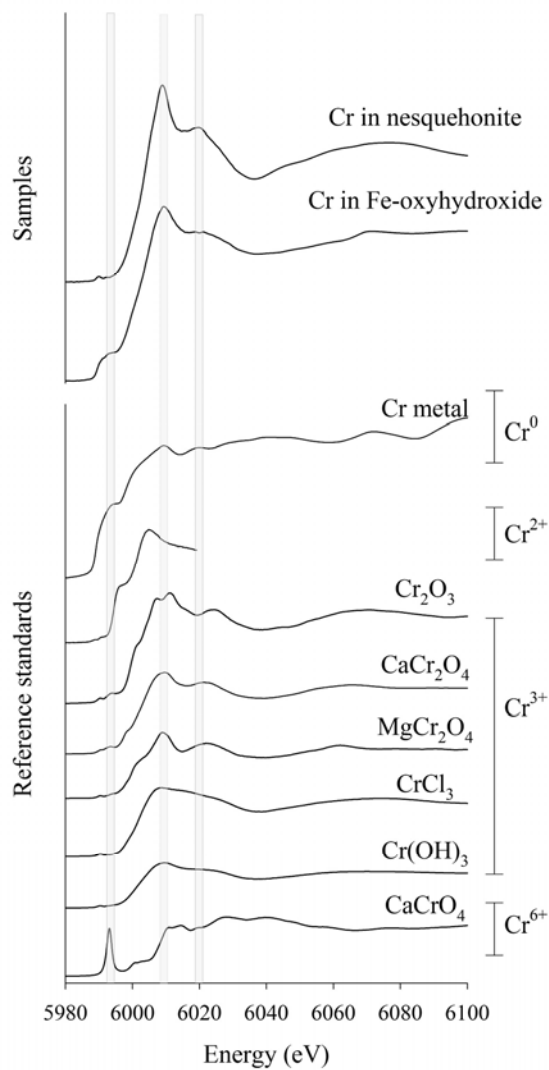
Appendix 1: Figure S2. Maps of spatial distribution of Mn highlight its association with nesquehonite and Fe-oxyhydroxides in the Mn-doped sample. (A) Synchrotron XFM image showing the distribution and concentration of Mn within the Mn-doped sample. (A) Mn versus Fe concentration plot, with region 1 (high Mn, low Fe) selected in the green field. (C) Region 1, highlighted in green on the XFM Mn map, characterises Mn uptake in nesquehonite. (D) XFM image of contaminant Fe in the Mn doped sample. (E) Mn versus Fe concentration plot, with region 2 (high Mn, high Fe) selected in the green field. (F) Region 2 is highlighted in green on the XFM Fe map and characterises Mn uptake in Fe-bearing trace phases.



Appendix 1: Figure S3. Maps of spatial distribution of Cu highlight its association with nesquehonite and Fe-oxyhydroxides in the Cu-doped sample. (A) Synchrotron XFM image showing the distribution and concentration of Cu within the Cu-doped sample. (B) Cu versus Fe concentration plot, with region 1 (high Cu, low Fe) selected in the green field. (C) Region 1, highlighted in green on the XFM Cu map, characterises Cu uptake in nesquehonite. (D) XFM image of contaminant Fe in the Cu doped sample. (E) Cu versus Fe concentration plot, with region 2 (high Cu, high Fe) selected in the green field. (F) Region 2 is highlighted in green on the XFM Fe map and characterises Cu uptake in Fe-bearing trace phases.



Appendix 1: Figure S4. Maps of spatial distribution of Cr highlight its association with nesquehonite and Fe-oxyhydroxides in the Cr-doped sample. (A) Synchrotron XFM image showing the distribution and concentration of Cr within the Cr-doped sample. (B) Cr versus Fe concentration plot, with region 1 (high Cr, low Fe) selected in the green field. (C) Region 1, highlighted in green on the XFM Cr map, characterises Cr uptake in nesquehonite. (D) XFM image of contaminant Fe in the Cr doped sample. (E) Cr versus Fe concentration plot, with region 2 (high Cr, high Fe) selected in the green field. (F) Region 2 is highlighted in green on the XFM Fe map and characterises Cr uptake in Fe-bearing trace phases.



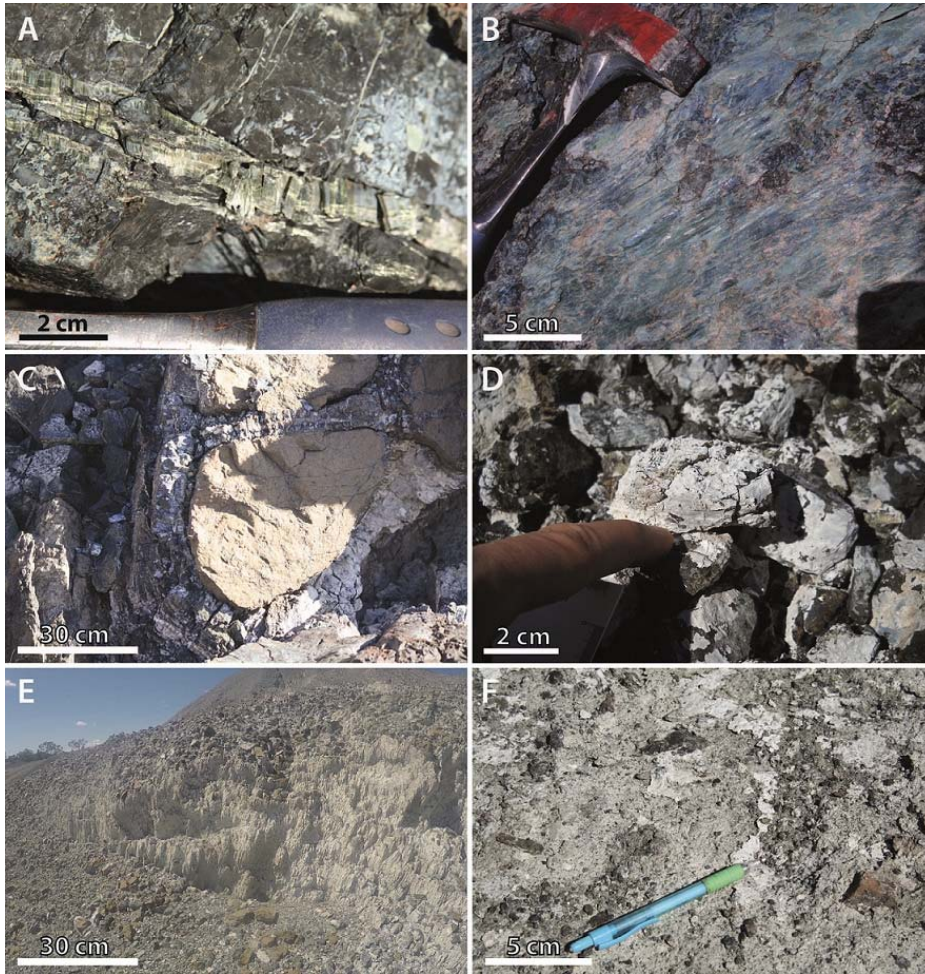
Appendix 1: Figure S5. XANES data for regions representing nesquehonite, and Fe-oxyhydroxide phases, with Cr metal reference spectra from Low et al. (2015), Cr²⁺ spectra from Berry et al. (2004) and all other reference spectra from Vogel et al. (2014).

Appendix 2

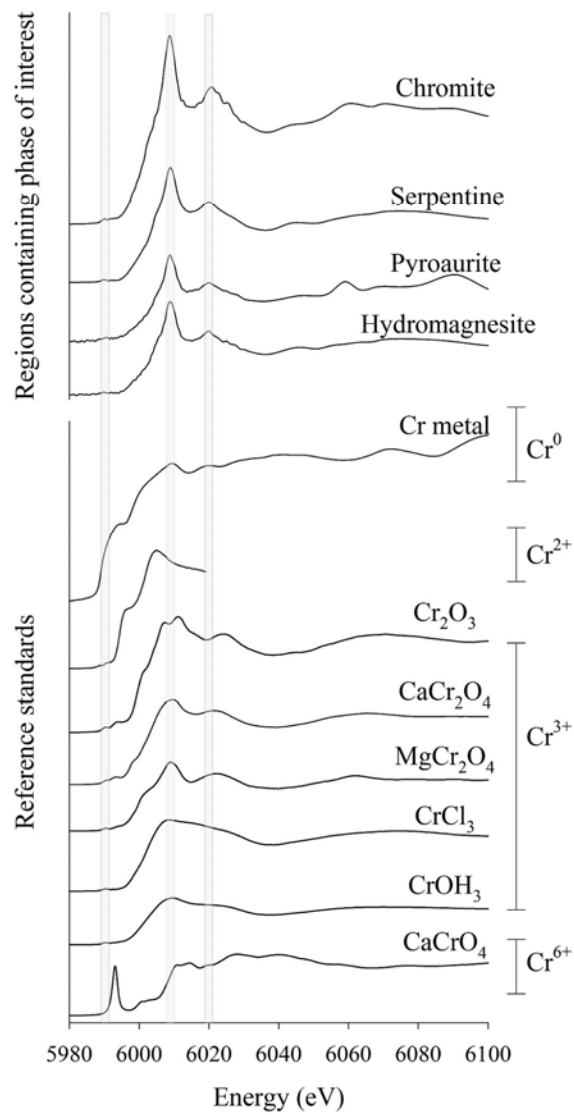
Supplementary information for Chapter 3

Jessica L. Hamilton^a

^aSchool of Earth, Atmosphere and Environment, Monash University, Australia



Appendix 2: Figure S1 (A) Chrysotile fibres in vein. (B) Chrysotile slickenside. (C) Partially serpentinised harzburgite kernel. (D) Carbonate minerals forming in cracks appear to aid in the disintegration of serpentinite boulders into smaller cobbles. (E) Vertical carbonate crusts; field of view approximately 2 m. (F) Horizontal carbonate crust as viewed from above. Pen for scale.



Appendix 2: Figure S2 XANES spectra for regions shown in SI Figure 3 compared to standard spectra from the literature (Berry and O'Neill, 2004; Low et al., 2015; Vogel et al., 2014).

Appendix 2: Table S1. Site location, description, and analysis performed for sample set.

Sample Name	Description	Easting	Northing	Elevation (m)	XRF	Thin Section	XRD	XFM	ICP-MS
<i>Pit lake water</i>									
L1	Water sample from Lake 1	56J 0282183	6633784	521					✓
L2	Water sample from Lake 2	56J 0282173	6634141	519					✓
L3	Water sample from Lake 3	56J 0282536	6634381	486					✓
L4	Water sample from Lake 4	56J 0282704	6634395	506					✓
<i>Waste rock (least weathered)</i>									
13WR1-1	Serpentinite (partially serpentinised harzburgite)	56J 0281512	6634788	490	✓	✓			
13WR1-2	Serpentinite (partially serpentinised harzburgite)	56J 0281512	6634788	490	✓				
13WR5-1	Serpentinite (partially serpentinised harzburgite)	56J 0282292	6633824	555	✓	✓			
13WR5-3	Serpentinite (partially serpentinised harzburgite)	56J 0282292	6633824	555	✓	✓	✓		
13WR3-2	Serpentinite (massive serpentine)	56J 0282711	6633902	561	✓				
13WR4-1	Serpentinite (massive serpentine)	56J 0282412	6634109	532	✓	✓	✓		
<i>Weathered waste rock and shallow tailings</i>									
13WR1-3	Carbonated Chrysotile Vein	56J 0281512	6634788	490	✓		*		
13WR1-4	Carbonated Chrysotile Vein	56J 0281512	6634788	490	✓	✓	✓	✓	
13WR1-5	Serpentinite cobble (partially serpentinised harzburgite) with carbonate coating	56J 0281512	6634788	490	✓	✓	✓	✓	
13WR3-1	Tailings (bulk)	56J 0282716	6633946	575	✓				
13WR2-6	Tailings (bulk)	56J 0282971	6633560	602	✓		*		
<i>Tailings carbonate crust (most weathered)</i>									
13WR2-1	Tailings carbonated crust (vertical)	56J 0282912	6633864	564	✓				
13WR2-2	Tailings carbonated crust (horizontal)	56J 0282995	6633818	578	✓		*		
13WR2-4	Tailings carbonated crust (vertical)	56J 0282971	6633560	602	✓	✓	✓	✓	
13WR2-5	Tailings carbonated crust (vertical)	56J 0282971	6633560	602	✓		*		
13WR2-8	Tailings carbonated crust (horizontal)	56J 0282928	6633486	604	✓	✓	✓*	✓	

*Published in Turvey et al. (2017).

Appendix 2: Table S2. Chemical analysis of water samples from pit lakes.

Sample	pH	Temperature	EC	TDS	Total alkalinity	Bicarbonate alkalinity	Ca	Mg	Na	K	Fe	Mn	Cr	Ni	Co	Cu	Cl	SO ₄ ²⁻
	<i>0.01</i>	-	<i>1</i>	<i>10</i>	<i>1</i>	<i>1</i>	<i>1</i>	<i>1</i>	<i>1</i>	<i>1</i>	<i>0.05</i>	<i>0.001</i>	<i>0.001</i>	<i>0.001</i>	<i>0.001</i>	<i>0.001</i>	<i>1</i>	<i>1</i>
	<i>pH units</i>	<i>°C</i>	<i>µS/cm</i>	<i>mg/L</i>	<i>mg/L</i>	<i>mg/L</i>	<i>mg/L</i>	<i>mg/L</i>	<i>mg/L</i>	<i>mg/L</i>	<i>mg/L</i>	<i>mg/L</i>	<i>mg/L</i>	<i>mg/L</i>	<i>mg/L</i>	<i>mg/L</i>	<i>mg/L</i>	<i>mg/L</i>
L1	9.24	21.3	383	249	169	107	1	44	13	1	b.d.	b.d.	b.d.	b.d.	b.d.	b.d.	28	1
L2	9.20	20.7	656	426	264	162	1	69	25	2	b.d.	b.d.	b.d.	b.d.	b.d.	0.002	62	3
L3	9.12	22.2	558	363	257	173	2	67	23	2	b.d.	b.d.	b.d.	b.d.	b.d.	b.d.	55	2
L4	8.88	21.9	103	67	191	86	3	45	71	8	b.d.	b.d.	b.d.	b.d.	b.d.	b.d.	125	2

Appendix 2: Table S3. Major oxide abundance data for rock samples measured using XRF.

Sample Name	Element or oxide (wt. %)																
	C (LECO)	S (LECO)	Al ₂ O ₃	CaO	Cl	CoO	Cr ₂ O ₃	Cu	Fe ₂ O ₃	K ₂ O	MgO	MnO	Na ₂ O	NiO	S	SiO ₂	TiO ₂
<i>Detection limit</i>	0.005	0.005	0.01	0.01	0.005	0.01	0.01	0.01	0.01	0.01	0.01	0.01	0.01	0.01	0.005	0.01	0.01
<i>Waste rock (least weathered)</i>																	
13WR1-1	0.360	0.049	0.62	0.07	0.005	0.01	0.46	b.d.	4.56	b.d.	40.6	0.10	0.03	0.32	0.005	39.6	b.d.
13WR1-2	0.266	0.048	0.35	0.03	b.d.	b.d.	0.07	b.d.	21.30	b.d.	33.5	0.07	0.04	0.04	0.014	34.5	b.d.
13WR5-1	0.252	0.050	0.46	0.46	0.027	0.01	0.37	b.d.	7.64	b.d.	41.0	0.11	0.03	0.30	b.d.	39.2	b.d.
13WR5-3	0.404	0.050	0.59	0.16	0.005	0.02	0.42	b.d.	3.63	b.d.	40.8	0.10	0.03	0.37	b.d.	40.1	b.d.
13WR3-2	0.298	0.050	0.51	0.05	0.006	0.02	0.42	b.d.	3.24	b.d.	41.0	0.11	0.03	0.40	b.d.	40.8	b.d.
13WR4-1	0.260	0.051	0.74	0.02	0.007	0.01	0.43	b.d.	4.62	b.d.	40.1	0.12	0.03	0.32	0.033	40.8	0.02
<i>Weathered waste rock and shallow tailings</i>																	
13WR1-3	1.110	0.048	0.29	0.12	b.d.	b.d.	0.01	0.01	8.09	0.01	39.2	0.17	0.04	0.16	0.005	32.6	b.d.
13WR1-4	1.950	0.050	0.25	0.18	b.d.	b.d.	0.06	b.d.	13.40	b.d.	37.9	0.24	0.04	0.04	b.d.	23.2	b.d.
13WR1-5	0.787	0.051	0.41	0.10	0.007	0.01	0.22	b.d.	10.50	b.d.	38.5	0.10	0.02	0.17	b.d.	35.0	b.d.
13WR3-1	0.657	0.051	0.65	0.61	0.012	b.d.	0.34	b.d.	7.78	b.d.	38.7	0.13	0.05	0.23	0.006	37.2	0.02
13WR2-6	0.367	0.049	0.61	0.38	b.d.	0.01	0.33	b.d.	6.93	b.d.	39.2	0.11	0.04	0.28	b.d.	39.7	b.d.
<i>Tailings carbonate crust (most weathered)</i>																	
13WR2-1	1.040	0.050	0.56	0.15	0.008	0.02	0.33	b.d.	7.81	0.01	38.8	0.10	0.04	0.24	0.007	36.5	0.01
13WR2-2	1.240	0.050	0.58	0.36	0.008	0.01	0.31	b.d.	6.78	b.d.	39.5	0.10	0.04	0.25	b.d.	35.2	b.d.
13WR2-4	1.860	0.049	0.55	0.51	0.005	0.01	0.28	b.d.	6.38	b.d.	39.3	0.11	0.03	0.22	0.006	33.0	b.d.
13WR2-5	1.280	0.048	0.66	0.53	b.d.	0.01	0.32	b.d.	7.54	0.03	38.5	0.11	0.04	0.24	b.d.	35.7	0.01
13WR2-8	0.731	0.050	0.50	0.22	0.010	0.01	0.37	b.d.	7.37	b.d.	39.4	0.10	0.03	0.28	b.d.	36.9	b.d.

Appendix 2: Table S4. Mineralogical abundance data (in wt. %) determined using XRD.

Sample	Description	Serpentine	Pyroaurite	Brucite	Magnetite	Enstatite	Forsterite	Hydro-magnesite	Quartz	Calcite	Total	R _{wp} ^a	χ^2 ^b	d ^c
13WR4-1	Serpentinite (massive serpentinite)	95.6	0.9	0.3	1.4	0.7	1.0		0.1	0.1	100.0	11.4	2.6	0.3
13WR5-3	Serpentinite (partially serpentinitised harzburgite)	96.6	0.5	1.1	0.2	0.6	0.7		0.1	0.1	100.0	11.9	2.8	0.3
13WR1-4	Carbonated chrysotile vein	66.7	18.9	0.2	2.7	0.5	0.6	10.1		0.3	100.0	10.1	2.3	0.5
13WR1-5	Serpentinite cobble (partially serpentinitised harzburgite) with carbonate coating	89.9	2.8	0.9	2.7	1.0	0.6	2.7		0.1	100.0	10.3	2.2	0.5
13WR2-4	Tailings carbonated crust (vertical)	78.2	1.9	0.5	1.4	1.9	1.3	14.2	0.2	0.4	100.0	9.4	2.2	0.5
13WR2-8	Tailings carbonated crust (horizontal)	87.3	2.8	1.9	1.9	1.8	1.6	3.3		0.3	100.0	10.1	2.3	0.5

^a Weighted pattern residual, a function of the least-squares residual (%).

^b Reduced chi-squares statistic for the least-squares fit.

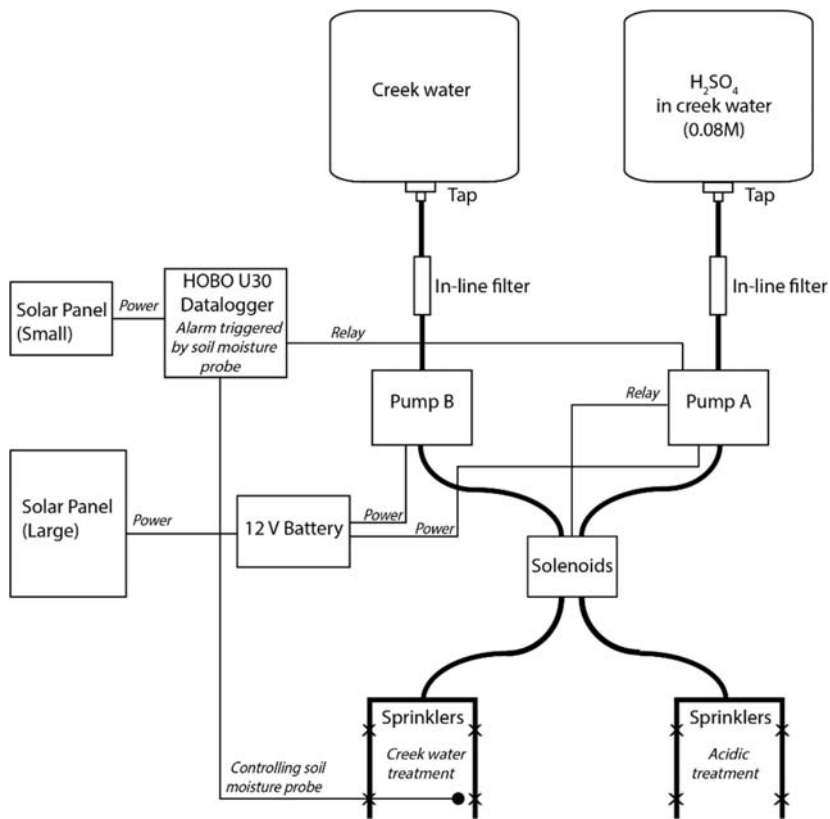
^c Weighted Durbin Watson statistic

Appendix 3

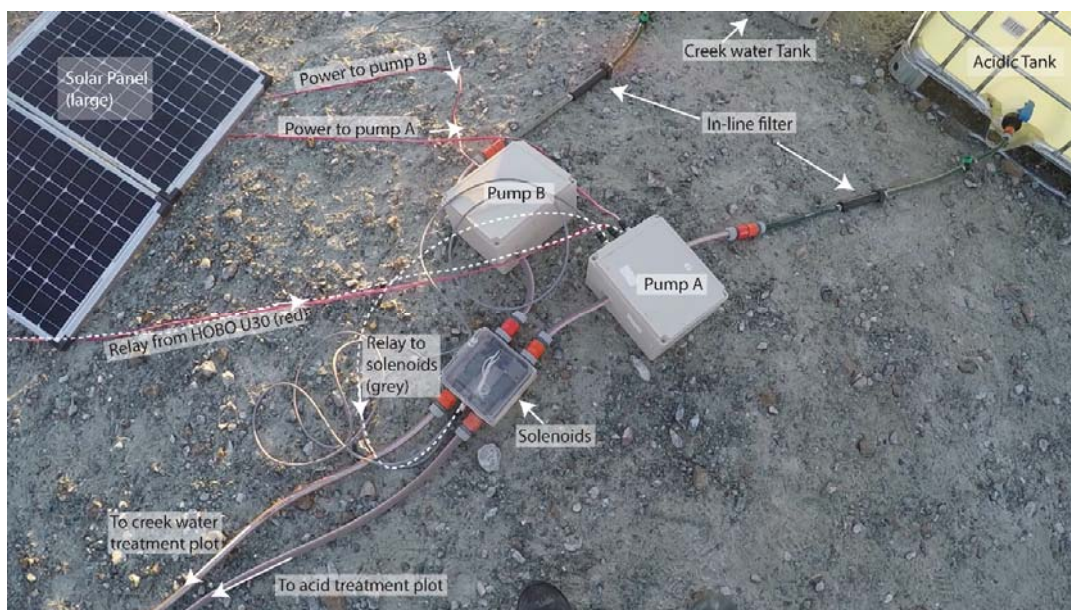
Supplementary information for Chapter 4

Jessica L. Hamilton^a

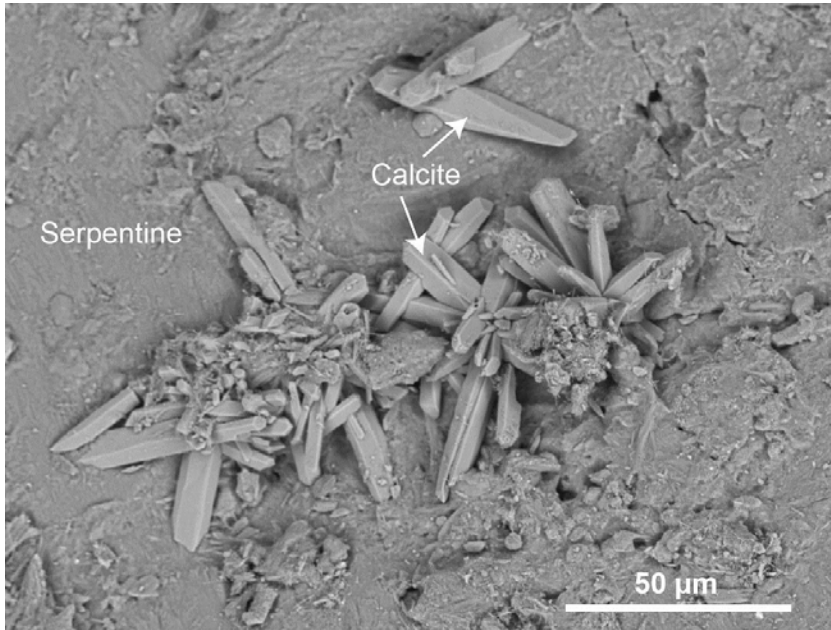
^aSchool of Earth, Atmosphere and Environment, Monash University, Australia



Appendix 3: Figure S1. Schematic describing the experiment set up.



Appendix 3: Figure S2. Photo of the experiment set up.



Appendix 3: Figure S3. Backscattered electron (BSE) micrograph of calcite precipitate on a serpentine grain surface, in sample 15WRDC5-12, collected from 110 to 120 cm depth in a site survey described by Turvey et al. (in prep).

Appendix 3: Table S1. Water chemistry of Ironbark Creek.

Creek Water			
<i>Parameter</i>	<i>Units</i>	<i>D.L.</i>	<i>Value</i>
pH	pH Unit		8.5
Alkalinity	mg/L		212
Mg	mg/L	0.001	46
Ca	mg/L	0.0001	25
Fe	mg/L	0.001	0.02
Cl	mg/L	≈0.01	21
SO₄	mg/L	≈0.01	30
NO₃	mg/L	≈0.01	0.05
Si	mg/L	0.04	4.9
Na	mg/L	0.03	52
K	mg/L	0.06	2.7
Al	ppb	0.21	1
Mn	ppb	0.09	4
Ni	ppb	0.52	< D.L
Cr	ppb	0.14	< D.L
Cu	ppb	0.29	2
Co	ppb	0.79	0.5
Ti	ppb	0.51	3.5
Zn	ppb	0.32	4

Appendix 3: Table S2. Sample characterisation.

SAMPLE NAME	Depth Range (cm)	Wet weight (g)	Dry weight (g)	Bulk Density	Porosity	Soil H₂O content (g/g)	Vol Water content %
<i>Pre Experiment</i>							
Pre-Exp C1-1	0-10	283.3	271.9	1.4	0.5	0.004	0.005
Pre-Exp C1-2	10-20	340.3	326.7	1.7	0.3	0.003	0.005
Pre-Exp C1-3	20-30	376.3	358.7	1.8	0.3	0.003	0.005
Pre-Exp C2-1	0-10	202.3	196.5	1.0	0.6	0.005	0.005
Pre-Exp C2-2	10-20	339.3	427.4	2.2	0.1	0.002	0.004
Pre-Exp C2-3	20-30	294.3	281.6	1.4	0.4	0.004	0.005
Pre-Exp C3-1	0-10	247.3	238.1	1.2	0.5	0.004	0.005
Pre-Exp C3-2	10-20	376.3	358.7	1.8	0.3	0.003	0.005
Pre-Exp C3-3	20-30	311.3	294.2	1.5	0.4	0.004	0.005
Pre-Exp C4-1	0-10	261.3	254.4	1.3	0.5	0.004	0.005
Pre-Exp C4-2	10-20	290.3	278.9	1.4	0.4	0.004	0.005
Pre-Exp C4-3	20-30	324.3	312.3	1.6	0.4	0.003	0.005
Pre-Exp C5-1	0-10	242.3	235.7	1.2	0.5	0.004	0.005
Pre-Exp C5-2	10-20	334.3	320.7	1.6	0.4	0.003	0.005
Pre-Exp C5-3	20-30	282.3	269.8	1.4	0.5	0.004	0.005
Pre-Exp C6-1	0-10	226.3	217.9	1.1	0.6	0.005	0.005
Pre-Exp C6-2	10-20	339.3	327.2	1.7	0.3	0.003	0.005
Pre-Exp C6-3	20-30	269.3	258.0	1.3	0.5	0.004	0.005
Pre-Exp C7-0 (crust)	0-2		49.4				
Pre-Exp C7-1	0-10		219.6	1.1	0.6		
Pre-Exp C7-2	10-20		229.9	1.2	0.5		
Pre-Exp C7-3	20-30		219.6	1.1	0.6		
Pre-Exp C8-0 (crust)	0-2		110.4				
Pre-Exp C8-1	0-10		290.4	1.5	0.4		
Pre-Exp C8-2	10-20		275.8	1.4	0.4		
Pre-Exp C8-3	20-30		278.3	1.4	0.4		

Appendix 3: Table S2 continued.

SAMPLE NAME	Depth Range (cm)	Wet weight (g)	Dry weight (g)	Bulk Density	Porosity	Soil H₂O content (g/g)	Vol Water content %
<i>Post Experiment</i>							
Acid Treated Plot							
Acid-C1-0	0-2	53.5	44.8			0.027	
Acid-C1-1	0-10	228.3	211.1	1.1	0.6	0.005	0.006
Acid-C1-2	10-20	329.3	311.0	1.6	0.4	0.003	0.005
Acid-C1-3	20-30	324.3	277.7	1.4	0.4	0.004	0.006
Acid-C1-4	30-40	96.5	81.7			0.014	
Acid-C1-5	40-50	91.6	75.9			0.016	
Acid-C1-6	50-60	76.6	63.3			0.019	
Acid-C1-7	60-70	76.7	63.3			0.019	
Acid-C1-8	70-80	77.5	63.6			0.019	
Acid-C1-9	80-90	84.0	70.3			0.017	
Acid-C1-10	90-100	69.4	54.9			0.023	
Acid-C2-0	0-2	65.5	55.2			0.021	
Acid-C2-1	0-10	293.3	271.7	1.4	0.5	0.004	0.006
Acid-C2-2	10-20	301.3	279.6	1.4	0.4	0.004	0.005
Acid-C2-3	20-30	288.3	270.9	1.4	0.5	0.004	0.005
Acid-C2-4	30-40	125.6	109.5			0.010	
Acid-C2-5	40-50	76.3	62.0			0.020	
Acid-C2-6	50-60	149.4	131.0			0.009	
Acid-C2-7	60-70	117.9	101.6			0.011	
Acid-C2-8	70-80	88.6	73.7			0.016	
Acid-C2-9	80-90	92.5	76.9			0.016	
Acid-C2-10	90-100	87.7	73.0			0.016	
Acid-C3-0	0-2	85.5	75.9			0.015	
Acid-C3-1	0-10	259.3	242.0	1.2	0.5	0.004	0.005
Acid-C3-2	10-20	295.3	302.7	1.5	0.4	0.003	0.005
Acid-C3-3	20-30	316.3	295.1	1.5	0.4	0.004	0.005
Acid-C3-4	30-40	76.6	63.3			0.019	
Acid-C3-5	40-50	82.5	68.6			0.018	
Acid-C3-6	50-60	100.1	85.9			0.014	
Acid-C3-7	60-70	135.4	118.8			0.010	
Acid-C3-8	70-80	117.3	100.1			0.012	
Acid-C3-9	80-90	161.3	144.4			0.008	
Acid-C3-10	90-100	134.3	122.3			0.009	

Appendix 3: Table S2 continued.

SAMPLE NAME	Depth Range (cm)	Wet weight (g)	Dry weight (g)	Bulk Density	Porosity	Soil H₂O content (g/g)	Vol Water content %
<i>Post Experiment</i>							
Water Treated Plot							
Water-C1-0	0-2	78.5	69.8			0.016	
Water-C1-1	0-10	275.3	254.1	1.3	0.5	0.004	0.006
Water-C1-2	10-20	298.3	278.8	1.4	0.4	0.004	0.005
Water-C1-3	20-30	323.3	305.2	1.6	0.4	0.003	0.005
Water-C1-4	30-40	113.7	99.6			0.011	
Water-C1-5	40-50	179.5	162.9			0.007	
Water-C1-6	50-60	200.9	184.3			0.006	
Water-C1-7	60-70	159.2	142.4			0.008	
Water-C1-8	70-80	154.6	137.6			0.008	
Water-C1-9	80-90	184.2	166.4			0.007	
Water-C1-10	90-100	186.3	167.8			0.007	
Water-C2-0	0-2	66.0	58.7			0.019	
Water-C2-1	0-10	278.6	260.4	1.3	0.5	0.004	0.005
Water-C2-2	10-20	293.1	280.3	1.4	0.4	0.004	0.005
Water-C2-3	20-30	297.6	285.9	1.5	0.4	0.004	0.005
Water-C2-4	30-40	121.0	107.1			0.011	
Water-C2-5	40-50	93.7	80.1			0.015	
Water-C2-6	50-60	87.7	73.7			0.016	
Water-C2-7	60-70	85.9	72.2			0.016	
Water-C2-8	70-80	64.8	51.3			0.025	
Water-C2-9	80-90	88.5	74.8			0.016	
Water-C2-10	90-100	65.0	52.0			0.024	
Water-C3-0	0-2	67.5	59.0			0.019	
Water-C3-1	0-10	249.3	231.4	1.2	0.5	0.005	0.005
Water-C3-2	10-20	329.3	309.8	1.6	0.4	0.003	0.005
Water-C3-3	20-30	291.3	272.4	1.4	0.5	0.004	0.005
Water-C3-4	30-40	86.8	73.2			0.016	
Water-C3-5	40-50	93.0	79.1			0.015	
Water-C3-6	50-60	106.6	91.5			0.013	
Water-C3-7	60-70	136.4	117.7			0.010	
Water-C3-8	70-80	130.3	114.4			0.010	
Water-C3-9	80-90	123.4	104.0			0.011	
Water-C3-10	90-100	134.2	117.0			0.010	

Appendix 3: Table S2 continued.

SAMPLE NAME	Depth Range (cm)	Wet weight (g)	Dry weight (g)	Bulk Density	Porosity	Soil H₂O content (g/g)	Vol Water content %
<i>Post Experiment</i>							
Control Plot							
Control-C1-0	0-2	107.5	93.5			0.012	
Control-C1-1	0-10	223.3	198.0	1.0	0.6	0.006	0.006
Control-C1-2	10-20	322.3	302.3	1.5	0.4	0.004	0.005
Control-C1-3	20-30	321.3	299.8	1.5	0.4	0.004	0.005
Control-C1-4	30-40	94.8	88.6			0.012	
Control-C1-5	40-50	116.2	107.2			0.010	
Control-C1-6	50-60	135.9	125.3			0.009	
Control-C1-7	60-70	80.9	75.4			0.014	
Control-C1-8	70-80	93.4	87.6			0.012	
Control-C1-9	80-90	134.5	126.7			0.008	
Control-C1-10	90-100	103.2	97.5			0.011	
Control-C2-0	0-2	88.5	78.5			0.014	
Control-C2-1	0-10	290.3	270.8	1.4	0.5	0.004	0.005
Control-C2-2	10-20	320.3	298.8	1.5	0.4	0.004	0.005
Control-C2-3	20-30	333.3	311.7	1.6	0.4	0.003	0.005
Control-C2-4	30-40	70.3	57.4			0.021	
Control-C2-5	40-50	114.7	99.1			0.012	
Control-C2-6	50-60	102.9	87.1			0.014	
Control-C2-7	60-70	147.9	129.1			0.009	
Control-C2-8	70-80	166.8	149.6			0.007	
Control-C2-9	80-90	112.9	98.4			0.012	
Control-C2-10	90-100	108.4	94.7			0.012	
Control-C3-0	0-2	75.5	67.3			0.017	
Control-C3-1	0-10	271.3	251.2	1.3	0.5	0.004	0.006
Control-C3-2	10-20	290.3	275.3	1.4	0.4	0.004	0.005
Control-C3-3	20-30	306.3	287.8	1.5	0.4	0.004	0.005
Control-C3-4	30-40	115.2	100.1			0.011	
Control-C3-5	40-50	102.7	89.1			0.013	
Control-C3-6	50-60	84.7	71.4			0.017	
Control-C3-7	60-70	142.9	127.2			0.009	
Control-C3-8	70-80	144.7	129.5			0.009	
Control-C3-9	80-90	129.7	114.3			0.010	
Control-C3-10	90-100	93.1	79.1			0.015	

Appendix 3: Table S2 continued.

SAMPLE NAME	Depth Range (cm)	Wet weight (g)	Dry weight (g)	Bulk Density	Porosity	Soil H₂O content (g/g)	Vol Water content %
<i>Post Experiment</i>							
Horizontal Profiles							
Acid-HC-1	0-10	62.0	50.7			0.024	
Acid-HC-2	10-20	54.0	41.6			0.031	
Acid-HC-3	20-30	43.3	31.3			0.044	
Acid-HC-4	30-40	53.6	41.5			0.031	
Water-HC-1	0-10	157.4	143.3			0.008	
Water-HC-2	10-20	152.3	137.9			0.008	
Water-HC-3	20-30	177.3	162.5			0.007	
Water-HC-4	30-40	203.8	186.9			0.006	
Control-HC-1	0-10	93.4	88.8			0.012	
Control-HC-2	10-20	103.6	97.6			0.011	
Control-HC-3	20-30	92.0	85.8			0.012	
Control-HC-4	30-40	85.9	80.7			0.013	

Appendix 3: Table S3. Mineralogical data.

Sample	Depth (cm)	Serpentine (+ amorphous)	Pyroaurite	Brucite	Magnetite/ Chromite	Enstatite	Forsterite	Hydro-magnesite	Quartz	Calcite	Magnesite	Coalingite	Chlorite	Tremolite	Total	R _{wp} ^a	χ ² ^b	d ^c
<i>Pre Experiment</i>																		
Pre-Exp C1-1	0-10	93.1	0.4	0.1	2.7	1.3	1.0	1.0	0.2	0.3					100.0	14.4	3.5	0.2
Pre-Exp C1-2	10-20	86.4	2.3	0.4	2.1	2.7	4.5	1.3	0.1	0.3					100.0	10.4	2.6	0.4
Pre-Exp C1-3	20-30	85.7	2.1	0.6	1.9	3.0	4.8	1.4	0.2	0.3			*		100.0	10.3	2.6	0.4
Pre-Exp C2-1	0-10	88.8	1.2	0.7	2.1	2.0	3.4	1.3	0.1	0.4			*	*	100.0	9.7	2.4	0.4
Pre-Exp C2-2	10-20	85.2	1.3	0.9	2.1	3.5	5.2	1.3	0.1	0.5			*	*	100.0	9.9	2.5	0.5
Pre-Exp C2-3	20-30	86.4	2.0	0.4	1.9	3.6	4.2	1.1	0.2	0.3					100.0	10.3	2.6	0.4
Pre-Exp C3-1	0-10	84.2	1.3	0.5	2.1	3.0	7.1	1.3	0.1	0.3					100.0	9.6	2.3	0.4
Pre-Exp C3-2	10-20	88.0	1.6	0.8	1.9	2.0	3.9	1.4	0.1	0.3					100.0	10.1	2.5	0.4
Pre-Exp C3-3	20-30	89.5	1.7	0.3	1.9	1.9	3.5	0.8	0.1	0.3					100.0	10.3	2.5	0.4
Pre-Exp C4-1	0-10	85.5	2.2	0.3	2.3	3.6	4.2	1.3	0.2	0.3			*	*	100.0	10.2	2.5	0.4
Pre-Exp C4-2	10-20	89.9	1.2	0.3	2.0	2.1	2.6	1.5	0.1	0.3					100.0	11.0	2.8	0.3
Pre-Exp C4-3	20-30	86.2	1.9	1.1	1.9	3.9	3.8	0.8	0.2	0.4			*	*	100.0	11.0	2.9	0.3
Pre-Exp C5-1	0-10	87.1	1.2	0.4	2.1	3.0	4.0	1.7	0.2	0.4			*		100.0	9.7	2.4	0.5
Pre-Exp C5-2	10-20	89.8	1.1	0.5	2.0	2.3	3.1	0.8	0.1	0.2			*		100.0	9.8	2.5	0.4
Pre-Exp C5-3	20-30	86.6	1.9	0.5	2.3	2.7	4.9	0.8	0.1	0.2					100.0	10.1	2.5	0.4
Pre-Exp C6-1	0-10	84.8	1.8	1.1	1.6	2.8	6.8	0.7	0.1	0.3					100.0	10.2	2.5	0.3
Pre-Exp C6-2	10-20	85.4	2.1	0.9	2.0	2.9	5.5	0.8	0.1	0.2					100.0	10.3	2.6	0.3
Pre-Exp C6-3	20-30	87.3	1.4	1.2	1.8	2.7	4.4	0.6	0.2	0.4			*		100.0	10.4	2.7	0.4
Pre-Exp C7-0	0-2	92.0	1.8	0.6	2.6	0.6	1.5	0.4	0.2	0.4				*	100.0	10.3	2.6	0.5
Pre-Exp C7-1	0-10	89.1	1.7	0.5	1.9	2.2	2.5	1.3	0.1	0.6					100.0	10.6	2.3	0.5
Pre-Exp C7-2	10-20	90.0	1.4	0.8	1.8	2.5	2.4	0.6	0.1	0.4					100.0	10.1	2.1	0.5
Pre-Exp C7-3	20-30	89.6	2.2	0.4	2.5	1.6	2.7	0.5	0.1	0.6					100.0	11.1	2.3	0.4
Pre-Exp C8-0	0-2	76.5	1.4	0.9	1.4	7.5	11.4	0.4	0.1	0.3			*		100.0	11.4	2.9	0.3
Pre-Exp C8-1	0-10	84.4	2.0	0.6	3.1	1.9	6.7	0.9	0.2	0.2					100.0	9.9	2.2	0.5
Pre-Exp C8-2	10-20	80.6	1.3	0.8	3.8	3.7	8.6	0.7	0.3	0.1					100.0	10.7	2.4	0.4
Pre-Exp C8-3	20-30	84.5	1.1	0.5	2.7	3.1	7.1	0.5	0.4	0.1					100.0	11.8	2.7	0.3

^a Weighted pattern residual, a function of the least-squares residual (%).

^b Reduced χ² statistic for the least-squares fit.

^c Weighted Durbin Watson statistic.

*Trace mineral identified qualitatively, but not included in refinement.

Appendix 3: Table S3 continued.

Sample	Depth (cm)	Serpentine (+ amorphous)	Pyroaurite	Brucite	Magnetite	Enstatite	Forsterite	Hydro-magnesite	Quartz	Calcite	Magnesite	Coalingite	Chlorite	Tremolite	Total	R _{wp} ^a	χ ^{2b}	d ^c
<i>Post Experiment</i>																		
Acid Plot																		
Orange Precipitate	0-2	91.4	1.8	0.3	2.7	1.2	2.3		0.2	0.2					100.0	10.9	2.6	0.3
Acid-C1-0	0-2	90.9	0.3	0.1	2.6	2.1	3.8		0.3	0.0					100.0	11.9	3.0	0.3
Acid-C1-1	0-10	87.1	1.9	0.5	2.5	1.9	4.4	1.0	0.4	0.4			*	*	100.0	11.0	2.8	0.4
Acid-C1-2	10-20	87.7	1.8	0.7	2.2	1.7	3.8	1.8	0.1	0.3			*		100.0	11.2	2.8	0.3
Acid-C1-3	20-30	84.0	1.9	0.6	2.1	3.6	5.8	1.9		0.1					100.0	10.9	2.8	0.3
Acid-C1-4	30-40	86.6	1.1	0.9	2.0	2.8	5.3	1.0	0.1	0.2			*		100.0	10.8	2.8	0.3
Acid-C1-5	40-50	87.9	0.8	1.3	2.0	2.1	4.6	0.9	0.1	0.2			*		100.0	10.8	2.7	0.3
Acid-C1-6	50-60	86.7	0.7	1.3	2.5	2.4	5.7	0.4	0.1	0.2					100.0	11.9	2.9	0.3
Acid-C1-7	60-70	85.9	1.1	0.9	2.0	3.5	6.1		0.1	0.4			*		100.0	10.4	2.6	0.3
Acid-C1-8	70-80	87.4	1.1	0.8	2.5	2.6	5.1		0.1	0.4			*		100.0	10.9	2.7	0.3
Acid-C1-9	80-90	86.1	0.5	0.6	3.1	3.2	6.0		0.1	0.4			*		100.0	11.9	2.9	0.3
Acid-C1-10	90-100	92.0	0.5	0.4	2.3	0.9	2.9		0.1	0.8			*		100.0	10.8	2.8	0.3
Acid-C2-0	0-2	90.0	1.5	0.1	2.0	2.9	3.0		0.2	0.3					100.0	9.9	2.5	0.4
Acid-C2-1	0-10	86.4	2.2	0.6	1.9	3.4	3.8	1.3	0.1	0.4			*		100.0	10.5	2.6	0.4
Acid-C2-2	10-20	87.7	2.3	0.5	2.2	1.7	3.6	1.6	0.1	0.3					100.0	10.8	2.6	0.3
Acid-C2-3	20-30	85.1	1.8	0.8	2.0	3.1	5.9	1.0	0.1	0.1			*		100.0	10.7	2.7	0.3
Acid-C2-4	30-40	87.3	1.3	0.8	1.7	3.2	4.9	0.5	0.1	0.2			*		100.0	10.1	2.6	0.4
Acid-C2-5	40-50	89.1	1.0	0.7	2.3	1.8	4.1	0.5	0.1	0.4			*		100.0	10.9	2.8	0.3
Acid-C2-6	50-60	87.2	1.1	0.9	2.9	1.8	4.6	0.2	0.6	0.6					100.0	10.8	2.3	0.4
Acid-C2-7	60-70	88.0	1.1	0.8	3.2	2.0	4.1		0.4	0.5					100.0	10.5	2.3	0.5
Acid-C2-8	70-80	88.0	0.7	0.8	4.0	2.5	3.3		0.1	0.6					100.0	9.9	2.1	0.5
Acid-C2-9	80-90	86.3	0.6	0.6	3.0	2.0	6.3		0.6	0.6					100.0	10.7	2.3	0.4
Acid-C2-10	90-100	88.2	0.9	0.9	3.4	2.4	3.4		0.1	0.6					100.0	10.0	2.1	0.5
Acid-C3-0	0-2	87.2	0.4	0.4	2.2	3.1	6.3	0.0	0.2	0.1			*		100.0	10.7	2.7	0.4
Acid-C3-1	0-10	86.8	1.7	0.6	2.2	1.9	5.5	1.0		0.2					100.0	10.6	2.7	0.4
Acid-C3-2	10-20	85.6	2.2	0.8	2.2	3.0	4.4	1.5	0.1	0.3			*		100.0	10.9	2.8	0.3
Acid-C3-3	20-30	87.7	1.4	0.3	2.3	2.4	4.3	1.2	0.1	0.3			*		100.0	10.4	2.6	0.3
Acid-C3-4	30-40	87.7	1.2	0.8	2.7	2.0	4.5	0.6		0.4					100.0	11.2	2.8	0.3
Acid-C3-5	40-50	83.3	1.0	0.8	2.0	4.7	6.9	0.7	0.1	0.5		*	*	*	100.0	10.3	2.7	0.5
Acid-C3-6	50-60	89.0	0.7	0.7	2.2	2.2	4.6		0.1	0.5			*		100.0	10.2	2.6	0.4
Acid-C3-7	60-70	90.2	0.9	0.7	2.4	1.4	3.4		0.1	0.7			*	*	100.0	10.7	2.7	0.4
Acid-C3-8	70-80	88.6	0.8	0.7	3.3	2.0	4.0		0.1	0.4			*	*	100.0	10.5	2.6	0.4
Acid-C3-9	80-90	90.0	1.2	0.6	2.8	1.8	3.0		0.1	0.5				*	100.0	10.7	2.7	0.4
Acid-C3-10	90-100	81.0	0.6	1.1	1.3	6.1	9.7		0.1	0.1			*	*	100.0	10.1	2.6	0.4

^a Weighted pattern residual, a function of the least-squares residual (%).

^b Reduced χ² statistic for the least-squares fit.

^c Weighted Durbin Watson statistic.

*Trace mineral identified qualitatively, but not included in refinement.

Appendix 3: Table S3 continued.

Sample	Depth (cm)	Serpentine (+ amorphous)	Pyroaurite	Brucite	Magnetite	Enstatite	Forsterite	Hydro-magnesite	Quartz	Calcite	Magnesite	Coalingite	Chlorite	Tremolite	Total	R _{wp} ^a	χ^2 ^b	d ^c
Water Plot																		
Water-C1-0	0-2	89.5	1.3	0.2	3.0	1.4	3.7	0.3	0.4	0.2					100.0	11.2	2.7	0.3
Water-C1-1	0-10	86.1	2.1	0.6	1.8	2.4	5.3	1.4	0.1	0.3			*		100.0	10.9	2.7	0.4
Water-C1-2	10-20	83.5	2.4	1.2	2.6	2.2	6.2	1.6	0.1	0.2					100.0	11.1	2.8	0.3
Water-C1-3	20-30	78.0	1.7	1.9	2.0	5.2	9.6	1.3	0.1	0.4			*		100.0	10.7	2.7	0.5
Water-C1-4	30-40	84.7	0.1	1.8	1.7	3.4	7.2	0.9		0.2					100.0	13.1	3.4	0.2
Water-C1-5	40-50	87.5	1.0	1.0	1.8	2.9	5.2	0.3	0.1	0.2					100.0	11.1	2.8	0.3
Water-C1-6	50-60	87.6	1.4	1.6	1.9	2.2	4.6	0.4	0.1	0.3			*		100.0	10.8	2.8	0.4
Water-C1-7	60-70	87.8	1.4	1.3	1.9	2.0	4.6	0.3	0.5	0.2			*	*	100.0	11.2	2.9	0.3
Water-C1-8	70-80	88.5	2.0	2.9	2.5	1.5	2.2	0.2		0.2			*		100.0	11.7	3.0	0.3
Water-C1-9	80-90	88.3	1.1	1.1	1.8	1.9	5.4		0.2	0.1					100.0	10.8	2.7	0.3
Water-C1-10	90-100	87.6	1.3	1.0	2.1	2.3	5.2		0.2	0.3			*		100.0	10.5	2.6	0.3
Water-C2-0	0-2	88.7	1.5	0.6	2.1	2.4	4.1		0.1	0.6			*		100.0	10.7	2.8	0.4
Water-C2-1	0-10	83.3	2.0	1.2	2.2	3.7	6.2	1.0	0.1	0.3					100.0	10.4	2.7	0.4
Water-C2-2	10-20	85.5	1.4	0.6	1.5	5.0	4.6	1.1	0.1	0.2					100.0	11.4	2.9	0.3
Water-C2-3	20-30	85.9	1.3	1.0	2.7	4.0	4.3	0.5	0.1	0.3					100.0	11.4	2.8	0.3
Water-C2-4	30-40	86.2	0.8	1.1	1.9	3.9	5.2	0.8		0.1					100.0	10.7	2.7	0.4
Water-C2-5	40-50	87.7	0.8	1.0	2.0	3.8	4.0	0.5		0.3					100.0	11.5	2.9	0.4
Water-C2-6	50-60	83.7	1.1	1.7	3.9	2.7	6.5	0.1	0.3	0.1					100.0	10.2	2.2	0.5
Water-C2-7	60-70	85.3	1.3	1.3	3.7	2.5	5.6		0.2	0.2					100.0	11.1	2.3	0.4
Water-C2-8	70-80	85.8	1.0	1.3	4.2	2.1	5.3		0.1	0.2					100.0	10.6	2.3	0.5
Water-C2-9	80-90	86.8	0.7	1.1	2.6	3.1	5.3		0.3	0.2					100.0	11.0	2.3	0.4
Water-C2-10	90-100	85.7	1.2	1.5	3.3	2.6	5.3		0.2	0.2					100.0	10.4	2.2	0.5
Water-C3-0	0-2	89.2	1.1	0.9	2.8	0.9	3.2	1.3	0.0	0.6			*		100.0	10.3	2.4	0.5
Water-C3-1	0-10	88.1	1.7	0.4	2.2	2.6	3.9	0.7	0.0	0.3			*		100.0	10.5	2.7	0.4
Water-C3-2	10-20	87.9	1.0	0.5	2.2	2.6	4.3	1.3	0.0	0.1			*		100.0	10.4	2.6	0.4
Water-C3-3	20-30	87.2	2.2	0.7	2.1	1.9	5.2	0.5	0.1	0.2			*		100.0	10.9	2.8	0.4
Water-C3-4	30-40	88.0	1.2	1.1	1.9	2.4	4.5	0.5	0.1	0.2			*		100.0	11.2	2.9	0.4
Water-C3-5	40-50	88.5	1.2	1.0	1.9	3.1	3.9			0.3					100.0	10.5	2.7	0.4
Water-C3-6	50-60	84.2	0.8	1.3	3.5	3.3	6.6		0.1	0.2					100.0	11.5	2.9	0.4
Water-C3-7	60-70	88.5	1.5	1.1	2.1	2.4	4.1		0.1	0.3					100.0	10.7	2.8	0.4
Water-C3-8	70-80	89.1	0.8	1.3	2.0	2.1	4.5			0.2			*		100.0	10.3	2.7	0.4
Water-C3-9	80-90	88.8	1.4	1.0	1.9	1.9	4.4		0.1	0.4					100.0	10.7	2.8	0.4
Water-C3-10	90-100	85.7	1.3	1.0	2.1	3.1	6.4		0.1	0.3					100.0	10.5	2.7	0.4

^a Weighted pattern residual, a function of the least-squares residual (%).

^b Reduced χ^2 statistic for the least-squares fit.

^c Weighted Durbin Watson statistic.

*Trace mineral identified qualitatively, but not included in refinement.

Appendix 3: Table S3 continued.

Sample	Depth (cm)	Serpentine (+ amorphous)	Pyroaurite	Brucite	Magnetite	Enstatite	Forsterite	Hydro-magnesite	Quartz	Calcite	Magnesite	Coalingite	Chlorite	Tremolite	Total	R _{wp} ^a	χ ² ^b	d ^c
Control Plot																		
Control-C1-0	0-2	90.3	1.5	0.1	2.3	1.4	3.4	0.0	0.6	0.4					100.0	10.6	2.3	0.4
Control-C1-1	0-10	88.9	2.6	0.4	2.0	1.3	2.8	1.5	0.2	0.4			*		100.0	10.2	2.5	0.3
Control-C1-2	10-20	87.6	1.8	0.8	2.0	2.0	4.3	1.2	0.2	0.2					100.0	10.3	2.3	0.4
Control-C1-3	20-30	87.9	1.8	0.8	2.0	2.0	4.0	1.1	0.2	0.3					100.0	10.1	2.3	0.4
Control-C1-4	30-40	87.4	1.8	0.8	1.9	2.2	4.3	1.2	0.2	0.3					100.0	10.1	2.3	0.4
Control-C1-5	40-50	86.6	1.7	1.1	2.3	2.3	4.6	1.0	0.2	0.2			*		100.0	10.4	2.3	0.4
Control-C1-6	50-60	86.8	2.0	0.7	2.1	2.2	4.4	1.3	0.3	0.3					100.0	10.4	2.3	0.4
Control-C1-7	60-70	87.7	1.7	0.9	1.9	2.0	4.2	1.0	0.2	0.3			*		100.0	10.2	2.3	0.5
Control-C1-8	70-80	87.2	1.6	1.0	2.3	2.0	4.5	0.9	0.2	0.2					100.0	10.3	2.3	0.4
Control-C1-9	80-90	88.0	1.6	0.8	2.2	2.4	4.3	0.2	0.2	0.3					100.0	10.7	2.7	0.4
Control-C1-10	90-100	88.9	1.1	0.9	2.1	2.6	3.9		0.2	0.2					100.0	10.9	2.7	0.3
Control-C2-0	0-2	89.7	1.0	0.6	1.5	3.2	2.5	1.0	0.1	0.5			*		100.0	11.5	2.9	0.3
Control-C2-1	0-10	89.6	1.2	0.5	1.7	2.2	3.3	0.9	0.1	0.3					100.0	10.3	2.6	0.3
Control-C2-2	10-20	88.4	1.4	0.8	1.6	1.9	4.9	0.6	0.1	0.4					100.0	10.7	2.7	0.3
Control-C2-3	20-30	89.5	1.1	0.7	2.0	2.6	3.2	0.5	0.1	0.3					100.0	10.7	2.7	0.4
Control-C2-4	30-40	88.5	0.6	0.6	1.8	3.2	4.7	0.2	0.1	0.4					100.0	11.3	2.9	0.3
Control-C2-5	40-50	86.0	0.8	0.8	1.9	4.9	4.7	0.3	0.2	0.4					100.0	10.8	2.7	0.3
Control-C2-6	50-60	85.7	0.8	1.0	2.2	4.8	4.4	0.2	0.1	0.7					100.0	10.7	2.7	0.4
Control-C2-7	60-70	87.0	0.8	1.0	2.2	4.4	3.8		0.1	0.6					100.0	10.4	2.6	0.4
Control-C2-8	70-80	90.1	0.7	1.0	1.9	1.9	4.0		0.2	0.2					100.0	10.8	2.6	0.4
Control-C2-9	80-90	88.4	0.6	1.0	2.9	2.1	4.4		0.3	0.2					100.0	10.3	2.4	0.4
Control-C2-10	90-100	86.8	1.3	0.9	2.1	3.6	4.7		0.3	0.4					100.0	10.2	2.4	0.4
Control-C3-0	0-2	88.9	1.1	0.3	2.2	1.8	3.7	1.3	0.1	0.6			*	*	100.0	9.7	2.4	0.4
Control-C3-1	0-10	88.4	1.3	0.6	1.8	2.6	3.6	1.4		0.3			*		100.0	9.8	2.3	0.5
Control-C3-2	10-20	80.7	2.0	0.9	2.1	4.8	7.9	1.2		0.3			*		100.0	10.1	2.3	0.5
Control-C3-3	20-30	85.1	1.3	0.8	2.2	3.6	6.1	0.6	0.1	0.3					100.0	10.8	2.8	0.3
Control-C3-4	30-40	87.0	1.2	1.0	1.6	2.6	6.1		0.1	0.3					100.0	10.6	2.7	0.3
Control-C3-5	40-50	86.4	1.3	1.1	2.2	2.1	6.6		0.1	0.1					100.0	11.0	2.4	0.4
Control-C3-6	50-60	88.7	1.6	1.1	2.3	1.7	4.1		0.1	0.3					100.0	10.0	2.3	0.5
Control-C3-7	60-70	88.0	1.5	1.0	2.4	2.5	4.3		0.1	0.2					100.0	10.2	2.3	0.5
Control-C3-8	70-80	85.5	1.4	1.0	2.3	4.1	5.6			0.2					100.0	10.5	2.3	0.5
Control-C3-9	80-90	90.0	0.9	1.0	1.7	2.5	3.5		0.1	0.2		*	*		100.0	10.8	2.7	0.3
Control-C3-10	90-100	83.6	1.6	1.1	1.7	5.3	5.9		0.2	0.5			*		100.0	11.0	2.8	0.4

^a Weighted pattern residual, a function of the least-squares residual (%).

^b Reduced χ² statistic for the least-squares fit.

^c Weighted Durbin Watson statistic.

*Trace mineral identified qualitatively, but not included in refinement.

Appendix 3: Table S3 continued.

Sample	Depth (cm)	Serpentine (+ amorphous)	Pyroaurite	Brucite	Magnetite	Enstatite	Forsterite	Hydro-magnesite	Quartz	Calcite	Magnesite	Coalingite	Chlorite	Tremolite	Total	R _{wp} ^a	χ ² ^b	d ^c
Horizontal Profiles																		
Acid-HC-1	0-10	87.1	2.5	0.6	2.2	2.2	4.1	0.7	0.5	0.2					100.0	11.1	2.6	0.3
Acid-HC-2	10-20	84.1	1.8	0.8	2.6	3.7	5.9	0.4	0.5	0.3					100.0	11.1	2.6	0.3
Acid-HC-3	20-30	87.2	1.3	0.8	3.2	2.9	4.0	0.1	0.2	0.4					100.0	10.7	2.5	0.4
Acid-HC-4	30-40	84.7	0.8	1.5	3.1	3.3	6.1	0.0	0.4	0.2					100.0	11.2	2.6	0.3
Water-HC-1	0-10	84.5	2.1	0.9	3.5	2.3	5.7	0.6	0.3	0.2					100.0	11.7	2.8	0.3
Water-HC-2	10-20	84.4	2.2	0.9	2.2	3.5	6.0	0.4	0.4	0.2					100.0	10.9	2.6	0.3
Water-HC-3	20-30	80.8	1.4	1.0	2.0	7.4	6.5	0.4	0.3	0.2					100.0	11.2	2.6	0.4
Water-HC-4	30-40	73.1	1.3	2.3	2.4	7.9	12.3	0.4	0.2	0.1					100.0	11.4	2.7	0.4
Control-HC-1	0-10	85.0	2.0	0.6	2.2	3.2	5.6	0.7	0.4	0.3					100.0	12.1	3.0	0.3
Control-HC-2	10-20	85.8	1.8	0.8	3.1	2.5	4.7	0.4	0.4	0.4					100.0	10.9	2.6	0.4
Control-HC-3	20-30	84.4	1.5	1.0	2.6	3.6	5.8	0.0	0.4	0.7					100.0	12.4	3.0	0.3
Control-HC-4	30-40	86.0	1.4	1.3	2.2	3.5	4.9	0.0	0.1	0.6					100.0	10.2	2.5	0.5

^a Weighted pattern residual, a function of the least-squares residual (%).

^b Reduced χ² statistic for the least-squares fit.

^c Weighted Durbin Watson statistic.

*Trace mineral identified qualitatively, but not included in refinement.

Appendix 3: Table S4. Total and organic carbon measurements, and calculated estimates for the abundance of unaccounted crystallographic carbon.

Sample	Depth	Total C	Organic C	Unaccounted C	Expected Hydromagnesite	% of Expected hydromagnesite detected by XRD	OR Expected Artinite	OR Expected Coalingite
	(cm)	wt. %	wt. %	wt. %	wt. %	% relative	wt. %	wt. %
Pre Experiment								
Pre-Exp C1-1	0-10	0.31	<0.01	0.17	2.60	37	2.75	11.98
Pre-Exp C1-2	10-20	0.32		0.08	2.15	62	1.36	5.92
Pre-Exp C1-3	20-30	0.33		0.09	2.25	60	1.50	6.53
Pre-Exp C3-1	0-10	0.31		0.10	2.27	59	1.56	6.82
Pre-Exp C3-2	10-20	0.38		0.15	2.89	50	2.45	10.70
Pre-Exp C3-3	20-30	0.29		0.12	1.98	41	1.96	8.54
Pre-Exp C5-1	0-10	0.37		0.11	2.78	60	1.86	8.11
Pre-Exp C5-2	10-20	0.29		0.14	2.16	38	2.26	9.86
Pre-Exp C5-3	20-30	0.28		0.12	1.94	39	1.98	8.63
Pre-Exp C7-0	0-2	0.20	0.01	0.08	1.26	34	1.39	6.07
Pre-Exp C7-1	0-10	0.34		0.16	2.53	36	2.70	11.78
Pre-Exp C7-2	10-20	0.27		0.13	2.04	37	2.17	9.48
Pre-Exp C7-3	20-30	0.25		0.14	1.92	27	2.37	10.34
Pre-Exp C8-0	0-2	0.34	0.02	0.20	2.38	16	3.34	14.59
Pre-Exp C8-1	0-10	0.41		0.15	2.74	46	2.48	10.83
Pre-Exp C8-2	10-20	0.38		0.22	2.74	23	3.53	15.42
Pre-Exp C8-3	20-30	0.29		0.11	1.54	30	1.83	7.98
Post Experiment								
Acid Plot								
Orange Precipitate	0-2	0.20	0.01	0.11	1.28	16	1.82	7.95
Acid-C1-0	0-2	0.15		0.11	1.22	0	1.81	7.88
Acid-C1-1	0-10	0.30		0.09	1.91	53	1.49	6.52
Acid-C1-2	10-20	0.38		0.11	2.88	61	1.87	8.14
Acid-C1-3	20-30	0.36		0.10	2.81	66	1.60	6.98
Acid-C1-4	30-40	0.28		0.12	2.10	46	1.92	8.39
Acid-C1-5	40-50	0.28		0.12	2.12	44	2.01	8.78
Acid-C2-0	0-2	0.30		0.20	2.09	0	3.29	14.35
Acid-C2-1	0-10	0.38		0.15	2.68	47	2.40	10.46
Acid-C2-2	10-20	0.38		0.12	2.78	56	2.03	8.87
Acid-C2-3	20-30	0.32		0.15	2.46	42	2.41	10.53
Acid-C2-4	30-40	0.28		0.16	2.05	26	2.55	11.12
Acid-C2-5	40-50	0.18		0.04	0.86	57	0.63	2.75
Acid-C3-0	0-2	0.19	0.02	0.15	1.47	0	2.48	10.82
Acid-C3-1	0-10	0.26	0.03	0.07	1.68	60	1.13	4.91
Acid-C3-2	10-20	0.31	0.02	0.06	2.07	72	0.99	4.32
Acid-C3-3	20-30	0.30	0.01	0.11	2.24	52	1.80	7.87
Acid-C3-4	30-40	0.30		0.15	2.06	31	2.38	10.39
Acid-C3-5	40-50	0.26		0.10	1.64	40	1.65	7.19
Acid-C3-6	50-60	0.25		0.16	1.56	0	2.63	11.46
Acid-C3-7	60-70	0.25		0.13	1.28	0	2.16	9.42
Acid-C3-8	70-80	0.28		0.19	1.88	0	3.15	13.77
Acid-C3-9	80-90	0.23		0.13	1.23	0	2.08	9.06
Acid-C3-10	90-100	0.17		0.12	1.21	0	2.04	8.90

Appendix 3: Table S4. continued.

Sample	Depth	Total C	Organic C	Unaccounted C	Expected Hydromagnesite	% of Expected hydromagnesite detected by XRD	OR Expected Artinite	OR Expected Coalingite
	(cm)	wt. %	wt. %	wt. %	wt. %	% relative	wt. %	wt. %
Water Plot								
Water-C1-0	0-2	0.27		0.17	1.97	14	2.84	12.40
Water-C1-1	0-10	0.36		0.13	2.65	54	2.06	8.98
Water-C1-2	10-20	0.36		0.11	2.67	60	1.80	7.86
Water-C1-3	20-30	0.34		0.12	2.39	53	1.90	8.29
Water-C1-4	30-40	0.27		0.12	2.15	44	2.03	8.84
Water-C1-5	40-50	0.21		0.11	1.38	22	1.80	7.87
Water-C2-0	0-2	0.28		0.16	1.58	0	2.66	11.60
Water-C2-1	0-10	0.36		0.16	2.55	40	2.57	11.22
Water-C2-2	10-20	0.34		0.16	2.63	41	2.58	11.27
Water-C2-3	20-30	0.33		0.20	2.48	20	3.34	14.60
Water-C2-4	30-40	0.25		0.11	1.95	43	1.88	8.19
Water-C2-5	40-50	0.22		0.10	1.46	31	1.69	7.39
Water-C3-0	0-2	0.24	0.02	-0.01	1.29	104	-0.09	-0.40
Water-C3-1	0-10	0.25	0.02	0.09	1.62	45	1.51	6.58
Water-C3-2	10-20	0.35	0.03	0.15	2.78	46	2.51	10.96
Water-C3-3	20-30	0.29	0.01	0.17	2.08	22	2.73	11.92
Water-C3-4	30-40	0.26		0.14	1.88	25	2.36	10.31
Water-C3-5	40-50	0.23		0.15	1.46	0	2.46	10.72
Water-C3-6	50-60	0.20		0.14	1.40	0	2.35	10.25
Water-C3-7	60-70	0.21		0.13	1.29	0	2.16	9.45
Water-C3-8	70-80	0.20		0.14	1.40	0	2.35	10.24
Water-C3-9	80-90	0.23		0.13	1.31	0	2.20	9.60
Water-C3-10	90-100	0.19		0.11	1.11	0	1.86	8.14
Control Plot								
Control-C1-0	0-2	0.31		0.22	2.13	0	3.58	15.61
Control-C1-1	0-10	0.40		0.14	2.83	53	2.23	9.73
Control-C1-2	10-20	0.32		0.12	2.35	52	1.89	8.26
Control-C1-3	20-30	0.33		0.14	2.41	44	2.26	9.85
Control-C1-4	30-40	0.29		0.08	2.01	59	1.37	6.00
Control-C1-5	40-50	0.22		0.04	1.40	74	0.62	2.69
Control-C2-0	0-2	0.36		0.17	2.46	40	2.82	12.32
Control-C2-1	0-10	0.32		0.14	2.31	39	2.37	10.35
Control-C2-2	10-20	0.30		0.15	2.05	27	2.52	10.98
Control-C2-3	20-30	0.29		0.17	2.07	22	2.71	11.85
Control-C2-4	30-40	0.24		0.14	1.61	12	2.37	10.35
Control-C2-5	40-50	0.23		0.12	1.44	22	1.90	8.29
Control-C3-0	0-2	0.38	0.01	0.15	2.75	48	2.40	10.47
Control-C3-1	0-10	0.34	0.02	0.11	2.50	56	1.83	8.00
Control-C3-2	10-20	0.30	0.02	0.09	2.05	59	1.40	6.11
Control-C3-3	20-30	0.28	0.03	0.13	1.87	30	2.20	9.62
Control-C3-4	30-40	0.20		0.12	1.19	0	2.00	8.73
Control-C3-5	40-50	0.22		0.16	1.58	0	2.66	11.61
Control-C3-6	50-60	0.21		0.12	1.18	0	1.99	8.67
Control-C3-7	60-70	0.21		0.14	1.35	0	2.28	9.94
Control-C3-8	70-80	0.24		0.17	1.67	0	2.80	12.24
Control-C3-9	80-90	0.20		0.14	1.33	0	2.23	9.72
Control-C3-10	90-100	0.22		0.11	1.07	0	1.79	7.82

Appendix 3: Table S5. Stable and radiogenic carbon data.

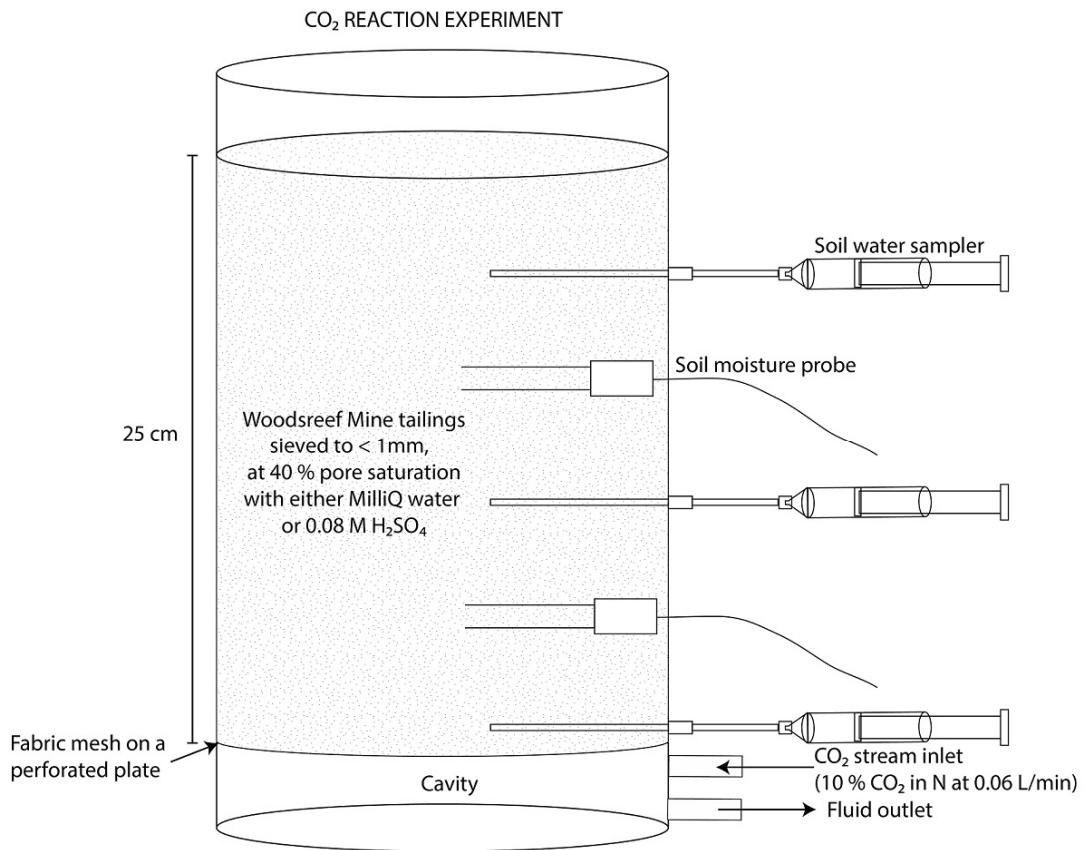
Sample	Depth	$\delta^{13}\text{C}$	1σ	$F^{14}\text{C}$	1σ	^{14}C age	1σ
	<i>cm</i>	<i>‰</i>	<i>‰</i>	-	-	<i>years</i>	<i>years</i>
Control-C3-1	0-2	-2	1	0.8969	0.0021	874	24
Control-C3-5	40-50	-4	1	0.8279	0.0021	1517	26
Control-C3-10	90-100	-5	1	0.8027	0.0020	1765	25

Appendix 4

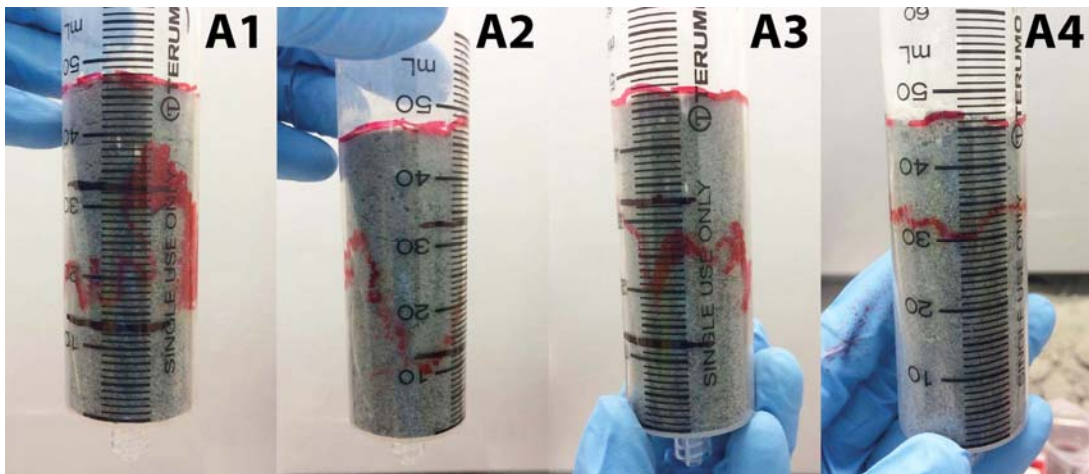
Supplementary information for Chapter 5

Jessica L. Hamilton^a

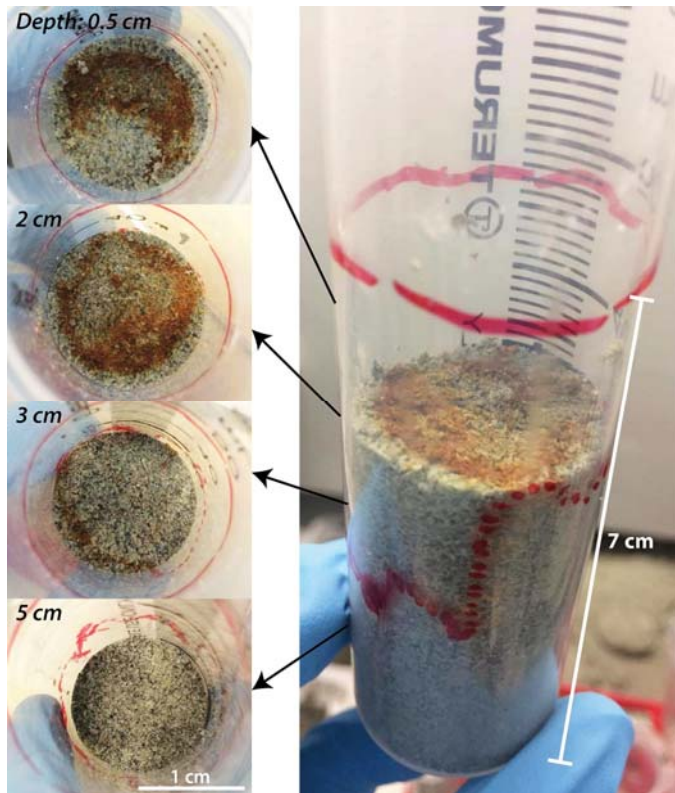
^aSchool of Earth, Atmosphere and Environment, Monash University, Australia



Appendix 4: Figure S1. CO₂ reaction column design.



Appendix 4: Figure S2. Photographs of acid-leached columns at the completion of the experiment, showing the rusted layer traced in red marker, and the 2 cm and 5 cm intervals chosen for dissection marked in black on columns A1-3.



Appendix 4: Figure S3. Photographs taken during dissection of acid leached column (replicate A3). Note: although the red dotted line on the outside of the column shows the rusted horizon reaches approximately 4 cm depth in places, the bulk of the rusted material is present at 0.5 to 2 cm depth, in the centre of the column. The rusted horizon moved outwards with depth, intersecting the exterior of the column where the dotted red line is marked, and is not present below that point.

Appendix 4: Table S1. Parameters used in MIN3P model.

Parameter	Input	Reference	Notes
Porosity, ϕ	0.49		measured
Hydraulic conductivity K [m s^{-1}]	5.00E-08	estimated after Stolburg (2005)	all directions
<i>Retention curve</i>			
α [m^{-1}]	0.8	Bea et al. (2012)	
n	1.4	Bea et al. (2012)	
Solid density, ρ_s [kg m^{-3}]	1300		measured
Gas phase diffusion coefficient [$\text{m}^2 \text{s}^{-1}$]	1.65E-05	Bea et al. (2012)	
Aqueous phase diffusion coefficient [$\text{m}^2 \text{s}^{-1}$]	8.00E-10	Bea et al. (2012)	
Initial temperature	22		measured

Appendix 4: Table S2. Initial mineral abundances, input surface areas, and dissolution rate laws used in MIN3P model.

Phase	Abundance (wt. %)	Abundance (mineral vol. fraction)	Mineral density	Effective Surface area (m ² /g)	Input surface area (m ² /L bulk)	Rate	Dissolution / precipitation reaction
Chrysotile	86.6	4.38E-01	2.55	0.6	6.76E+02	n/a	kinetic (Thom et al., 2013)
Lizardite (to make up total vol. to 100 %)	3.2	3.80E-02	2.57	0.6	4.73E+01	n/a	kinetic (Daval et al., 2013)
Forsterite	1.4	1.15E-03	3.20	0.8	1.48E+01	n/a	kinetic (Klein and Hurlbut, 1993)
Magnetite	2.9	7.28E-03	5.18	0.001	3.80E-01	n/a	Kinetic (Paladri and Kharaka, 2004)
Brucite	2.5	1.36E-02	2.39	0.30	9.24	n/a	kinetic (Pokrovsky and Schott, 2004)
Hydro-magnesite	2.9	1.74E-02	2.18	n/a	n/a	1.00E-07	quasi-equilibrium
Calcite	0.2	1.15E-03	2.71	0.04	0.12	n/a	kinetic (Chou et al., 1989)
Quartz	0.2	1.08E-03	2.65	n/a	n/a	1.00E-09	quasi-equilibrium
Chalcedony	0.0	0.00	2.65	n/a	n/a	1.00E-07	quasi-equilibrium
Nesquehonite	0.0	0.00	1.85	n/a	n/a	1.00E-07	quasi-equilibrium
Gypsum	0.0	0.00	2.30	n/a	n/a	1.00E-09	quasi-equilibrium
Epsomite	0.0	0.00	1.67	n/a	n/a	1.00E-09	quasi-equilibrium
Hexahydrite	0.0	0.00	1.76	n/a	n/a	1.00E-09	quasi-equilibrium
Hematite	0.0	0.00	5.30	n/a	n/a	1.00E-09	quasi-equilibrium
Ferrihydrite	0.0	0.00	3.80	n/a	n/a	1.00E-09	quasi-equilibrium
Fe(OH) ₂ (s)	0.0	0.00	3.40	n/a	n/a	1.00E-09	quasi-equilibrium

^aEffective surface areas for chrysotile and calcite are from Bea et al. (2012), effective area for brucite is from Wilson et al. (2014). Effective surface area is reduced from geometric surface area reported in White et al. (1994).

Appendix 4: Table S3. Water chemistry of initial pore water and acidic water used for leaching.

	Initial Condition*	Boundary condition - acidic water
Variable	(M)	(M)
pH ^a	9.5	1
Mg	9.66E-02	1.60E-06
Ca	4.69E-05	1.77E-09
H ₄ SiO ₄	4.49E-05	1.00E-10
SO ₄	1.00E-10	8.00E-02
pCO ₂ ^b	4.00E-04	4.00E-04
pO ₂ ^b	0.21	0.21

*Initial pore water chemistry based on measurements from the first leachate collected from the acid leached column.

Appendix 4: Table S4. Tailings properties after CO₂ reaction experiment.

Sample	Depth	Sample dry weight	Water content	Bulk Density	Vol. water content	Soil Porosity	Pore saturation
units	cm	g	g/g	g/cm³	m³/m³	-	%
BIG W 0-5	0-5	1363.1	0.01	1.5	0.02	0.4	4.4
BIG W 5-10	5-10	1247.9	0.04	1.4	0.05	0.5	10.2
BIG W 10-25	10-25	3456.6	0.02	1.3	0.02	0.5	4.7
	Total:	6067.6			weight gain:	169.6 g	
BIG A 0-5	0-5	1226.0	0.01	1.3	0.02	0.5	3.2
BIG A 5-10	5-10	1239.6	0.04	1.4	0.05	0.5	11.0
BIG A 10-25	10-25	3533.4	0.06	1.3	0.07	0.5	14.3
	Total:	5998.9			weight gain:	100.9 g	

Appendix 4: Table S5. XRF data (in wt. %) for CO₂ reacted columns.

Sample	Detection Limit	Bulk 1	BIG W 0-5	BIG W 5-10	BIG W 10-25	BIG W 20-25 hand sample	BIG A 0-5	BIG A 5-10	BIG A 10-25	BIG A 20-25 hand sample
Depth (cm)			0-5	5-10	10-25	20-25	0-5	5-10	10-25	20-25
SiO ₂	0.01	35.73	35.09	35.08	34.79	34.86	35.26	35.25	34.99	34.91
Al ₂ O ₃	0.01	0.58	0.58	0.57	0.55	0.56	0.57	0.58	0.56	0.57
CaO	0.01	0.26	0.26	0.26	0.25	0.25	0.25	0.25	0.26	0.26
Fe ₂ O ₃	0.01	7.73	7.93	7.64	7.6	7.58	7.66	7.64	7.62	7.73
K ₂ O	0.001	0.001	0.002	0.002	0.001	0.001	0.002	0.001	0.001	0.001
MgO	0.01	39.4	38.5	38.5	38.4	38.4	39	38.8	38.6	38.5
Na ₂ O	0.01	0.05	0.05	0.05	0.05	0.06	0.05	0.05	0.05	0.05
P ₂ O ₅	0.001	0.011	0.011	0.011	0.011	0.011	0.011	0.012	0.012	0.011
SO ₃	0.001	0.076	0.073	0.071	0.071	0.070	0.203	0.180	0.166	0.165
TiO ₂	0.001	0.003	0.005	0.003	0.005	0.005	0.004	0.005	0.004	0.007
MnO	0.001	0.099	0.097	0.097	0.096	0.097	0.097	0.098	0.097	0.097
BaO	0.001	0.007	0.006	0.008	0.006	0.008	0.009	0.007	0.008	0.002
Cr ₂ O ₃	0.001	0.355	0.365	0.352	0.346	0.355	0.357	0.357	0.338	0.361
Ni	0.001	0.189	0.181	0.184	0.183	0.184	0.186	0.184	0.185	0.184
Co	0.001	0.009	0.008	0.008	0.007	0.008	0.008	0.008	0.008	0.008
Total C	0.01	0.48	0.86	1.03	1.07	1.00	0.77	0.86	0.98	0.93
Organic C	0.01		0.02				0.04			
LOI1000 as received*	0.01	15.63	16.94	17.29	17.79	17.76	16.61	16.87	17.36	17.38
Total		100.61	100.98	101.16	101.23	101.21	101.09	101.15	101.24	101.17

*Loss on ignition at 1000°C in a Thermo-Gravimetric Analyser

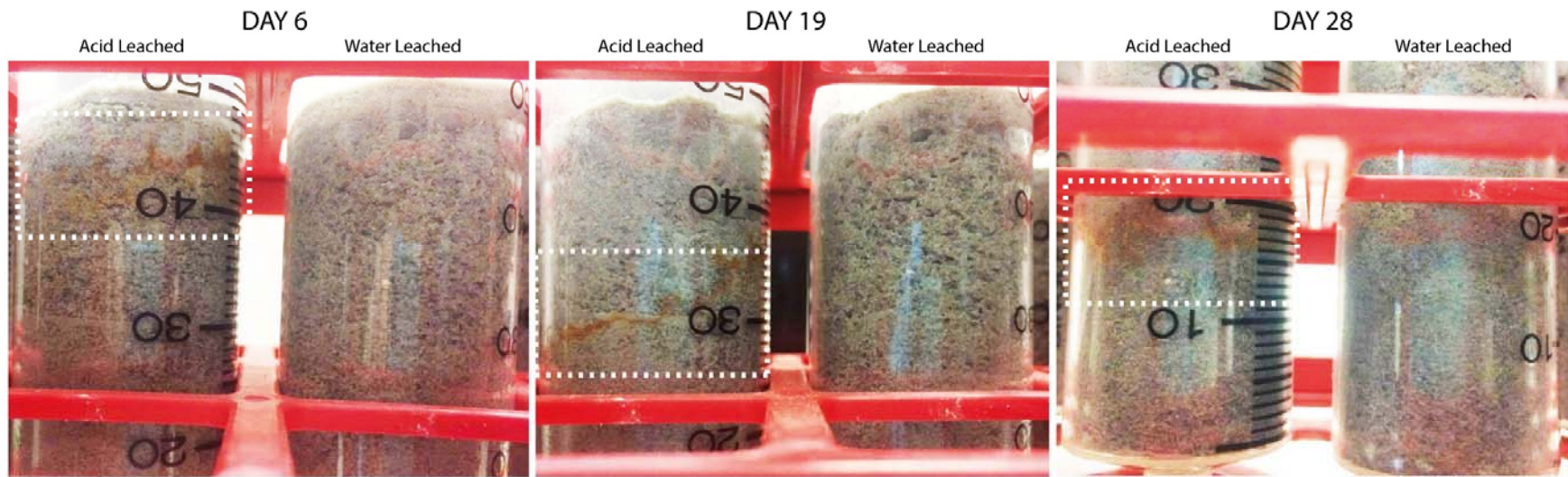
Appendix 4: Table S6. Rietveld refinement results for CO₂ reacted experiment.

	Bulk 1	Bulk 2	Bulk 3	CO₂ W 0-5	CO₂ W 5-10	CO₂ W 10-25	CO₂ W 20-25	CO₂ A 0-5	CO₂ A 5-10	CO₂ A 10-25	CO₂ A 20-25
Depth (cm)				0-5	5-10	10-25	20-25	0-5	5-10	10-25	20-25
Serpentine	85.9	86.7	87.3	85.0	85.5	85.3	85.8	88.4	87.7	87.1	87.5
Pyroaurite	3.1	3.2	2.2	2.5	2.8	2.5	2.3	2.3	2.5	2.6	2.5
Brucite	1.3	1.2	1.1	0.7	0.5	0.8	0.4	0.7	0.6	0.6	0.3
Magnetite / Chromite	2.9	2.6	3.2	3.1	3.0	2.5	2.8	2.8	2.3	2.6	3.1
Enstatite	1.5	1.3	1.4	2.6	1.9	1.6	2.4	1.0	1.5	1.1	2.1
Forsterite	1.6	1.7	1.6	2.1	1.6	1.8	2.1	1.2	1.7	1.5	1.4
Hydromagnesite	3.1	2.9	2.7	2.7	3.1	2.7	2.2	3.0	3.1	2.9	2.3
Quartz	0.3	0.2	0.2	0.5	0.8	0.2	0.4	0.2	0.3	0.4	0.2
Calcite	0.3	0.2	0.2	0.7	0.3	0.4	0.3	0.3	0.3	0.3	0.3
Nesquehonite	0.0	0.0	0.0	0.1	0.6	2.2	1.2	0.1	0.0	0.9	0.2
Magnesite	0.0	0.0	0.0	0.0	0.0	0.0	0.0	0.0	0.0	0.0	0.0
Chlorite	0.0	0.0	0.0	0.0	0.0	0.0	0.0	0.0	0.0	0.0	0.0
Tremolite	0.0	0.0	0.0	0.0	0.0	0.0	0.0	0.0	0.0	0.0	0.0
Total	100.0	100.0	100.0	100.0	100.0	100.0	100.0	100.0	100.0	100.0	100.0
R_{wp}^a	10.1	10.3	11.5	11.4	10.6	9.5	9.9	10.4	10.3	9.9	10.4
χ²^b	2.6	2.5	2.9	2.8	2.7	2.3	2.4	2.6	2.6	2.5	2.6
d^c	0.4	0.4	0.3	0.4	0.4	0.4	0.4	0.4	0.4	0.4	0.4

^a Weighted pattern residual, a function of the least-squares residual (%).

^b Reduced χ² statistic for the least-squares fit.

^c Weighted Durbin Watson statistic.



Appendix 4: Figure S3. Photographs of acid treated column (replicate A1) and water leached column (replicate W3), showing migration of the rusted layer downwards through the column over time.

Appendix 4: Table S7. Average tailings properties after leaching experiment.

Sample	Depth	Sample dry weight (g)	Water content (g/g)	Bulk Density (g/cm³)	Vol. water content (g/cm³)	Soil Porosity	Pore saturation
units	cm	g	g/g	g/cm³	m³/m³	-	%
Average W 0-2	0-2	14.3	0.1	1.1	0.1	0.6	25.5
Average W 2-5	2-5	25.7	0.1	1.3	0.2	0.5	38.7
Average W 5-7	5-7	20.0	0.1	1.5	0.2	0.4	49.8
Average A 0-2	0-2	14.4	0.3	1.1	0.3	0.6	49.0
Average A 2-5	2-5	25.0	0.2	1.3	0.3	0.5	55.8
Average A 5-7	5-7	18.9	0.2	1.4	0.3	0.4	66.6

Appendix 4: Table S8. Leachate chemistry for leaching experiment.

		Column name and day-month of sampling															
		Acid	Water	A1 14-5	A4 15-5	A4 17-5	A4 18-5	A4 19-5	A4 20-5	A4 23-5	A4 26-5	A4 29-5	A4 01-6	A4 04-6	A4 07-6	A4 10-7	
	Units	DL	N/A	N/A	Day 1	2	4	5	6	7	10	13	16	19	22	25	28
Mg	mg/L	0.001	b.d.	b.d.	917	739	1945	2165	2618	2299	2389	2503	2449	2520	2404	2084	2728
Fe	mg/L	0.001	0.033	0.012	0.122	0.003	0.008	0.060	0.020	0.017	0.117	0.010	0.012	0.052	0.008	0.004	0.010
Si	mg/L	0.04	b.d.	b.d.	28.9	15.2	5.52	6.76	2.66	3.20	2.28	1.33	1.46	0.84	0.43	0.75	0.56
Cl	mg/L	≈10ppb	N/A	0.06	740*	344	32.43	2.43	1.01	0.45	0.80	0.74	0.81	0.90	0.85	0.64	1.46
SO₄²⁻	mg/L	≈10ppb	N/A	0.02	18*	799	6571	9026	9715	9168	9580	9688	9449	10165	9959	8200	468
NO₃	mg/L	≈10ppb	N/A	0.03	70.6*	76.9	7.16	1.33	0.48	0.13	0.01	0.04	0.06	0.04	0.05	0.09	1.74
Ca	ppb	0.15	71	44	3380	2476	14270	24609	29400	28720	28315	29014	26731	27415	27579	22608	33135
Na	ppb	31	b.d.	b.d.	52508	6675	1496	1238	999	1074	853	937	460	294	454	293	649
K	ppb	59	b.d.	b.d.	27842	3544	421	1156	966	540	514	402	b.d.	465	55	59	210
Sr	ppb	0.07	0.66	0.49	16.3	12.1	45.6	35.2	31.6	27.4	24.3	31.1	23.8	30.0	33.6	34.3	53.1
Ba	ppb	0.03	b.d.	b.d.	6.72	1.67	8.41	10.7	10.1	6.81	4.67	3.06	2.79	3.09	4.55	3.99	6.88
Al	ppb	0.21	8	b.d.	25	5	b.d.	b.d.	b.d.	b.d.	90	b.d.	3	b.d.	b.d.	b.d.	-12
Mn	ppb	0.09	1	1	4	b.d.	b.d.	2	b.d.	1	1	b.d.	b.d.	b.d.	b.d.	b.d.	0
Ni	ppb	0.52	3	2	19	1	3	2	2	4	4	4	4	2	2	1	1
Cr	ppb	0.14	b.d.	0.33	0.94	3.39	10.8	7.76	5.06	2.22	0.85	0.63	0.18	0.56	0.28	0.18	0.43
Cu	ppb	0.29	b.d.	b.d.	2.96	0.75	1.19	b.d.	1.37	b.d.	1.26	1.08	b.d.	b.d.	0.60	b.d.	b.d.
Co	ppb	0.79	1.97	b.d.	10.4	2.15	4.71	3.88	1.15	1.85	2.44	b.d.	b.d.	1.18	3.30	6.26	3.14
Ti	ppb	0.51	0.78	b.d.	b.d.	b.d.	3.22	4.00	3.92	4.54	13.02	4.59	6.05	3.52	6.38	5.18	3.99
Zn	ppb	0.32	9	7	33	6	5	8	6	8	13	7	9	5	5	3	6

*Sample A3 and W3 used for anions analysis due to the small sample volume available for analysis.

Appendix 4: Table S8. continued.

		Column name and day-month of sampling														
		W1 14-5	W4 15-5	W4 15-5 REP	W4 17-5	W4 18-5	W4 19-5	W4 20-5	W4 23-5	W4 26-5	W4 29-5	W4 01-6	W4 01-6 REP	W4 07-6	W4 10-6	
	Units	DL	Day 1	2	2	4	5	6	7	10	13	16	19	19	25	28
Mg	mg/L	0.001	858	278	283	170	132	111	107	95	88	82	80	78	69	72
Fe	mg/L	0.001	0.197	0.007	0.005	0.022	0.007	0.011	0.435	0.012	0.020	0.001	0.013	0.001	0.003	0.010
Si	mg/L	0.04	29.6	24.5	24.2	17.5	6.34	3.85	2.32	1.94	1.11	0.98	0.66	1.13	0.47	0.80
Cl	mg/L	≈10ppb	621*	274	N/A	117	42.7	10.1	2.71	0.36	0.17	0.25	0.28	0.14	0.12	2.08
SO₄²⁻	mg/L	≈10ppb	14.1*	3.42	N/A	2.78	2.62	2.57	2.12	2.20	2.01	1.91	1.83	1.48	1.47	1.80
NO₃	mg/L	≈10ppb	56.3*	35.6	N/A	13.2	5.51	2.31	0.89	0.12	0.08	0.19	0.20	0.06	0.05	1.73
Ca	ppb	0.15	2282	1356	1359	1094	1029	927	851	923	926	933	1010	934	897	1168
Na	ppb	31	43818	5249	5078	1362	904	682	553	b.d.	97	51	b.d.	b.d.	516	723
K	ppb	59	23542	2452	2446	694	733	b.d.	b.d.	336	b.d.	b.d.	b.d.	240	b.d.	b.d.
Sr	ppb	0.07	13.32	5.93	5.56	3.85	3.57	2.64	2.42	3.28	2.98	2.95	3.37	2.89	4.49	15.88
Ba	ppb	0.03	5.47	1.57	0.58	1.13	2.69	0.66	0.37	2.24	0.83	1.02	2.30	b.d.	1.58	1.68
Al	ppb	0.21	5	b.d.	b.d.	b.d.	b.d.	b.d.	b.d.	b.d.	b.d.	b.d.	b.d.	b.d.	b.d.	b.d.
Mn	ppb	0.09	0	0	0	0	0	0	7	0	0	0	0	1	0	0
Ni	ppb	0.52	5	0	0	0	0	1	1	0	0	0	0	1	0	0
Cr	ppb	0.14	3.16	0.94	b.d.	0.36	0.64	b.d.	5.24	0.65	0.14	1.14	0.21	0.20	0.95	b.d.
Cu	ppb	0.29	2.09	0.47	b.d.	b.d.	0.96	1.00	1.34	1.36	1.21	0.77	0.35	0.38	0.83	0.72
Co	ppb	0.79	12.1	b.d.	b.d.	b.d.	2.63	2.30	0.94	b.d.	3.54	b.d.	3.27	b.d.	2.23	b.d.
Ti	ppb	0.51	2.76	b.d.	b.d.	b.d.	1.79	0.62	b.d.	b.d.	0.97	b.d.	1.60	b.d.	3.84	b.d.
Zn	ppb	0.32	19	8	7	11	4	7	4	3	5	3	2	6	2	5

*Sample A3 and W3 used for anions analysis due to the small sample volume available for analysis.

Appendix 4: Table S9. Volume of recovered leachates, and calculated Mg mass leached.

Day	Volume of leachate collected	Mg concentration	Mg mass in collected leachate	Mg in 8 mL subsample for evaporation	Mg mass in leachate if treatment applied to 1 m²
<i>Units</i>	<i>mL</i>	<i>mg/L</i>	<i>mg</i>	<i>mg</i>	<i>mg</i>
<i>Acid-leached</i>					
1*	1.23	916.66	1.13	7.33	849.65
2	19.77	738.71	14.60	5.91	11005.10
4	17.76	1945.29	34.55	15.56	26036.54
5	17.79	2165.45	38.53	17.32	29034.63
6	19.59	2617.83	51.28	20.94	38640.35
7	20.34	2298.76	46.76	18.39	35235.24
8	19.74	2343.67 [†]	46.26	18.75	34861.69
9	20.28	2343.67 [†]	47.53	18.75	35816.65
10	19.08	2388.58	45.57	19.11	34342.14
11	21.52	2445.97 [†]	52.63	19.57	39658.03
12	20.18	2445.97 [†]	49.37	19.57	37204.51
13	21.42	2503.35	53.63	20.03	40414.69
14	19.50	2476.36 [†]	48.29	19.81	36391.69
15	20.36	2476.36 [†]	50.41	19.81	37985.37
16	19.74	2449.37	48.36	19.59	36441.38
17	19.73	2484.51 [†]	49.01	19.88	36930.85
18	19.75	2484.51 [†]	49.06	19.88	36972.98
19	19.39	2519.65	48.86	20.16	36822.22
20	19.63	2461.72 [†]	48.33	19.69	36422.44
21	19.43	2461.72 [†]	47.83	19.69	36040.85
22	20.46	2403.78	49.19	19.23	37068.57
23	19.68	2445.97 [†]	48.14	19.57	36278.14
24	19.74	2445.97 [†]	48.28	19.57	36379.70
25	20.06	2083.78	41.80	16.67	31498.14
26	18.83	2445.97 [†]	46.05	19.57	34704.94
27	19.69	2445.97 [†]	48.16	19.57	36295.84
28	19.69 [†]	2727.51	53.86	21.82	40589.27

*Because of sample size constraints, for day 1, samples A1 and W3 were analysed in place of A4 and W4, respectively.

[†]Average of the Mg concentrations from the previous- and next-day samples; applied to leachate volume on day 28 due to a sample spill, and for Mg concentrations on days when samples were not analysed.

Appendix 4: Table S9. continued.

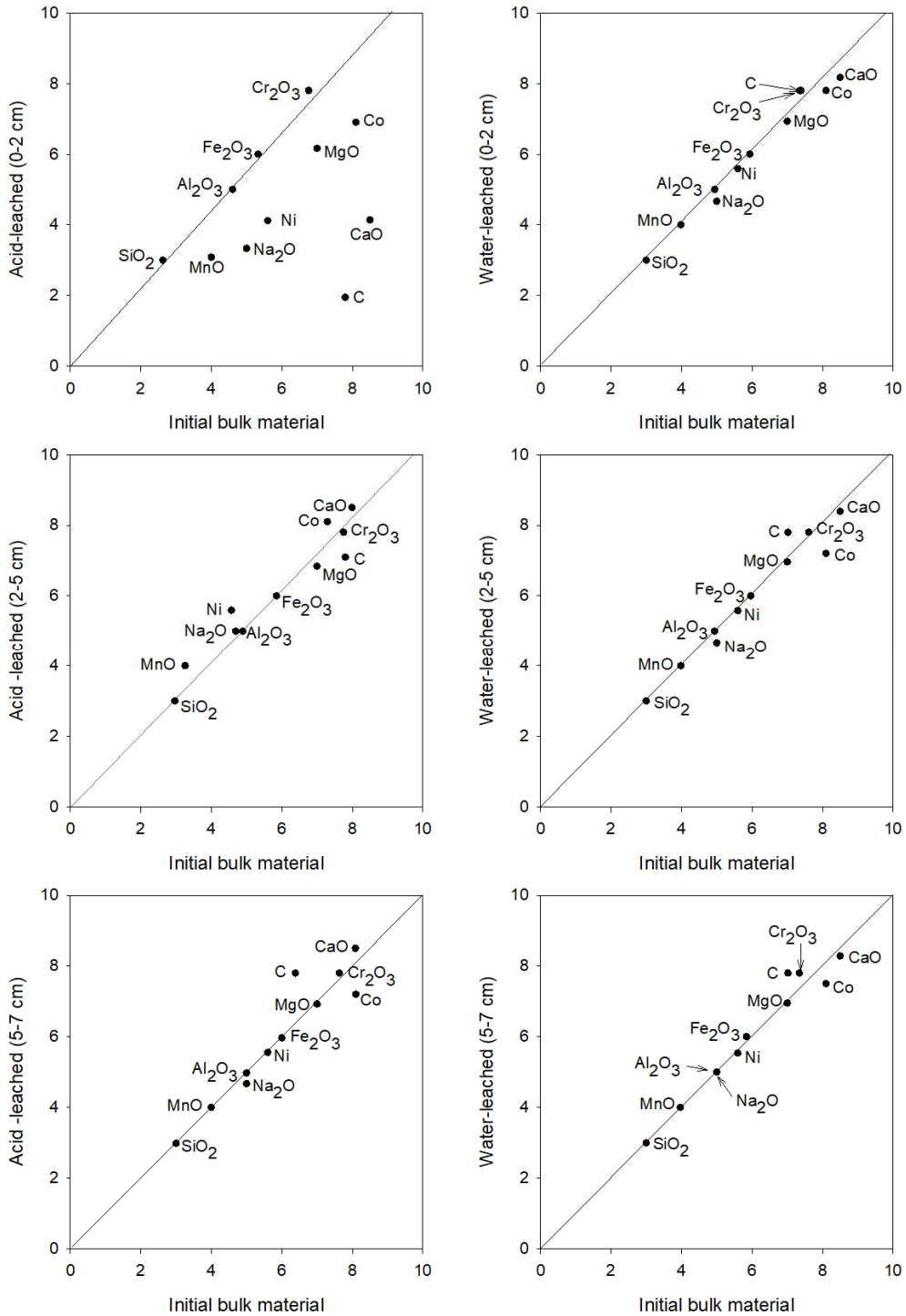
Day	Volume of leachate collected	Mg concentration	Mg mass in collected leachate	Mg in 8 mL subsample for evaporation	Mg mass in leachate if treatment applied to 1 m ²
<i>Units</i>	<i>mL</i>	<i>mg/L</i>	<i>mg</i>	<i>mg</i>	<i>mg</i>
<i>Water-leached</i>					
1*	1.67	858.10	1.43	6.86	1079.90
2	18.80	277.82	5.22	2.22	3936.04
4	20.13	170.13	3.42	1.36	2580.74
5	19.87	131.55	2.61	1.05	1969.77
6	20.10	110.95	2.23	0.89	1680.72
7	22.15	107.02	2.37	0.86	1786.35
8	19.24	101.11 [†]	1.95	0.81	1466.00
9	20.34	101.11 [†]	2.06	0.81	1549.36
10	19.77	95.19	1.88	0.76	1418.20
11	20.33	91.40 [†]	1.86	0.73	1400.25
12	20.13	91.40 [†]	1.84	0.73	1386.74
13	21.16	87.60	1.85	0.70	1396.96
14	18.89	84.70 [†]	1.60	0.68	1205.72
15	19.83	84.70 [†]	1.68	0.68	1265.39
16	15.57	81.79	1.27	0.65	959.65
17	21.38	80.89 [†]	1.73	0.65	1303.37
18	19.23	80.89 [†]	1.56	0.65	1172.02
19	16.31	79.99	1.30	0.64	983.37
20	21.57	74.06 [†]	1.60	0.59	1204.11
21	19.28	74.06 [†]	1.43	0.59	1076.12
22	20.17	68.13	1.37	0.55	1035.83
23	19.68	68.53 [†]	1.35	0.55	1016.08
24	19.66	68.53 [†]	1.35	0.55	1015.06
25	19.80	68.93	1.36	0.55	1028.31
26	18.83	70.63 [†]	1.33	0.57	1002.29
27	19.71	70.63 [†]	1.39	0.57	1049.13
28	19.71 [†]	72.34	1.43	0.58	1074.49

*Because of sample size constraints, for day 1, samples A1 and W3 were analysed in place of A4 and W4, respectively.

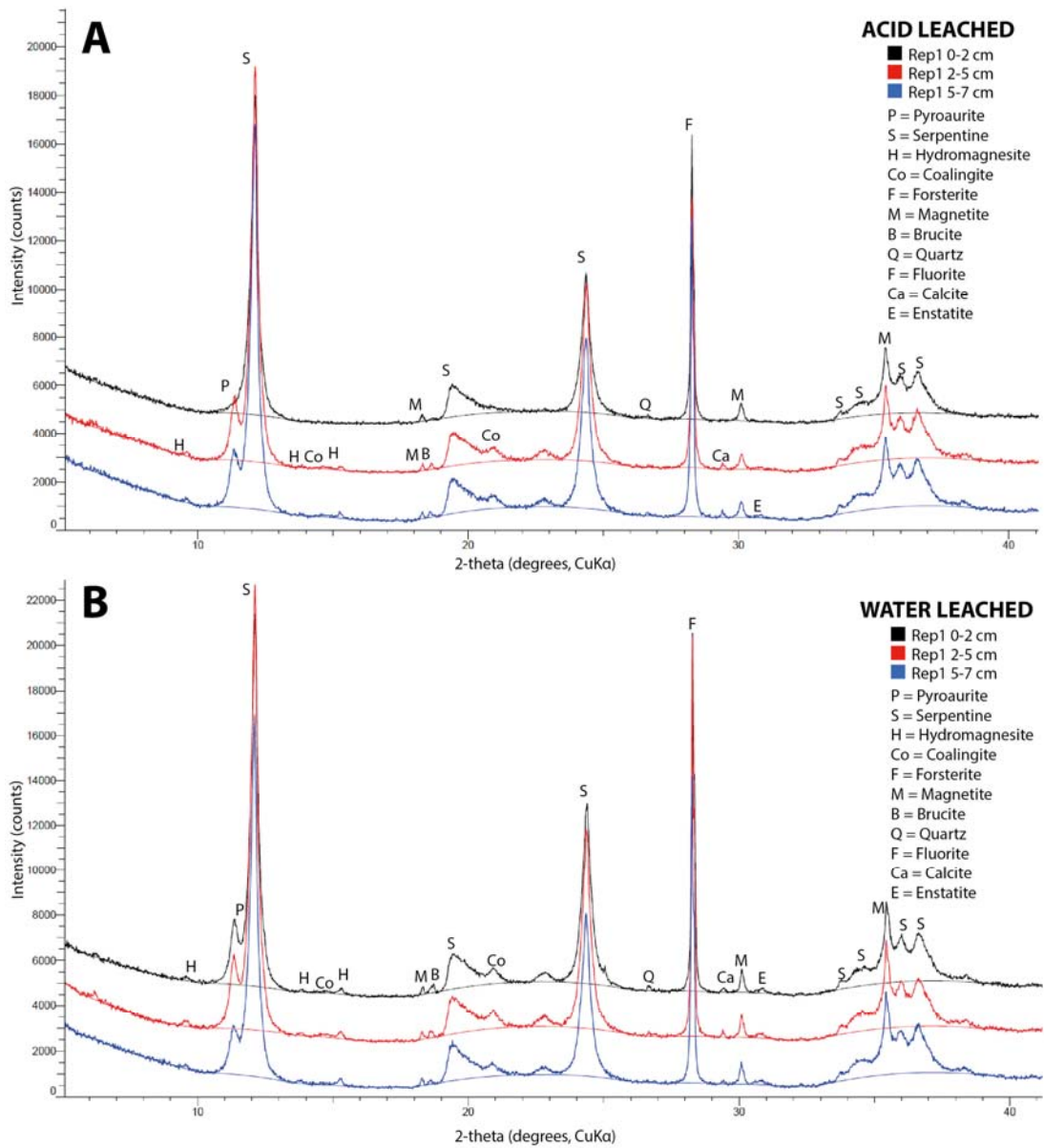
[†]Average of the Mg concentrations from the previous- and next-day samples; applied to leachate volume on day 28 due to a sample spill, and for Mg concentrations on days when samples were not analysed.

Appendix 4: Table S10. Summary of total leached Mg and calculated carbon sequestration potential (assuming Mg is precipitated as 100 % nesquehonite) in the collected leachate, the subsamples evaporated in Petri dishes, and normalised to a 1-m² treated area.

		Collected leachate	Subsample for evaporation	1-m ² treated area
<i>Acid-leached (A4)</i>				
	<i>Units</i>			
Total Mg leached	g	1.21	0.50	909.92
% of original Mg leached	%	8.46	N/A	N/A
Nesquehonite equivalent	g	6.87	2.82	5178.84
Expected carbon content	g	0.60	0.24	449.52
Expected C uptake rate	g C/year	7.75	3.18	5843.80
Expected CO₂ uptake rate	g CO ₂ / year	28.42	11.67	21414.29
<i>Water-leached (W4)</i>				
Total Mg leached	g	0.05	0.02	36.96
% of original Mg leached	%	0.34	N/A	N/A
Nesquehonite equivalent	g	0.28	0.11	210.37
Expected carbon content	g	0.02	0.01	18.26
Expected C uptake rate	g C/year	0.32	0.13	237.38
Expected CO₂ uptake rate	g CO ₂ / year	1.15	0.47	869.87



Appendix 4: Figure S5. Isocons (Grant, 1986) plotted using average XRD data for each depth interval in water and acid leached columns.



Appendix 4: Figure S6. XRD plot showing mineralogy of each interval. Patterns have been offset for ease of comparison and intensity has been scaled by a factor of two to emphasise low-intensity peaks.

Appendix 4: Table S11. XRF data (in wt. %) for water and acid leached tailings residues.

<i>Water leached</i>												
Sample	Detection Limit	Bulk 1	W1 0-2	W1 2-5	W1 5-7	W1 5-7 REP	W2 0-2	W2 2-5	W2 5-7	W3 0-2	W3 2-5	W3 5-7
Depth (cm)			0-2	2-5	5-7	5-7	0-2	2-5	5-7	0-2	2-5	5-7
SiO ₂	0.01	35.73	35.64	35.52	35.52	35.53	35.69	35.84	35.71	35.86	35.73	35.61
Al ₂ O ₃	0.01	0.58	0.58	0.59	0.59	0.58	0.59	0.58	0.58	0.59	0.59	0.57
CaO	0.01	0.26	0.25	0.26	0.24	0.25	0.26	0.25	0.26	0.24	0.26	0.26
Fe ₂ O ₃	0.01	7.73	7.97	7.87	8.05	8.03	7.77	7.7	7.78	7.69	7.76	7.98
K ₂ O	0.001	0.001	b.d.	0.002	b.d.	0.001	0.001	0.001	0.001	b.d.	b.d.	0.001
MgO	0.01	39.4	39	39.1	39	39.1	38.9	39.3	39.2	39.2	39.2	39.2
Na ₂ O	0.01	0.05	0.05	0.05	0.05	0.06	0.04	0.04	0.05	0.05	0.05	0.05
P ₂ O ₅	0.001	0.011	0.011	0.011	0.011	0.012	0.011	0.011	0.012	0.012	0.011	0.011
SO ₃	0.001	0.076	0.074	0.071	0.071	0.069	0.068	0.071	0.07	0.068	0.072	0.071
TiO ₂	0.001	0.003	0.004	0.004	0.007	0.005	0.003	0.005	0.004	0.004	0.005	0.005
MnO	0.001	0.099	0.099	0.099	0.099	0.099	0.099	0.099	0.1	0.1	0.1	0.1
BaO	0.001	0.007	0.006	0.007	0.007	0.008	0.008	0.011	0.006	0.011	0.005	0.01
Cr ₂ O ₃	0.001	0.355	0.389	0.367	0.378	0.38	0.365	0.357	0.363	0.375	0.368	0.39
Ni	0.001	0.189	0.189	0.188	0.186	0.186	0.188	0.188	0.187	0.189	0.189	0.187
Co	0.001	0.009	0.009	0.008	0.008	0.008	0.008	0.008	0.008	0.009	0.008	0.009
Total C	0.01	0.48	0.5	0.56	0.53	0.54	0.54	0.51	0.54	0.48	0.53	0.52
Organic C	0.01		0.04									
LOI as received	0.01	15.63	15.83	15.96	15.9	15.86	16.13	15.74	15.85	15.65	15.71	15.7
Total			100.6	100.7	100.6	100.7	100.7	100.7	100.7	100.5	100.6	100.7

Appendix 4: Table S11. continued.

<i>Acid leached</i>														
Sample	Detection Limit	Bulk 1	A1 0-2	A1 0-2 REP	A1 2-5	A1 5-7	A2 0-2	A2 2-5	A2 5-7	A2 5-7 REP	A3 0-2	A3 2-5	A3 5-7	A3 5-7 REP
Depth (cm)			0-2	0-2	2-5	5-7	0-2	2-5	5-7	5-7	0-2	2-5	5-7	5-7
SiO ₂	0.01	35.73	40.78	40.88	36.07	35.6	40.82	36.52	35.43	35.36	40.9	35.91	35.36	35.38
Al ₂ O ₃	0.01	0.58	0.62	0.63	0.59	0.58	0.63	0.6	0.58	0.57	0.64	0.59	0.57	0.57
CaO	0.01	0.26	0.12	0.12	0.28	0.26	0.13	0.26	0.29	0.29	0.13	0.29	0.27	0.28
Fe ₂ O ₃	0.01	7.73	8.6	8.62	7.93	7.59	8.75	8	7.76	7.77	8.77	7.86	7.71	7.71
K ₂ O	0.001	0.001	b.d.	b.d.	0.001	b.d.	b.d.	0.001	b.d.	b.d.	0.001	0.001	0.001	0.001
MgO	0.01	39.4	34.8	34.9	38.7	39.1	34.9	38.3	39	39.1	34.4	38.5	38.8	38.8
Na ₂ O	0.01	0.05	0.05	0.03	0.06	0.05	0.03	0.05	0.04	0.04	0.02	0.05	0.05	0.05
P ₂ O ₅	0.001	0.011	0.010	0.011	0.012	0.011	0.010	0.011	0.012	0.011	0.010	0.011	0.011	0.011
SO ₃	0.001	0.076	1.080	1.080	0.548	0.553	1.060	0.633	0.568	0.568	1.080	0.588	0.569	0.572
TiO ₂	0.001	0.003	0.006	0.006	0.005	0.004	0.008	0.006	0.004	0.003	0.004	0.005	0.005	0.005
MnO	0.001	0.099	0.075	0.074	0.123	0.098	0.077	0.119	0.100	0.101	0.077	0.123	0.099	0.099
BaO	0.001	0.007	0.009	0.005	0.004	0.007	0.006	0.008	0.008	0.007	0.008	0.008	0.011	0.007
Cr ₂ O ₃	0.001	0.355	0.409	0.412	0.358	0.361	0.398	0.354	0.371	0.369	0.422	0.360	0.357	0.356
Ni	0.001	0.189	0.134	0.135	0.235	0.186	0.147	0.224	0.189	0.191	0.136	0.236	0.187	0.186
Co	0.001	0.009	0.007	0.007	0.010	0.008	0.008	0.010	0.008	0.008	0.008	0.010	0.008	0.008
Total C	0.01	0.48	0.11	0.11	0.44	0.61	0.12	0.42	0.55	0.55	0.13	0.45	0.6	0.56
Organic C	0.01		0.05	0.05										
LOI as received	0.01	15.63	14.17	14.1	15.38	16.22	13.91	15.53	16.06	16.06	14.5	15.77	16.51	16.56
Total			101.0	101.1	100.7	101.2	101.0	101.0	101.0	101.0	101.2	100.8	101.1	101.2

Appendix 4: Table S12. Rietveld refinement results for water and acid leached tailings residues.

	Bulk 1	Bulk 2	Bulk 3	W1 0-2	W1 2-5	W1 5-7	W2 0-2	W2 2-5	W2 5-7	W3 0-2	W3 2-5	W3 5-7
Depth (cm)				0-2	2-5	5-7	0-2	2-5	5-7	0-2	2-5	5-7
Properties												
Bulk density (g/cm³)				1.1	1.3	1.5	1.1	1.2	1.6	1.0	1.4	1.5
Porosity				0.58	0.50	0.41	0.56	0.52	0.39	0.60	0.47	0.43
Pore saturation (%)				21	34	44	28	34	52	27	49	54
Mineralogy wt. %												
Serpentine	85.9	86.7	87.3	87.5	87.3	86.7	87.8	87.7	86.3	89.2	86.1	88.3
Pyroaurite	3.1	3.2	2.2	2.2	2.7	2.1	1.7	2.7	2.8	1.5	3.1	1.7
Brucite	1.3	1.2	1.1	0.8	0.7	0.6	0.7	0.9	1.1	0.9	1.0	0.9
Magnetite/Chromite	2.9	2.6	3.2	3.4	3.2	3.2	3.2	2.7	2.8	2.4	2.6	3.4
Enstatite	1.5	1.3	1.4	1.9	1.5	2.6	2.3	0.7	1.4	1.7	1.5	0.6
Forsterite	1.6	1.7	1.6	1.2	1.1	2.1	1.9	1.6	3.1	1.0	1.9	2.1
Hydromagnesite	3.1	2.9	2.7	2.5	3.1	2.4	2.0	3.2	2.2	2.8	3.5	2.7
Quartz	0.3	0.2	0.2	0.2	0.2	0.2	0.1	0.2	0.2	0.1	0.1	0.1
Calcite	0.3	0.2	0.2	0.3	0.3	0.2	0.3	0.3	0.2	0.2	0.3	0.2
Nesquehonite	0.0	0.0	0.0	0.0	0.0	0.0	0.0	0.0	0.0	0.0	0.0	0.0
Magnesite	0.0	0.0	0.0	0.0	0.0	0.0	0.0	0.0	0.0	0.0	0.0	0.0
Chlorite	0.0	0.0	0.0	0.0	0.0	0.0	0.0	0.0	0.0	0.0	0.0	0.0
Tremolite	0.0	0.0	0.0	0.0	0.0	0.0	0.0	0.0	0.0	0.0	0.0	0.0
Total	100.0	100.0	100.0	100.0	100.0	100.0	100.0	100.0	100.0	100.0	100.0	100.0
R_{wp}^a	10.1	10.3	11.5	10.2	9.8	9.9	9.0	9.3	9.8	8.8	9.7	10.2
χ²^b	2.6	2.5	2.9	2.4	2.3	2.3	2.1	2.1	2.1	2.1	2.4	2.5
d^c	0.4	0.4	0.3	0.4	0.5	0.4	0.6	0.5	0.5	0.5	0.4	0.4

^a Weighted pattern residual, a function of the least-squares residual (%).

^b Reduced χ^2 statistic for the least-squares fit.

^c Weighted Durbin Watson statistic.

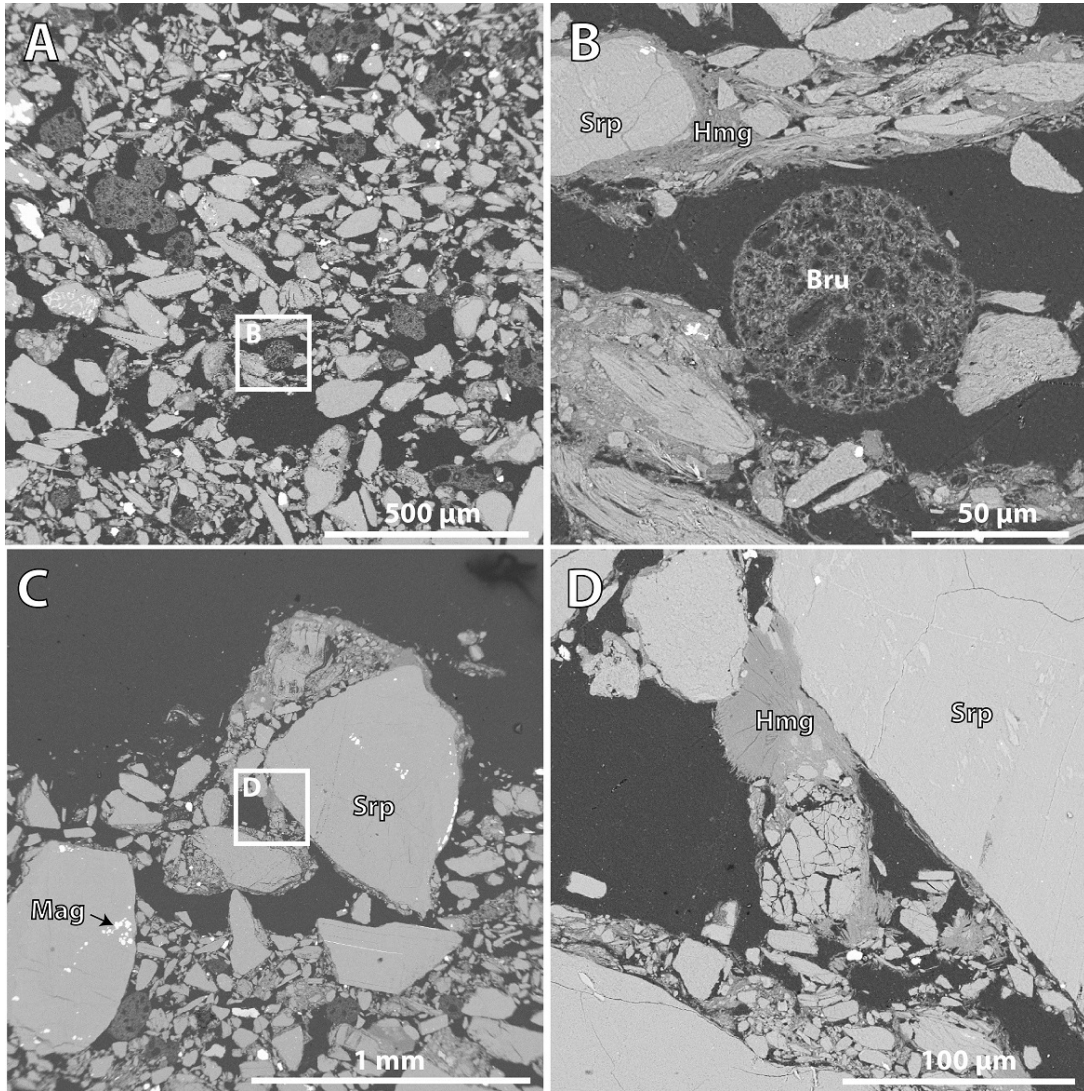
Appendix 4: Table S12. continued.

	A1	A1	A1	A2	A2	A2	A3	A3	A3
	0-2	2-5	5-7	0-2	2-5	5-7	0-2	2-5	5-7
Depth (cm)	0-2	2-5	5-7	0-2	2-5	5-7	0-2	2-5	5-7
Properties									
Bulk density (g/cm³)	1.1	1.2	1.5	1.0	1.3	1.4	1.1	1.3	1.4
Porosity	0.56	0.52	0.43	0.60	0.49	0.45	0.57	0.51	0.45
Pore saturation (%)	46	45	58	48	67	74	53	55	67
Mineralogy wt. %									
Serpentine	90.9	87.1	87.9	89.3	89.8	87.3	89.6	88.9	87.8
Pyroaurite	0.0	2.5	2.2	0.1	1.2	1.9	0.2	1.4	1.3
Brucite	0.4	0.6	0.9	0.5	0.6	1.3	0.3	0.7	0.8
Magnetite/Chromite	3.5	3.2	2.5	3.7	2.9	3.0	3.9	3.0	3.1
Enstatite	2.1	1.3	2.4	2.3	1.7	1.7	2.8	1.7	3.0
Forsterite	2.7	2.5	1.7	3.7	2.3	1.6	2.8	2.2	2.0
Hydromagnesite	0.0	2.1	2.0	0.0	1.2	2.8	0.0	1.8	1.6
Quartz	0.4	0.4	0.1	0.3	0.2	0.1	0.4	0.1	0.2
Calcite	0.0	0.3	0.3	0.1	0.2	0.3	0.1	0.2	0.2
Nesquehonite	0.0	0.0	0.0	0.0	0.0	0.0	0.0	0.0	0.0
Magnesite	0.0	0.0	0.0	0.0	0.0	0.0	0.0	0.0	0.0
Chlorite	0.0	0.0	0.0	0.0	0.0	0.0	0.0	0.0	0.0
Tremolite	0.0	0.0	0.0	0.0	0.0	0.0	0.0	0.0	0.0
Total	100.0	100.0	100.0	100.0	100.0	100.0	100.0	100.0	100.0
R_{wp}^a	9.7	9.4	9.1	10.3	10.3	10.2	11.5	10.2	10.0
χ²^b	2.1	2.1	2.1	2.5	2.6	2.6	2.9	2.5	2.6
d^c	0.6	0.5	0.5	0.4	0.4	0.4	0.3	0.4	0.5

^a Weighted pattern residual, a function of the least-squares residual (%).

^b Reduced χ^2 statistic for the least-squares fit.

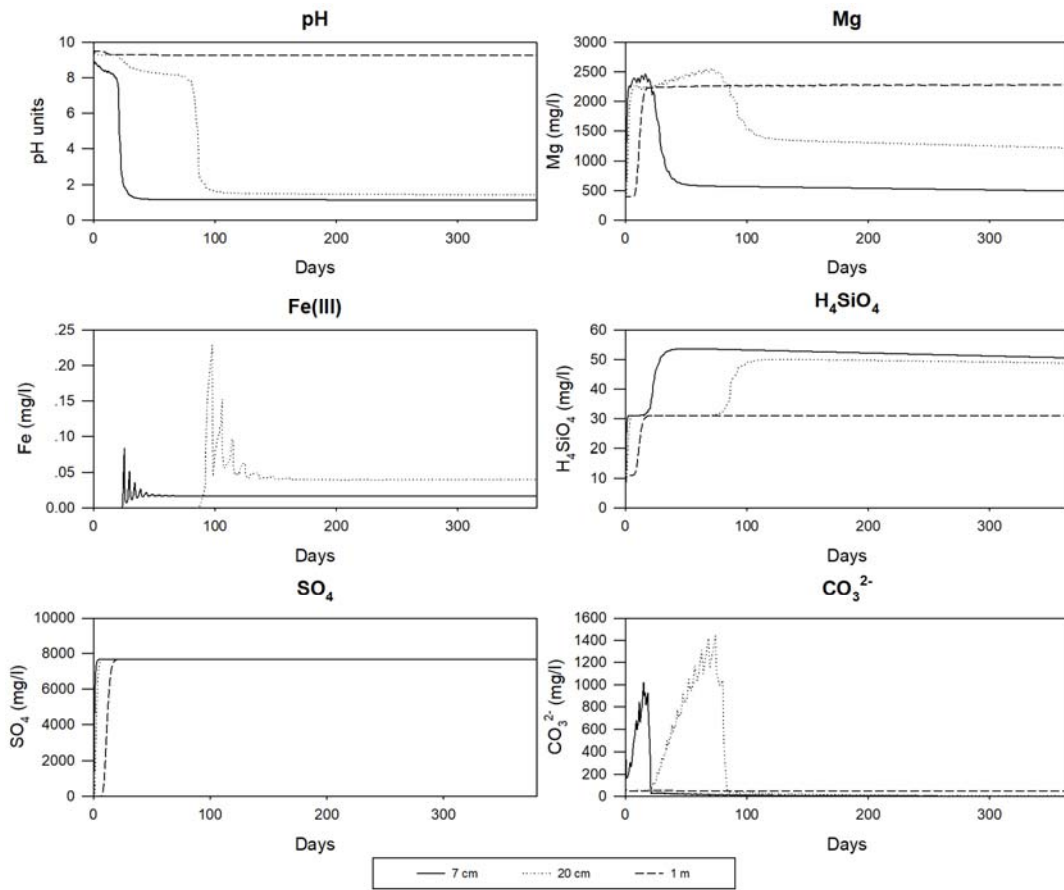
^c Weighted Durbin Watson statistic.



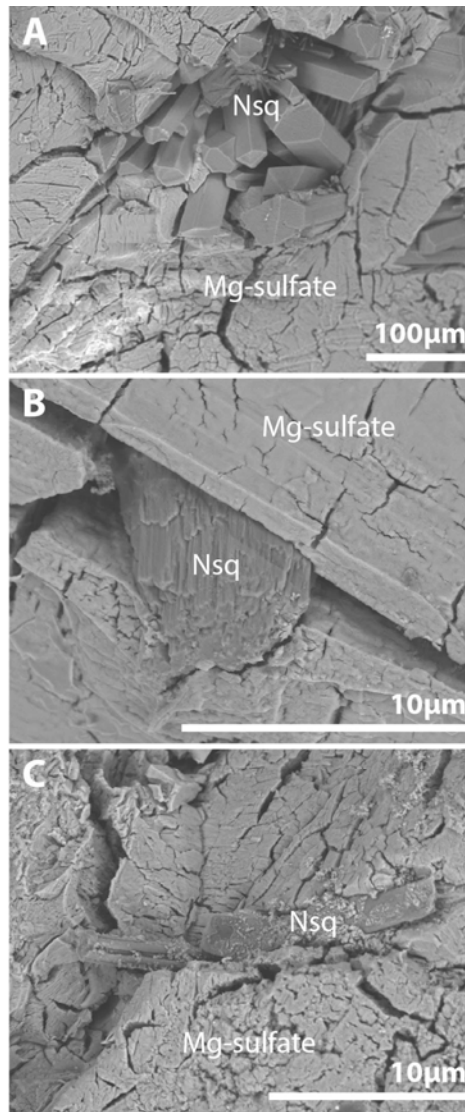
Appendix 4: Figure S7. SEM-BSE (backscattered electron) micrographs of the water-leached column. (A) Spherical, porous brucite (Bru) grains (darker grey) intermixed with serpentine (Srp) grains (lighter grey). (B) Higher magnification image of the brucite grain from A. (C) Serpentine grains, with magnetite (Mag) inclusions, at the surface of the water leached column. (D) Higher magnification image of region highlighted in C, showing hydromagnesite (Hmg) cementation at the surface of the water leached column.

Appendix 4: Table S13. Nitrogen, carbon and hydrogen contents of precipitates evaporated from leachates. Measured mass of C in precipitates is reported as a percentage of predicted carbon mass in precipitates, as calculated from Mg-concentrations in leachate.

	%N	%C	%H	Precipitate mass (g)	C mass (g)	% of predicted C uptake (from Table S10)
<i>Acid-leached</i>						
Average	0.00	0.24	5.19	3.97	0.009	3.9
Min	0.00	0.19	5.06	3.78	0.008	3.3
Max	0.00	0.29	5.48	4.08	0.012	5.0
<i>Water-leached</i>						
Average	0.00	7.90	4.07	0.09	0.007	70.8
Min	0.00	7.69	3.95	0.09	0.007	66.6
Max	0.01	8.14	4.21	0.09	0.007	74.6



Appendix 4: Figure S9. MIN3P acid-leaching model predictions of leachate chemistry at 7 cm, 20 cm and 1 m depth.



Appendix 4: Figure S9. (A–C) Nesquehonite crystals within larger Mg-sulfate crystals, all of which precipitated during evaporation of acid-treated column leachates.